Numerical and Experimental Study of Interactions between Surface Acoustic Waves, Fluids and Particles in Acoustofluidic Systems

Sadaf MaramiZonouz

M.Sc. B.Sc.

Ph.D.

2021

Numerical and Experimental Study of Interactions between Surface Acoustic Waves, Fluids and Particles in Acoustofluidic Systems

Sadaf MaramiZonouz

M.Sc. B.Sc.

A thesis submitted in partial fulfilment of the requirements of

the University of Northumbria at Newcastle

for the degree of Doctor of Philosophy

Research undertaken in the faculty of

Engineering and Environment

2021

Declaration

I declare that the work contained in this thesis has not been submitted for any other award and that it is all my own work. I also confirm that this work fully acknowledges opinions, ideas, and contributions from the work of others.

Ethical approval for the present research has been sought and granted by the Faculty Ethics Committee on 25/10/2018.

I declare that the Word Count of this Thesis is 44,217 words.

Name: Sadaf MaramiZonouz

Signature:

Date: 30 August 2021

Acknowledgements

Firstly, I would like to express my sincere gratitude to my supervisors Dr Mohammad Rahmati and Professor YongQing (Richard) Fu whose support, guidance, and encouragements have been invaluable throughout my PhD and without whom I would not have been able to complete this research.

Furthermore, I would like to thank Professor Thomas Franke and Dr Andreas Link from the Biomedical Engineering group at University of Glasgow, Dr Xin (Chris) Yang and his team from the Medical Ultrasound and Sensor Laboratory (MUSL) at Cardiff University, and Dr Jeremy J. Hawkes from Acoustic Machines Liverpool for granting me access to their laboratories and equipment and assisting me in my experimental study.

I would also like to thank Professor Glan McHale from University of Edinburgh, Dr Hamdi Torun, Dr Ran Tao, the Smart Microsystems group members, and the technical staff at Northumbria University for providing me with helpful advice and feedback throughout my research.

I gratefully acknowledge the funding I received towards my PhD form Northumbria University. I am also grateful to the funding received through the UK Engineering and Physical Sciences Research Council (EPSRC), and the Special Interest Group of Acoustofluidics from UK Fluids Network (UKFN).

Finally, I would like to offer my special thanks to my family particularly my mother, my sister, and my partner for their unwavering support and belief in me.

Abstract

Acoustofluidics refers to the multidisciplinary field of investigating the integration of acoustics with microfluidics which can be used to develop tools to manipulate and control microfluids and particles. Acoustofluidic technologies present numerous advantages including small size, simple design, low cost, reliability, efficiency, and as a result can be adapted to various applications. Moreover, for biomedical applications, acoustofluidics offer benefits such as non-invasive and contact-free manipulation with high biocompatibility, conserving cell viability and proliferation. With these advantages, acoustofluidics present a great potential to be utilised in many clinical and biomedical applications such as lab-on-chip, organ-on-chip, and controllable drug delivery platforms.

Most of the current studies on acoustofluidics are based on an experimental investigation which is essential for testing a hypothesis scientifically and to ensure that the acoustofluidic system functions properly. Experimental methods can be used for optimising acoustofluidic systems or evaluating a new design based on trial-and-error approaches. However, experimental acoustofluidcs could be costly and time-consuming. Computational modelling can provide detailed information of the underlying physics of the complex acoustofluidic systems in a more cost and time-effective manner. These details, which can be useful for adapting acoustofluidic systems in practical devices, are sometimes hard or even impossible to obtain through experimental work.

In this thesis, computational models are utilised in order to investigate the behaviour of fluids and particles in novel acoustofluidic platforms including flexible acoustofluidics and capillary bridge channels. The models are first validated using the experimental results reported in the literature and then, they are used to analyse the behaviour and to understand the underlying physics of novel acoustofluidic platforms such as flexible thin film surface acoustic wave devices and capillary bridges for the purpose of particle manipulation.

Typically, most acoustofluidic systems presented in existing literature are designed using rigid piezoelectric materials to generate acoustic fields. These rigid piezoelectric materials are generally brittle, fragile, and prone to breaking when applied with higher powers. In this thesis, flexible thin film surface acoustic wave devices with metal substrates are utilised for particle and cell manipulations, and to study their acoustofluidic behaviour in different conformations obtained through bending and to investigate the effects of bending curvatures on

microparticle's manipulation inside a microchamber. These flexible thin film devices present advantages including high wave speed and reasonable electro-mechanical properties for the flexible thin film devices.

Additionally, for continuous flow applications to enable the fluid flow, microchannels are typically fabricated with solid materials and in cleanroom environment using complicated and time-consuming processes. This thesis presents the idea to integrate flexible thin film surface acoustic wave devices with continuous flow wall-less microfluidic platforms designed using capillary bridges. Using capillary bridge channels simplifies the production of microchannels while decreasing the fabrication cost and time.

This new platform which comprises of flexible thin film surface acoustic wave devices with metal substrates and capillary bridge channels is utilised for particle and cell manipulation and is investigated in detail through both computational modelling and experimental study. These novel acoustofluidic platforms can offer potential applications in flexible microfluidics, bio-inspired and body conforming wearable devices, and wearable point-of-care applications.

The significant contributions of this thesis can be summarised as follows:

1. For the first time, flexible thin film surface acoustic wave devices with metal substrates are utilised for the purpose of particle and cell manipulation. Through both experimental study and computational modelling, the effects of various vibration modes, different bending curvatures, and twisting geometries are investigated.
   It was presented that flexible surface acoustic wave devices bent in concave/convex geometries produce particle patterns converged with a slope towards/ diverged with a slope away from the centre of the curvature of the geometry.
2. Glass microtubes (with both rectangular and circular cross-sections) are integrated with flexible thin film surface acoustic wave devices for the purpose of particle and cell manipulation with and without fluid flow. The effects of different microtube cross-sections, microtube inclination angle regarding the electrodes of the surface acoustic wave device, and different fluid flow rates on particle patterning are systematically investigated.
   For rectangular microtubes placed at an angle relative to the electrodes, particle pattern lines were parallel to the tube walls.
   For circular microtubes, different particle patterns were observed which were dependent on their positions along the tube's height. In the bottom/middle height of the tube, the particle

pattern lines were parallel to the tube direction due to the acoustic wave propagation into the water and formation of a standing wave along the direction of the circular tube/ perpendicular to the tube direction as the standing wave propagated around the circular cross-section of the tube perpendicular to the tube direction.

3. For the first time, capillary bridge channels are integrated with flexible thin film surface acoustic wave devices with metal substrates to develop a continuous flow acoustofluidic setup for particle and cell manipulations. Through both experimental work and three-dimensional numerical modelling, the effects of different frequencies, channel geometries, particle properties, and flow rates are investigated.

   It was shown that the particles were aligned on the pressure node lines of the acoustic pressure field and parallel to the air-water walls of the capillary bridge channels due to the combined effects of the acoustic wave field inside the water channel and the fluid flow.

4. The effects of acoustic streaming on fluid and microparticles in a microchannel flow are investigated through both experimental studies and three-dimensional numerical modelling. Two different modelling approaches are compared:

   1st Approach: The whole acoustic field coupled to the flow field is simulated and the acoustic streaming force is calculated using the first order acoustic density and velocity which predicted the acoustofluidic system more accurately.

   2nd Approach: The acoustic streaming is modelled by assuming the velocity of a one-dimensional attenuating surface acoustic wave and using the acoustic streaming force formula which is more efficient in terms of computational cost and time while still presenting results with reasonable accuracy.

Publications

Journals:

- **S. Maramizonouz**, X. Tao, M. Rahmati, C. Jia, R. Tao, H. Torun, T. Zheng, H. Jin, S. Dong, J. Luo, Y. Fu, "Flexible and Bendable Acoustofluidics for Particle and Cell Patterning", *International Journal of Mechanical Sciences*, 2021. (Published)
- **S. Maramizonouz**, M. Rahmati, A. Link, T. Franke, Y. Fu, "Numerical and Experimental Studies of Acoustic Streaming Effects on Microparticles/Droplets in Microchannel Flow", *International Journal of Engineering Science*, 2021. (Published)
- **S. Maramizonouz**, C. Jia, M. Rahmati, T. Zheng, Q. Liu, H. Torun, Q. Wu, Y. Fu, "Acoustofluidic Patterning inside Capillary Tubes Using Standing Surface Acoustic Wave", *International Journal of Mechanical Sciences*, 2021. (published)
- **S. Maramizonouz**, J. Hawkes, C. Jia, M. Rahmati, T. Zheng, G, McHale, P. Agrawal, C. Sun, X. Yang, Y. Fu, "Wall-less Capillary Bridge Channels for Acoustofluidic Manipulation", *International Journal of Engineering Science*, 2022. (Under review)
- J. Hawkes, **S. Maramizonouz**, C. Jia, M. Rahmati, T. Zheng, M. McDonnell, Y. Fu, "Node Formation Mechanisms in Acoustofluidic Capillary Bridges", *ultrasonics*, 2022. (published)

Conferences:

- **S. Maramizonouz**, M. Rahmati, C. Jia, T. Zheng, Y. Fu, "Acoustic Manipulation of Microparticles in Glass Tubes Using Flexible SAW Devices", UK Fluids Conference 2021, 8^{th}-10^{th} September 2021, University of Southampton, UK.
- **S. Maramizonouz**, M. Rahmati, C. Jia, T. Zheng, Y. Fu, "Microparticle Patterning inside Capillary Tubes on Bendable Thin Film SAW Devices", Acoustofluidics 2021 Conference, 26^{th}-27^{th} August 2021, Virtual Conference, UK.
- **S. Maramizonouz**, M. Rahmati, Y. Fu, "Microparticle Patterning on Bendable and Flexible SAW Devices", Acoustofluidics 2020 Conference, 26^{th}-27^{th} August 2020, Virtual Conference, UK.
- J. Hawkes, **S. Maramizonouz**, C. Jia, M. Rahmati, T. Zheng, M. McDonnell, Y. Fu, "Capillary Bridge Acoustofluidics", Acoustofluidics 2020 Conference, 26th-27th August 2020, Virtual Conference, UK.

- **S. Maramizonouz**, M. Rahmati, Y. Fu, "Numerical Study of The Effects of Inclined IDT Placement with Respect to Microchannel on Microparticles of Different Diameters", Acoustofluidics 2019 Conference, 25th -28th August 2019, Enschede, Netherlands.
- **S. Maramizonouz**, M. Rahmati, Y. Fu, "Numerical and Experimental Study of Acoustic Streaming inside Microchannels", 9th UKFN SIG Acoustofluidics Conference, 16th and 17th October 2019, Cardiff University, Cardiff, UK.
- **S. Maramizonouz**, M. Rahmati, Y. Fu, "Numerical and Experimental Study of Acoustic Streaming in a Microchannel Flow", 7th UKFN SIG Acoustofluidics Forum and Olympics, 26th and 27th June 2019, University of Bristol, Bristol, UK.
- **S. Maramizonouz**, M. Rahmati, Y. Fu, "Numerical Study of Interactions of Acoustic Waves with Fluid and Particles Using ANSYS", 5th UKFN SIG Acoustofluidics Conference, 7th December 2018, Heriot-Watt University Edinburgh, Edinburgh, UK.

Table of Contents

List of Figures

List of Tables

Nomenclature

Symbol	*SI Unit*	*Name*
A	m	wave displacement amplitude
A_x	m	wave displacement amplitude in x-direction
A_y	m	wave displacement amplitude in y-direction
C_i	kg/s	interphase momentum exchange coefficient of fluid-solid interaction
c_f	m/s	isentropic derivative of pressure equal to wave speed in the fluid
c_s	m/s	wave speed in the piezoelectric substrate
c_{wall}	m/s	wave propagation velocity in the wall
D	m	distance between particle pattern lines
d	m	particle diameter
E_{ac}	Pa	acoustic energy density of the wave
$\boldsymbol{F}_I$	N	interaction force among the phases
$\boldsymbol{F}_{AR}$	N	acoustic radiation force
F_{AR_x}	N	acoustic radiation force in x-direction
$\boldsymbol{F}_{AS}$	N	acoustic streaming force
F_{AS_x}	N	acoustic streaming force in x-direction
F_{AS_y}	N	acoustic streaming force in y-direction
f	Hz	frequency
$\tilde{f}$	-	drag function
$\boldsymbol{G}$	N	gravity force on the bulk of the fluid
$\boldsymbol{g}$	m/s^2	gravitational acceleration vector
I_{ac}	W/m^2	wave intensity
$\boldsymbol{k}$	-	wave vector

k	-	wavenumber
L	m	length scale
n	-	number of particles
P	Pa	fluid pressure
P_{ac}	Pa	acoustic pressure amplitude
P_{in}	Pa	acoustic pressure field
P_s	Pa	solid phase pressure
$\boldsymbol{r}$	m	wave position vector
r	m	particle radius
Re	-	Reynolds number
$\boldsymbol{S}$	-	a source term
T	s	wave period
t	s	time
U_{ac}	m/s	wave velocity amplitude
U_{a_x}	m/s	wave velocity in x-direction
U_{a_y}	m/s	wave velocity in y-direction
$\boldsymbol{U}_f$	m/s	fluid velocity vector
$\boldsymbol{U_p}$	m/s	particle velocity vector
$\boldsymbol{U}_{relative}$	m/s	fluid velocity relative to the particle velocity
$\boldsymbol{U}_{wall}$	m/s	wall velocity
$\mathcal{U}$	-	a scalar conserved quantity
$\tilde{\mathcal{U}}$	-	an approximate solution
u_{x-wall}	m/s	SAW velocity in x-direction
u_{y-wall}	m/s	SAW velocity in y-direction

$\boldsymbol{V}_{in}$	m/s	velocity field of the incoming wave
$\forall_p$	m^3	particle volume
$\boldsymbol{W}$	N	gravity and buoyancy force on particle
w	m	channel width
$\boldsymbol{X}_p$	m	particle position vector
x	m	fluid location along the wave propagation direction
$\tilde{x}$	m	particle's distance from the nearest pressure node (or anti-node) along the wave propagation direction
y	m	curve equation
y'	-	first order derivative of the curve equation
y''	1/m	second order derivative of the curve equation
Z_{wall}	Pa s/m^3	wall impedance
α	1/m	wave attenuation parameter or wave attenuation coefficient
α_p	-	solid phase volume fraction
β	rad	angle between microtube and IDTs
β_f	m^2/N	fluid compressibility
β_p	m^2/N	particle compressibility
$\boldsymbol{\Gamma}$	-	flux of quantity $\mathcal{U}$
δ	m	thickness of the viscous, acoustic boundary layer
δx	m	width of the particle line
ζ	-	ratio of the displacement amplitudes in x- and y-directions
θ_R	rad	Rayleigh angle
Κ	1/m	curvature
λ	m	wavelength

μ_f	Pa s	fluid viscosity
μ_s	Pa s	solid phase viscosity
ρ_f	kg/m^3	fluid density
ρ_p	kg/m^3	particle density
ρ_{wall}	kg/m^3	wall density
σ^{-1}	m	fluid attenuation length
$\boldsymbol{\tau}$	Pa	fluid stress tensor
τ_p	s	particle characteristic time
$\emptyset_s$	-	acoustic contrast factor
φ	-	weighting or test function
φ_j	-	a basic function
ω	Hz	angular frequency

Abbreviation	***Name***
3D	three-dimensional
Al	aluminium
AlN	aluminium nitride
ARF	acoustic radiation force
BAW	bulk acoustic wave
CFD	computational fluid dynamics
CTC	circulating tumour cell
DC	direct current
DI	deionised
DNS	direct numerical simulation
FEM	Finite element method

FPW	flexural plate wave
IDT	interdigital transducer
$LiNbO_3$	lithium niobate
LoC	lab-on-chip
PDE	partial differential equation
PDMS	polydimethylsiloxane
PET	polyethylene terephthalate
PI	polyimide
PIV	particle image velocimetry
PMMA	polymethyl methacrylate
PoC	point-of-care
PVD	physical vapour deposition
PZT	lead zirconate titanate
RBC	red blood cell
RF	radio frequency
RPM	revolutions per minute
SAW	surface acoustic wave
SCCM	standard cubic centimetre per minute
SSAW	standing surface acoustic wave
taSSAW	tilt-angle standing surface acoustic wave
TSAW	travelling surface acoustic wave
UV	ultraviolet
ZnO	zinc oxide

Chapter 1. Introduction and Scope of the Thesis

1.1 Introduction

Microfluidic technologies realise the small-scale manipulation of microparticles, bubbles, and biological cells in fluid mediums. One of the most recent and promising manipulation techniques is the integration of acoustic-based devices especially surface acoustic waves (SAWs) with microfluidic technologies often called acoustofluidics [1-7]. SAWs are the product of applying an electric signal to the electrodes patterned on a piezoelectric substrate which then transforms electrical signal into mechanical stress, resulting in propagation of the surface acoustic wave [1, 3].

Using acoustofluidic devices as a tool to manipulate and control fluids and particles especially in continuous flow platforms have drawn significant attention of many researchers in recent years for collecting, manipulating, and investigating fluids, particles, and/or biological cells [1-7]. This is because acoustofluidic technologies offer many advantages such as simple design, small size, and low cost. They are adaptable to be used for different purposes and are sensitive, reliable, and efficient with fast processing and precise control of the biological samples. Using acoustofluidic platforms can decrease sample usage and improve non-invasive and contact-free handling of samples with high biocompatibility which conserves cell viability and proliferation and are convenient for on-chip integration with other techniques [1, 2, 8-17].

These advantages show their great potentials and make them excellent candidates to be integrated in lab-on-chip (LoC) and organ-on-chip devices [3, 18], controllable drug delivery platforms to administer the medicine directly to the desired point without affecting healthy cells [18-24], and also be integrated with flexible microfluidics to design bio-inspired, body-conforming, and wearable point-of-care devices [11-17] for clinical and biomedical applications. Acoustofluidics have been used for applications such as separation of blood [25-27], tumour [9] and cancer [28] cells, bacteria [29], lipids [10], and other types of biological cells [30, 31] for cell studies [32], cancer diagnosis and tissue engineering [6, 7, 33].

However, the uses of acoustofluidic technologies have been mostly restricted to academic research and conceptual designs while the utilisation of these acoustofluidic technologies for practical applications in clinical and biomedical capacity have yet to be widely applied [34-36]. One reason for this shortcoming can be the lack of knowledge on the exact details of their working principles. As an example, Ghahremani et al. [24] proposed a conceptual design for

programmable drug delivery devices that used SAW-induced acoustic streaming to deliver the drug from the device to the patient's eye by placing it under the eyelid on the surface of the eye and controlling the drug amount and application time. However, their conceptual design was not transformed into a practical device.

Having detailed information on the underlying physics and working principles of these acoustofluidic systems comprehensively determines the behaviours of every component of these systems including fluid and particles under the acoustic effects. This knowledge which can be obtained through analytical investigations, experimental studies and computational modelling is vital in designing, development, and optimisation of practical and novel acoustofluidic devices suitable for widespread applications.

Analysing the acoustofluidic systems in order to understand their underlying physics and operation mechanisms can be very difficult. This is due to the physics of the two major components of these systems i.e., the acoustic field and the flow field operating on vastly different time and length scales with the acoustic field operating on length and time scales in the order of $\sim 10^{-9}$ m and $\sim 10^{-8}$ s and the fluid flow operating on length and time scales in the order of $\sim 10^{-3}$ m and ~1 s, respectively. In order to analytically investigate the acoustofluidic system, a technique called perturbation method is often used [37-42]. Using this method and assuming steady states for both the acoustic and flow fields, the field variables are written as a combination of unperturbed and perturbed approximations. Analytical investigation works best for simple setups as for the complicated setups more simplifications need to be made.

Experimental work is helpful and useful to study the fluid and particle behaviours under the effect of acoustic waves in acoustofluidic devices and most of the current literature on acoustofluidics is focused on the experimental study. It can present the proof of the concept for new systems and to test that system functioning. It can also provide benchmark for the validation of the computational results. However, experimental study is a time-consuming process as for each individual experiment a new set up might need to be designed and built. It requires a systematic approach to optimise the setups for each experiment too. It is often not cost-efficient due to the requirement for equipment and material which need to be used to fabricate all the components of the acoustofluidic setup and to obtain the data. Sometimes, it is also hard or impossible to obtain the detailed information of the acoustic and flow fields interactions using experimental methods. This presents a challenge for proposing ideas for improvement or optimisation of the acoustofluidic system.

Computational simulation provides detailed information of the acoustofluidic system including the values for the acoustic field parameters, fluid flow field's variables and particle motion and behaviour in a more cost and time effective manner by numerically solving the governing equations of the system. Computational simulation can help the studies of different effects of various parameters for a set of different acoustofluidic cases. The knowledge that comes from computational simulation can help to improve and optimise the acoustofluidic system and implement acoustofluidics in a more effective and efficient way and can be crucial for the design of practical devices.

The behaviour of an acoustofluidic system can be predicted by modelling the fully coupled acoustic-fluid interactions and the effects of the acoustic-fluid field on the particles' mechanics. For this purpose, microscale pressure and velocity fields of the SAW, the large-scale pressure and velocity fields of the bulk fluid and their effects on the particle dynamics should be simulated which will require an extremely fine computational grid (considering the wave's displacement amplitude is in the order or $\sim 10^{-9}$) in order to resolve the interactions of the different components of the acoustofluidic system which operate on vastly different time and length scales. This makes the fully coupled modelling approach highly expensive and time-consuming even with high-performance computers which is often impractical using the current available computational resources. Another way to model the acoustofluidic system is to include the acoustic effects on the fluid (acoustic streaming) and microparticles (acoustic radiation) in the governing equations of fluid flow and particle dynamics as external body forces. Previous studies have been performed on numerical simulations of acoustofluidic systems, modelling both acoustic streaming and acoustic radiation effects including simulating acoustic streaming flow field [43], particle deflection using acoustic streaming [44], standing SAW (SSAW)-based [27, 29, 45-47] and travelling SAW (TSAW)-based [48] acoustic pressure fields as well as microparticle behaviour under the acoustic radiation force [28, 47, 49, 50]. However, few attempts have been made to assess the basis, strengths, and limitations of the computational methods which can help to optimise acoustofluidic devices and can potentially lead to development of novel SAW devices.

In most of the previous studies on acoustofluidic devices, the acoustic components of the setup are typically made with rigid piezoelectric materials which are generally brittle, fragile, and prone to breaking when handled improperly or applied with higher power [3, 16, 51-53]. The microfluidic components of the acoustofluidic setups (microchambers and microchannels) are generally fabricated with solid materials in a cleanroom environment utilising complicated and

time-consuming processes [4, 5, 7, 32]. The idea to utilise flexible thin film acoustic wave devices and integrate them with continuous flow wall-less microfluidic platforms offers advantages such as high wave speed and reasonably good electro-mechanical coupling coefficient for the flexible thin film acoustic wave devices [3, 16, 51-53] as well as simplifying the fabrication process, decreasing the fabrication cost, and reducing the production time for the wall-less microfluidics. These platforms can have potential applications in flexible microfluidics, body conforming wearable devices, flexible sensors/electronics, and soft robotics [3, 16, 51-53].

1.2 Aims and Objectives of the Thesis

This research investigates the interactions among fluid, microparticles and surface acoustic waves in a microchannel flow by using both numerical simulation and experimental work. The aims of this thesis are threefold:

The first aim is to utilise computational models for investigating novel acoustofluidic platforms including flexible acoustofluidics and capillary bridge channels. The computational models will be validated using the available experimental data reported in literature and then used to model the acoustofluidic experiments which are carried out throughout this research for the purpose of analysing and understanding underlying physics in acoustofluidics.

The second aim is to develop an acoustofluidic setup using flexible thin film surface acoustic wave devices for the purpose of particle and cell manipulations, in order to understand the acoustofluidic behaviour in different bent situations and investigate the effects of bending curvatures on microparticle's manipulation and patterning inside a microchamber.

The third aim of the research is to integrate the flexible thin film surface acoustic wave devices with capillary bridge channels, and then design/build a novel continuous flow acoustofluidic platform, which can used as a possible component of flexible microfluidic systems. This new platform is then utilised for particle and cell manipulation and is thoroughly investigated using the numerical modelling and experimental setups.

Followings are the defined objectives of the thesis in order to achieve these aims:

- Investigating the available numerical methods for the simulations of different acoustofluidic setups, choosing the most suitable numerical method to model different acoustofluidic setups, and comparing the results of the numerical modelling with the experimental data available in literature for the purpose of validating the numerical model.

- Studying acoustic streaming in a microchannel through both experiments and numerical modelling using different simulation approaches.
- Designing and building an experimental setup to study microparticle manipulation in different flexible acoustofluidic settings.
- Performing experimental work on different geometries of flexible surface acoustic wave devices to study bending effects of the devices on microparticle manipulation.
- Numerical modelling of acoustic particle manipulation in an acoustofluidic setup using bent geometries of flexible surface acoustic wave devices.
- Proposing a new idea for continuous flow acoustofluidic devices with the use of capillary bridge channels.
- Designing and building an experimental setup to study microparticle manipulation in a capillary bridge channel using flexible surface acoustic wave devices.
- Experimental study of integrating capillary-bridge channels with flexible surface acoustic wave devices used for microparticle manipulation.
- Numerical simulation of microparticle manipulation inside capillary bridge channels using flexible surface acoustic wave devices.

1.3 Distinctiveness and Novelty of the Thesis

In order to utilise acoustofluidics in practical applications, it would be crucial to understand all these details and present a solid explanation for the observed phenomenon. In-depth and detailed analysis of acoustofluidic platforms using numerical simulation can help in this endeavour by providing these detailed information of the acoustic field, fluid flow and microparticle dynamics but has not been done extensively. Numerical simulation requires an accurate model of the acoustofluidic platform which can effectively represent the largely different time and length scales of the acoustic and fluid field in order to provide verified and reliable results.

This research will present extensive experimental work and numerical modelling as well as in-depth and detailed analysis of the results. The experimental study shows the working principle and the feasibility of the acoustofluidic systems. It offers the real-world results and the data to validate the simulation results. While the computational simulation provides details of

acoustofluidic fields including the values for all the parameters of the acoustic and flow fields such as acoustic pressure, fluid velocity and particle dynamics which are sometimes hard or even impossible to obtain through experimental work. By using both the experimental and simulation data, the verified and reliable results will be obtained and can help implement acoustofluidics in a more effective and efficient way in practical applications.

This research is distinctive in the following areas:

- The first is utilising computational models to investigate novel acoustofluidic platforms (flexible acoustofluidics and capillary bridge channels) in order to study the underlying physics of these acoustofluidic setups.
- The second is the use of flexible thin film surface acoustic wave devices in particle and cell manipulation. This research, for the first time, investigates the effects of different curvatures geometries of flexible thin film surface acoustic wave devices on microparticle and cell patterning through both experimental studies and numerical simulations.
- The third is the integration of capillary bridge channels with flexible thin film SAW devices in order to design and build a continuous flow acoustofluidic setup for particle and cell manipulation. This research, for the first time, develops a wall-less acoustofluidic platform based on capillary bridges and flexible thin film surface acoustic wave devices and studies the effects of various parameters related to the acoustic field and fluid flow on manipulation of different microparticles through both experimental studies and numerical simulations.

1.4 Overview of the Thesis

This thesis is divided into nine chapters:

Chapter one introduces the motivations, aims and objectives of this research as well as its contribution to the research field. Chapter one also presents the scope of this thesis.

Chapter two reviews the literature on various aspects of this study including the complete theory of acoustofluidic systems along with the governing equations of these systems, particle and cell manipulation using SAW devices, investigation of the existing flexible microfluidic and acoustofluidic setups and wall-less microchannels for continuous flow purposes.

Chapter three covers the details of the methodology used for the computational modelling of the acoustofluidic systems. In this chapter, numerical methods used for simulating the behaviour of the acoustofluidic systems are studied, and the simulation results are compared to

the experimental data in the existing literature for the purpose of verifying and validating the numerical methods.

In Chapter four, the experimental methodology of acoustofluidic systems is presented. SAW device fabrication, design and building of the experimental setup, and the methodologies in which the experiments are handled and performed are all introduced in this chapter.

Chapter five investigates the use of acoustic streaming phenomena in particle manipulation through both experimental work and numerical modelling. In this chapter, different methods of modelling the acoustic streaming phenomena and its effects on particle and fluid manipulation are presented, and the simulation results are verified and validated by the experimental data.

Chapter six presents the use of flexible thin film SAW devices for particle manipulation and patterning in a bendable acoustofluidic setup. In this chapter, effects of different bent geometries and curvatures of the flexible SAW devices as well as different frequencies and wave modes on acoustic fields and particle patterning are studied using both experimental data and computational modelling.

In chapter seven, particle manipulation and patterning inside glass microtubes using flexible thin film SAW devices are studied through both experiments and numerical simulation and the effects of different cross-sections and flow rates on acoustic fields and particle patterning are investigated.

Chapter eight uses a capillary bridge channel in a continuous flow system for the purpose of particle and cell manipulation and alignment. In this chapter, effects of different frequencies, channel geometries, particle properties and flow rates on acoustic fields and particle patterning are investigated through both experimental studies and three-dimensional numerical modelling.

Finally, chapter nine presents the concluding remarks and suggests future work to expand this research.

Chapter 2. Literature Review

2.1 Introduction

Microfluidics, the science and technology of fluid mechanics and manipulation of fluids and particles in microscale, has become one of the most popular areas of research in recent decades. The small length scales along with the little amounts of fluid used in microfluidics, offers great potential to design and fabricate devices suitable in the fields of biology, medicine, and chemistry [1-4, 8, 54, 55]. Manipulation and control of microparticles, bubbles, and biological cells in fluid mediums are all possible using microfluidic-based systems [2, 29, 56-58].

Manipulation techniques are divided into two main categories, passive, and active manipulation. Passive manipulation mainly includes utilising hydrodynamics and different geometries to control the objects, whereas active manipulation techniques use external fields such as acoustic, electrical, magnetic, and optical fields to control fluid and particles [4, 59, 60].

Integration of acoustic wave fields from both ultrasonics and SAWs with microfluidic devices (often called acoustofluidics) have started to gain interest in recent years for manipulating and controlling fluids and particles in clinical and biomedical applications, especially in continuous flow setups [3-7]. The use of acoustic wave fields allows manipulation and control of fluids and particles in microfluidic devices based on their mechanical properties such as size [25, 27-30, 45, 49, 61-65], density [31, 49, 66] or compressibility [49].

Acoustofluidics is capable of performing various fluid and particle manipulation operations of fluid, particles, bubbles and cells, for example, focusing [9, 43, 46, 67, 68], directing [58], sorting [44, 69, 70], separation [9, 25-31, 45, 49, 61-66, 71], traping [72], patterning [73], enriching [74] and aligning [47] in two and three dimensions as well as mixing [75] and pumping fluids and suspensions in microfluidic devices [1, 3].

Using SAWs as a tool in microfluidic devices has many advantages. The devices are simple in design, compact and small. They have a low fabrication cost and are sensitive and efficient as well as requiring low power. Acoustofluidic devices have abilities to properly handle biological cells and particles and offer precise and controllable manipulation in a non-invasive and contact-free manner, with good biocompatibility, conserving cell viability and proliferation [1, 2, 8-10]. Additionally, it is convenient to integrate all the SAW devices and microfluidic components on the same chip with the potential to fabricate on-chip devices [1, 2, 8, 9, 50].

2.2 Acoustic Waves

2.2.1 Piezoelectric Effects

Using piezoelectric effects is one of the most common ways to generate acoustics waves. Piezoelectric materials can produce an electric charge when they are under mechanical stress. The reverse piezoelectric effect also happens when an electric field is exerted to a piezoelectric material which results in its mechanical deformation (contraction or expansion). Piezoelectric materials can be sorted in two categories: they either possess piezoelectric properties due to their crystal structures such as quartz, or the materials can be forced to show piezoelectricity by applying an external electric polarization such as lead zirconate titanate (PZT) [3, 4, 76, 77].

2.2.2 Bulk Acoustic Waves

When a bulk piezoelectric material (e.g., a quartz crystal) sandwiched between two metallic electrodes is applied with an alternating current electric signal, the electrical field is transformed into mechanical stress as the full body of the bulk piezoelectric material contracts and expands. This mechanical deformation of the piezoelectric material results in the production of bulk acoustic waves (BAWs). BAWs typically have lower sensitivity to surface disturbances since the wave propagates through the bulk of the material [3, 4]. Figures 2.1(a) and (b) show schematics of the BAW, including both longitudinal bulk wave mode (particle displacement parallel to wave's propagation direction) and thickness shear bulk wave (particle displacement perpendicular to the wave's propagation direction).

2.2.3 Lamb Waves

When the thickness of the substrate (δ_s) is smaller than or approximately equal to the wavelength (λ), i.e. ${\delta_s}/{\lambda} \leq 1$, Lamb wave modes are generated. At low frequencies, Lamb waves have normally two modes: the zero-order antisymmetric mode (A0) and the zero-order symmetrical mode (S0) [3].

The zero-order antisymmetric Lamb wave modes (A0), also called flexural plate waves (FPWs), are greatly dispersive in the low frequencies, but their velocity will converge towards the Rayleigh wave velocity at higher frequencies. Increasing the substrate layer thickness will transform the A0 wave into the Rayleigh wave or a higher order A-mode wave [3].

The zero-order symmetrical Lamb wave modes (S0), also called extensional mode, are generally less dissipative, but they will converge towards the Rayleigh mode at high frequencies. Decreasing the substrate layer thickness (approaching zero) will transform the S0 wave into a longitudinal wave. Some of the higher Lamb wave modes are particularly affected by the substrate layer thickness [3]. Figures 2.1(c) and (d) show schematics of antisymmetric and symmetric Lamb wave modes, respectively.

2.2.4 Surface Acoustic Waves

SAWs are generated when an appropriate electric field is exerted to a piezoelectric material such as lithium niobate ($LiNbO_3$) or zinc oxide (ZnO). To do this an alternating current electric signal in radio frequency (RF) range is applied to the interdigital transducers (IDTs) which are patterned on the piezoelectric substrate. As a result, the surface of the piezoelectric material then contracts and expands transforming the electrical stress to mechanical stress. This continuous deformation of the piezoelectric substrate causes the production and propagation of the TSAW along the surface of the substrate. When two identical SAWs propagate in the opposite directions to one another the superposition of the two waves can lead to constructive or destructive interference resulting in a SSAW [1, 3].

Rayleigh wave mode is the vibration mode that propagates on the surface of the piezoelectric materials and most of the SAW devices are designed based on this mode. When the Rayleigh wave is generated, surface particles have an elliptical trajectory and their oscillations decay fast as the depth of the substrate increases. On the surface of the piezoelectric material, Rayleigh wave has a significant normal displacement, however, when it comes into contact with the fluid above, the wave's energy dissipates into the fluid and the wave dampens [3]. Figure 2.1(e) shows a schematic illustration of a Rayleigh wave. Figures 2.1(f) and (g) show the travelling and standing SAWs, respectively.

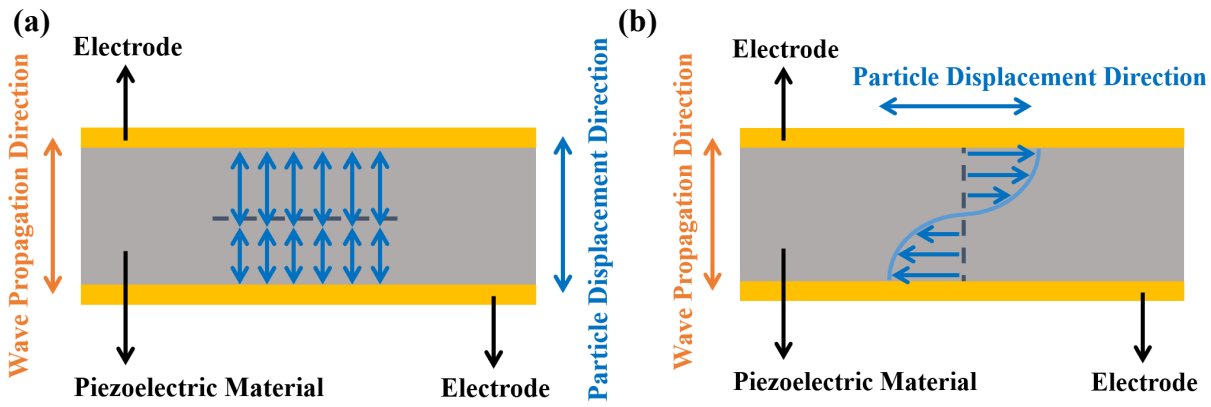

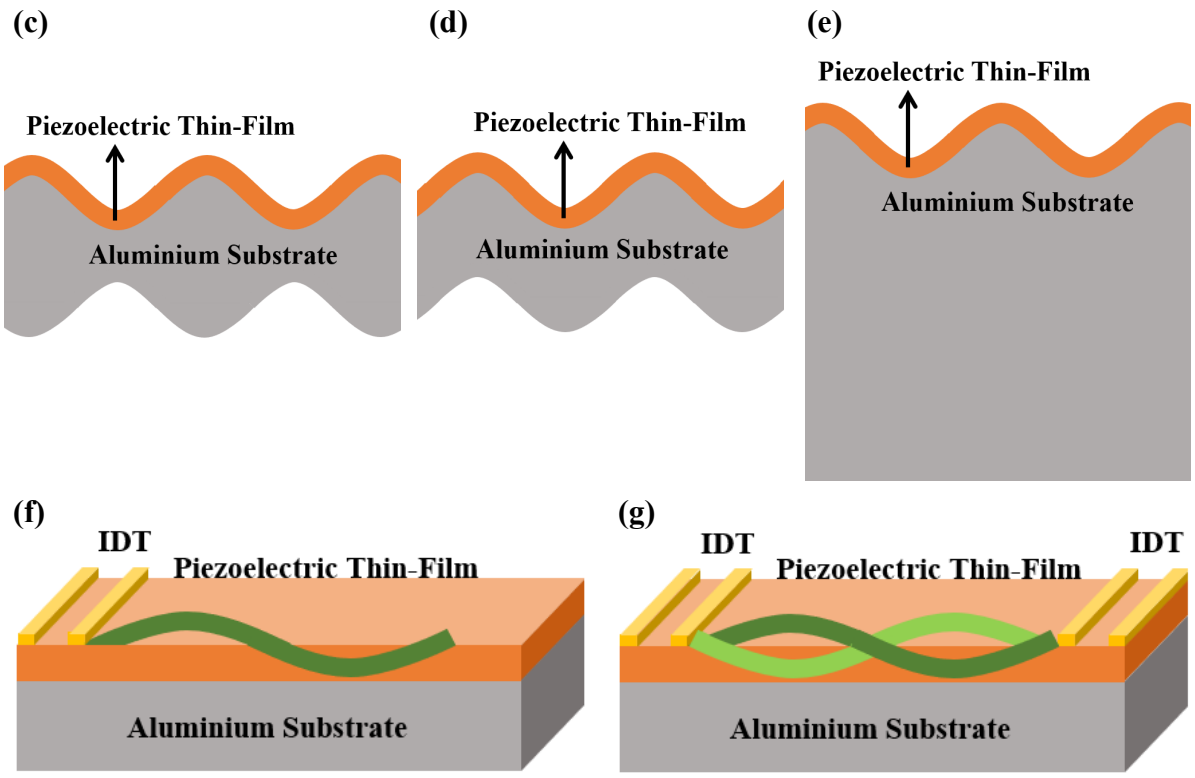

Figure 2.1 Schematics of different acoustic waves: (a) thickness shear bulk acoustic wave, (b) longitudinal bulk acoustic wave, (c) antisymmetric, and (d) symmetric Lamb wave modes, (e) surface acoustic wave (SAW) Rayleigh mode, (f) travelling SAW, and (g) standing SAW.

2.2.5 Surface Acoustic Wave Applications

Most acoustic wave devices including SAW devices are able to act as sensors or biosensors since their surfaces can be sensitive to minor perturbations. SAW-based sensors have been used for sensing various mechanical, physical, chemical, optical, or electrical properties including but not limited to temperature, humidity, pressure, acceleration, flow, pH levels, electric, magnetic and radiation fields. The main sensing technique using SAW devices includes the measurement of the changes of SAW device resonant frequency (i.e. SAW propagation velocity) [3].

SAW-based devices can also be integrated with microfluidic technologies in either a digital format for the purpose of mixing, pumping, jetting and nebulisation of sessile droplets, or continuous flow platforms for mixing and pumping fluids and particle/biological cell manipulation inside a microchamber/microchannel [1, 3].

2.3 Acoustofluidics: Integrating Acoustics with Microfluidics

2.3.1 Digital Acoustofluidics

Digital acoustofluidics deals with manipulation of sessile droplets through the usage of acoustic wave effects in the form of either internal streaming which can result in mixing inside the droplet, or transportation (pumping), jetting, and nebulisation (atomization) of the droplet. Digital microfluidics require controllable, accurate and continuous droplet generation as well as manipulation and offers potentials in drug delivery applications [3, 78, 79].

SAW devices can be used to induce acoustic streaming and thus realise mixing inside sessile droplets. When the radius of the droplet and the attenuation length of the SAW are nearly equal, acoustic mixing will be fast and efficient inside the droplet. However, as the radius of the droplet increases, the streaming velocity decreases which will result in a more irregular and weaker mixing [3, 78, 79]. Increasing the power applied to the SAW device will excite the droplet more significantly and realise droplet transportation (pumping) along the SAW propagation direction with a combination of sliding and rolling motions. Further increase in the power applied to the SAW device can result in droplet place over a hydrophobic surface to be jetted into a thin fluid column or complete separation of the droplet from the surface. When even higher power is applied to the SAW device, nebulisation (or atomization) of the droplet is realised which can produce aerosol droplets and has been applied in drug delivery applications for inhaled drugs [3, 78, 79].

2.3.2 Continuous Flow Acoustofluidics

Utilising SAW devices in continuous flow microfluidic platforms to build SAW-based continuous flow acoustofluidics have been shown to be capable of performing various fluid-related tasks including mixing and pumping fluids and suspensions using acosutic streaming effects inside microchambers and microchannels as well as controlled droplet production in microfluidic devices [1, 3]. Additionally, SAW-based acoustofluidics have been explored for the purpose of precise and contact-free manipulation and control of particles, bubbles, and biological cells while using acoustic streaming and radiation forces to perform manipulation tasks such as focusing [9, 43, 46, 67, 68], directing [58], sorting [44, 69, 70], separation [9, 25-31, 45, 49, 61-66, 71], traping [72], patterning [73], enriching [74] and aligning [47] of micro-objects inside a microchamber/microchannel.

2.3.3 Acoustic Streaming for Particle Manipulation

When a TSAW comes across the liquid, the difference between the wave propagation speed in the piezoelectric substrate and its speed in the liquid causes the wave's acoustic energy to refract into the fluid. This phenomenon is called acoustic refraction. The amplitude of the acoustic wave starts to attenuate when it propagates into the fluid [1, 2, 80]. As the acoustic waves attenuate in the fluid medium, its kinetic energy or momentum is transferred to the fluid. This results in the refracted acoustic waves inducing movement in the fluid by generating a force in the waves' propagation direction. The boundaries reflect the moving fluid and cause an internal streaming. This phenomenon is called acoustic streaming [1, 80, 81].

The analytical study on acoustic streaming was first presented by Nyborg [37] as he calculated acoustic streaming in a fluid, assuming a steady state for both the acoustic and flow fields using perturbation method. This was further improved by Lighthill [38]. Liu et al. [56] investigated the force conditions on microparticles in SAW fields and studied the effects of acoustic streaming and radiation force on microparticles with different diameters. They found that for the larger microparticles, the acoustic radiation force is dominant, whereas for the smaller ones, the acoustic streaming effect is dominant.

Acoustic streaming can be used to direct [58], sort [44, 69], focus [43], separate and capture [71] and pattern [73] microparticles and to mix and pump the fluids and suspensions in the microfluidic devices [1-3]. Acoustic streaming effects have been used to direct microparticles and droplets in continuous flow microfluidic devices [58]. Franke et al. [58] introduced a method to direct the motion of water droplets in oil and then polyacrylamide particles in water in a microfluidic channel using a SAW device. Their method was successful in directing droplets and microparticles with high volume flow rates along separate microchannel paths and can be used for sorting purposes. Their method was unique in turning the acoustic wave field on and off. However, it lacks numerical analysis.

Label-free sorting of different microparticles and biological cells with a desired sorting ratio has been achieved using acoustic streaming effects in continuous flow microfluidic setups [44, 69, 70]. One microfluidic device was proposed by Franke et al. [69] to sort three different biological cell types in the continuous flow using the SAW. The cells were directed by acoustic streaming force and did not need any prior labelling. They used acoustic streaming in a small region of the microchannel with a "periodically oscillating SAW amplitude". By adjusting the position of the inlet jet, they were able to set the desired sorting ratio between two outlets.

Their method was successful and gentle in handling cells and ensured that cells survive after sorting. Another microfluidic cell sorter was introduced by Schmid et al. [44] using surface acoustic wave streaming effect to sort cells independent of the cells mechanical properties to the desired outlet. Their device can sort cells with a high rate, a low power or force, good cell viability and without a need for labelling. This microfluidic cell sorter can be combined with other microfluidic devices easily. They showed that both their experimental and numerical particle tracks complemented each other very well. Skowronek et al. [70] introduced an acoustic filter to separate and sort microparticles based on their sizes. They were successful in filtering microparticles of a desirable size or size range based on the frequency of the SAW device. Their method was label-free with both hight throughput and efficiency.

Micro-vortices formed due to the acoustic streaming have been utilised to focus microparticles and nanoparticles, which was demonstrated by Collins et al. [43]. They presented a technique to focus microparticles with a diameter even below 1 μm using strong surface acoustic wave streaming and causing micro-vortices to form. Their method was capable of concentrating nanoparticles in a continuous fluid flow within a microchannel without using any filters. They presented both their experimental and numerical particle tracks which are comparable well with each other.

Acoustic streaming effect have also been used to separate and capture microparticles and biological cells in continuous flow microfluidic devices. Collins et al. [71] maximized the surface acoustic wave streaming effect to separate and capture microparticles with diameter of 2 μm from 1 μm in a mixture. They used acoustic streaming to generate micro-vortices in a continuous microchannel flow. Their method showed to be effective with a high throughput. Sivanantha et al. [26] utilised the acoustic streaming to separate the healthy blood cells from the infected blood cells. Their method showed promise to be used for biomedical and clinical applications either as a biomarker or for rapid diagnosis. Using acoustic streaming, on-demand droplet trapping and releasing was realised in a continuous flow microfluidic device by Rambach et al. [72]. They used SAW pulses to capture and release an individual droplet in a continuous flow setup. Table 2.1 summarises the uses of SAW-based acoustic streaming for microparticle, cell and fluid manipulations.

Table 2.1 Application of acoustic streaming effect to manipulate microparticles.

Manipulation Task	Objects	Research Group	Investigation
Directing	Polyacrylamide microparticles, Droplets	Franke et al. [58]	Experimental
Separating & Sorting	Droplets, Cells: B16F10 mouse melanoma	Schmid et al. [44]	Experimental Simulation
	Cells: HaCaTcells, murine fibroblasts, L929 cells, and MV3 melanoma cells	Franke et al. [69]	Experimental
	Polystyrene microparticles	Skowronek et al. [70]	Experimental
Focusing	Polystyrene microparticles	Collins et al. [43]	Experimental Simulation
Separating & Capturing	Polystyrene microparticles	Collins et al. [71]	Experimental
	Cells: healthy, Glutaraldehyde treated, and malaria-infected red blood cells	Sivanantha et al. [26]	Experimental
Trapping & Releasing	Droplets	Rambach et al. [72]	Experimental

Figure 2.2 shows schematics of different acoustic streaming-based fluid and particle manipulation techniques inside a channel, which include (a) directing, (b) separating, (c) focusing of microparticles, and (d) mixing and (e) pumping of fluids for continuous flow applications.

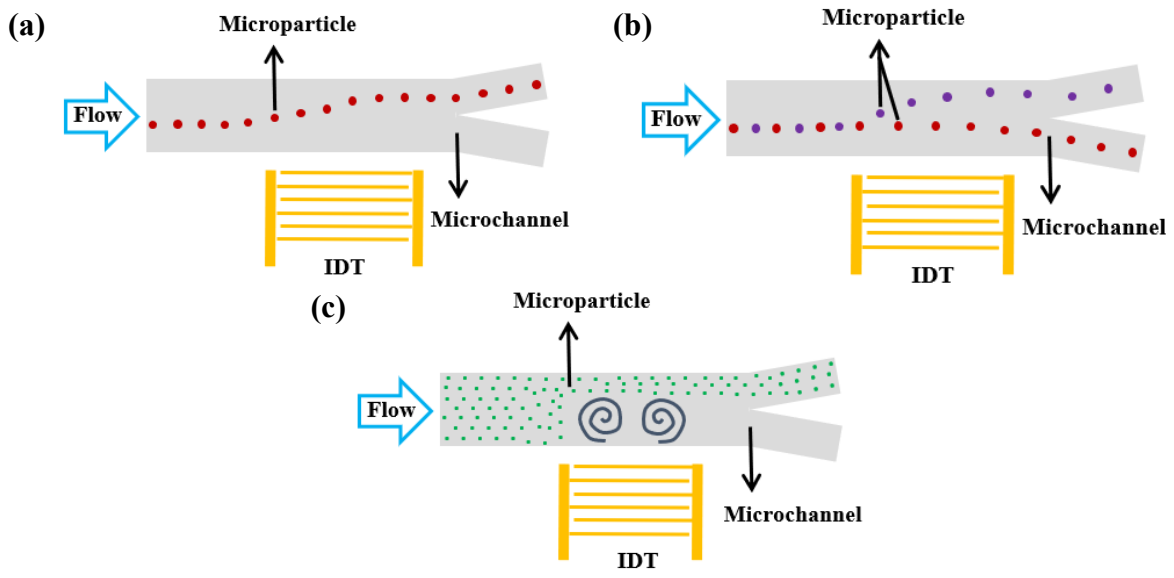

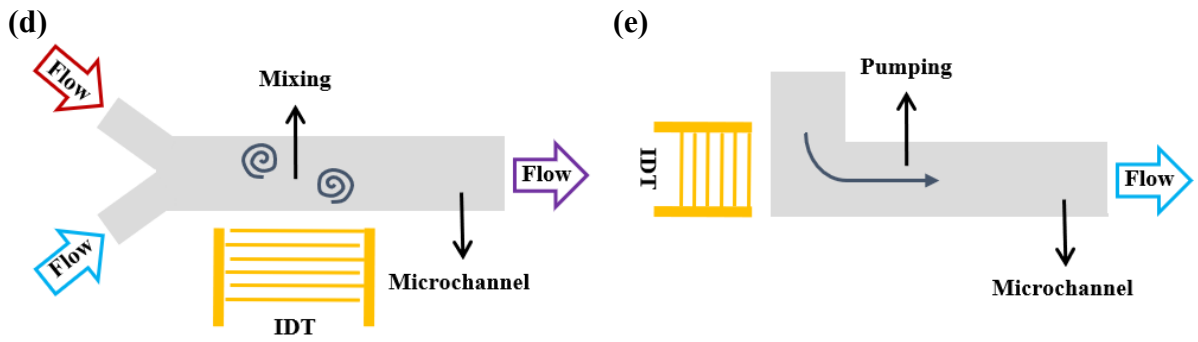

Figure 2.2 Schematic illustration of (a) directing, (b) separating, (c) focusing of microparticles, and (d) mixing, and (e) pumping of fluids using acoustic streaming in a continuous flow inside a channel.

2.3.4 Acoustic Radiation Force for Particle Manipulation

Each particle suspended in a fluid is subjected to two different types of acoustic forces, i.e., acoustic streaming force and acoustic radiation force. The acoustic streaming induces a movement in the fluid medium. Because the fluid is in motion, all the particles suspended in it will also experience a drag force [1, 56].

Acoustic radiation force (ARF), also known as acoustic radiation pressure, acts directly on the particles. When a SAW comes across the liquid, the acoustic energy is refracted into the fluid thus affects the fluid and the particles suspended inside. As the acoustic waves comes into contact with particles suspended in a fluid medium, its momentum or kinetic energy is transferred to the particles. This interaction results in the acoustic radiation force [1, 2, 81, 82].

In the case of a TSAW, the acoustic radiation force will push the particles towards the wave's propagation direction. Whereas for a SSAW, the acoustic radiation force will direct each particle towards either the pressure node (i.e., minimum pressure amplitude) or the pressure antinode (i.e., maximum pressure amplitude), depending on the physical and mechanical properties of the particle and the fluid [1, 39-42, 56, 74, 83, 84].

The dominant force for each particle depends on the size of the particle. For particles with a size larger than a size limit, the acoustic radiation force is the dominant force and pushes the particles out of the fluid streamlines. For the particles with a size smaller than the size limit, the acoustic streaming force dominates the motion of the particles, and the particles will follow the fluid streamlines [1, 56]. It was reported that this "size limit" depends on many variables such as frequency, density, compressibility, and viscosity [1, 85].

The acoustic radiation force applied on a single particle is caused by the interactions between the acoustic wave and the particles and is considered the primary acoustic radiation force. The

acoustic interaction of one particle with another (i.e., interparticle interactions) will cause the secondary acoustic radiation forces on the particle (also called indirect or Bjerknes ARF). The total effect of these primary and secondary forces is the net acoustic radiation force [1, 33].

The analytical study on acoustic radiation force was first introduced by King [39] when they calculated the acoustic radiation force on rigid spheres ignoring the fluid viscosity and using perturbation method. Yosioka and Kawasima [40] successfully extended the calculations for compressible spheres accounting for the effects of the microparticles' compressibility. These studies were then summarised and generalised by Gorkov [86]. Doinikov [41, 42] derived the relation for the acoustic radiation force on a rigid [41] and compressible [42] sphere in a viscous fluid, respectively. Liu et al. [56] studied the force conditions on microparticles in SSAW fields experimentally and numerically, and showed that the ARF is the most effective force applied on the large particles while the effect of acoustic streaming increases with decreasing particle size.

Acoustic radiation force generated by the SSAWs have been used to focus microparticles [67] in a three dimensional manner [46] and a laminar flow system [68] without a need for sheath flows [9] as well as to enrich microparticles in a continuous flow setup [74]. Shi et al. [67] presented a focusing technique using the SSAWs on polystyrene microparticles. Their method proved simple, fast, effective, dilution-free, and applicable to almost all kinds of microparticles with much lower power consumption compared to those using the bulk acoustic wave devices. A three-dimensional particle focusing technique setting was presented by Shi et al. [46] with the use of SSAWs in a continuously laminar flow of the polystyrene microparticles. They modelled their study numerically and the simulations matched well with their experimental observations. This focusing method proved to be non-invasive, power efficient, easy to implement, and appropriate for different types of microparticles. Another particle focusing method with the use of SAWs was presented by Zeng et al. [68]. They were successful in focusing polystyrene microparticles in a laminar flow with the expected efficiency. Wang et al. [9] used the SSAWs to focus microparticles with two sizes as well as circulating tumour cells (CTCs) and red blood cells (RBCs) without a need for sheath flows. Acoustic radiation forces have also been used in a continuous flow microfluidic device by Nilsson et al. [74], who focused and enriched the polyamide microparticles using the SSAW. They have successfully collected the microparticles at the outlets of the microchannel with a high recovery rate.

Additionally, ARFs have been utilized to pattern [73] and align [47] microparticles with different line spacing. Shi et al. [73] demonstrated their "acoustic tweezer" using a SSAW device to pattern polystyrene microparticles and E. coli cells and it was capable of manipulating microparticles with any physical property. Their experimental and simulation data matched well with each other. Johansson et al. [47] presented an acoustic device for the continuous flow particle alignment. They investigated the acoustic node positions and spacing based on different device designs and SAW frequencies inside a polydimethylsiloxane (PDMS) channel through both experiments and simulations.

Acoustic radiation force can also separate microparticles in continuous flow microfluidic devices based on the microparticles' physical attributes such as size [25, 27-30, 45, 49, 61-65], density [31, 49, 66] or compressibility [49].

Size-based separation using SSAWs have been performed on microparticles with different sizes and equal densities [49, 61, 62] and have been utilized to separate blood cells [27], platelets [25], and bacteria [29]. A sized-based method to separate particles using SSAW in a microfluidic channel was introduced by Shi et al. [61]. Their method separated the polystyrene microparticles of equal density but dissimilar sizes in a continuous laminar flow and was simple, highly efficient, cost effective and applicable to virtually all kinds of particles regardless of their physical properties. Numerical simulation of the separation of platelets, red blood cells and white blood cells in a SSAW field was done by Shamloo and Boodaghi [50]. They used a comprehensive finite element-based method to model a microfluidic channel with two inlets and one sheath flow. They obtained particle trajectories for different cells and compared them with theoretical results. They verified their numerical results with the experimental data of Shi et al. [61]. Another size-based method to separate microparticles has been proposed by Nam et al. [62] using a SSAW in a continuous microchannel flow. Their method was applied to a colloidal suspension containing polystyrene microparticles with three different sizes but the same density and compressibility. They also presented an analytical model to predict the results of their experiments. They achieved rapid, efficient, and continuous separation of particles and their analytical results matched well with their experiments. Simon et al. [49] also reported a size-based separation technique using pseudo-SSAWs in a continuous flow system. They presented the separation of polystyrene microparticles through both experiments and simulations with high efficiency, purity, and selectivity. Wu et al. [27] developed an acoustofluidic platform utilising both hydrodynamic properties of their microchannel along with SSAWs to separate biological cells based on their sizes. They were

also successful in separating microparticles with three different sizes from each other. A size-based particle separation method has been presented by Nam et al. [25] to separate platelets from an undiluted blood sample using a SSAW-based microfluidic device. Their technique could separate platelets from the blood sample based on their sizes with a very high efficiency and purity. Another size-based microfluidic device to separate microparticles was developed by Ai and Marrone [29]. Their device could separate dissimilar microspheres in a two-type particle mixture and then E. coli bacteria were separated from peripheral blood mononuclear cell (PBMC) sample both in continuous flows. They also developed a numerical model to predict the experimental results. Their experimental work matched ell with their numerical results.

In addition, by placing the microchannel with an inclined position regarding to the direction of the IDTs, the microparticles were separated based on their sizes using tilt-angle SSAWs (taSSAWs) [28, 64]. Liu et al. [64] proposed a microfluidic device to separate microparticles based on their size using SSAW. They used a pair of IDTs placed with an incline angle with respect to the microchannel. Their device was successful in separating the polystyrene microparticles with high purity, separation rate and accuracy. In their experiments, rather than showing the actual tracks of particles, the particles' approximate tracks based on fitting a line between the particles of each size were depicted. A cell separation technique using taSSAWs was also developed by Ding et al. [28]. They systematically analysed and optimised the angle between the IDTs and the flow direction and were successful in separating microparticles of different sizes and also the cancer cells from blood cells. Their label-free method showed a good potential for biological and biomedical applications.

Using TSAWs for size-based separation, microparticles with various sizes [45, 65], different biological cell types [30], and tumour cells from blood [9] have been separated. Ma et al. [45] demonstrated a contact-less and continuous flow microparticle separation technique using a TSAW. They successfully separated polystyrene microparticle based on their size with a high efficiency, showing the potential for biomedical applications. Another TSAW-based continuous flow separation device was introduced by Destgeer et al. [65]. They used an IDT with curved electrodes to separate microparticles based on their sizes with a 100% efficiency. Mutafopulos et al. [30] used the TSAWs to separate different biological cell types depending on their sizes. Their devices achieved a high separation efficiency while conserving cell's viability. A sized-based separation of cells using SAWs in a microchannel flow was presented by Wang et al. [9]. They developed a microfluidic device to separate the particles in a two-type

mixture and then to separate CTCs from RBCs in the blood stream. Their device was capable of effectively separating particles and cells providing a reliable and flexible method for sorting microparticles. In an attempt to better understand the effect of TSAWs, Fakhfouri et al. [48] investigated the effects of a TSAW on microparticles of different sizes experimentally and numerically.

Density-based separation of two types of microparticles with the same size but different densities [49, 66] have been previously investigated using SSAWs. Additionally, density-based separation of encapsulated cells in a laminar flow [31] has also been realised. Particle's compressibility has been explored to assist the separation of microparticles made from different materials [49]. One density-based method was presented by Jo and Guldiken [66], who separated two types of microparticles with same size using the SSAWs. They first focused the Melamine microparticle flow and then separated the particles based on their densities, both using the SSAWs. Their method was successful in separating the microparticles with a high efficiency. The technique presented by Nam et al. [31] introduced a density-based separation method to separate encapsulated cells using the SSAW. The beads were dispersed in a continuous laminar microchannel flow and were focused hydrodynamically. Their label-free method offered high purity and recovery rate conserving cells viability and proliferation. Simon et al. [49] investigated a separation technique based on the density and compressibility of the microparticles through both experiments and simulations. They used pseudo-SSAWs in a continuous flow system to separate polystyrene, iron-oxide, and poly (methyl methacrylate) microparticles with high efficiency, and showed their method is stable regardless of the flow rate. Table 2.2 summarizes the literature for using acoustic radiation force on microparticle manipulations.

Table 2.2 Application of acoustic radiation force to manipulate microparticles.

Manipulation Task	**Objects**	**Research Group**	**Investigation**
Focusing	Polystyrene microparticles	Shi et al. [67]	Experimental
	Polystyrene microparticles	Shi et al. [46]	Numerical Experimental
	Polystyrene microparticles	Zeng et al. [68]	Experimental
	Microparticles and CTCs from RBCs	Wang et al. [9]	Experimental
Enriching	Polyamide microparticles	Nilsson et al. [74]	Experimental
Patterning	Polystyrene microparticles and E. coli cells	Shi et al. [73]	Analytical Numerical Experimental

Aligning	Polystyrene microparticles and Fat microparticles	Johansson et al. [47]	Numerical Experimental
Size-based Separating using SSAWs	Polystyrene microparticles	Nam et al. [62]	Analytical Experimental
	Polystyrene microparticles	Shi et al. [61]	Experimental
	Polystyrene microparticles and Blood cells	Wu et al. [27]	Numerical Experimental
	Platelets from blood	Nam et al. [25]	Experimental
	Microparticles and E. coli bacteria from PBMC	Ai & Marrone [29]	Numerical Experimental
	Polystyrene microparticles	Simon et al. [49]	Analytical Numerical Experimental
Size-based Separating using taSSAWs	Polystyrene microparticles	Liu et al. [64]	Experimental
	Polystyrene microparticles and Breast cancer cells from blood cells	Ding et al. [28]	Numerical Experimental
Size-based Separating using TSAWs	Polystyrene microparticles	Ma et al. [45]	Numerical Experimental
	Microparticles	Destgeer et al. [65]	Experimental
	Different biological cell types	Mutafopulos et al. [30]	Experimental
	Microparticles and CTCs from RBCs	Wang et al. [9]	Experimental
Density-based Separating	Melamine microparticles	Jo & Guldiken [66]	Experimental
	Encapsulated cells	Nam et al. [31]	Experimental
	Polystyrene, iron-oxide and poly(methyl-methacrylate) microparticles	Simon et al. [49]	Analytical Numerical Experimental
Compressibility-based Separating	Polystyrene, iron-oxide and poly(methyl-methacrylate) microparticles	Simon et al. [49]	Analytical Numerical Experimental

Figure 2.3 shows schematic illustrations of different particle manipulation techniques inside a channel, including (a) microparticle focusing, (b) SSAW-based microparticle separation, (c) taSSAW-based microparticle separation, and (d) TSAW-based microparticle separation using acoustic radiation force for continuous flow applications.

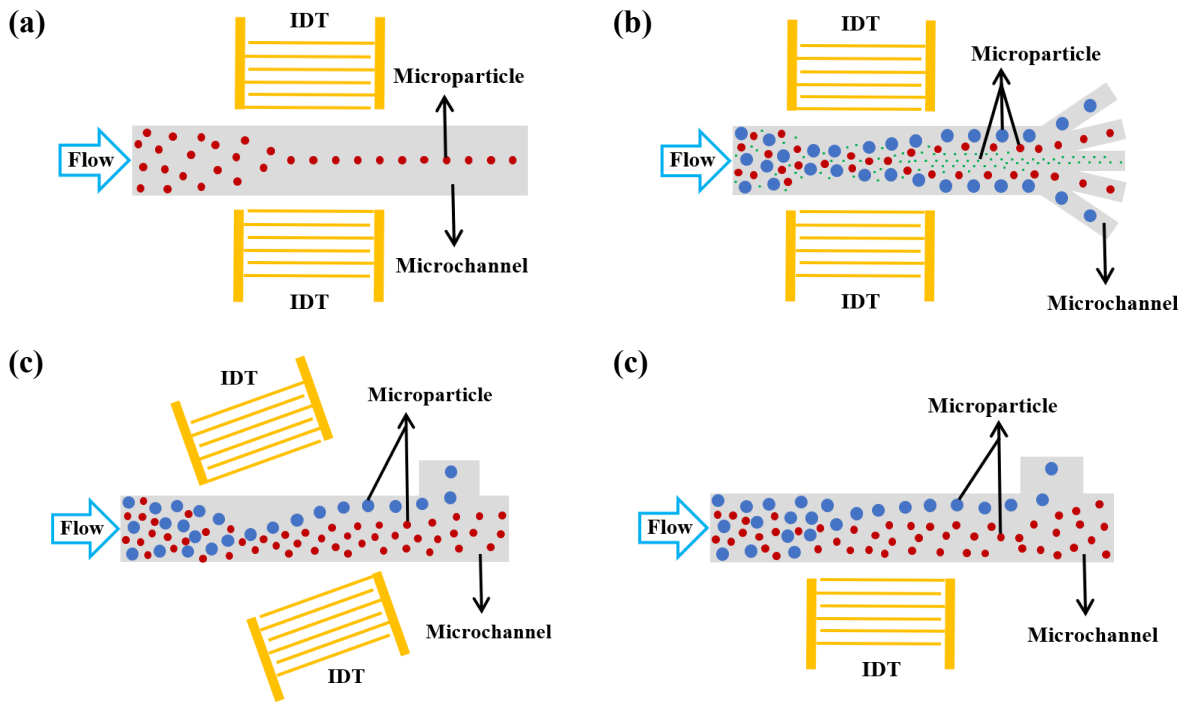

Figure 2.3 Schematic illustrations of (a) microparticle focusing, (b) SSAW-based microparticle separation, (c) taSSAW-based microparticle separation, and (d) TSAW-based microparticle separation using acoustic radiation force for a continuous flow inside a channel.

2.3.5 Rigid Acoustofluidics

As previously discussed, applying an electric signal to the piezoelectric material is a typical method to generate the acoustic waves. Most of the previous studies on acoustofluidics are concentrated on rigid piezoelectric materials including PZT (which is used for its high electro-mechanical coupling coefficient), 128° Y-X-cut $LiNbO_3$, and piezoelectric thin films. Acoustic wave devices made with those piezoelectric ceramic materials are generally brittle and fragile and will easily break when handled improperly or applied with higher power. They are not easy to integrate with microelectronic devices and fluidic components and are often expensive. Whereas thin film acoustic wave devices deposited onto flexible substrates such as aluminium-based SAW devices offer advantages including high wave speed, reasonably good electro-mechanical coupling coefficient, and easy integration with other acoustofluidic components with potential applications in flexible microfluidic platforms, body conforming wearable devices, flexible sensors/electronics, and soft robotics [3, 16, 51-53].

2.3.6 Flexible Microfluidics

Flexible microfluidics with the ability to conform to different curved surfaces present a great potential in designing wearable devices for point-of-care, clinical and biomedical applications for collecting, manipulating, and investigating bodily fluids [11-17].

Flexible lab-on-foil [11] and lab-on-tube [12] devices have been utilised in biomedical settings which can offer new and adaptable solutions for the current LoC technology [11]. For the very first time, an acoustofluidic lab-on-foil active micromixer were developed by Lin et al. [13]. Firstly, they used polyethylene terephthalate (PET) film as well as dome-shaped porous microstructures to reduce bubble instability in a fluid-bubble mixture and studied the effect of pore size on the device's functionality. Then they utilized their device in a microchannel with a continuous flow to mix water and fluorescent dye with high performance. Using nanoimprint and photolithography, a novel lab-on-tube technology was proposed by Yang et al. [12] to fabricate microstructures on a capillary tube. Their method was successful in creating nanoimprinted patterns on the tubes curved surface, with significant potential in biomedical applications.

In addition, flexible polymer-based [14, 16, 17] and fabric-based [15] devices have been used in biomedical applications for point-of-care (PoC) diagnosis as well as wearable devices for detecting various materials and monitoring different parameters [14]. To make a compact tuneable mixer, a flexible, rollable microfluidic device was developed by Kim et al. [17] using a parylene microchannel with two inlets and one outlet to reduce the size of the device and to make some features of the device to be tuneable. Along with their experimental studies, they performed simulation of the fluid flow to study the generated vortices in detail. For the purpose of directing and controlling flow, a flexible microfluidic device was demonstrated by Holmes et al. [16]. They utilized elastic deformations of the flexible PDMS microchannel to control the flow rate of the fluid inside. As well as experimental data, they presented analytical and numerical analysis, all in good agreement with each other. As a successful example, a wearable fabric-based microfluidic device was proposed by Yang et al. [15] to collect and analyse perspiration on a specified skin area in real-time. They also offered a theoretical model to study and optimise different design parameters. Their device was successful in measuring and monitoring the flow rate of simulated perspiration in real-time with a good precision, thus offering a good potential to be used in wearable clinical technologies.

The potential to integrate wireless communication devices such as smart phones in combination with wearable devices to analyse and report the data makes flexible microfluidics an interesting candidate for clinical use. However, more effort is needed for the wearable PoC diagnosis devices to become widespread [14].

2.3.7 Thin Film Flexible Acoustic Wave Devices

Recently, several ideas have been explored to design bendable, flexible, deformable, and even stretchable acoustic wave devices [87-89] to meet the increasing demand for wearable technologies. These devices present high potentials in healthcare monitoring and point-of-care technologies, flexible microfluidic systems, and LoC applications [53, 87-93].

Flexible thin film SAW devices can be fabricated by depositing a thin layer of a piezoelectric material such as ZnO [53, 87-89, 91, 92, 94-96], aluminium nitride (AlN) [90], or PZT onto a thin flexible substrate that can be made from either polymer [87, 88, 90-92], bendable glass [89, 92] or metallic foil such as aluminium (Al) [53, 94-96], followed by patterning of IDTs on top of the piezoelectric thin film to form flexible SAW devices [3, 53, 87-98].

Flexible ZnO/polymer SAW devices were used as a flexible humidity sensor [88], potential flexible temperature sensor [87, 91] and as humidity, temperature, strain and ultra violet (UV) light sensors [92] with their potentials for practical applications. He et al. [88] proposed using ZnO deposited on flexible kapton polyimide substrate as a very first flexible humidity sensor. They fabricated and characterized flexible SAW devices with various wavelengths which showed good performance, high sensitivity, and fair repeatability with a great potential for utilization in flexible microsystems and sensors. ZnO SAW devices on flexible kapton polyimide were studied by Jin et al. [87] and by Zhou et al. [91]. These devices performed in both Rayleigh and Lamb wave modes and showed good streaming and microparticle accumulation abilities with a potential as temperature sensor, microfluidic systems, and LoC applications. Luo et al. [92] investigated transparent and flexible SAW devices fabricated by depositing thin film ZnO on polyimide (PI) and PET polymers and used them as humidity, temperature, strain and UV light sensors.

AlN film have also been deposited onto kapton PI polymer substrate by Zhou et al. [90]. They studied AlN thin film SAW device in experiment and simulation and their device generated Lamb waves and showed good piezoelectric capabilities. They claimed that the use of piezoelectric thin films on flexible substrates is cost effective and will be a potential choice when designing a health-care monitor wearable on the wrist. Flexible transparent SAW devices with bendable glass substrates were introduced by Chen et al. [89] and Luo et al. [92] with the device working only in Rayleigh wave mode. These devices are reliable and repeatable under periodic bending with a high potential as flexible transparent SAW devices used for practical applications.

Additionally, flexible thin film ZnO/Al SAW devices were characterized and analysed through both experimental work and simulation methods by Tao et al. [53]. They fabricated different flexible thin film SAW devices by depositing ZnO thin film on Al substrate in plate and foil thicknesses. After that they characterized, simulated, and analysed their devices. They also compared the devices' functionality based on the wavelengths and the thickness of piezoelectric thin film and substrates. Their devices showed a wide range of resonance frequencies from Rayleigh and Lamb wave modes to higher harmonic ones. They claimed their devices to be simple, low cost and accurate thus having potential to be used in flexible microfluidic applications. These flexible thin film ZnO/Al SAW devices have been shown to drive liquid sessile droplets on both flat, inclined, and even randomly bent and curved surfaces efficiently [94, 95].

However, there are few studies on bendable, flexible, or deformable devices in acoustofluidic setups for patterning of microparticles and cells inside a microchamber or microchannel.

2.3.8 Novel Alternatives to Conventional Microchannels

Continuous flow acoustofluidic platforms are comprised of acoustic wave sources (e.g. SAW devices) combined with microfluidic elements i.e., microchambers and microchannels to contain the liquid and to enable the continuous flow [5, 7]. In a conventional continuous flow acoustofluidic device, solid and walled microchannels are typically integrated with SAW devices for fluid and particle manipulation. These microchannels are generally fabricated in a cleanroom environment utilising complicated and time-consuming processes including photolithography, soft lithography, milling, or injection moulding [4, 32] and using materials such as PDMS [9, 25, 29, 44, 69], polymethyl methacrylate (PMMA) [99, 100], polystyrene [101-103], silicon elastomer [104], or glass [10, 63, 74]. Exploring, designing, and utilising alternatives to these conventional microchannels will simplify the fabrication process, decrease the fabrication cost, and reduce the production time.

2.3.9 Using Microtubes in Microfluidic and Acoustofluidic Setups

Microtubes have been integrated with acoustic devices and used to manipulate [105, 106], deform [107], trap [108-111] enrich [112, 113], align [114], arrange [115], focus [116], pattern [117] and separate [118] microparticles and biological cells.

For non-flowing applications, Lei et al. [105] as well as Sriphutkiat and Zhou [106] glued a PZT transducers to rectangular glass microtubes [105] and cylindrical glass microtubes with a

tapered nozzle [106] to manipulate and accumulate microparticles. Using a glass microtube with square cross-section glued to a PZT, Mishra et al. [107] deformed the blood cells. Mao et al. [112] enriched nanoparticles inside glass microtubes with square cross-sections place on the top of a $LiNbO_3$ SAW device. Glass and polyimide microtubes with square cross-sections coupled with $LiNbO_3$ SAW devices were used by Guo et al. [117] to manipulate and pattern polystyrene beads and protein crystals. Sobanski et al. [118] utilised glass microtubes with circular and square cross-sections inside a tubular PZT transducer on its axis to manipulate and separate polystyrene and silica particles. For cell studies, Lata et al. [114] and Gherardini et al. [115] used circular glass microtubes to immobilise cells and bacteria in the photosensitive polymer which was then cured into gel to form a fibre with fixed positions of the cells.

For continuous flow applications, Raiton et al. [108], Gralinski et al. [109], O'Mahoney et al. [110], and Hammarström et al. [111] used microtubes bonded onto piezoelectric transducers to trap microparticles inside the tube when the fluid flow direction and the acoustic radiation force are in the opposite directions. They also investigated the acoustic pressure fields and ARF through simulations. Additionally, Goddard et al. [116] managed to focus microparticles in a continuous flow platform by attaching a piezoceramic crystal to a soft glass microtube with circular cross-section to build a sheath-less flow cytometer.

There have also been a few studies on modelling of the integrated microtube and acoustofluidics platforms, and finite element simulations have been performed to investigate the fundamentals of particle manipulation inside microtubes [105-107, 110-112]. For example, Gralinski et al. [109, 119] simulated the effects of different configurations of the piezoelectric transducers connected to a circular glass microtube for particle trapping along the length of the tube in both non-flowing [109, 119] and flowing [109] platforms. Ley and Bruss [120] presented three-dimensional numerical modelling of particles trapped inside a glass microtube with a rectangular cross-section using a piezoelectric transducer and with continuous flow inside the tube. Bach and Bruus [121] further proposed a theory for particle trapping inside glass microtubes with an arbitrary cross-section. They modelled piezoelectric transducer actuation without any flow inside the microtube.

These microtubes are mostly made of glass but in some cases microtubes made of different materials such as polyimide [117] and cellulose [108] have also been used. They have a variety of different cross-sections such as circular [106, 108, 109, 114-116, 118], square [107, 110,

117, 118] and rectangular [105, 111], and are generally disposable, low-cost and easy to use in acoustofluidic setups.

2.3.10 Wall-less Microfluidic and Acoustofluidic Systems

Continuous flow acoustofluidic platforms require a microchannel to enable the fluid flow. For a conventional acoustofluidic device, solid microchannels are generally used and have been fabricated using PDMS [9, 25, 29, 44, 69], PMMA [99, 100], polystyrene (PS) [101-103] or glass [10, 63, 74], all of which require complicated and time-consuming processes such as soft lithography, cleanroom fabrication, milling, or injection moulding [4, 32]. To simplify the process and decrease the fabrication cost, wall-less microfluidic devices have become increasingly popular to be explored and developed [122-124].

Capillary bridges can offer a solution for designing wall-free acoustofluidic platforms and several types of capillary bridge systems have been developed to produce wall-less microfluidic platforms [124-132]. Capillary bridges are formed by fluids filling the gaps between two solid surfaces due to the fluid's surface tension [133]. They require a fluid guide in the form of a surface [122, 130, 134] or a thread [135] to hold the fluid. The virtual side walls of these capillary bridge channels is in contact with either air [124-126, 131, 132] or another liquid [122, 123, 128-130, 136].

Capillary bridges have been previously used in non-flowing acoustic systems by Hawkes et al. [137-139]. Yeon et al. [127] also designed a microfluidic device with a ladder microstructure for the fluid to form capillary bridges in between to study vascular biology.

For continuous flow applications, in order to facilitate the fluid flow, these wall-less microfluidic setups include a fluid guide which is either a flat surface [122-126, 131, 132] or consists of an array of apertures [127-130]. Programmable and reconfigurable continuous flow setups have also benefited from capillary bridges formed between arrays of electrodes for electrowetting and dielectrophoresis designed by Renaudot et al. [129]. Also an array of apertures with the ability to inject and withdraw liquid flowing inside another fluid medium was used by Taylor and Kaigala [130] to form any arbitrary channel. Lee et al. [128] used an array of micro-rings as fluid guides to reduce the liquid-solid interface area. In addition, capillary bridge channels can also be formed between two guide surfaces with hydrophilic (inside the channel) and hydrophobic (outside the channel) coatings to guide the fluid flow and prevent leakage as proposed by Bunge et al. [126]. and have been used to create hydrogel

membranes and pump fluid inside the channel. Also Nag et al. [125] used capillary bridges to perform various chemical reactions.

2.4 Governing Equations of Fluid Flow for Acoustofluidic Systems

For the continuous fluid, the first governing equation of motion is the continuity equation. It represents the conservation of mass of the fluid within a finite volume throughout the flow and the general form of this equation is written as follows:

$$\frac{\partial \rho_f}{\partial t} + \boldsymbol{\nabla}.\left(\rho_f \boldsymbol{U}_f\right) = 0 \qquad (2\text{-}1)$$

where ρ_f is the fluid density, $\boldsymbol{U}_f$ is the fluid velocity vector and t is the time.

The second equation represents the conservation of momentum in each direction within a finite volume. The general form of this equation is written as follows [140]:

$$\frac{\partial \rho_f \boldsymbol{U}_f}{\partial t} + \left(\boldsymbol{\nabla}.\rho_f \boldsymbol{U}_f \boldsymbol{U}_f\right) = -\boldsymbol{\nabla} P + \boldsymbol{\nabla}.(\boldsymbol{\tau}) + \boldsymbol{G} + \boldsymbol{F}_{AS} \qquad (2\text{-}2)$$

For Newtonian fluids, $\boldsymbol{\tau}$ can be defined as:

$$\boldsymbol{\tau} = \mu_f \left(\left(\boldsymbol{\nabla U}_f + \boldsymbol{\nabla U}_f{}^T\right) - \frac{2}{3}\left(\boldsymbol{\nabla}.\boldsymbol{U}_f\right) \right) \qquad (2\text{-}3)$$

where P is the fluid pressure, $\boldsymbol{\tau}$ is the stress tensor and μ_f is the fluid viscosity, $\boldsymbol{G} = \rho_f \boldsymbol{g}$ is the gravity force and $\boldsymbol{g}$ is the gravitational acceleration vector, and $\boldsymbol{F}_{AS}$ is the force which the fluid experiences due to the acoustic field [140]. The system of equations including the continuity and the conservation of momentum equations are called Navier-Stokes equations.

Assuming an incompressible flow because of the low velocities in the problem and thus having a constant fluid density, the set of above equations can further be simplified to [140]:

$$\boldsymbol{\nabla}.\boldsymbol{U}_f = 0 \qquad (2\text{-}4)$$

$$\rho_f \left(\frac{\partial \boldsymbol{U}_f}{\partial t} + \left(\boldsymbol{U}_f.\boldsymbol{\nabla}\right)\boldsymbol{U}_f \right) = -\boldsymbol{\nabla} P + \mu_f \boldsymbol{\nabla}^2 \boldsymbol{U}_f + \boldsymbol{F}_{AS} \qquad (2\text{-}5)$$

The above equations govern the motion of three-dimensional, viscous, and incompressible flow. Here, the effects of gravity force can be neglected compared to other forces [140].

Simplifying the Navier-Stokes equations for a steady, incompressible and laminar fluid flow leads to [140]:

$$\boldsymbol{\nabla}.\boldsymbol{U}_f = 0 \qquad (2\text{-}6)$$

$$\rho_f \left((\boldsymbol{U}_f.\boldsymbol{\nabla})\boldsymbol{U}_f \right) = -\boldsymbol{\nabla}P + \mu_f \boldsymbol{\nabla}^2 \boldsymbol{U}_f + \boldsymbol{F}_{AS} \qquad (2\text{-}7)$$

Equations (2-6) and (2-7) are used to model the fluid flow of the acoustofluidic setup in this research.

2.5 Equations of Acoustic Waves in Liquids

When an acoustic wave propagates in a liquid, the oscillatory pressure and velocity of the wave with length and time scales in the order of ~10^{-9} m and ~10^{-8} s affect the liquid and any particle suspended in it, both of which operate on length and time scales in the order of ~10^{-3} m and ~1 s. These acoustic changes in the field variables such as pressure and velocity with ~10^{-5} and ~10^{-3} orders of magnitude, although very small, are important for microfluidics with small length scales (~10^{-3} m). This is because they can affect the pressure and velocity fields of the fluid flow and can be even more noticeable for microfluidics compared to large scale fluid dynamics (with length and time scales in the order of ~1 m and ~1 s or larger). The compressibility of the liquid (negligible in hydrodynamics) is the cause of the acoustic wave propagation. Therefore, in order to derive the governing equations of the acoustic wave propagation in the liquid, a system of equations is considered which consists of Equations (2-1) and (2-2) and the pressure-density relation as following [81]:

$$P = P(\rho_f) \qquad (2\text{-}8)$$

The changes to the fluid variables caused by the acoustic effects can be considerd as small perturbations added to the unperturebd state of the fluid. The field variable can then be written as a combination of unperturbed and first order (perturebed) approximations [81]:

$$P = P_0 + P_a \qquad with \qquad P_a = \rho_a {c_f}^2 \qquad (2\text{-}9)$$

$$\rho_f = \rho_0 + \rho_a \qquad with \qquad \rho_a = \frac{P_a}{{c_f}^2} \qquad (2\text{-}10)$$

$$\boldsymbol{U}_f = 0 + \boldsymbol{U}_a \qquad (2\text{-}11)$$

where 0 and a indices denote unperturbed state and first order approximation and where $c_f = \sqrt{\left(\frac{\partial P}{\partial \rho}\right)_s}$ is the isentropic derivative of pressure equal to wave speed in the fluid. It can be assumed that the fluid is at rest $\boldsymbol{U}_0 = 0$ for the sake of simplicity [81]. Substituting the above equations in Equations (2-1), (2-2) and (2-8) and solving for the zeroth order equations, the system of equations becoms [81]:

$$P = P(\rho_0) = P_0 \tag{2-12}$$

$$\frac{\partial \rho_0}{\partial t} = 0 \tag{2-13}$$

$$0 = -\boldsymbol{\nabla} P_0 \tag{2-14}$$

Solving Equations (2-1), (2-2) and (2-8) for the first order equations and assuming the viscousity of the fluid is negligible, the govering equations of acoustic field becomes [81]:

$$P_a = \rho_a {c_f}^2 \tag{2-15}$$

$$\frac{\partial \rho_a}{\partial t} = \rho_0(\boldsymbol{\nabla}.\boldsymbol{U}_a) \tag{2-16}$$

$$\rho_0 \frac{\partial \boldsymbol{U}_a}{\partial t} = -{c_f}^2 \boldsymbol{\nabla} \rho_a \tag{2-17}$$

With some modifications, the above set of equations can also be presented as follows [81]:

$$\frac{\partial^2 P_a}{\partial t^2} = {c_f}^2 \boldsymbol{\nabla}^2 P_a \tag{2-18}$$

$$\frac{\partial^2 \rho_a}{\partial t^2} = {c_f}^2 \boldsymbol{\nabla}^2 \rho_a \tag{2-19}$$

$$\frac{\partial^2 \boldsymbol{U}_a}{\partial t^2} = {c_f}^2 \boldsymbol{\nabla}^2 \boldsymbol{U}_a \tag{2-20}$$

Introducing the velocity potential $\varphi(\boldsymbol{r}, t)$ as $\boldsymbol{U}_a = \boldsymbol{\nabla}\varphi$, where $\boldsymbol{r}$ is position vector, substituting it in Equation (2-20) and simplifying the formula, the wave equation is derived as follows [81]:

$$\frac{\partial^2 \varphi}{\partial t^2} = {c_f}^2 \boldsymbol{\nabla}^2 \varphi \tag{2-21}$$

A solution to the above wave equation is the plane wave with an angular frequency of ω as $\varphi(\boldsymbol{r}, t) = \varphi(\boldsymbol{r}) e^{i\omega t}$ and substituting it in Equation (2-21) leads to the Helmholtz equation [81]:

$$\nabla^2\varphi(\boldsymbol{r}) = -\frac{\omega^2}{{c_f}^2}\varphi(\boldsymbol{r}) = -k^2\varphi(\boldsymbol{r}) \qquad (2\text{-}22)$$

Another form of the Helmholtz equation can be derived by substituting the wave pressure equation $P(\boldsymbol{r},t) = P(\boldsymbol{r})e^{i\omega t}$ into Equation (2-18):

$$\nabla^2 P(\boldsymbol{r}) + \frac{\omega^2}{{c_f}^2}P(\boldsymbol{r}) = 0 \qquad (2\text{-}23)$$

Solving the Helmholtz equation needs proper boundary conditions such as hard wall, soft wall, impedance or moving boundaries. For Helmholtz equation, the time scale is set by the wave's frequency and is defined as the wave's period $T = 1/f$.

2.5.1 Acoustic Streaming

2.5.1.1 Acoustic Streaming Effects by Modelling the Acoustic Field

Analytical study on acoustic streaming effect was first introduced by Nyborg [37] and was later improved by Lighthill [38]. The acoustic streaming forces can be calculated in a fluid assuming a steady state for both the acoustic and flow fields using the perturbation method. The field variables can be written as a combination of unperturbed state, first order, and second order approximations [37, 38, 141]:

$$P = P_0 + P_a + P_b \qquad with \qquad P_a = \rho_a {c_f}^2 \qquad (2\text{-}24)$$

$$\rho_f = \rho_0 + \rho_a + \rho_b \qquad with \qquad \rho_a = \frac{P_a}{{c_f}^2} \qquad (2\text{-}25)$$

$$\boldsymbol{U}_f = \boldsymbol{U}_0 + \boldsymbol{U}_a + \boldsymbol{U}_b \qquad (2\text{-}26)$$

where 0 , a and b indices denote unperturbed state, first order and second order approximations of the three variables. Substituting the above equations in Equations (2-1) and (2-2) of the fluid flow and solving for the first and second order equations result in the acoustic field equations. The acoustic streaming force, $\boldsymbol{F}_{AS}$, acts as a body force on the fluid and is calculated using the second order source terms of the equations as follows [37, 38, 141]:

$$\boldsymbol{F}_{AS} = \langle \rho_a \partial_t \boldsymbol{U}_a \rangle + \rho_f \langle (\boldsymbol{U}_a . \boldsymbol{\nabla}) \boldsymbol{U}_a \rangle \qquad (2\text{-}27)$$

where $\langle \Psi \rangle$ denotes the time average of Ψ over the period (i.e. time scale) of the acoustic wave [37, 38, 141]. Using the first order continuity equation, the above can be further simplified to [37, 38, 141]:

$$\boldsymbol{F}_{AS} = \rho_f \langle \boldsymbol{U}_a (\boldsymbol{\nabla}.\boldsymbol{U}_a) \rangle + \rho_f \langle (\boldsymbol{U}_a.\boldsymbol{\nabla}) \boldsymbol{U}_a \rangle \quad (2\text{-}28)$$

The acoustic streaming force components from Equation (2-28) can be calculated as follows [37, 38, 141]:

$$F_{AS_x} = \left(\frac{\rho_f}{2} U_{a_x} \left(\frac{\partial U_{a_x}}{\partial x} + \frac{\partial U_{a_y}}{\partial y} \right) \right) + \left(\frac{\rho_f}{2} \left(U_{a_x} \frac{\partial U_{a_x}}{\partial x} + U_{a_y} \frac{\partial U_{a_x}}{\partial y} \right) \right) \quad (2\text{-}29)$$

$$F_{AS_y} = \left(\frac{\rho_f}{2} U_{a_y} \left(\frac{\partial U_{a_x}}{\partial x} + \frac{\partial U_{a_y}}{\partial y} \right) \right) + \left(\frac{\rho_f}{2} \left(U_{a_x} \frac{\partial U_{a_y}}{\partial x} + U_{a_y} \frac{\partial U_{a_y}}{\partial y} \right) \right) \quad (2\text{-}30)$$

where U_{a_x} and U_{a_y} are the wave velocities in x- and y-directions, respectively. For the TSAW propagating in the x-direction with velocity components of $U_{a_x} = \bar{U}_{a_x} e^{i\omega t}$ and $U_{a_y} = \bar{U}_{a_y} e^{i\omega t}$ (where $\bar{U}$ is the the non-oscillatory part of the velocity) and using Equation (2-27) and $\rho_a = {P_a}/{{c_f}^2}$, the acoustic streaming force components are derived as [37, 38, 141]:

$$F_{AS_x} = \left(\frac{P_a}{2{c_f}^2} \omega \bar{U}_{a_x} \right) + \left(\frac{\rho_f}{2} \left(\bar{U}_{a_x} \frac{\partial \bar{U}_{a_x}}{\partial x} + \bar{U}_{a_y} \frac{\partial \bar{U}_{a_x}}{\partial y} \right) \right) \quad (2\text{-}31)$$

$$F_{AS_y} = \left(\frac{P_a}{2{c_f}^2} \omega \bar{U}_{a_y} \right) + \left(\frac{\rho_f}{2} \left(\bar{U}_{a_x} \frac{\partial \bar{U}_{a_y}}{\partial x} + \bar{U}_{a_y} \frac{\partial \bar{U}_{a_y}}{\partial y} \right) \right) \quad (2\text{-}32)$$

Equations (2-29) to (2-32) model the acoustic streaming forces using the first order density and velocity caused by the acoustic filed.

2.5.1.2 Acoustic Streaming Effects by Approximation

As the microchannel's height is considerably smaller than its width in most cases, to simplify the acoustic streaming force, a one-dimensional attenuating TSAW propagating in the x-direction is considered, and the wave's velocity component in the y-direction can be negligible. The wave velocity can be written as:

$$U_{a_x} = U_{ac} e^{-(\alpha+ik)x} e^{i\omega t} \tag{2-33}$$

where U_{ac} is the wave velocity amplitude, α is the attenuation parameter, $k = \frac{2\pi}{\lambda}$ is the wavenumber, $\lambda = \frac{c_f}{f}$ is the wavelength, f is the frequency, and x is the fluid location along the wave propagation direction. Substituting Equation (2-33) in Equation (2-28), the acoustic streaming force can be derived without the need for the first order density and velocity caused by the acoustic field:

$$\boldsymbol{F}_{AS} = -\alpha \rho_f {U_{ac}}^2 e^{-2\alpha x} \tag{2-34}$$

Using the wave intensity $I_{ac} = \frac{1}{2}\omega^2 A^2 \rho_f c_f$ in Equation (2-34):

$$\boldsymbol{F}_{AS} = -\sigma {c_f}^{-1} I_{ac} e^{-\sigma x} \tag{2-35}$$

where A is the wave displacement amplitude and $\sigma^{-1} = \frac{1}{2\alpha}$ is the fluid attenuation length, [37, 38, 44, 141]. The attenuation of the wave occurs due to the acoustic refraction, as the amplitude of the "leaky" wave starts to attenuate when it propagates into the fluid. The refraction angle, which is called the Rayleigh angle, is calculated using the ratio of the sound velocity in the piezoelectric substrate to the sound velocity in the liquid [1].

$$\theta_R = \arcsin\left(\frac{c_f}{c_s}\right) \tag{2-36}$$

where c_f is the wave speed in the fluid and c_s is the wave speed in the piezoelectric substrate [1]. This means that the acoustic streaming force is in the Rayleigh wave direction [37, 38, 44, 141]:

$$F_{AS_x} = -\alpha \rho_f {U_{ac}}^2 e^{-2\alpha x} \sin\theta_R \tag{2-37}$$

$$F_{AS_y} = -\alpha \rho_f {U_{ac}}^2 e^{-2\alpha x} \cos\theta_R \tag{2-38}$$

The acoustic streaming force acts as a body force on the fluid [1] and thus Equations (2-29) to (2-32) or (2-37) and (2-38) are substituted as the term $\boldsymbol{F}_{AS}$ in equations of motion of the fluid [37, 38, 44, 141].

2.5.2 Acoustic Radiation Force

Analytical study on acoustic radiation force was first presented by King [39]. He calculated the acoustic radiation force on a rigid sphere suspended in inviscid fluid using perturbation method.

The calculations was then expanded by Yosioka and Kawasima [40] to account for the effects of the microparticles' compressibility. Gorkov [86] summarised and generalised these studies. The acoustic radiation force on a rigid [41] and a compressible [42] sphere suspended in a viscous fluid was derived by Doinikov [41, 42].

The acoustic radiation force is the result of the momentum transfer from the acoustic wave to the particles. The first step in the derivation of the acoustic radiation force is using the perturbation method described in the previous section to obtain an equation for the time-averaged second order pressure. In addition, as the small particle acts as a weak point-scatterer of the acoustic waves, the first-order scattering theory is used to obtain the fist-order scattered field for the incoming acoustic field. The acoustic radiation force can then be calculated as the surface integral of the time-averaged second-order pressure and momentum flux tensor. The scattering theory is used to calculate the monopole and dipole coefficients which are the coefficients resulting from the integration used to calculate the acoustic radiation.

2.5.2.1 Acoustic Radiation Force due to TSAW

The primary acoustic radiation force, $\boldsymbol{F}_{AR}$, acting on a spherical particle suspended in a fluid in a TSAW field is described as follows [33, 39-42, 84, 86]:

$$\boldsymbol{F}_{AR} = f_2^i(\tilde{\rho},\tilde{\delta})\pi r^3 \rho_f \langle \boldsymbol{V}_{in}.\boldsymbol{\nabla}\boldsymbol{V}_{in}\rangle \boldsymbol{k} \qquad with \qquad \tilde{\rho} = \frac{\rho_p}{\rho_f} \qquad and \qquad \tilde{\delta} = \frac{\delta}{r} \tag{2-39}$$

$$f_2^i(\tilde{\rho},\tilde{\delta}) = Im\left[\frac{2[1-\gamma(\tilde{\rho})](\tilde{\rho}-1)}{2\tilde{\rho}+1-3\gamma(\tilde{\rho})}\right] \tag{2-40}$$

where r is the particle radius, $\boldsymbol{V}_{in}$ is velocity field of the incoming wave, $\boldsymbol{k}$ is the wave vector, and δ is the thickness of the viscous, acoustic boundary layer. The term $f_2^i(\tilde{\rho},\tilde{\delta})$ can be calculated as follows [33, 39-42, 84, 86]:

$$f_2^i(\tilde{\rho},\tilde{\delta}) = \frac{6(1-\tilde{\rho})^2(1+\tilde{\delta})\tilde{\delta}}{(1+2\tilde{\rho})^2 + 9(1+2\tilde{\rho})\tilde{\delta} + \frac{81}{2}\left(\tilde{\delta}^2 + \tilde{\delta}^3 + \frac{1}{2}\tilde{\delta}^4\right)} \tag{2-41}$$

The terms with higher powers of $\tilde{\delta}$ are ignored for calculation simplicity [33, 39-42, 84, 86]. For a one directional TSAW propagating in x-direction, the force is presented as follows [33, 39-42, 84, 86]:

$$F_{AR_x} = f_2^i(\tilde{\rho},\tilde{\delta})\pi r^3 E_{ac} k \tag{2-42}$$

where $E_{ac} = \frac{1}{2}\beta_f {P_{ac}}^2$ is the acoustic energy density of the wave, β_f is the fluid compressibility, and P_{ac} is the acoustic pressure amplitude [33, 39-42, 84, 86].

If the effects of fluid viscosity are negligible, the acoustic radiation force is reduced by a factor of $(kr)^3$. If the effects of compressibility of the particles are also negligible, the acoustic radiation force for a travelling acoustic wave is calculated using the following equations [33, 39-42, 84, 86]:

$$F_{AR_x} = \left(\frac{2\pi^3 {P_{ac}}^2 {\forall_p}^2 \beta_f}{\lambda^4}\right)\emptyset_t(\rho) \qquad (2\text{-}43)$$

$$\emptyset_t(\rho) = \frac{9 + 2(1 - {\rho_f}/{\rho_p})^2}{(2 + {\rho_f}/{\rho_p})^2} \qquad (2\text{-}44)$$

where $\forall_p$ is the particle volume [33, 39-42, 56, 74, 83, 84, 86].

2.5.2.2 Acoustic Radiation Force due to SSAW

The primary acoustic radiation force, F_{AR}, acting on a single spherical particle suspended in a fluid medium in a standing acoustic wave field is described as follows [33, 39-42, 84, 86]:

$$\boldsymbol{F}_{AR} = \frac{-4\pi}{3} r^3 \left[f_1(\tilde{\beta})\beta_f \langle P_{in} \boldsymbol{\nabla} P_{in} \rangle - f_2(\tilde{\rho})\rho_f \frac{3}{2} \langle (\boldsymbol{V}_{in} \cdot \boldsymbol{\nabla}) \boldsymbol{V}_{in} \rangle \right] \qquad (2\text{-}45)$$

$$f_1(\tilde{\beta}) = 1 - \tilde{\beta} \qquad with \qquad \tilde{\beta} = \frac{\beta_p}{\beta_f} \qquad (2\text{-}46)$$

$$f_2^r(\tilde{\rho}) = Re\left[\frac{2[1 - \gamma(\tilde{\rho})](\tilde{\rho} - 1)}{2\tilde{\rho} + 1 - 3\gamma(\tilde{\rho})}\right] \qquad with \qquad \tilde{\rho} = \frac{\rho_p}{\rho_f} \qquad (2\text{-}47)$$

$$\gamma(\tilde{\rho}) = -\frac{3}{2} Re\left[1 + i\left(1 + \tilde{\delta}\right)\right]\tilde{\delta} \qquad with \qquad \tilde{\delta} = \frac{\delta}{r} \qquad (2\text{-}48)$$

where P_{in} is the acoustic pressure field and β_p is the particle compressibility. The terms with higher powers of $\tilde{\delta}$ are ignored for simplicity of calculation [33, 39-42, 84, 86]. By simplifying the acoustic radiation force for a one-dimensional standing acoustic wave, the force can be presented as follows [33, 39-42, 84, 86]:

$$F_{AR_x} = 2\pi r^3 \emptyset\left(\tilde{\beta}, \tilde{\rho}, \tilde{\delta}\right) E_{ac} k \sin(2k\tilde{x}) \qquad (2\text{-}49)$$

$$\emptyset_s(\tilde{\beta},\tilde{\rho},\tilde{\delta}) = \frac{1}{3}f_1(\tilde{\beta}) + \frac{1}{2}f_2^r(\tilde{\rho},\tilde{\delta}) \quad (2\text{-}50)$$

where $\tilde{x}$ is the particle's distance from the nearest pressure node (or anti-node) along the wave propagation direction [33, 39-42, 84, 86]. The term $f_2^r(\tilde{\rho},\tilde{\delta})$ can be calculated as follows:

$$f_2^r(\tilde{\rho},\tilde{\delta}) = \frac{2(\tilde{\rho}-1)\left[(2\tilde{\rho}+1)+3\tilde{\delta}(\tilde{\rho}+2)+\frac{27}{2}\left(\tilde{\delta}^2+\tilde{\delta}^3+\frac{1}{2}\tilde{\delta}^4\right)\right]}{(2\tilde{\rho}+1)^2+9\tilde{\delta}(2\tilde{\rho}+1)+\frac{81}{2}\left(\tilde{\delta}^2+\tilde{\delta}^3+\frac{1}{2}\tilde{\delta}^4\right)} \quad (2\text{-}51)$$

The terms with higher powers of $\tilde{\delta}$ can be ignored for calculation simplicity [39-42, 84].

If the effects of fluid viscosity and particle compressibility are negligible, the acoustic radiation force for a standing acoustic wave can be calculated using the following equations [33, 39-42, 84, 86]:

$$F_{AR_x} = \left(\frac{\pi {P_{ac}}^2 \forall_p \beta_f}{2\lambda}\right)\emptyset_s(\rho)\sin(2k\tilde{x}) \quad (2\text{-}52)$$

$$\emptyset_s(\rho) = \frac{5\rho_p - 2\rho_f}{2\rho_p + \rho_f} \quad (2\text{-}53)$$

The acoustic radiation force from the standing wave directs the particles towards either the pressure node (the minimum pressure amplitude) or the pressure antinode (the maximum pressure amplitude), depending on the physical and mechanical properties of fluid and particle [10]. $\emptyset_s(\tilde{\beta},\tilde{\rho},\tilde{\delta})$ is called the acoustic contrast factor and its sign defines whether each particle moves towards the pressure node ($\emptyset_s(\tilde{\beta},\tilde{\rho},\tilde{\delta}) > 0$) or the pressure antinode ($\emptyset_s(\tilde{\beta},\tilde{\rho},\tilde{\delta}) < 0$) under the effect of acoustic radiation force [33, 39-42, 56, 74, 83, 84, 86]. Polystyrene, silica, and yeast particles were used in this study, which were driven to the pressure nodes.

Equations (2-24) and (2-52) show that the radiation force has a sinusoidal distribution with a period of half of the wavelength. Thus the distance between particle pattern lines D is theoretically equal to half of the wavelength [56], in other words,

$$D = \frac{\lambda}{2} \quad (2\text{-}54)$$

2.6 Fluid-Particle Interactions

Many flows in the real-world consists of more than one phase and many of the industrial processes depend on multiphase flows to happen. Acoustofluidic flow consisting of particle and droplets moving in a fluid medium is one such example. In a multiphase flow, a phase is defined as an identifiable class of material that has a particular inertial response to and interaction with the flow and the potential field in which it is immersed. In other words, a phase is defined by the difference in densities, sizes and shapes [142, 143].

The theory of fluid-particle interactions explains how the phases in a multiphase flow affect each other, couple with each other and exchange mass, momentum, and energy. To model a multiphase flow, two main approaches are used i.e., the Euler-Lagrange approach and the Euler-Euler approach. The continuous phase is generally assumed to be Eulerian [142, 143]. The governing equations of motion for the continuous fluid phase (Eulerian phase) were presented in the previous section.

2.6.1 Euler-Lagrange Approach

In the Euler-Lagrange approach, the fluid flow is considered as the Eulerian phase and is modelled by solving Navier-Stokes equations. The secondary phase is simulated by individually tracking a large number of particles using a Lagrangian approach. Using this approach provides the detailed information for each particle including its position, velocity, and temperature. An important but limiting assumption in the Euler-Lagrange approach is that the dispersed secondary phase of microparticles should occupy a low volume fraction compared to the primary fluid phase [142].

The governing equations of the dispersed microparticle phases utilizing the Euler-Lagrange approach for a single particle can be written as follows [142]:

$$\rho_p = const. \tag{2-55}$$

$$\frac{\partial \boldsymbol{X}_p}{\partial t} = \boldsymbol{U}_p \tag{2-56}$$

$$\frac{\partial \rho_p \boldsymbol{U}_p}{\partial t} = \boldsymbol{D} + \boldsymbol{W} + \boldsymbol{F}_{AR} \tag{2-57}$$

where ρ_p is the particle's density, $\boldsymbol{X}_p$ is the particle's position vector, $\boldsymbol{U_p}$ is the particle velocity vector, $\boldsymbol{D}$ is the drag force acting on the particle, $\boldsymbol{W} = (\rho_p - \rho_f)\boldsymbol{g}$ is the gravity and buoyancy force and $\boldsymbol{F}_{AR}$ is the acoustic force acting on the particle.

The drag force $\boldsymbol{D}$ in Equation (2-57) that the particles experience when moving through the fluid depends on the properties of the fluid, the properties of the particles and the velocity of the particle relative to the flow [142]. For spherical particles, this viscous drag force is given by the Stokes' drag law [56, 142]:

$$\boldsymbol{D} = 6\pi\mu_f r\boldsymbol{U}_{relative} = \rho_p \frac{\boldsymbol{U}_f - \boldsymbol{U}_p}{\tau_p} \qquad (2\text{-}58)$$

where $\boldsymbol{U}_{relative} = \boldsymbol{U}_f - \boldsymbol{U}_p$ is the fluid velocity relative to the particle velocity, $\tau_p = \rho_p d^2/18\mu_f$ is the particle characteristic time which is the time the particle takes to respond to a velocity change, d is the particle's diameter [56, 142]. For non-spherical particles, the drag force can be modelled using other models such as "Haider-Levenspiel" which uses different empirical correlations and coefficients to calculate the viscous drag force.

2.6.2 Euler-Euler Approach

In the Euler-Euler approach, all phases are considered continuous and Eulerian and are modelled by solving the conservation of mass and momentum equations. The system of equations is closed by application of kinetic theory in the case of granular (fluid-solid) flows. Using the approach will not set a limit on the volume fraction but add the complexity in modelling particle size distribution and particle-particle interactions [142].

If the Euler-Euler approach is used to model the microparticle phases, the governing equations for the secondary phase which is assumed to be continuous are as follows [142]:

$$\frac{\partial(\alpha_p\rho_p)}{\partial t} + \boldsymbol{\nabla}.\left(\alpha_p\rho_p\boldsymbol{U}_p\right) = 0 \qquad (2\text{-}59)$$

$$\frac{\partial(\alpha_p\rho_p\boldsymbol{U}_p)}{\partial t} + \boldsymbol{\nabla}.\left(\alpha_p\rho_p\boldsymbol{U}_p\boldsymbol{U}_p\right) = -\alpha_p\boldsymbol{\nabla}P + \alpha_p\mu_p\boldsymbol{\nabla}^2\boldsymbol{U}_p + \alpha_p\rho_p\boldsymbol{g} + \boldsymbol{F}_I + \boldsymbol{F}_{AR} \qquad (2\text{-}60)$$

where $\alpha_p = n\pi d^3/6$ and n is the number of particles and $\sum_{p=1}^{n} \alpha_p = 1$. $\boldsymbol{F}_I = \sum_{p=1}^{n} -C_i\left(U_f - U_p\right)$ is the interaction force among the phases, $C_i = \frac{\alpha_p \rho_p \tilde{f}}{\tau_p}$ is the interphase momentum exchange coefficient of fluid-solid interaction and $\tilde{f}$ is the drag function [142].

In the case of granular (fluid-solid) flows, the momentum equation is slightly changed as follows:

$$\frac{\partial(\alpha_p \rho_p \boldsymbol{U}_p)}{\partial t} + \nabla.\left(\alpha_p \rho_p \boldsymbol{U}_p \boldsymbol{U}_p\right) = -\alpha_p \boldsymbol{\nabla} P - \boldsymbol{\nabla} P_s + \alpha_p \mu_p \boldsymbol{\nabla}^2 \boldsymbol{U}_p + \mu_s \boldsymbol{\nabla}^2 \boldsymbol{U}_p + \alpha_p \rho_p \boldsymbol{g} + \boldsymbol{F}_I + \boldsymbol{F}_{AR} \quad \textit{(2-61)}$$

where P_s and μ_s are the solid pressure and viscosity, respectively [142].

2.6.3 Comparing Euler-Lagrange and Euler-Euler Approaches

The Euler-Lagrange approach models each particle individually and thus presents the position and velocity components of each individual particle. However this approach is only suitable for dilute flows where the dispersed phase occupies a low volume fraction compared to the primary fluid phase and the fluid-particle interaction dictates the particles' movement [142].

Whereas for the Euler-Lagrange approach, there are no limits on the volume fraction of the second phase so it can be used to model dense flows. Using this approach, however, adds the complexity to modelling the particle size distribution and particle-particle interactions [142].

In this research, the multiphase flow of one primary phase of continuous fluid and secondary phases of dispersed microparticles are of interest. Since the volume fraction of the dispersed phase is smaller than the volume fraction of the continuous fluid phase, the fluid-particle mixture is sparsely distributed, and the Euler-Lagrange approach can be used to model the microparticles.

2.6.4 Other Forces Acting on Particles

Aside from the drag force, the acoustic radiation force, the gravity and buoyancy force, there are other forces that can act on the particles, including the virtual mass force and lift force. The virtual mass force is important only when the continuous phase density is much larger than the particle phase, whereas the lift force is neglected unless the particles are large enough or the phases are quickly separated [142].

2.6.5 Particle-Particle Interactions

The theory of particle-particle interactions in a multiphase flow explains the collisions between the particles and how this causes the loss of momentum and kinetic energy associated with inter-particle collisions. The particle-particle interactions are important in dense multiphase flows whereas inter-particle collisions and the associated kinetic energy loss are negligible in dilute multiphase flows [142].

To model particle-particle interactions, two main models are used, i.e., the hard sphere model and the soft sphere model. The hard sphere model represents the collision of two particles using the velocities before and after collision to calculate the coefficient of restitution and friction coefficient. For a dispersed particle phase, the hard sphere model is sufficient. The soft sphere model represents the collision of one particle with a group of particles. The particles are all assumed deformable under the force and the deformation is replaced by overlapping of the particles [142].

2.6.6 Particle-Wall Interactions

In dense multiphase flows and wall-dominated flows, the interactions between particle and wall are important. The particle-wall interactions can be categorised into two groups: the hydrodynamic interactions caused by the presence of the wall and the mechanical interactions caused by the particle-wall contact [142].

The mechanical particle-wall interactions are defined by the inertia of the particles. If a large or a dense particle collides with the wall boundary of the flow domain, it reflects off the wall with a loss in its momentum and kinetic energy. On the other hand, if a small particle collides with the wall, the particle is trapped at the wall due to the dominance of the molecular forces compared to the inertial forces. In conclusion, when the particle collides with the wall boundary of the flow domain, three main interactions can be considered: reflect, trap or escape [142].

In the reflect condition, the particle is reflected off from the wall and its momentum changes due to friction and inelasticity effects. In the trap condition, the particle is trapped at the wall and it neither reflects nor slides along the wall. In the escape condition, the particle escapes through the wall and it can be used for walls made of porous materials [142].

2.7 Numerical Models to Investigate the Acoustofluidic Systems

As thoroughly discussed in the previous sections, acoustofluidics have shown great promise to be integrated in clinical and biomedical devices for investigation and manipulation of microparticles and biological cells for cell analysis [25-27, 30-32] and cancer diagnosis [9, 28] with a high biocompatibility, cell viability and conserving proliferation. However, most of the existing literature utilised acoustofluidic-based platforms in a small-scale laboratory setting. Even though this new technology was successful in trials and offered significant potentials for large-scale and real-life practical applications its use has still not been widespread. One reason for this shortcoming could be the lack of knowledge on the exact details of acoustic devices' working principles which can be acquired from either analytical investigation, experimental work, or computational simulation.

Most of the present literature on acoustofluidics focuses on experimental work to investigate focusing [9, 43, 46, 67, 68], directing [58], sorting [44, 69, 70], separation [9, 25-31, 45, 49, 61-66, 71], traping [72], patterning [73], enriching [74] and aligning [47] of microparticles, bubbles and even biological cells. Through experimental work the effects of different properties of acoustic fields such as frequency, wavelength and power, various fluids and flow rates, as well as the properties of the microparticles including size [25, 27-30, 45, 49, 61-65], density [31, 49, 66], and compressibility [49] were studied. However, for experimental studies, an experimental setup containing SAW devices, microchannels and other laboratory equipment is needed which are often costly, time consuming and complicated to manufacture and maintain. Additionally, new setups might be needed to be built in order to study even a small detail of the acoustofluidic setups. The underlying physics and some details of the acoustofluidic systems are often challenging to obtain through experiments.

Numerical modelling of the acoustofluidic systems can help in understanding the underlying physics of these complex multi-physics systems by providing detailed information about the acoustic and fluid flow fields, the behaviours of microparticles affected by hydrodynamic and acoustic forces. It can offer the different effects of various parameters in a cost and time effective manner, which is essential in designing and fabricating acoustofludic platforms. Numerical modelling is a very powerful technique which uses computer-based simulations to analyse the acoustofluidic systems by discretising the governing equations of the system and converting them into a system of algebraic equations and solving them using an iterative method. Numerical modelling of acoustofluidic systems need computers to perform simulation

and can present the solution to the governing equations with an acceptable accuracy. When the desired accuracy is too high or the system is complicated, the computers need to be powerful enough to perform the simulations and they may consume more resources. However, for the typical acoustofluidic systems, numerical simulations present all the details of the system, which are sometimes impossible to obtain through the experimental work, including the acoustic field parameters, the fluid flow variables, and the particle behaviour.

There are previous studies on numerical simulations of acoustofluidic systems. For example, Schmid et al. [44] simulated particle deflection based on acoustic streaming effect and Collins et al. [43] presented acoustic streaming flow field and fluid streamlines in two dimensions, both without modelling the acoustic field. Two-dimentional simulations of the acoustic field in the microchannel cross-sections have often been used to predict the microparticle behaviour under the effects of SSAWs and TSAWs. Acoustic presure is one of the main parameters of a SAW field and simulating it often help to study microparticle manipulations. For the SSAWs, the acoustic pressure fields in the microchannel cross-section were simulated by Wu et al. [27] and Ai and Marrone [29]. Ma et al. [45] and Fakhfouri et al. [48] simulated the acoustic pressure field in the microchannel cross-section resulted from TSAWs to investigate the microparticles' behaviour. Shi et al. [46] simulated both the acoustic pressure and velocity fields caused by the SSAW in the cross-section of their channel to investigate particle focusing. Microparticle properties and moving tracks have also been modelled to gain the information of their behaviours. Simon et al. [49] numerically modelled the particle's velocity profiles in a microchannel flow for different manipulation cases. Johansson et al. [47] studied particle alignment using the SSAW by simulating the acoustic pressure field and particle traces and compared them to their experimental data. Ding et al. [28] numerically simulated particle separation particle trajectories within a taSSAW field. Shamloo and Boodaghi [50] performed numerical simulations of cell separations in a SSAW field, based on the acoustic pressure field and particle trajectories for the experimental data of Shi et al. [61]. However, few attempts have been made to assess the basis, strengths, and limitations of various computational methods. Such investigation can help to optimise acoustofluidic devices and can potentially lead to development of novel devices.

Acoustofluidic systems are multi-physics and complicated with different time and length scales and are comprised of three main components, i.e., the acoustic field, the fluid field, and the particles. It is essential to have a thorough understanding of the theory behind each component in order to choose the most efficient approach for modelling the acoustofluidic system while

maintaining a reasonable computational time and cost. In this section, different modelling methods are discussed and investigated.

2.7.1 Direct Numerical Simulation

The most accurate approach to model an acoustofluidic system is the direct numerical simulation (DNS). In this approach the flow and acoustic fields are modelled based on three-dimensional and compressible Navier-Stokes equations which are able to fully couple the acoustic and fluid fields and simulate the interactions between them. DNS can resolve the wide range of length and time scales of the acoustofluidic system from the extra small-scale and fluctuating pressure and velocity fields of the SAWs (with length and time scales in the order of $\sim 10^{-9}$ and $\sim 10^{-8}$ s, respectively) to the large-scale pressure and velocity fields of the bulk fluid (with length and time scales in the order of $\sim 10^{-3}$ m and ~1 s, respectively). The computational mesh needed for such accurate simulations needs to be extremely fine in order to resolve the smallest of interactions, which makes this approach highly costly and time-consuming even with high-performance computers.

2.7.2 Separation of Scales and Perturbation Method

In order to reduce the computational cost and time for modelling of the acoustofluidic system while still presenting accurate results, the separation of scales and perturbation method are used to derive the governing equations of the acoustic field inside the fluid. In this approach, the oscillatory pressure and velocity of the acoustic field can be assumed as small-scale perturbations added to the unperturbed large-scale state of the fluid field. The field variables can then be considered as a combination of unperturbed and perturbed approximations [81].

Assuming a steady state for both the acoustic and flow fields, Nyborg [37] and later Lighthill [38] used perturbation methods to model the acoustic-fluid inteactions in an acoustofluidic system which was disscussed in detail in section 2.5.

2.7.3 Using Body Forces to Apply the Acoustic Effects

The separation of scales modelling approach can be used to develop a more simplified yet still accurate modelling method. Using the governing equations of the acoustic field inside the fluid which were derived using the perturbation method and also assuming one-dimensional attenuating acoustic waves, the acoustic effects can be described by the explicit formulas [141]. These formulas represent the acoustic effects acting on the fluid (acoustic streaming) and

microparticles (acoustic radiation) and can be added to the to the governing equations of motion as external body forces [43, 44, 141]. This approach will significantly decrease the computational cost and time while still presenting results with a reasonable accuracy. It has been used by Schmid et al. [44] to model particle deflection by acoustic streaming, and by Collins et al. [43] to model acoustic streaming in two dimensions. This method was disscussed in detail in section 2.5.

2.8 Summary

In this chapter, the existing literature on SAW-based microfluidic platforms, potential applications of SAW-based acoustofluidic systems, the complete theory and formulation of acoustofluidic systems, and the governing equations necessary for modelling each part of these systems were reviewed.

Based on the literature review presented in this chapter, the following are the identified gaps in the existing literature:

- Most of the existing literature on SAW-based acoustofluidic platforms concentrate on experimental investigation which can present the proof of the concept, the evidence of the system functioning and the data to verify the simulation results. However, experimental investigation can neither provide detailed information including acoustic and fluid flow variables and particle behaviours, nor an explanation for the observed experimental results. Computational modelling of the acoustofluidic platforms utilising accurate models is capable of providing the underlying physics and working principles of these platforms, determining the behaviours of every component of the system, offering verified and reliable results of the acoustic and fluid fields and microparticle dynamics, and helping to improve and optimise the acoustofluidic system but has not been investigated extensively.
- Additionally, most of the previous research on SAW-based acoustofluidics is focused on rigid piezoelectric materials such as lithium niobate which are typically expensive and brittle, normally fragile at high RF powers, prone to breaking when handled improperly, and are non-compatible with microelectronics and other fluidic components. Flexible thin film SAW devices offer a solution to the fragile nature of the rigid SAW devices with advantages such as high SAW speed, reasonably good electro-mechanical coupling coefficient, easy integration with other acoustofluidic components and potential applications such as body conforming wearable devices. However, these flexible and

deformable SAW devices have not been used in continuous flow acoustofluidic platforms for patterning of microparticles and biological cells.

- Conventional continuous flow acoustofluidic platforms include solid microchannels to enable the fluid flow which are typically fabricated in a cleanroom using complicated, expensive and/or time-consuming procedures. In order to simplify the process and decrease the fabrication time and cost, capillary bridges can be utilised to design a continuous flow wall-less acoustofluidic platform. They have been previously used in non-flowing acoustic systems but using them in continuous flow setups have not been extensively investigated.

In order to remedy the gaps mentioned above, this thesis aims to address the following:

- To develop accurate yet cost-efficient computational models for investigating novel acoustofluidic platforms including flexible acoustofluidics and capillary bridge channels in order to study the underlying physics and working principles of these platforms using the commercial software package COMSOL Multiphysics 5.6.
- To model the acoustofluidic system by adding external body forces to the governing equations of fluid flow and particle dynamics to account for the acoustic effects on the fluid (acoustic streaming) and microparticles (acoustic radiation). This modelling technique significantly decreases the computational cost and time while presenting the results with a desirable accuracy.
- To experimentally investigate novel acoustofluidic platforms including flexible acoustofluidics and capillary bridge channels in order to show the proof of the concept and the evidence of the system properly working. Additionally, the obtained experimental data can help to verify the simulation results
- To use flexible thin film SAW devices made by depositing ZnO on aluminium substrates in particle and cell manipulation.
- To integrate capillary bridge channels with flexible thin film SAW devices in order to design and build a continuous flow acoustofluidic setup for particle and cell manipulation.

Chapter 3. Computational Modelling of Acoustofluidic Systems

3.1 Introduction

Computational modelling of acoustofluidic systems has been utilised to numerically investigate the behaviours of these multi-physics systems by simulating three major components: the acoustic field, the fluid flow field, and the micro-objects in the liquid such as particles/cells using computers and software.

For the computational modelling of the acoustofluidic systems, the governing equation of the acoustic field, the fluid flow field, and the microparticles (presented in the sections 2.4, 2.5, and 2.6, respectively) are used and the fluid-particle interactions as well as the effects of acoustic field on fluid and microparticles are modelled. The governing equations of the system are then discretised and iteratively solved to obtain the solution.

3.2 Modelling Acoustofluidic Systems

The fundamental physics of this study is mainly based on the behaviours and motions of fluid and the microparticles dispersed in it affected by an acoustic wave field. Due to the piezoelectricity effects, by applying power to the SAW device, an acoustic field is generated. When a microchannel filled with fluid-particle mixture is placed inside this acoustic field, the oscillatory velocity and pressure fields of the acoustic wave affects both the fluid and the microparticles suspended it. These acoustic effects can be modelled with acoustic streaming and acoustic radiation force on the fluid and microparticles, respectively. Microparticles also experience a viscous drag force when moving inside a fluid medium.

Numerical simulations of the acoustofluidic systems were performed using the commercial software package COMSOL Multiphysics (version 5.6) which has an integrated finite-element solver. COMSOL offers different modules for modelling various physics. To simulate the three components of the acoustofluidic systems, i.e. the acoustic field, the fluid flow and the microparticle dynamics, three different COMSOL modules are utilised. (1) The “pressure acoustics” module was used for modelling the SAW propagation and the generation of the acoustic field; (2) The “laminar flow” module was used to model the fluid flow; and (3) The “particle tracing” module was used for modelling the microparticle dynamics.

The interactions between the “pressure acoustics” module simulating the acoustic field and the “laminar flow” module simulating the fluid flow was modelled by the acoustic streaming force.

The effects of "pressure acoustics" module simulating the acoustic field and the "laminar flow" module simulating the fluid flow on the "particle tracing" module simulating the microparticle dynamics was modelled by the acoustic radiation force.

3.3 Finite Element Method for Discretisation of the Governing Equations

Discretisation of the governing equations results in an approximation of the exact solution in the form of finite number of values related to vertices, edges, faces, cells, or control volumes of the computational grid. Finite element method (FEM) is a versatile technique used in computational fluid dynamics (CFD) simulations as well as structural analysis modelling.

In order to discretise the governing equation of the system using FEM, first a flux balance equation is considered as follows [145, 146]:

$$\frac{\partial \mathcal{U}}{\partial t} + \boldsymbol{\nabla}.\boldsymbol{\Gamma} = \boldsymbol{S} \quad in \quad \Omega \tag{3-1}$$

where $\mathcal{U} = \mathcal{U}(\boldsymbol{x}, t)$ is a conserved physical quantity such as momentum or mass, $\boldsymbol{\Gamma}$ is the flux of quantity $\mathcal{U}$, and $\boldsymbol{S}$ is a source term [145, 146].

Multiplying Equation (3-1) by a proper "weighting (or test) function", φ, and integrating the result over the whole domain [145, 146]:

$$\int_{\Omega} \varphi \frac{\partial \mathcal{U}}{\partial t} dV + \int_{\Omega} \varphi(\boldsymbol{\nabla}.\boldsymbol{\Gamma}) dV = \int_{\Omega} \varphi \boldsymbol{S} dV \tag{3-2}$$

Applying the divergence theorem to $\boldsymbol{\varphi\Gamma}$, substituting it in Equation (3-2) and simplifying the resulting equation provides the "weak form" of Equation (3-1)[145, 146]:

$$\int_{\Omega} \varphi \frac{\partial \mathcal{U}}{\partial t} dV - \int_{\Omega} \varphi(\boldsymbol{\Gamma}.\boldsymbol{\nabla}) dV + \int_{\partial\Omega} \varphi(\boldsymbol{\Gamma}.\boldsymbol{n}) ds = \int_{\Omega} \varphi \boldsymbol{S} dV \tag{3-3}$$

One common choice for the weighting (or test) functions is polynomials but other types of functions can also be used. In FEM, a finite number of weighting (or test) functions $\varphi = \varphi_h$ is selected in a way that Equation (3-3) is true for all of them [145, 146].

For a simple computational domain, the nodes overlap with the mesh vertices, and can also be located at the middle of the edges or the centre of the faces or mesh cells. For the most common finite element approaches, the weighting (or test) functions have a nonzero value only at the nodes [145, 146].

In FEM, $\tilde{\mathcal{U}}$ is an approximate solution of Equation (3-3) and is described [145, 146]:

$$\tilde{\mathcal{U}}(\boldsymbol{x}, t) = \sum_j u_j(t)\varphi_j(\boldsymbol{x}) \qquad (3\text{-}4)$$

where φ_j is called a basic function with following properties:

• There exists a set of nodes $x_i \in \Omega$ such that $\varphi_j(x_i) = 1$ and $\phi_j(x_j) = 0$ for $j \neq i$.

• The restriction of ϕ_i to each cell is a polynomial function of local coordinates.

Using Equation (3-4) and the first property of ϕ_j, the approximate solution for each node of the computational domain is [145, 146]:

$$\tilde{\mathcal{U}}(\boldsymbol{x_i}, t) = u_i(t) \qquad (3\text{-}5)$$

If $\varphi = \varphi_j$ then the number of equations is the same as the number of unknowns and it this treatment is called the Galerkin method [146]. If $\varphi \neq \varphi_j$, then the finite element approximations are called Petrov–Galerkin methods [146]. FEM is a powerful tool for solving partial differential equations (PDEs) in three dimensions and offers advantages such as high accuracy and adaptability making it suitable for multi-physics systems [146].

3.4 Newton's Iterative Method for Solving Non-Linear Equations

The system of the governing equations for the fluid flow (Navier-Stokes equations) is a nonlinear system of equations which requires an iterative and nonlinear solver. One such solver is Newton's iterative method which are popular in the field of CFD for solving the equations resulted from the Galerkin discretisation [146]. For these solvers, proper initial guesses of the unknown variables are used to update the coefficients matrix and then solve the system of equations for the next step values of the unknown variables. This procedure is repeated until the difference between two consecutive values (i.e. the residual) is small enough [145-147].

3.5 Modelling the SAW-Fluid-Particle Interactions as Acoustofluidic Forces

3.5.1 Acoustic Streaming Force on the Fluid

A steady, incompressible, and laminar fluid flow, is modelled by the Navier-Stokes equation system presented by Equations (2-6) and (2-6) [140].

The interactions between the fluid flow and the acoustic field due to SAWs can be modelled by the SAW-induced acoustic streaming inside the fluid. For modelling the acoustic streaming

effects, the acoustic streaming force, $\boldsymbol{F}_{AS}$, shown in Equation (2-28), is added as an external body force to the conservation of momentum equation (Equation (2-7)) as follows [1, 37, 38, 44, 141]:

$$\rho_f\left(\left(\boldsymbol{U}_f.\boldsymbol{\nabla}\right)\boldsymbol{U}_f\right) = -\boldsymbol{\nabla}P + \mu_f\boldsymbol{\nabla}^2\boldsymbol{U}_f + \left(\rho_f\langle\boldsymbol{U}_a(\boldsymbol{\nabla}.\boldsymbol{U}_a)\rangle + \rho_f\langle(\boldsymbol{U}_a.\boldsymbol{\nabla})\boldsymbol{U}_a\rangle\right) \quad (3\text{-}6)$$

For a simplified case of a one-dimensional attenuating TSAW propagating in the x-direction, Equations (3-7) and (3-8) represent the components of acoustic streaming force [1, 37, 38, 44, 141].

$$F_{AS_x} = \left(\frac{P_a}{2{c_f}^2}\omega\overline{U}_{a_x}\right) + \left(\frac{\rho_f}{2}\left(\overline{U}_{a_x}\frac{\partial\overline{U}_{a_x}}{\partial x} + \overline{U}_{a_y}\frac{\partial\overline{U}_{a_x}}{\partial y}\right)\right) \quad (3\text{-}7)$$

$$F_{AS_y} = \left(\frac{P_a}{2{c_f}^2}\omega\overline{U}_{a_y}\right) + \left(\frac{\rho_f}{2}\left(\overline{U}_{a_x}\frac{\partial\overline{U}_{a_y}}{\partial x} + \overline{U}_{a_y}\frac{\partial\overline{U}_{a_y}}{\partial y}\right)\right) \quad (3\text{-}8)$$

3.5.2 Acoustic Radiation Force on the Particles

Numerical simulation of fluid-particle interactions models the effects of the fluid and particle phases on each other by simulating the mass, momentum, and energy exchange between them [142, 143]. In this research, the Euler-Lagrange approach [142] is used to model the microparticles by tracking them individually which provides the detailed information for each particle such as its position and velocity. The governing equations of motion for a single particle using the Euler-Lagrange approach is given by Equations (2-56) and (2-57) [142].

When using the Euler-Lagrange approach, the fluid-particle mixture should be sparsely distributed. This means that the volume fraction of the microparticle phase is smaller than the volume fraction of the fluid phase which is true throughout this research [142].

In order to choose the best coupling approach for the fluid and microparticle phases, the Reynolds number of the flow, Re, is introduced as follows:

$$Re = \frac{\rho_f U_f L}{\mu_f} \quad (3\text{-}9)$$

where L is the length-scale of the fluid flow which for the purpose of the research is considered to be the height of the microchannel. The Reynolds number is defined as the ratio of the inertial forces to the viscous forces in a fluid flow. It combines the effects of the channel dimensions,

flow velocity and fluid properties and shows the regime in which the fluid flow behaves. In this research, for all the cases $Re \ll 1$ which means that the fluid flow is in the creeping flow regime where the viscous forces are dominant.

Additionally, microparticles' sizes are significantly smaller compared to the dimensions of the microchannels. Given these conditions, a "one-way coupling" can be assumed to occur between the fluid and microparticle phases which means that the fluid flow affects the microparticle dynamics but not vice-versa [142].

Effects of the fluid flow on microparticles are determined by the viscous drag force the particles experience when they are moving through the fluid. This viscous drag force depends on the properties of both the fluid and the particles as well as the microparticle velocity relative to the fluid flow. It can be modelled using the Stokes' drag law given in Equation (2-58) [56, 142].

Each particle inside an acoustic field experiences two different types of acoustic forces, i.e., acoustic streaming force and acoustic radiation force. The acoustic radiation force acts directly onto the particles [1, 2, 82] whereas the acoustic streaming induces a movement in the fluid medium which forces the particle to follow the fluid's streamlines [1, 56]. In order to discover the dominant acoustic effect (either acoustic streaming or acoustic radiation force), a "size limit" can be introduced for the microparticles, and it depends on physical variables such as frequency, density, compressibility, and viscosity [1, 85]. For the particles smaller than the size limit, the acoustic streaming force affects the behaviour of the particles and forces them to follow the fluid streamlines due to the streaming movements. Whereas for particles larger than the size limit, the dominant acoustic effect is the acoustic radiation force which pushes the particles, which is normally out of the fluid streamlines [1, 56] .

To model the interactions between the particles and the acoustic field due to SAWs, the acoustic radiation force acting on the microparticles is calculated. The acoustic radiation force, $\boldsymbol{F}_{AR}$, applied on each microparticle is added as an external body force to the conservation of momentum equation for the particles using the Lagrange approach given by Equation (3-7).

When the ARF is resulted from TSAWs, Equation (2-39) can be substituted in Equation (2-57) which results [33, 39-42, 56, 74, 83, 84, 86]:

$$\frac{\partial \rho_p \boldsymbol{U}_p}{\partial t} = \rho_p \frac{\boldsymbol{U}_f - \boldsymbol{U}_p}{\tau_p} + (\rho_p - \rho_f)\boldsymbol{g} + (f_2^i(\tilde{\rho}, \tilde{\delta})\pi r^3 \rho_f \langle \boldsymbol{V}_{in}.\boldsymbol{\nabla}\boldsymbol{V}_{in}\rangle \boldsymbol{k}) \qquad (3\text{-}10)$$

It should be noted that the term $\frac{\boldsymbol{U}_f-\boldsymbol{U}_p}{\tau_p}$ in Equation (3-10) with $\tau_p = \rho_p d^2/18\mu_f$ represents the Stokes' drag force on the particles' unit volume. In addition, $(\rho_p - \rho_f)\boldsymbol{g}$ represents the gravity and buoyancy forces [56, 142].

In a TSAW field, the acoustic radiation force pushes the microparticles towards the wave's propagation direction [1, 39-42, 56, 74, 83, 84]. For a one-dimensional TSAW propagating in the x-direction, when the effects of fluid's viscosity and microparticles' compressibility are negligible, Equation (3-11) can be used to represent the acoustic radiation force [33, 39-42, 56, 74, 83, 84, 86]:

$$F_{AR_x} = \left(\frac{2\pi^3 {P_{ac}}^2 {\forall_p}^2 \beta_f}{\lambda^4}\right)\left(\frac{9 + 2\left(1 - {\rho_f}/{\rho_p}\right)^2}{\left(2 + {\rho_f}/{\rho_p}\right)^2}\right) \tag{3-11}$$

If the ARF is resulted from SSAWs, the acoustic radiation force given by Equation (2-45) is substituted it in Equation (2-57) as follows [33, 39-42, 56, 74, 83, 84, 86]:

$$\begin{aligned}\frac{\partial \rho_p \boldsymbol{U}_p}{\partial t} = \rho_p \frac{\boldsymbol{U}_f - \boldsymbol{U}_p}{\tau_p} + (\rho_p - \rho_f)\boldsymbol{g} \\ + \left(\frac{-4\pi}{3} r^3 \left[f_1(\tilde{\beta})\beta_f \langle P_{in} \boldsymbol{\nabla} P_{in}\rangle - f_2(\tilde{\rho})\rho_f \frac{3}{2}\langle (\boldsymbol{V}_{in}\cdot\boldsymbol{\nabla})\boldsymbol{V}_{in}\rangle\right]\right)\end{aligned} \tag{3-12}$$

Inside a SSAW field, the acoustic radiation force directs the microparticle towards either the pressure node or antinode depending on the physical and mechanical properties of the particle and the fluid [1, 39-42, 56, 74, 83, 84]. Simplifying the acoustic radiation force for a one-dimensional SSAW propagating in the x-direction and if the effects of fluid viscosity and particle compressibility are negligible, Equation (3-13) can be used for obtaining the acoustic radiation force [33, 39-42, 56, 74, 83, 84, 86]:

$$F_{AR_x} = \left(\frac{\pi {P_{ac}}^2 \forall_p \beta_f}{2\lambda}\right)\left(\frac{5\rho_p - 2\rho_f}{2\rho_p + \rho_f}\right)\sin(2k\tilde{x}) \tag{3-13}$$

3.6 Initial and Boundary Conditions

The complicated behaviour of the acoustofluidic systems requires properly defined initial and boundary conditions to solve the governing equations of the system. Inappropriate defining of these conditions may lead to incorrect or impossible solutions.

The initial conditions needed to solve the system are all the variables should be known at time $t = 0$ everywhere in the domain.

3.6.1 Fluid Flow Boundary Conditions

The boundary conditions to model the fluid flow for an incompressible, laminar, and viscous flow are as follows:

- On solid walls $\boldsymbol{U}_f = \boldsymbol{U}_{wall}$ (no-slip boundary condition).
- At the flow inlet: ρ_f and $\boldsymbol{U}_f$ known as a function of position or alternatively, the mass or volume flow rate should be known.
- At the flow outlet: $\frac{\partial u_n}{\partial n} = 0$ or P should be known or alternatively, the mass or volume flow rate should be known.

The subscript n indicates direction normal (outward) to the boundary.

3.6.2 Acoustic Boundary Conditions

To simulate the multi-physics acoustofluidic system, the propagations of SSAWs and TSAWs were modelled using the oscillating wall boundary conditions on the active portion of the lower channel/chamber wall. The velocity of the TSAW propagating on the active portion of the lower wall is defined as follows [144]:

$$u_{x-wall} = A_y \zeta \omega e^{-\alpha(0.5w-x)} e^{i[-k(0.5w-x)]} \quad (3\text{-}14)$$

$$u_{y-wall} = A_y \omega e^{-\alpha(0.5w-x)} e^{i[-k(0.5w-x)-\pi/2]} \quad (3\text{-}15)$$

The velocity of the SSAW propagating on the active portion of the lower wall is defined as follows [144]:

$$u_{x-wall} = A_y \zeta \omega \left[e^{-\alpha(0.5w-x)} e^{i[-k(0.5w-x)]} + e^{-\alpha(0.5w+x)} e^{i[k(0.5w-x)]} \right] \quad (3\text{-}16)$$

$$u_{y-wall} = A_y \omega \left[e^{-\alpha(0.5w-x)} e^{i[-k(0.5w-x)-\pi/2]} - e^{-\alpha(0.5w+x)} e^{i[k(0.5w-x)-\pi/2]} \right] \quad (3\text{-}17)$$

where u_{x-wall} and u_{y-wall} are the SAW velocities in x- and y-directions, respectively, A_y is the wave's displacement amplitude in y-direction, w is the channel width, α is the wave attenuation coefficient, x is the longitudinal direction and $\zeta = A_x / A_y$ is the ratio of the displacement amplitudes in x- and y-directions [144].

All the other walls were modelled using an impedance boundary condition as follows [144]:

$$Z_{wall} = \rho_{wall} c_{wall} \quad (3\text{-}18)$$

where Z_{wall} is the wall's impedance, ρ_{wall} is the wall density and c_{wall} is the wave's propagation velocity in the wall.

3.6.3 Boundary Conditions for the Particles

The wall boundary conditions for the microparticles are modelled by the "trap boundary condition" due to the small sizes of the microparticles compared to the dimensions of the microchannels. The trap boundary condition means that the particle neither reflects nor slides along the wall [142].

3.7 Mesh Dependency Analysis and Convergence of the Computational Method

In this section, the size-based separation of microparticles using the SSAWs reported by Shi et al. [61] is used as a case study for mesh dependancy analysis. For this purpose, a three-dimensional rectangular microchannel (length: 1.5 cm in z-direction, width: 150 µm in x-direction, and height: 80 µm in y-direction) with three inlets and three outlets was modelled, and structured hexahedron computational meshes with different sizes were generated. In this study, seven different mesh resolutions of 387, 1666, 14672, 128995, 213792, 387568, and 1031180 were used for the computational simulations. For the smallest mesh size of 387, the solution could not converge, whereas for the largest mesh size of 1031180, the simulation could not finish after one week.

The acoustic field in water in water was modelled by solving the Helmholtz equations (i.e., Equations (2-22) and (2-23)) using the oscillating wall boundary condition for the lower wall (i.e., Equations (3-14) to (3-17)). The fluid flow was modelled as steady, laminar, incompressible, and viscous using the Navier-Stokes equations (i.e. Equations (2-6) and (2-7)) with the boundary conditions of fixed volume flow rate at the inlet, fixed pressure at the outlet, and the no-slip boundary condition on the channel walls. All the governing equations were discretised and solved using FEM and Newton's iterative method with a convergence criteria of 10^{-6}.

Figure 3.2 shows the results of changes in the (a) maximum acoustic pressure, (b) minimum acoustic pressure, (c) maximum fluid velocity, and (d) computational time using different computational grid resolutions. From the results shown in Figures 3.2(a) to (c), it can be seen

that increasing the size of the computational grid increases the accuracy of the computational solution. Figure 3.2(d) shows that with increasing the mesh size, the computational time is exponentially increased. Therefore, the size of the computational mesh should be carefully chosen to offer a suitable accuracy of the solution while also offering reasonable computational time. Figures 3.2(a) to (c) show that increasing the size of the computational mesh from 213792 to 387568 does not have a significant effect on the accuracy of the solution while from Figure 3.2(d) it can be seen that the computational time drstically increases when the size of the computational mesh is increased from 213792 to 387568. For this case study the computational grid with ~200000 number of elements was chosen.

Throughout this research, mesh dependency analysis was performed for every case of computational simulation in order to find and utilise a computational grid with an optimised mesh resolution in order to obtain the solutions with a reasonable accuracy as well as the computational.

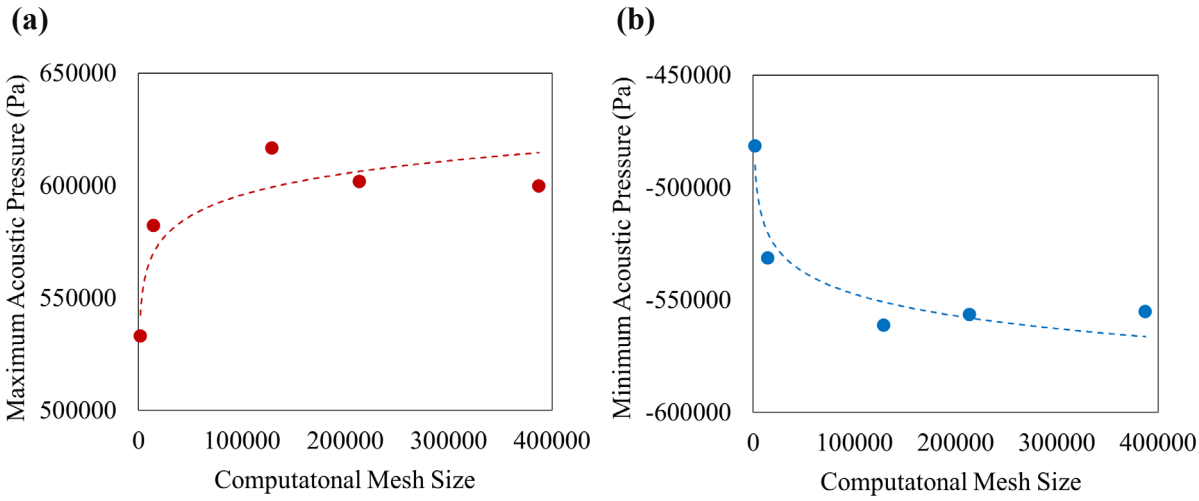

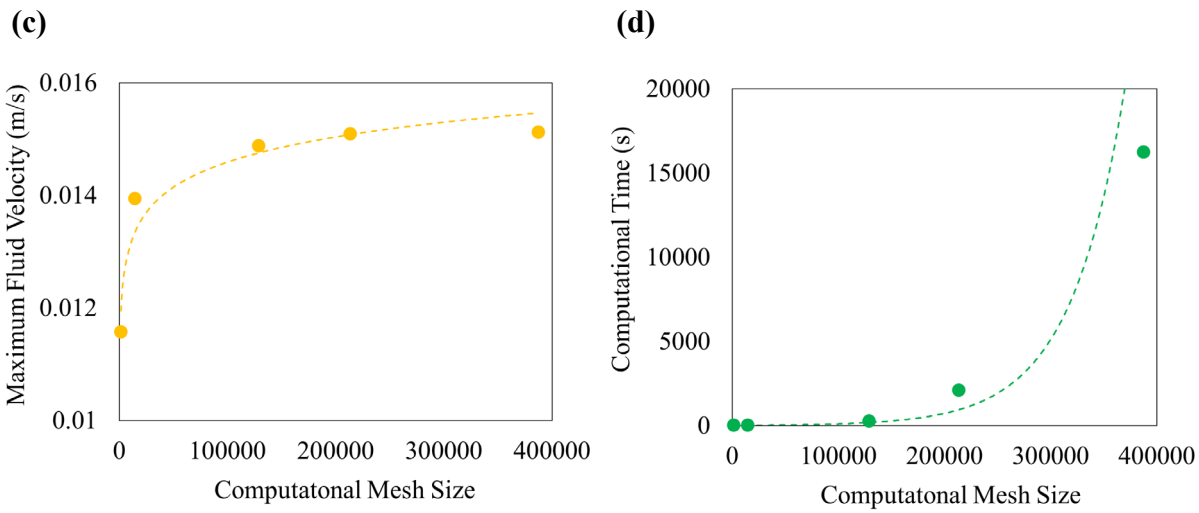

Figure 3.1 Mesh dependency analysis showing the changes in (a) maximum acoustic pressure (Pa), (b) minimum acoustic pressure (Pa), (c) maximum fluid velocity (m/s), and (d) computational time using different computational grid resolutions.

The computational modelling method should also be convergent, which means that the numerical solution should approach the exact solution through the iterative solver with a negligible residual after a sufficient number of iterations. For each iterative solver, convergence criteria are set, and the solver is stopped as soon as the convergence criteria is reached. The convergence criteria define the difference in solution values for two successive iterations and will show whether the solution residual is negligible. If the solver terminates before reaching the convergence criteria, the resulting solution is not accurate enough. Whereas if the solver continues on after reaching the convergence criteria, it will result in a waste of computational time and cost [146].

In some cases, the residual does not decrease, meaning it may increase or show fluctuations. In these cases, techniques such as underrelaxation is often used to accelerate the convergence. The idea behind this technique is to use a weighted average of a number or iterates in order to limit the differences in the solution and/or selecting optimum weights to achieve convergence [146].

In this thesis, a convergence criterion of 10^{-6} is set and reached which means that the difference in solution values for the two successive iterations is equal or less than 10^{-6}. Figure 3.1 shows the residual convergence during the iterative solution for the previous case study of the simulation of experiments for the size-based separation of microparticles using SSAWs reported by Shi et al. [61]. For this case, an structured hexahedron computational mesh with

~200000 number of elements was generated and the governing equations were discretised and solved using FEM and Newton's iterative method with a convergence criteria of 10^{-6}.

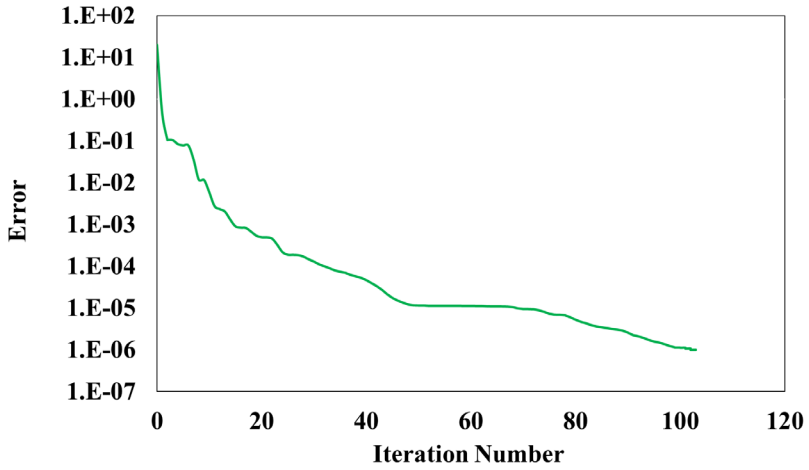

Figure 3.2 The residual convergence during the iterative solution.

3.8 Validation of the Numerical Modelling of Acoustofluidic Systems

Here, three different experimental studies described in the literature were used as validation cases for three dimensional numerical simulations, and these include (a) microparticle focusing by Shi et al. [67], (b) size-based separation of microparticles using SSAWs by Shi et al. [61], and (c) size-based separation of microparticles using TSAWs by Destgeer et al. [65]. The geometries were defined as three-dimensional rectangular microchannels and were discretized with structured hexahedron grids. Table 3.1 summarizes the channel dimensions and the grid elements for each case study.

Table 3.1 Channel dimensions and grid elements for each case study.

Simulation	**Channel Dimensions (µm)**	**Grid Elements**
Microparticle Focusing	length: 1.3 cm (z-direction) width: 50 µm (x-direction) height: 50 µm (y-direction)	203750
Size-based Separation of Microparticles Using SSAWs	length: 1.5 cm (z-direction) width: 150 µm (x-direction) height: 80 µm (y-direction)	213792
Size-based Separation of Microparticles Using TSAWs	length: 0.5 cm (z-direction) width: 200 µm (x-direction) height: 40 µm (y-direction)	213309

The discretized computational domain for each case study is shown in Figure 3.3 for (a) microparticle focusing, (b) size-based separation of microparticles using the SSAWs, and (c) size-based separation of microparticles using the TSAWs.

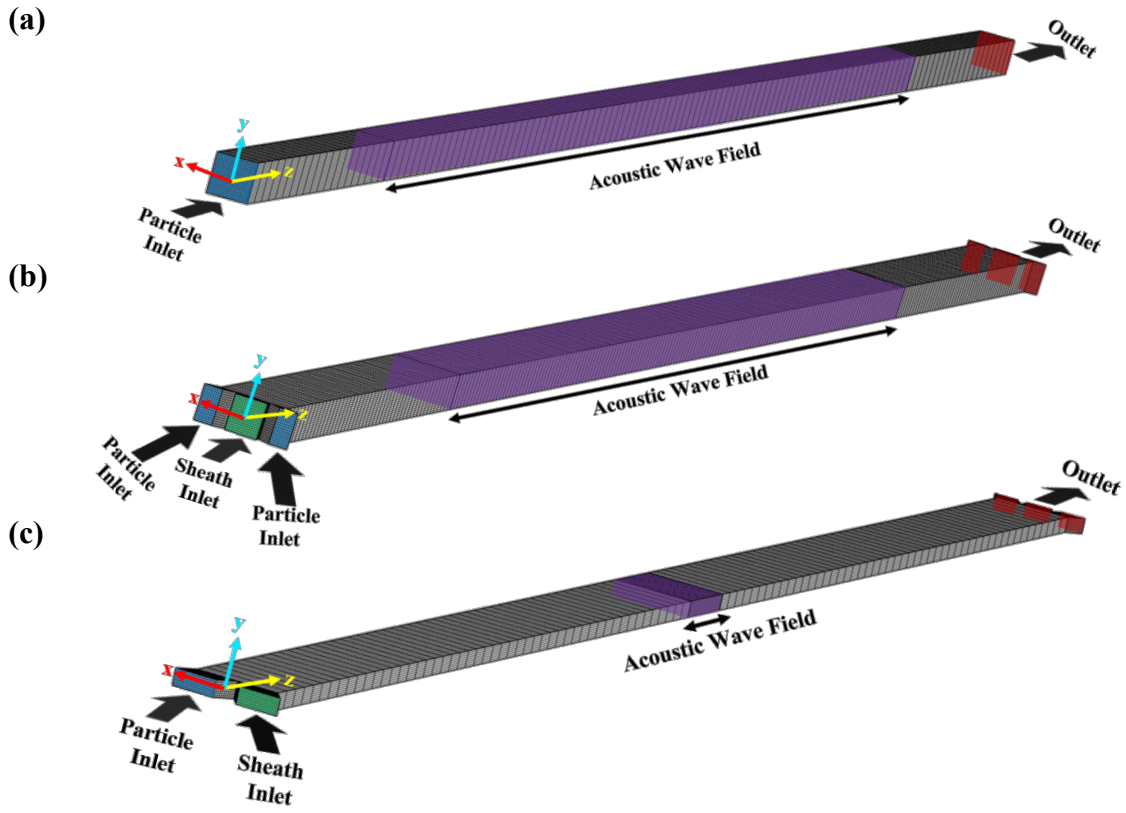

Figure 3.3 Computational domains and meshes for (a) microparticle focusing, (b) size-based separation of microparticles using SSAWs, and (c) size-based separation of microparticles using TSAWs. Main inlet is coloured blue, sheath inlets are coloured green, outlets are coloured red, the acoustic wave field is coloured purple and the acoustic wave travels in x-direction, the height of the microchannel is in y-direction.

To simulate the multi-physics acoustofluidic system including the SAW field, the fluid flow and the microparticles, different modelling approaches were used. The acoustic field was modelled as the SAW propagation in water by solving the Helmholtz equations (i.e., Equations (2-22) and (2-23)). The SAW propagation was modelled using the oscillating wall boundary condition for the lower wall (i.e., Equations (3-14) to (3-17)).

The fluid flow was considered steady in time, laminar, incompressible, and viscous. The Navier-Stokes equations (i.e. Equations (2-6) and (2-7)) were used to model the flow. The boundary conditions to model the fluid flow include the fixed value of volume flow rate at the inlet, the fixed value of pressure at the outlet, and the no-slip boundary condition on the channel walls.

The microparticles were modelled by solving the differential equations that govern their motions using the Euler-Lagrange approach (i.e., Equations (2-56) and (2-57)) for particles in three dimensions. In the case of the particles existing in the flow filed, the acoustic radiation force caused by the SAW was added to the simulation as an external body force on the particles.

Due to the fluid flow, a viscous drag force was applied to the particles, modelled by the Stokes drag force. At each time step, the acoustic radiation and drag forces affecting the particle movement were calculated based on the acoustic and fluid fields, respectively. Finally, the particles' positions were continuously tracked, and this process was repeated until the specified end time of the simulation was reached.

Since the volume fraction of the dispersed microparticle phase is smaller than the volume fraction of the continuous fluid phase, it is assumed that the mixture of fluid and particle is sparsely distributed. As the sizes of the microparticles are insignificant compared to the microchannel dimensions and the velocities of the microparticles are low, it is assumed that a "one-way coupling" occurs between the two phases (fluid and particle), which means that the continuous phase affects the dispersed phase but not vice-versa [145].

FEM was used to discretize all the governing equations and Newton's iterative method was used to solve the governing equations of the system with a convergence criteria of 10^{-6} which resulted in simulations finishing after 22 minutes and 47 seconds in real time. The microparticles movement was simulated for a duration of 2.5 s and with a time step of 0.001 s which was finished after 2 hours, 31 minutes and 47 seconds in real time using a an Intel(R) Xeon(R) CPU E5-1650 v4 and 32.0 GB of RAM.

3.8.1 Microparticle Focusing Using SSAWs

Figure 3.4 presents the simulation results of microparticles' focusing inside a microchannel using the SSAWs compared to the experimental results by Shi et al. [67]. It can be seen that the computational and experimental results are in a good agreement with each other. Microparticles enter the channel through the inlet and fill the width of the channel before entering the acoustic field (Figures 3.4(a-1) and (b-1)). At the beginning of the acoustic field, microparticles move towards the prssure node at the middle of the channle (Figures 3.4(a-2) and (b-2)). Then, in the middle of the acoustic field, microparticles form a focused line at the centerline of the channel where the pressure node is located (Figures 3.4(a-3) and (b-3)). Finally, the microparticles pass the acoustic field in a focused line (Figures 3.4(a-4) and (b-4)).

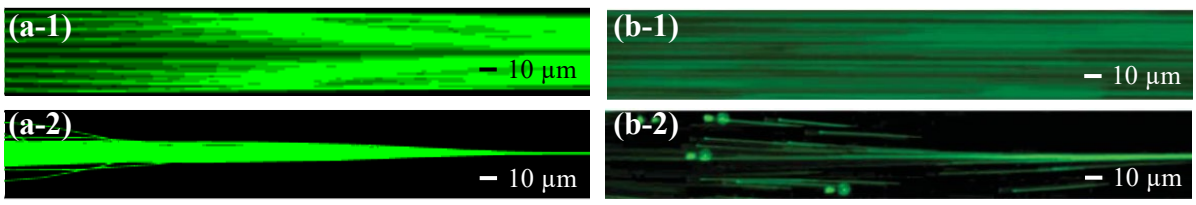

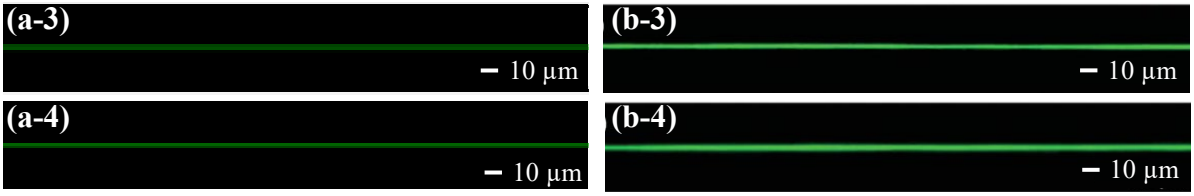

Figure 3.4 Focusing polystyrene microparticles with 1.9 µm diameter (green) flowing inside a microchannel with a velocity of 6.7 cm/s using a SSAW with frequency f = 38.2 MHz (a) simulation and (b) experimental (by Shi et al. [67]) results of particle tracks at several positions along the channel (1) before entering the acoustic field, (2) at the beginning of the acoustic field, (3) in the middle of the acoustic field and (4) after passing the acoustic field.

Figure 3.5 shows the effects of different frequencies on the particles' focusing. The simulation results of the acoustic pressure field and the pressure node inside the microchannel are compared to the experimental results by Shi et al. [67] for two different frequencies of (1) f = 38.2 MHz and (2) f = 19.116 MHz. It can be seen for both the computational and experimental results that decreasing the frequency from 38.2 MHz to f = 19.116 MHz will increase the width of the particle line form δx_1 to δx_2 (see Figure 3.5 (b)) due to the generation of a larger pressure node area for the lower frquency case.

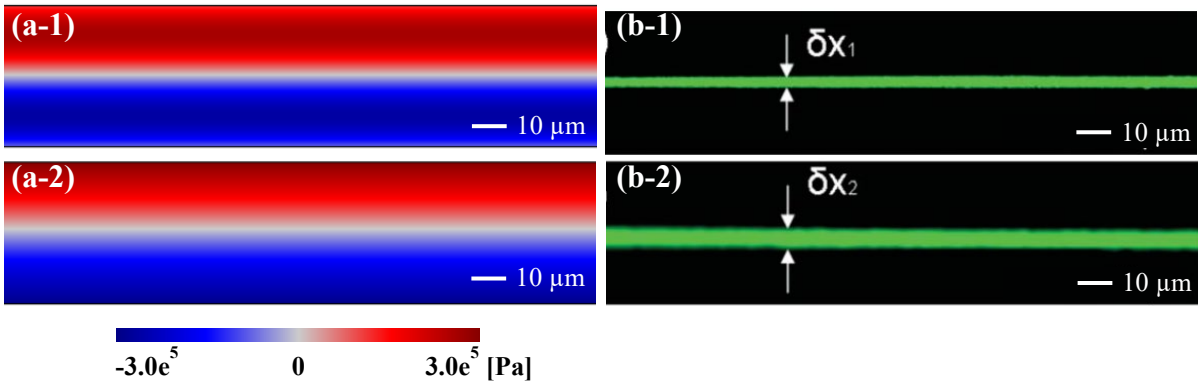

Figure 3.5 Focusing polystyrene microparticles with 1.9 µm diameter (green) flowing inside a microchannel with a velocity of 6.7 cm/s using a SSAW (a) simulation and (b) experimental (by Shi et al. [67]) results of particle tracks with frequency (1) f = 38.2 MHz and (2) f = 19.116 MHz.

3.8.2 Size-based Separation of Microparticles Using SSAWs

Figure 3.6 presents the simulation results of size-based separation of microparticles using the SSAWs compared to the experimental results reported by Shi et al. [61]. It can be observed that at the inlet of the channel, particles with both 0.87 µm diameter (red) and 4.16 µm diameter (green) are flowing along the side walls of the channel due to the middle inlet sheath flow (Figures 3.6(a-1) and (b-1)). At the starting point of the acoustic field region, (Figures 3.6(a-2) and (b-2)), larger particles with 4.16 µm diameter (green) start to move towards the pressure node line (at the center of the microcahnnel) , which is much faster than the smaller particles with 0.87 µm diameter (red). This is because the the acoustic radiation force has a stronger

effect on the larger particles. The microparticles were separated based on their sizes, where the larger ones (green) are flowing at the centreline while the smaller ones (red) are moving near the side walls. The particles exit the channel through different outlets (Figures 3.6(a-3) and (b-3)): i.e., the larger particles with 4.16 µm diameter (green) go through the middle outlet, whereas the smaller particles with 0.87 µm diameter (red) go through the two side outlets. The computational and experimental results are in good agreements with each other.

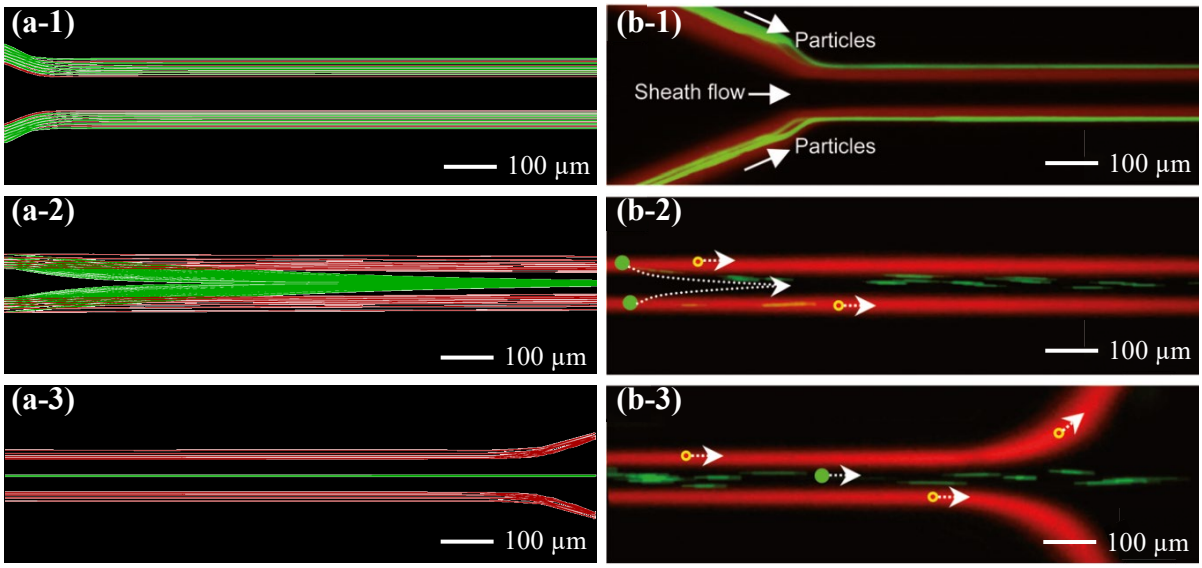

Figure 3.6 Size-based separation of polystyrene microparticles with 0.87 µm diameter (red) and 4.16 µm diameter (green) sizes flowing inside a microchannel with a velocity of 2.5 mm/s using a SSAW with frequency f = 12.6 MHz (a) simulation and (b) experimental (by Shi et al. [61]) results of particle tracks at several positions along the channel (1) at the inlet, (2) at the beginning of the acoustic field, (3) at the outlet and the end of the acoustic field.

Figure 3.7 shows (a) the simulation result of acoustic pressure field inside the microchannel caused by the SSAW and the pressure node line at the centreline of the channel, and (b) the time required for particles with different diameters to travel from the channel side walls to the pressure node at the centre line of the channel, from both the experimental results reported by Shi et al. [67] and simulation results performed for this thesis. It can be seen tha as the particle size increases, the time it takes for the particle to move from the channel side walls to the pressure node at the centreline decreases due to the the acoustic radiation force having a stonger effect on the larger particles.

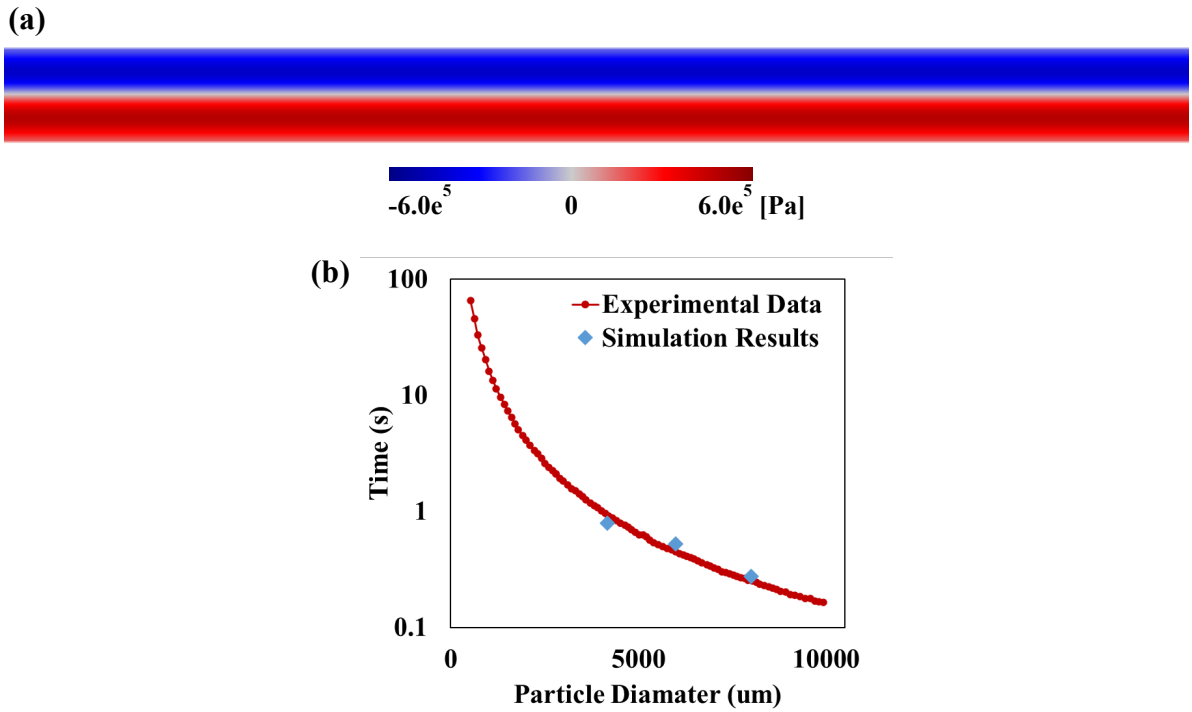

Figure 3.7 The results of (a) simulation of acoustic pressure field (Pa) inside the microchannel due to the SSAW and the pressure node line at the centreline of the channel, and (b) the time required for particles with different diameters to travel from the channel side walls to the pressure node at the centre line of the channel from simulation and experiments (by Shi et al. [67]).

3.8.3 Size-based Separation of Microparticles Using TSAWs

Figure 3.8 presents the simulation results of size-based separation of microparticles using the TSAWs compared to the experimental results reported by Destgeer et al. [65]. At the inlet of the channel, particles with both 3 µm and 10 µm diameters flow into the channel from the upper inlet, while a sheath flow from the lower inlet pushes them toward the side wall (Figures 3.8(a-1) and (b-1)). Due to the TSAW field, the larger particles (10 µm) are pushed towards the opposite side wall of the channle caused by the acoustic radiation force due to the TSAW, whereas the smaller particles (3 µm) continue to flow undisturbed (Figures 3.8(a-2) and (b-2)). At the outlets, the microparticles are completely separated based on their sizes, as the larger particles (10 µm) flow through the lower poutlet while the smaller particles (3 µm) exit the channel through the upper outlet (Figures 3.8(a-3) and (b-3)).

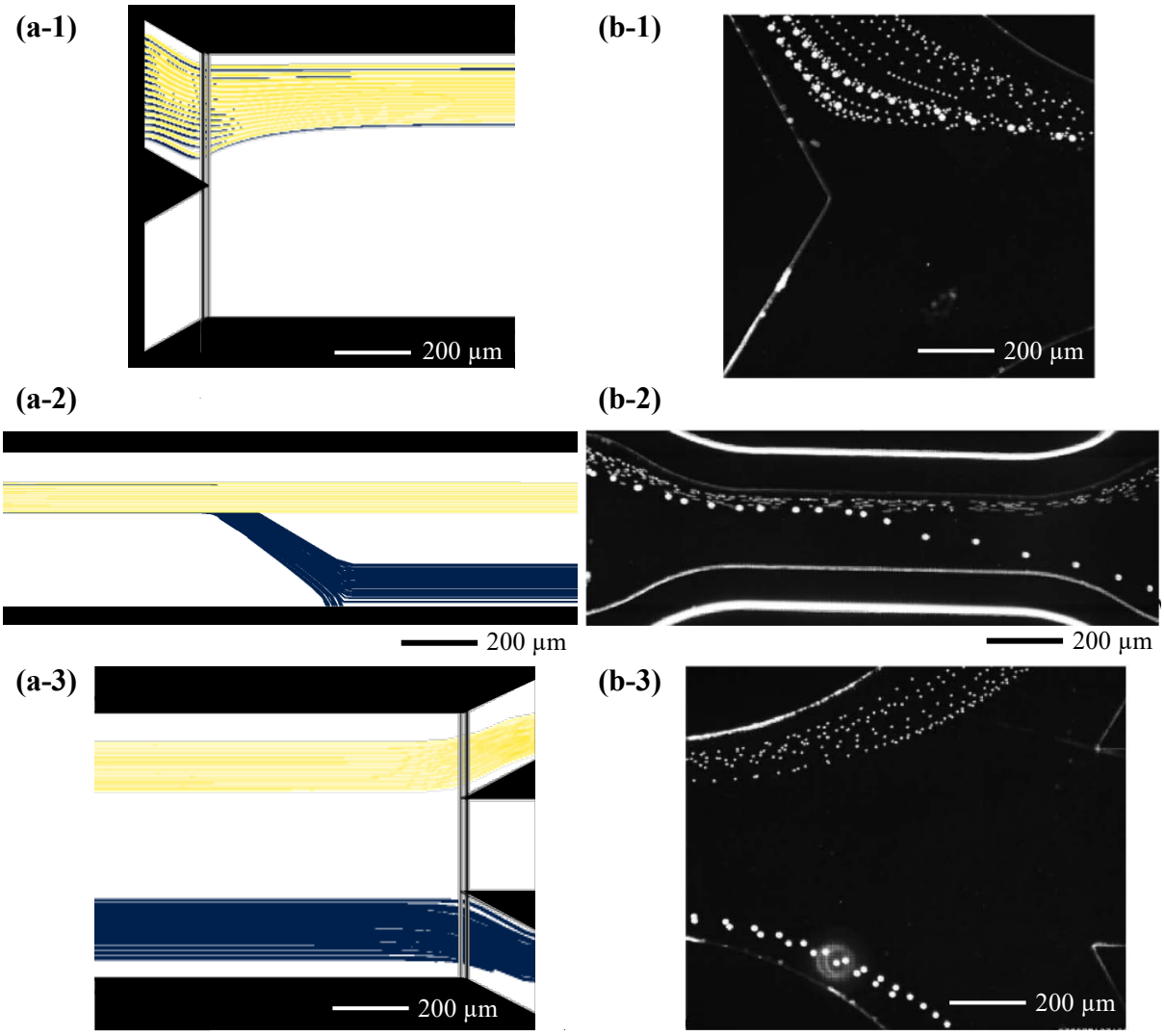

Figure 3.8 Size-based separation of polystyrene microparticles with 0.3 µm diameter (yellow) and 10 µm diameter (blue) sizes flowing inside a microchannel with a volume flow rate of 25 µL/h using a TSAW with frequency f = 133.3 MHz (a) simulation and (b) experimental (by Destgeer et al. [65]) results of particle tracks at several positions along the channel (1) at the inlet, (2) at the acoustic field, (3) at the outlet.

Figure 3.9 shows how particles are directed towards different outlets with different powers, obtained from both experimental results reported by Destgeer et al. [65] and simulation results performed for this thesis. It can be seen from Figure 3.9(a-1) that particles with both 3 µm and 10 µm diameters flow through the upper outlet witout acoustic power (0 mWatt). Figures 3.9(b-1) and (c-1) show the particle tracks inside the acoustic field and at the outlet witout acoustic power, respectively. Figure 3.9(a-2) presents the results for the separation of particles with 3 µm and 10 µm diameters. It can beseen that the larger particles (10 µm diameter) flow through the middle outlet while the smaller particles (3 µm diameter) exit the channel through the upper outlet while using the acoustic power of 55 mWatt. Figures 3.9(b-2) and (c-2) illustrates the particle tracks inside the acoustic field and at the outlet for the acoustic power of 55 mWatt, respectively. From Figure 3.9(a-3), it is observed that with the

acoustic power of 151 mW, the larger particles (10 µm diameter) exit the channel through the lower outlet whereas the smaller particles (3 µm diameter) flow through the upper outlet. Figures 3.9(b-3) and (c-3) present the particle tracks inside the acoustic field and at the outlet for the acoustic power of 151 mWatt, respectively. It can be concluded that, as the power increases the larger particles are pushed towards the farther outlet.

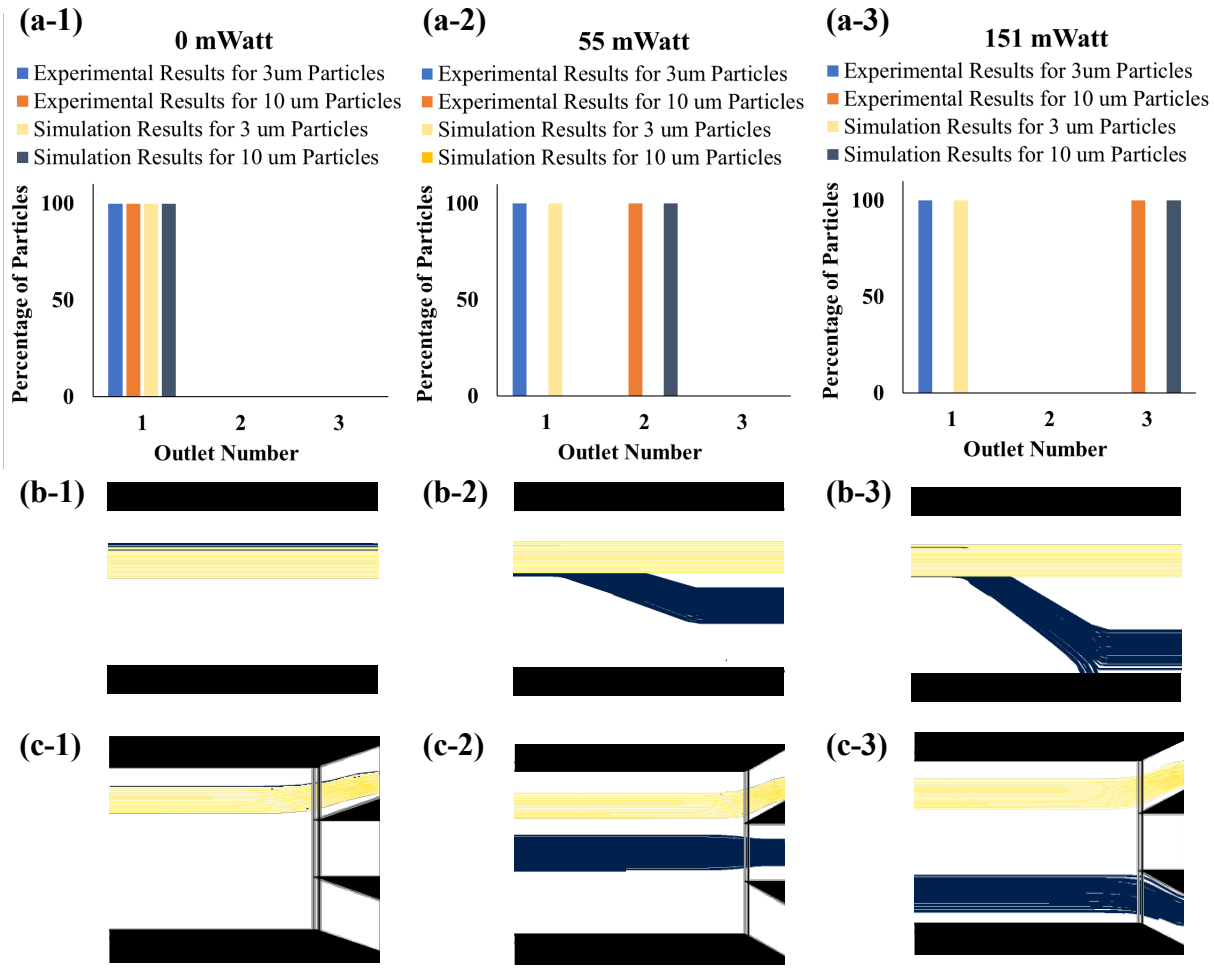

Figure 3.9 (a) Percentage of the polystyrene microparticles with 0.3 µm diameter (yellow) and 10 µm diameter (blue) sizes going through different outlets at different power values for simulation and experimental (by Destgeer et al. [65]) and Simulation results of particle tracks at (b) the acoustic field, and (c) the outlet for (1) 0 mW, (2) 55 mW, and (c) 151 mW.

3.9 Summary

In this chapter, the numerical modelling of the acoustofluidic platforms with fluid flow for several manipulation tasks were performed. The effects of surface acoustic waves were accounted for by adding the acoustic radiation force to the governing equations of the microparticle movement. The simulation results were then validated using the experimental results reported in the existing literature. The computational and experimental results were shown to be in good agreements.

For microparticle focusing inside a microchannel using SSAWs, the microparticles flow inside the channel through the inlet and fill the width of the channel. As they enter the acoustic field, the microparticles move towards the pressure node which is located at the middle of the channel and eventually form a focused line at the centerline of the channel. Decreasing the frequency of the SAW device increases the width of the pressure node area and thus the particle line.

Size-based separation of microparticles using the SSAWs were also studied where the microparticles with two different diameters flowed along the side walls of the channel due to the middle inlet sheath flow. Due to the the acoustic radiation force having a stonger effect on larger particles, partciles with larger diameter moved towards the pressure node line located at the center of the microcahnnel faster than the particles with smaller particles diameter. The microparticles were separated based on their sizes and exited the channel through different outlets as the larger ones flowed at the centreline and smaller ones continued to move near the side walls. Increasing the particle size decreases the time it takes for the particle to move from the channel side walls to the pressure node at the centreline.

Size-based separation of microparticles using TSAWs was studied for microparticles with two different diameters which flowed in the channel through the upper inlet while a sheath flow from the lower inlet pushed them toward the side wall. In the TSAW field, the larger particles were pushed towards the opposite side wall of the channle due to the acoustic radiation force wheras the smaller particles continued to flow undisturbed. The microparticles were separated as the larger particels exited the channel through the lower outlet while the smaller particles flowed out through the upper outlet. Increasing the acoustic power resulted in the larger particles to be pushed towards the farther outlet.

For all three case studies of focusing, SSAW-based and TSAW-based separation of microparticles, the data obtained from the computational simulation showed good agreement with experimental results reported in literature. Comparing the simulation data with the experimental results, the computational modelling was validated which means that the computational data is reliable and offers a realistic description of the physics of the setup. Mesh dependency and convergence analysis showed that the computational results offer a desirable accuracy while maintaining an efficient computational time and cost.

Computational modelling of the acoustofluidic systems is capable in prediction the various physics of the system. For the acoustic field, computational modelling can provide the details

of the acoustic field such as acoustic pressure, acoustic intensity, and the location of the pressure nodes and anti-nodes. Computational modelling of the fluid field can present accurate information of the flow field including the fluid pressure and velocities and how the acoustic fielded affects the fluid flow when acoustic streaming happens. For the microparticles, computational modelling is able to offer the details of their dynamic behaviours such as position and velocity. It can also show the effect of fluid flow on microparticles dynamics in the form of the drag force as well as the acoustic effects on the microparticles in the form of the acoustic radiation forces.

Using body forces to account for the acoustic effects on fluid and microparticles has its limitations as well. Due to the vastly different time and length scales of the acoustic and fluid field, the detailed interactions between these two physics may not be readily available with this modelling approach. However, for the present acoustofluidic systems, this approach offers a reasonable accuracy for the results.

Chapter 4. Experimental Investigation of Acoustofluidic Systems

4.1 Introduction

In order to investigate the key factors which, influence the patterning of particles/cells and verify the results of the computational modelling, various experiments were designed and performed.

The experimental setup for a typical acoustofluidic platform consists of the following:

- A SAW device with a piezoelectric substrate or film and a pair of IDTs.
- A microchamber for non-flowing particle patterning or a microchannel for continuous flow applications.
- A pumping system to control the flow for continuous flow applications.
- An RF signal generator to set the input power and frequency to the power amplifier.
- An RF power amplifier to increase the gain of the signal.
- A microscope or a camera to record the experimental videos and analyse the data.
- A computer with software to control the various components of the platform as well as to record the experimental data.

4.2 ZnO Film Deposition and Characterization

The flexible SAW devices were fabricated by depositing ZnO thin films onto Al substrates using a physical vapour deposition (PVD) technique. In this technique, a direct current (DC) magnetron sputter (NS3750, Nordiko) with a zinc target (99.99% purity) was utilised to deposit ~5 μm thick layer of ZnO thin film onto silicon, glass, and two types of Al substrates (Al foils with a thickness of 50 μm and Al sheets with a thickness of 200 μm and 300 μm (for the capillary bridge setup). The aluminium foils and sheets were cut into 10 cm × 10 cm squares and their surfaces were cleansed firstly using acetone and then ethanol. Then they were rinsed with deionised (DI) water and dried using the nitrogen gas. After these, the substrates were fixed on substrate holders (a rotary cylinder) and then placed in the DC magnetron sputter machine within 20 cm distance from the target.

During the deposition process, the substrates were rotated with a speed of 4 RPM without any intentional substrate heating. The vacuum was maintained at a pressure of ~0.35 Pa inside the chamber before the sputtering. Then both argon and oxygen gases flew into the chamber in order to sputter and/or oxidise the zinc to create ZnO to be deposited on the substrate surface.

The deposition parameters were: Ar/O_2 flow ratio of 10/15 (in standard cubic centimetre per minute, (SCCM)) and a plasma power of 400 Watts which was chosen based on the results of the ZnO thin film thickness and quality from the previous test runs [3, 53, 96]. Using these data and without any intentional substrate heating, the ZnO thin film was deposited with a ~0.3 µm/hour rate and the whole process was lasted for up to 18 hours.

The deposited ZnO thin film characterisation showed a strong texture of (0002) crystal orientation on Si, glass and Al substrates based on the X-ray diffraction analysis. Aluminium foils and thin sheets were chosen as the substrates because they are reasonably flexible and can be bent and twisted to form the desired shapes with minimal forces. They also have a low sound absorption coefficient, thus do not apparently absorb, or dampen the waves.

4.3 Flexible SAW Device Fabrication and Characterization

The IDTs (made from 20/100 nm thick of Cr/Au, or sometimes 200 nm Al) of the SAW devices were fabricated using a standard photolithography and lift-off process. For the first step, the ZnO thin film coated Al substrates were cleaned using acetone/ethanol, and then rinsed with DI water and dried using nitrogen gas. The samples were coated with a layer of positive photoresist S1813 (Rohm and Haas) using a spin coater machine (Laurell 650M) with a rotational speed of 10 RPM for 10 seconds, and then with a steady rise of rotational speed to 3,700 RPM within 60 seconds. After that, the samples were soft-baked on a hot-plate with a temperature of 95ºC for 10 minutes. Finally, the S1813 photoresist was developed by first applying an exposure ultraviolet dose of 90 mJ using EVG620 mask aligner and then immersing the sample in MF319 developer solution for 1 minute. The obtained SAW devices were then cleaned using DI water and dried with nitrogen gas. The designed IDTs had 30 pairs of fingers wavelengths of 160 µm and 1 mm (for the capillary bridge setup). Figure 4.1 shows a close-up picture and a schematic of a ZnO/Al thin film SAW device.

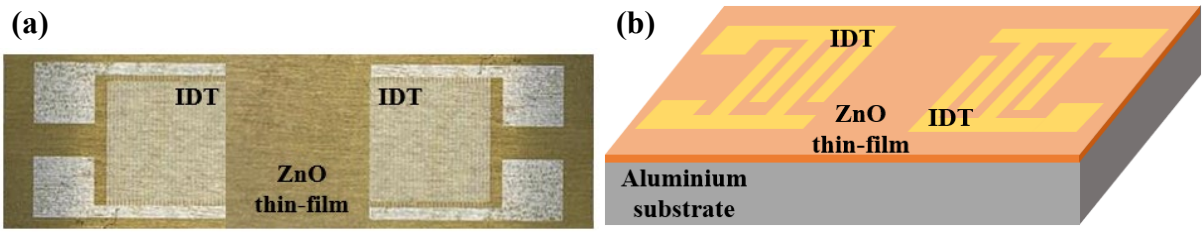

Figure 4.1 (a) A close-up look, and (b) a schematic of a ZnO on Al thin film SAW device showing two IDTs and the ZnO thin film.

An RF network analyser (Keysight, FieldFox N9913A) was used to measure the reflection spectra (S11 parameter) and resonant frequencies of the SAW devices. Two types of flexible

SAW devices (with different substrate thicknesses) were used in the experiments of microparticle patterning in a microchamber. Table 4.1 lists the detailed information of both flexible SAW devices and Figure 4.2 shows the obtained frequency S11 results and the simulated vibration modes of them using the COMSOL software.

Table 4.1 Substrate thickness, wavelengths, and resonance frequencies of the flexible SAW devices. Device 1 has Lamb wave modes, and Device 2 has Rayleigh wave mode.

Device Name	Al substrate thickness (µm)	Wavelength (µm)	R0 Frequency (MHz)	A0 Frequency (MHz)	S0 Frequency (MHz)	A1 Frequency (MHz)	S1 Frequency (MHz)
Device 1	~50	160	-	13.00	29.06	40.00	47.00
Device 2	200	160	17.00	-	-	-	-

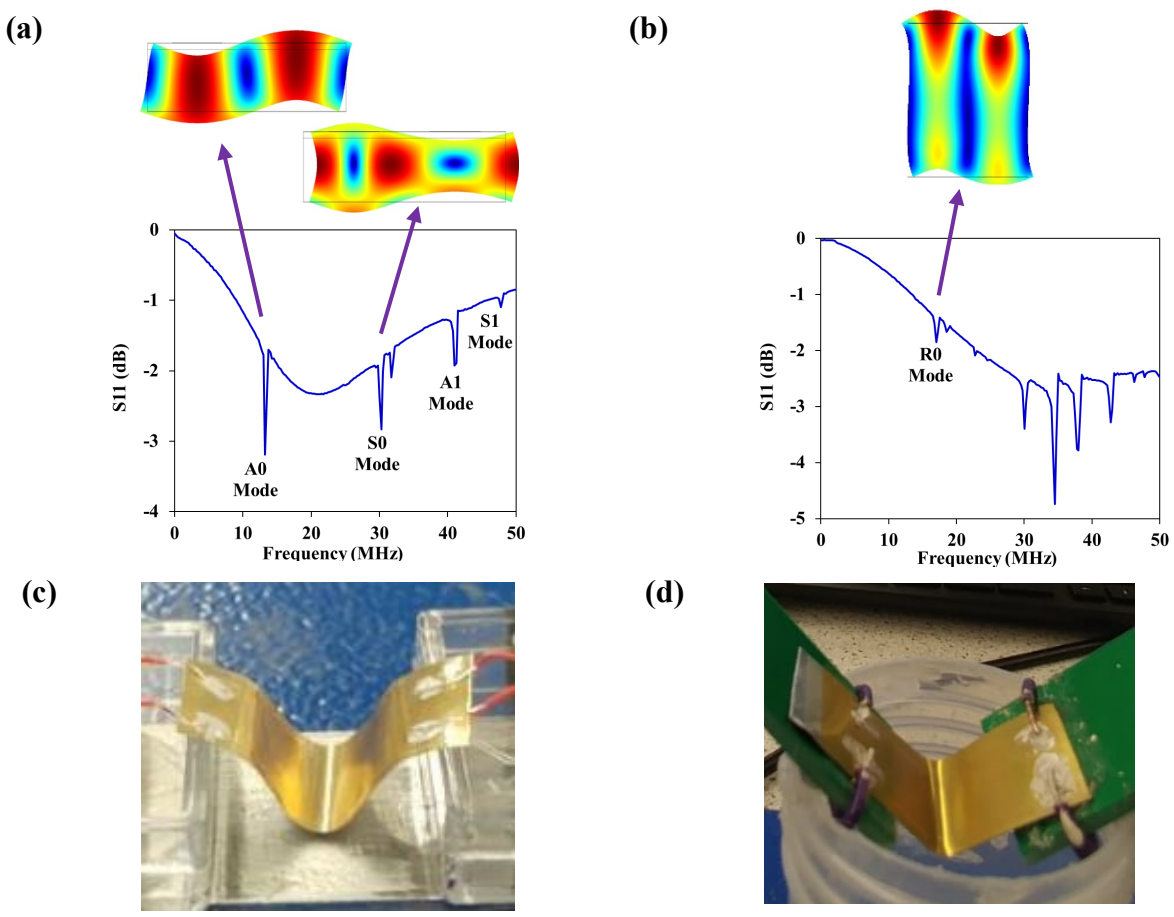

Figure 4.2 Different frequency modes of the (a) Device 1, (b) Device 2. SAW devices in their bent conditions (c) Devices 1, (d) Device 2.

4.4 Experimental Setup

4.4.1 Acoustic Streaming Experimental Setup

A PDMS microchannel (length: 1000 µm in z-direction, width: 200 µm in x-direction, and height: 50 µm in y-direction) with three inlets and one outlet was placed on a SAW device made of $LiNbO_3$ piezoelectric substrate and one single slanted IDT with a frequency range of 161 MHz to 171 MHz, which generated a TSAW. The slanted IDTs (also known as tapered IDTs) have a very broad bandwidth with a range of varying frequencies. These IDTs are operated by changing the electrode periodicities and are capable to deflect a moving particle or droplet by continuously changing the operating frequency [3, 44]. For the acoustic streaming experiments, a slanted IDT with a frequency of 164 MHz (λ ~25 µm) was used to position the acoustic sound path, and a straight IDT with the same position and frequency could also be used to generate the same function. The experiments were performed using two different acoustic powers of 16.3 mW and 65 mW. Due to the low acoustic power applied to the SAW device during the experiments, no significant heating was observed.

The SAW setup was placed on a holder and then positioned over an inverted microscope (Olympus IX73). Videos were recorded using a high speed camera (Photron, UX50). An RF signal generator (Rohde & Schwarz, SMB100A) was connected to the SAW device and set the input power and frequency. Three syringe pumps (Harvard Apparatus, PHD2000) were connected to the inlets to control their inlet flow rates and sheath flows while the outlets were connected to individual vials to collect the exiting fluid. The experiment was controlled with a computer which was also used for analysis of the captured videos. Figure 4.3 shows the experimental setup used for acoustic streaming experiments.

To study the acoustic streaming, two different cases of experiments were performed. In the first case to visualise acoustic streaming in a microchannel flow, DI water dyed with trypan blue colour was injected in the microchannel through the main inlet and pure water was injected in the flow field as sheath flows through the side inlets. The properties of both the pure water and the dyed water were defined as density ρ_f=998 kg/m^3, viscosity μ_f=0.001 kg/ms and compressibility β_f=4e^{-10} Pa^{-1}. In the second case to investigate the effects of acoustic streaming on microparticles, spherical polystyrene microparticles (with diameter d=1 µm and density ρ_p=1050 kg/m^3) dispersed in water as the carrier fluid were injected in the microchannel through the main inlet and pure water was injected in the flow field as the sheath flows through

side inlets. The effects of different inlet and sheath flow rates as well as different acoustic powers were studied.

To collect the experimental data, 400 images were taken and superimposed to visualize the particle trajectories for each case. The particle velocity values were extracted from the exprimental videos using a digital particle image velocimetry (PIV) method and utilising a MATLAB toolbox named PIVlab [148-150].

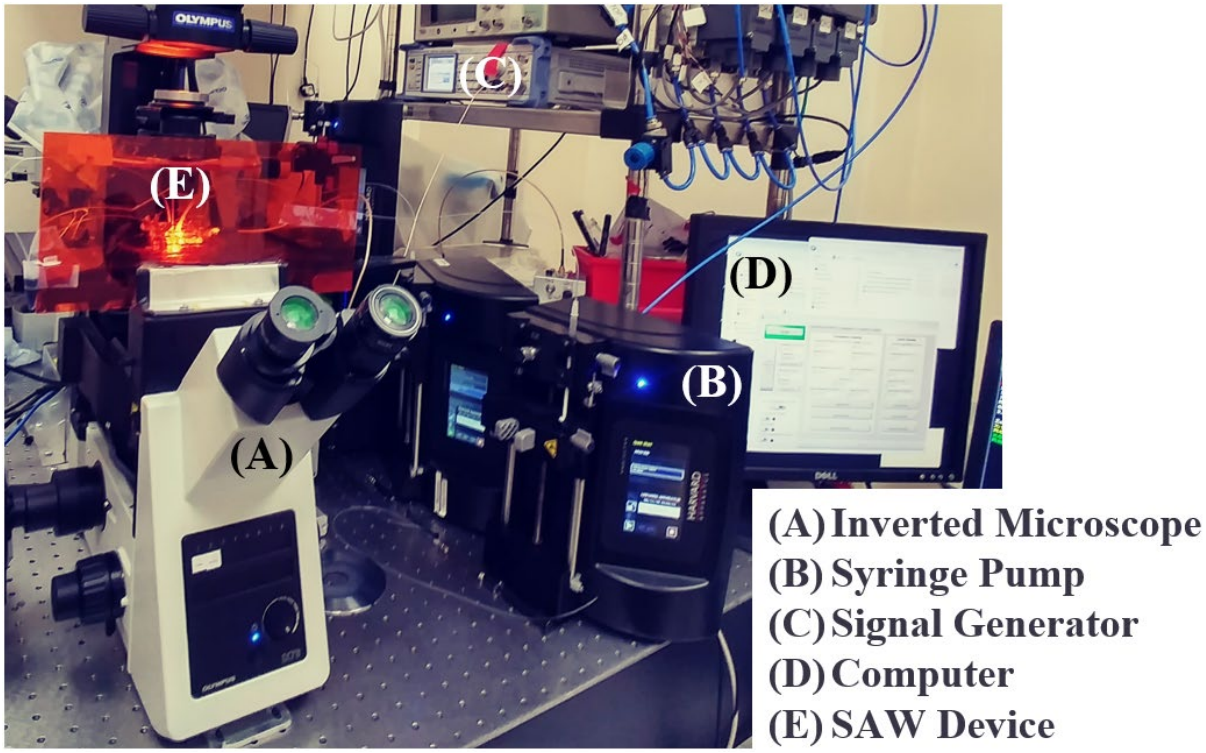

Figure 4.3 The experimental setup used for acoustic streaming experiments including (A) inverted microscope, (B) syringe pump, (C) signal generator, (D) computer, and (E) the SAW device.

4.4.2 Particle Manipulation Using Flexible SAW Setup

To visualise particle patterning under the effect of SSAWs, a rectangular PDMS microchamber (Sylgard 184 Silicone Elastomer; Dow Corning, USA) with dimensions 1000 µm × 700 µm × 1000 µm (W × H × L) was temporary bonded onto the bent SAW device surface using a small amount of liquid PDMS at the bottom of PDMS chamber and was pressed tightly onto the sample surface between a pair of identical IDTs. The microchamber was then filled with microparticle/cell suspension in DI water and was covered with a piece of glass (with a thickness of 50 µm). Particle patterning was visualized using particles of silica (with a diameter of 5 µm and a density of 1900 kg/m^3) and polystyrene (with a diameter of 10 µm and a density of 1500 kg/m^3). Yeast cells were also used for demonstration of biological applications since

yeast cells can be used as model organisms in cellular biological studies as they can be managed easily during experimental work [151]. The ability to manipulate yeast as model cells in an acoustofluidic setup has a significant potential in biological and biomedical applications such as tissue engineering and microarrays [33, 152].

An RF signal generator (Marconi Instruments 2024) was connected to an amplifier (Amplifier Research 75A) in order to generate the amplified RF signals of the resonant frequencies to the IDTs of the SAW devices. The experiments were performed using an acoustic powers of 2.8 W for a duration of ~5 s. Applying the acoustic power for such short duration of time resulted in no significant heating to be observed.

A video camera (Imaging Source, DFK 22BUC03) was used to capture the motion of the fluid and the microparticles. Figure 4.4 shows the experimental setup used for thin film SAW device experiments. The open-source image-processing software ImageJ (NIH, USA) was used for post-processing the experimental images and measuring the requires data [153-155].

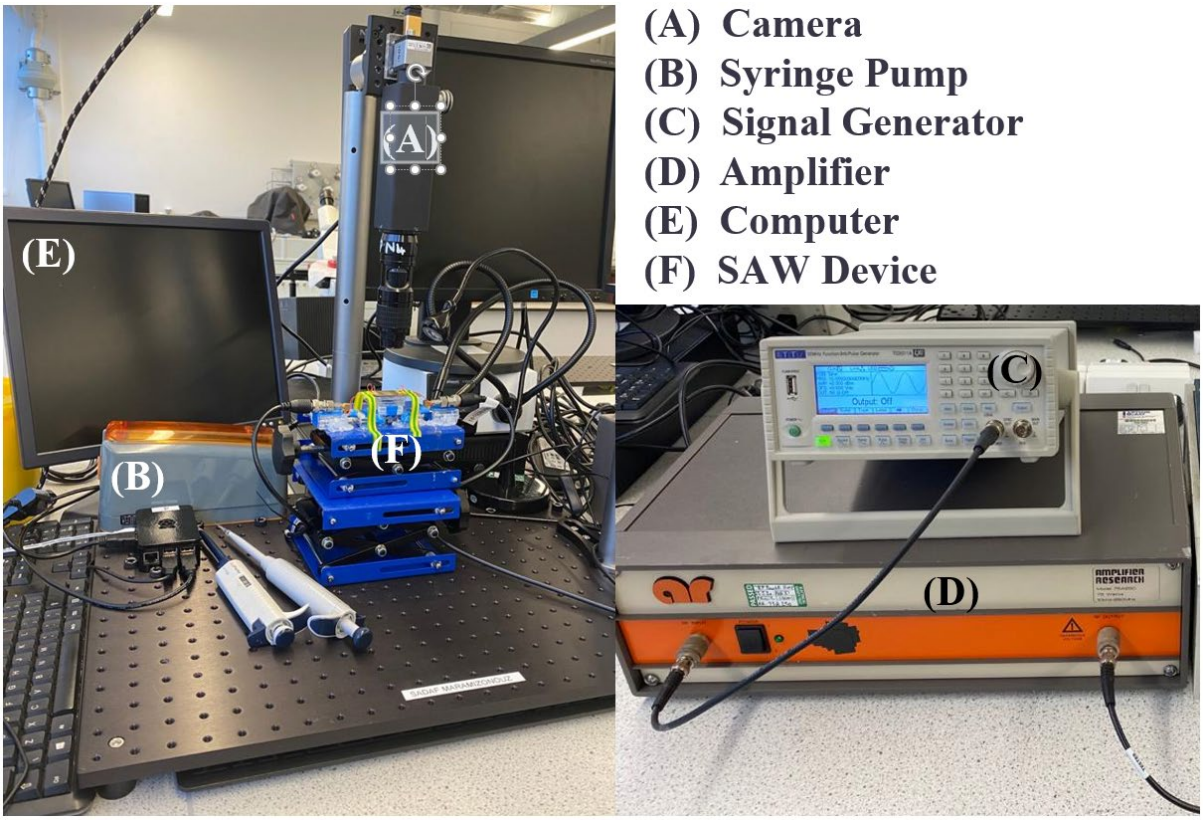

Figure 4.4 The experimental setup used for thin film SAW device experiments including (A) inverted microscope, (B) syringe pump, (C) signal generator, (D) computer, and (E) the SAW device.

4.4.3 Experimental Setup for Particle Manipulation inside Glass Microtubes

To visualise particle patterning under the effect of SAWs, glass microtubes with rectangular (with three sizes of 4.5 mm × 1.0 mm, 3.5 mm × 0.8 mm, and 2.3 mm × 0.5 mm the last one is mainly used for continuous flow experiments) and circular (with a diameter of 1.0 mm) cross-sections and with a length of 2 cm were placed on the SAW device's surface. DI water droplet of ~1.0 μL was added under the tube to transfer the wave energy from the SAW device directly into the glass tube. The glass microtube was then filled with a suspension of DI water with silica microparticles (with a diameter of 5 μm and a density of 1900 kg/m^3). To study the effects of patterning in a continuous flow in the tube, the fluid/particle mixture was pumped into the glass microtubes using a syringe pump (ExiGo pump) at the inlet and the mixtures were collected into a vial at the outlet. A continuous flow rate of 0.2 μL/s was applied.

An RF signal generator (Marconi Instruments 2024) was connected to an amplifier (Amplifier Research 75A) to generate the RF signals to drive the IDT of the SAW device. The experiments were performed using an acoustic powers of 2.8 W for a duration of ~5 s. Applying the acoustic power for such short duration of time resulted in no significant heating to be observed. A video camera (iDS, UI-3880CP-C-HQ-R2) was used to capture the motion of the fluid and the microparticles. The open-source image-processing software ImageJ (NIH, USA) was used for post-processing the experimental images and measuring the requires data [153-155].

4.5 Summary

In this chapter, the experimental methodology of the acoustofluidic systems was presented. Firstly, the details of SAW device fabrication from thin film deposition to soft lithography and lift-off processes were introduced. Then the characterisation of SAW devices by measuring the reflection spectra (S11 parameter) of the devices was discussed. After that the methods for preparing and post-processing the experimental data were explained. Finally, various experimental setups used for microparticle manipulation were demonstrated.

Chapter 5. SAW-Induced Acoustic Streaming in a Microchannel Flow

5.1 Introduction

Surface acoustic waves cause “acoustic streaming”, a phenomenon which happens when a TSAW propagates through a liquid and the difference between the wave propagation speed in the piezoelectric substrate and its speed in the liquid causes the wave’s acoustic energy to refract into the fluid (acoustic refraction). The refracted longitudinal waves generate a force in the waves’ propagation direction which results in a momentum transfer between the wave and the fluid and induces movement in the fluid. The boundaries reflect the moving fluid and cause internal streaming [1, 80]. Acoustic streaming can be used to deflect [58], separate and sort [44, 69, 70], focus [43], separate and capture [26, 71], trap [72], microparticles/cells, mix [75] and pump fluids and suspensions in microfluidic devices [1, 3].

Numerical simulation of SAW-based acoustofluidic systems can aid in understanding the underling physics of these complex multi-physics systems which is essential for designing and fabricating such devices [156, 157]. There are previous studies on numerical simulation of acoustofluidic systems, for example, Schmid et al. [44] simulated particle deflection using acoustic streaming effect and Collins et al. [43] presented acoustic streaming flow field and fluid streamlines in two dimensions, both without modelling the acoustic field. However, few attempts have been made to assess the basis, strengths, and limitations of various computational methods. Such an approach can help to optimise acoustofluidic devices and can potentially lead to development of novel devices.

This chapter aims to investigate the effects of SAW induced acoustic streaming on fluid and microparticles by using two different numerical simulation approaches to model the acoustic effects in three dimensions. In the first approach, the whole acoustic field which was caused by the oscillating lower wall was modelled. Here, the acoustic streaming effects were directly calculated from the density and velocity fields caused by the acoustic field. In the second approach a low fidelity model is employed to capture the effects of acoustic streaming without modelling the acoustic field itself. In this approach, the velocity of a one-dimensional attenuating wave was substituted in the acoustic streaming force formula, and the acoustic streaming force was calculated without using the density and velocity caused by the acoustic field as a simplified version of the acoustic streaming force which was implemented in the governing equations of fluid flow as an external body force. Although this approximation

method has its limitations, it has been used in as the more popular modelling approach to study the streaming effects in many of the previous works [43, 44].

In this chapter, fluid flow and microparticles' movement are studied under different inlet and sheath flow rates and different acoustic power conditions. Both computational methods are validated by the results obtained from microflow experiments. The results from the second approach are in reasonable agreement with experiments while being more efficient in terms of computational cost. On the contrary, the first approach, while being computationally more expensive, allows to estimate the pressure field resulting from acoustic waves and thus predicts the dynamic behaviour of microparticles more accurately. Results suggested that the first approach is best to use for analysing the mechanism of microparticle and fluid manipulation in microfluidic devices.

A schematic of the acoustic streaming effect on a pure fluid and a microparticle suspension in a continuous microchannel flow is shown in Figure 4.1. The acoustic field generates counterrotation vortical structures which cause the flow to divert from its original straight path shown in Figure 5.1(a). This streaming effect can help in mixing different flowing fluids inside a microchannel. To manipulate microparticles, the flowing system is designed in a way that without acoustic streaming the microparticles flow into the lower outlet while operating the acoustic device results in the microparticles deflecting into the upper outlet is/as shown in Figure 5.1(b).

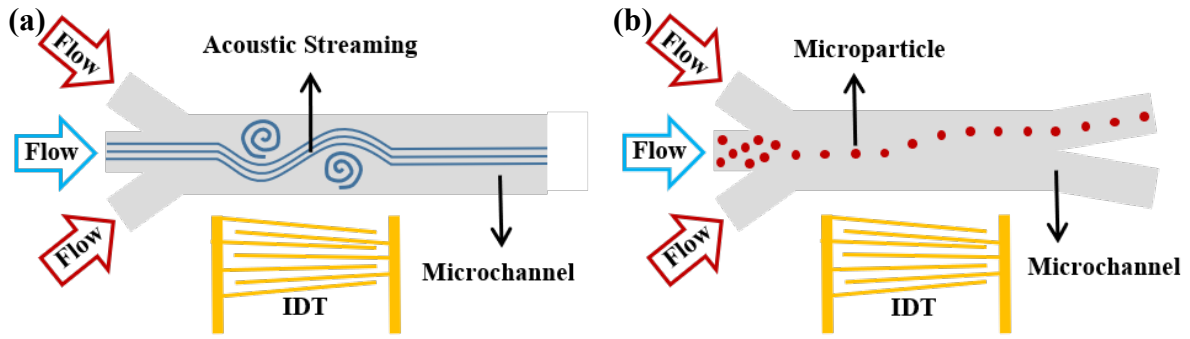

Figure 5.1 A schematic of (a) acoustic streaming effect on a fluid in a co-flowing microfluidic channel and (b) deflection of a suspension of microparticles by acoustic streaming across the channel. Sheath flows from two side inlets focus the liquid form the main inlet in the middle of the channel.

5.2 Numerical Modelling

In order to study the acoustic streaming effects inside the microchannel, the acoustofluidic setup was modelled using two different numerical simulation approaches. The discretized computational domain is shown in Figure 5.2(a) where the geometry was defined as a three-dimensional rectangular microchannel (length: 1000 µm (z-direction), width: 200 µm (x-

direction), height: 50 µm (y-direction)) and was discretized with a structured hexahedron grid with ~80000 elements. Mesh dependancy analysis was performed in order to choose a computational grid with minimal effects on the solution and reasonable computational time. The micrograph of the SAW setup is presented in Figure 5.2(b). It shows a part of the IDT on the bottom, the main and sheath inlets of the microchannel on the right and the outlet on the left (flow direction is from left to right).

To simulate the acoustic field, TSAW propagation in water was modelled using the Helmholtz equations (i.e., Equations (2-22) and (2-23)) with the oscillating wall boundary condition for the lower wall (i.e., Equations (3-14) and (3-15)). The steady, laminar, incompressible and viscous fluid flow was modelled using the Navier-Stokes equations (i.e. Equations (2-6) and (2-7)) with boundary conditions defined as fixed value of uniformly distributed volume flow rate at the inlet, and fixed value of pressure at the outlet, and no-slip boundary condition on the channel walls. The microparticles were modelled using Euler-Lagrange approach for their governing equations (i.e., Equations (2-56) and (2-57)) as well as adding the acoustic radiation force caused by the SAW (i.e. Equations (2-43) and (2-44)) to the governing quations as an external body force on the particles. The viscous drag force on the particles was modelled by the Stokes drag force. Since the volume fraction of the dispersed microparticle phase is smaller than the volume fraction of the continuous fluid phase, it is assumed that the fluid particle mixture is sparsely distributed. As both the sizes and velocies of the microparticles are relatively small compared to the fluid flow,t a “one-way coupling” was assumed between the fluid and particle phases which means that the continuous phase affects the dispersed phase but not vice-versa [145].

FEM was used to discretize the governing equations, Newton’s iterative method was used to solve the system of equations, and the solution was converged with 10^{-6} criteria for all the simulations. Microparticles movement was simulated for a duration of 5 s and with a time step of 0.001 s.

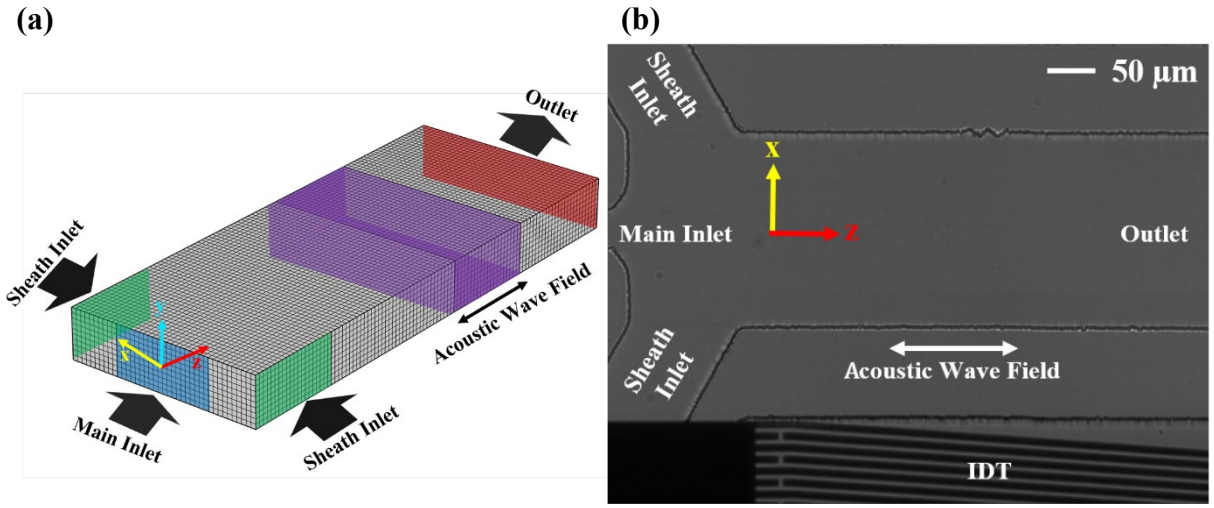

Figure 5.2 (a) A micrograph of the SAW setup. A part of the IDT on the bottom, the main and sheath inlets of the microchannel on the left and the outlet on the right (the flow direction is from left to right) is visible. The acoustic sound path is indicated by a double arrow. (b) A view of the computational domain and mesh. Main inlet (coloured blue) at the middle of the front side, sheath inlets (coloured green) on the two sides, outlet (coloured red) at the back and the flow is in z-direction. The acoustic wave field is coloured purple and the acoustic wave travels in x-direction, the height of the microchannel is in y-direction.

5.3 Investigation of the Acoustic and Fluid Flow Field Parameters

In order to verify the numerical simulation, velocity components in z- and x-directions and the velocity magnitude and vorticity magnitude in xz-plane from the simulations are compared with the data extracted from the experimental videos at the centreline of the microchannel (x=0 and y=0) at steady state. The comparison graphs are presented in Figure 5.3 for the acoustic power of 65 mW and the main inlet volume flow rate and each sheath flow volume flow rates are 25.0 µL/hr and 12.5 µL/hr, respectively.

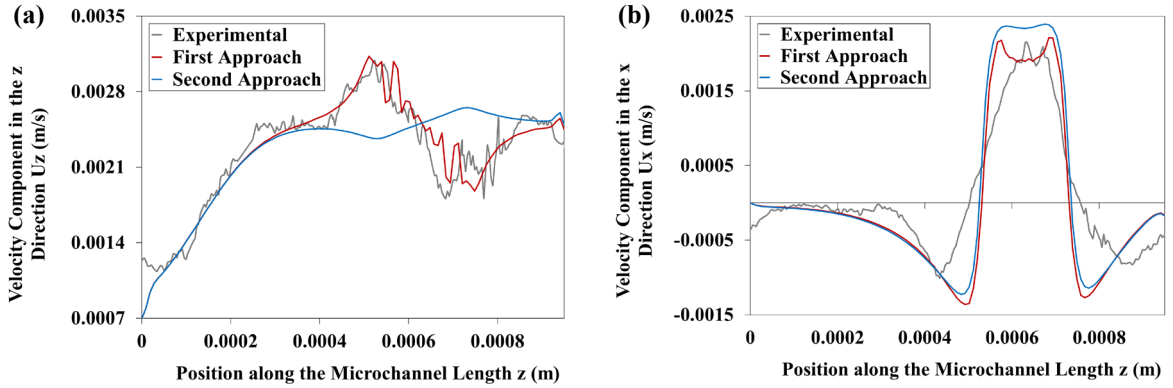

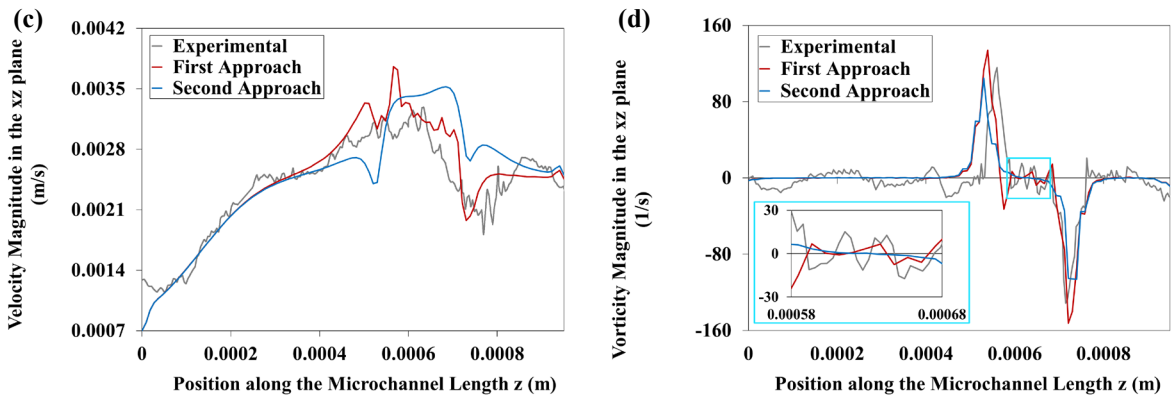

Figure 5.3 Velocity component in (a) z-direction and (b) x-direction, (c) velocity magnitude and (d) vorticity magnitude in x-z plane along the z-direction (length) of the microchannel for the acoustic power of 65 mW, the main inlet volume flow rate of 25 µL/hr and each of the sheath flow volume flow rates of 50 µL/hr from the experimental, first and second computational approach.

The graphs obtained from the experimental and both simulation approaches show agreements among each other. The results for the velocity component in z-direction (Figure 5.3(a)) from the first simulation approach follows the experimental data trend more accurately compared to the second simulation approach. According to Figure 5.3(a), the value for the z-velocity first increases and then decreases in the acoustic field for both the experiment and first approach. However, for the second approach, the trend for the z-velocity is reversed in the acoustic field. The difference in the maximum and minimum values of the z-velocity for the second approach is smaller compared to the other two graphs since the second approach underestimates the maximum/minimum value by 14 percent. This difference is expected as the second approach approximates the first approach. The results for the velocity component in x-direction (Figure 5.3(b)) is consistent with the experimental data for both simulation approaches. However, the second approach overestimates the maximum value by 19 percent. The velocity magnitude in xz-plane (Figure 5.3(c)) also shows a more accurate agreement between the experimental data and the first simulation approach compared to the second approach. For both the experiment and first approach the velocity magnitude in the acoustic field, first increases and then decreases. the velocity magnitude in the acoustic field increases to a near constant value for the second approach. For the vorticity magnitude in xz-plane (Figure 5.3(d)) the graphs show good agreement with each other. It can be seen from Figure 5.3(d) that both the computational approches predict the vorticities at the beginning and the end of the acoustic field accurately. However, through the width of the acoustic field (i.e., the zoomed section in Figure 5.3(d)) the first approach predicts the vorticity changes in the acoustic field similar to the experimental data, whereas for the second approach, the vorticity is nearly zero through the width of the acoustic field.

The comparisons among velocity component in y-direction, total velocity magnitude ($\sqrt{U_x^2 + U_y^2 + U_z^2}$), pressure and shear rate graphs along the centreline of the microchannel given by the two different acoustic simulation approaches are shown in Figure 5.4. The acoustic power is 65 mW, and the main inlet volume flow rate and each sheath flow volume flow rates are 25.0 µL/hr and 12.5 µL/hr, respectively. By comparing the graphs for the two computational methods, it can be seen how the flow field parameters are changed along the centreline of the microchannel. The velocity component in y-direction (Figure 5.4(a)) is drastically different between the first and second approaches. The peak of y-velocity graph is 25 times larger for the first approach compared to the second approach. This is due to the difference in calculating acoustic streaming effects in y-direction for each simulation approach. The total velocity magnitude (Figure 5.4(b)) is smooth and follows the trend for the typical pipe flow velocity graph for the second approach, with a small peak in the SAW field area caused by the body force acted on the fluid there. However, for the first approach the graph for velocity follows the same trend but has a very sharp and jagged peak with a value 6 times larger compared to the second approach because the difference between y-component of the velocity for first and second approaches. The pressure (Figure 5.4(c)) is smooth and looks like the typical pipe flow pressure graph for the second approach, whereas for the first approach it follows the same trend but then becomes uneven in the SAW field area because of the oscillatory velocity of SAW on the lower wall. The shear rates (Figure 5.4(d)) for both the computational methods follow the same trend as well. However, for the first approach the peaks are 50 times larger compared to the second approach because of the SAW fields being completely modelled.

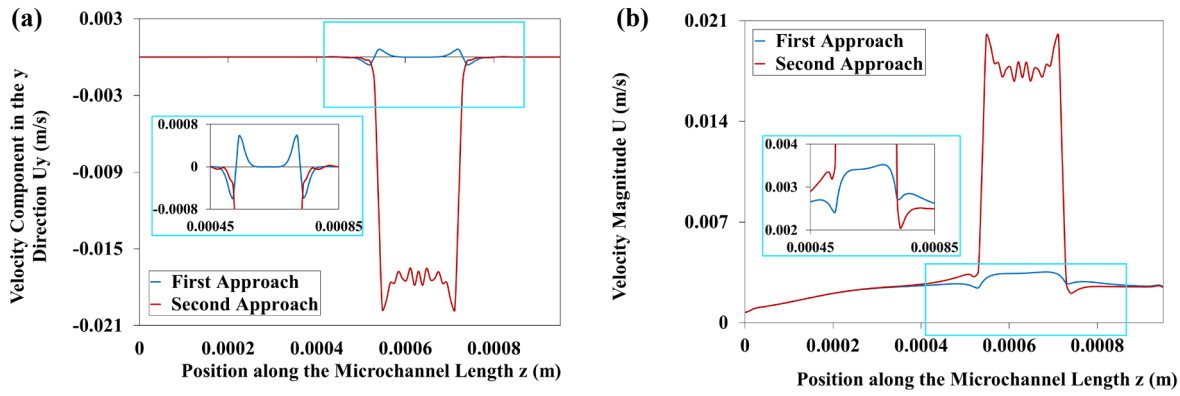

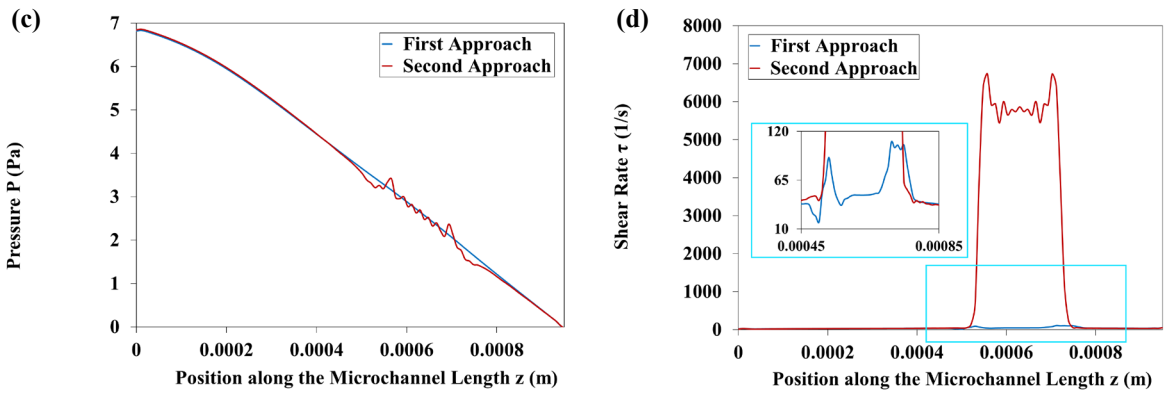

Figure 5.4 (a) Velocity component in y-direction, (b) Velocity magnitude, (c) Pressure and (d) Shear rate along the centreline of the microchannel for the acoustic power of 65 mW, the main inlet volume flow rate of 25 µL/hr and each of the sheath flow volume flow rates of 50 µL/hr and for first and second computational approaches.

The simulation results for the pressure field contours at the bottom layer y=-25 µm, middle layer y=0 µm and top layer y=25 µm of the microchannel as well as velocity contours and vectors at middle layer y=0 µm of the microchannel given by the two different acoustic simulation approaches is shown in Figure 5.5. Here the acoustic power is 65 mW, and for the two different flow conditions, the main inlet volume flow rate is 25.0 µL/hr and each of the sheath flow volume flow rates is 50.0 µL/hr.

The pressure fields are changed from bottom to top in the presence of the SAWs as shown in Figures 5.5(a-1) and 5.5(b-1). The pressure field results for both the computational approaches are similar outside the SAW field. However, inside the SAW field the difference in the pressure fields are quite noticeable. For the first computational approach, there seems to be a lot of fluctuations in the pressure field in the SAW region, due to the sinusoidal SAW patterns on the bottom wall of the channel. But for the second computational approach, the pressure field in the SAW region changes smoothly through the width of the channel as the acoustic streaming force changes in that direction.

The first approach estimates the pressure field resulting from the SAW, more accurate flow field parameters and the change in the flow field parameters through the height of the channel. While the second approach is more efficient in terms of computational cost and time while still presenting good results. The need for a more accurate prediction (i.e. the results from the first approach) would be significant in different situations. First, when the microparticles are smaller and/or lighter and thus can be pushed to the top of the microchannel more easily due to the vertical component of the streaming force. Second, when the height of the microchannel and/or the width of the acoustic field are larger and thus the micropartilces are under the effect of the

vertical component of the streaming force for a longer time. In these situations knoing what happens in the vertical direction is essential.

The computational results for velocity contours and vectors from both the first and the second approaches is shown in Figures 5.5(a-2) and 5.5(b-2). The results seem to be in good agreement with each other for every case. While for the second approach, the contours are smoother than the first approach.

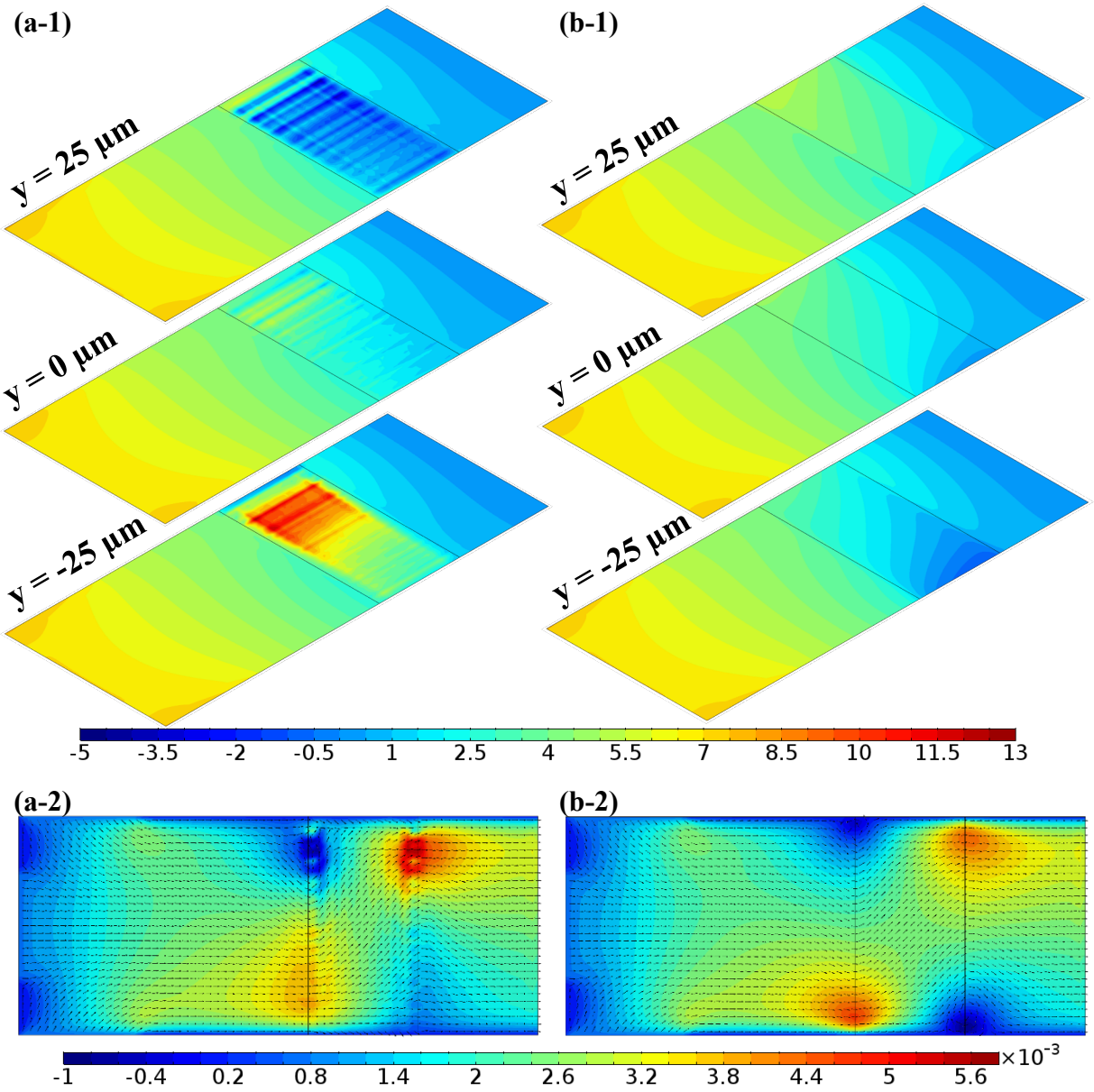

Figure 5.5 Simulation results using (a) the first approach and (b) the second approach for (1) the pressure (Pa) field contours at the bottom y=-25 µm, middle y=0 µm and top y=25 µm of the microchannel and (2) velocity (m/s) contours and vectors at microchannel middle y=0 µm for main inlet volume flow rate and each of the sheath flow volume flow rates of 25.0 µL/hr and 50.0 µL/hr and with acoustic power of 65 mW.

5.4 Comparing the First and Second Computational Approaches

Figures 5.6(a) and 5.6(b) present the comparisons among the velocity components in x-direction inside the microchannel with two different heights of 25 µm and 37 µm, resulted from the first and second computational approaches. Here the acoustic power is 65 mW, the main inlet volume flow rate and each sheath flow volume flow rates are 25.0 µL/hr and 50.0 µL/hr, respectively. For microchannels with heights of 50 µm (Figure 5.6(b)), 37 µm (Figure 5.6(a)), and 25 µm (Figure 5.6(b)), the percentage of the difference between the values for the x-velocity are 19%, 17% and 16%, respectively. It is evident that as the height of microchannel decreases, the difference between the values for the velocity components in the x-direction decreases as well. It can be concluded that for small heights of the microchannel (here 50 µm and below), both the computational approaches result in similar values for the velocity components in the x-direction.

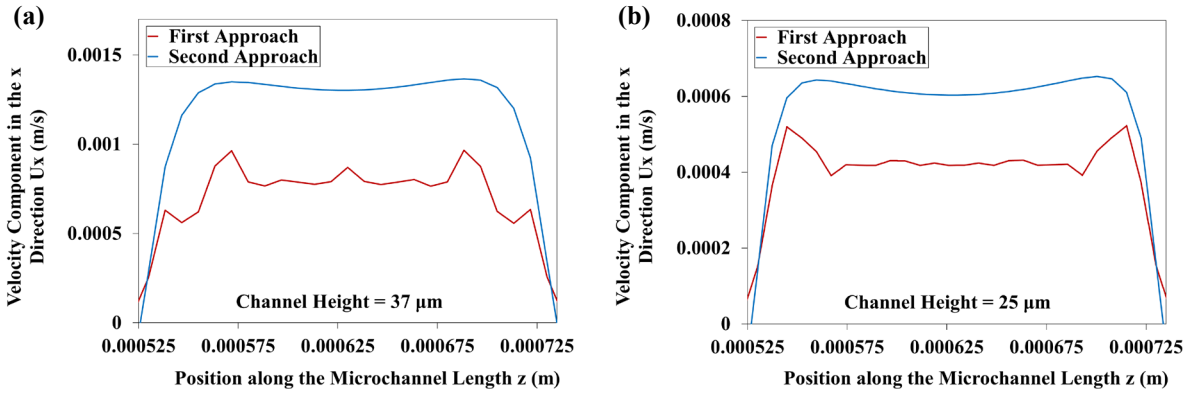

Figure 5.6 Velocity component in the x-direction along the z-direction (length) of the acoustic field with a height of (a) 37.0 µm and (b) 25.0 µm for the acoustic power of 65 mW, the main inlet volume flow rate of 25 µL/hr and each of the sheath flow volume flow rates of 50 µL/hr from the first and second computational approaches.

Choosing one of the computational approaches over the other depends on a number of factors. If the purpose of the study is to investigate the acoustic field in detail (especially through the width and height of the acoustic field), then the first computational approach is the best choice. If the height of the microchannel is small enough (here 50 µm and below), the second computational approach can be used to estimate the in-plane (i.e., xz-plane) parameters. However, to study the out-of-plane (i.e., y-direction) parameters, it is essential to use the first computational approach.

The Reynolds number of the flow, $Re = \frac{\rho_f U_f L}{\mu_f}$, which is defined as the ratio of the inertial forces to the viscous forces in a fluid flow, combines the effects of the channel dimensions, flow velocity and fluid properties. For water flowing in the microchannel, L is considered to

be the height of the microchannel with value of 50 μm and for the main inlet and sheath flow volume flow rates of 25.0 μL/hr and 50.0 μL/hr, the Reynolds number is equal to 0.2. Such a low Reynolds number shows that the fluid flow is in the creeping flow regime where the viscous forces are dominant. In this study for cases with $Re \leq 0.2$ (where the height of the microchannel is considerably smaller than its width), the second computational approach can be used for modelling the system.

In addition, if the acoustic field is present through the duration of the experiment and thus affects the domain for a large time frame, the first computational approach is the better option. Whereas the second computational approach can be used if the acoustic field is turned on as a pulse signal within a short time frame.

5.5 Acoustic Steaming in a Microchannel Flow

The experimental data and the computational results obtained using the two different approaches compared are shown in Figure 5.7. The results presented are for two different acoustic powers of 16.3 mW and 65 mW and with two different flow conditions, i.e., the main inlet volume flow rates of 25.0 μL/hr and 12.5 μL/hr and each of the sheath flow volume flow rates of 50.0 μL/hr and 25.0 μL/hr, respectively.

The experimental and computational fluid flow fields presented in Figure 5.7 are in good agreements with each other for every case. It can be seen in each case that for fixed volume flow rates of main and sheath inlets, increasing the acoustic power results in the increase in the acoustic streaming effect in both the experimental and computational flow fields. Also, for any fixed acoustic power, decreasing the volume flow rates results in the increase in the acoustic streaming effect in both the experimental and computational flow fields. The formation of two vortices at the channel sides under the effect of surface acoustic wave field is clearly observed through the simulation which is shown in Figure 5.7(b-2-ii) and 5.7(c-2-ii). The flow changes its direction even before encountering the acoustic field as displayed in Figure 4.8. The reason for this behaviour is mainly because of the low speed of the flow and continuity of fluid in this acoustofluidic problem.

For the first computational approach, the whole acoustic field resulted from the SAW is simulated and coupled to the flow field to obtain the results. This results in a more uneven streamline pattern in the SAW due to the change of flow field parameters caused by the SAW field. Whereas, for the second computational approach, the acoustic field is not simulated and

the effect of SAW on the flow field is modelled using only a body force. This causes the streamlines to be smooth in the SAW area.

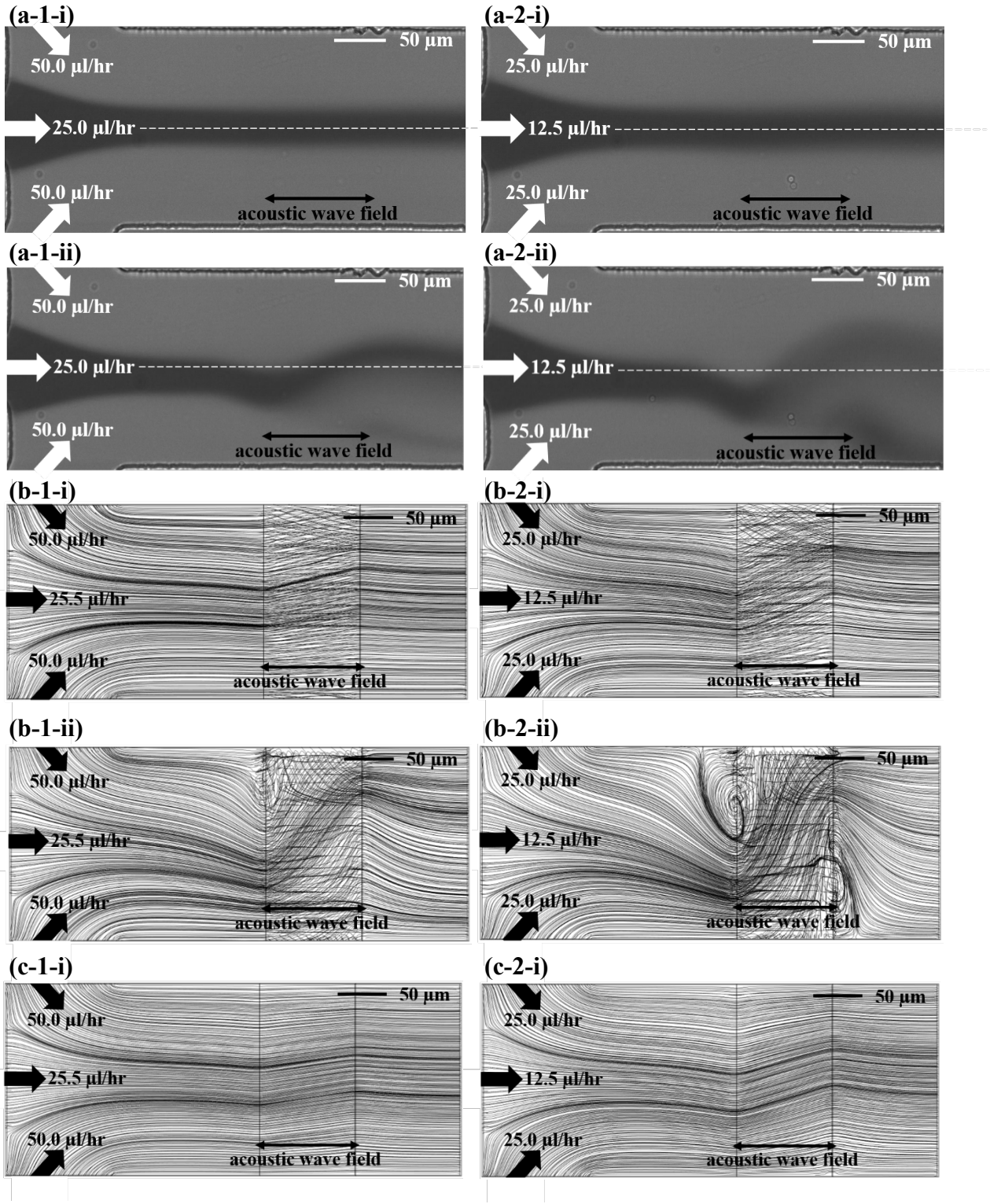

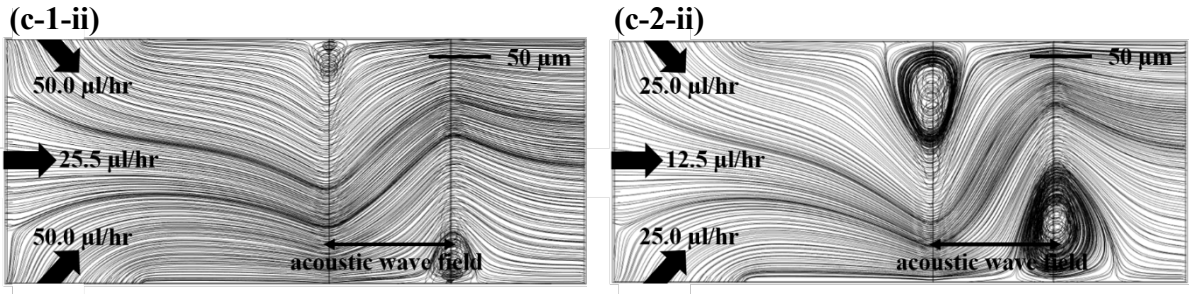

Figure 5.7 Flow field results of (a) experimental, (b) computational with the first approach and (c) computational with the second approach for main inlet volume flow rate and each of the sheath flow volume flow rates of (1) 25.0 µL/hr and 50.0 µL/hr, (2) 12.5 µL/hr and 25.0 µL/hr with two different acoustic powers of (i) 16.3 mW and (ii) 65 mW.

5.6 The Effects of Acoustic Steaming on Microparticles in a Microchannel Flow

The experimental and the computational results for microparticle tracks with the two different approaches is shown in Figure 5.8. The results presented are for two different acoustic powers of 16.3 mW and 65 mW and with two different flow conditions with main inlet volume flow rate of 25.0 µL/hr and each of the sheath flow volume flow rates of 50.0 µL/hr. The experimental and computational particle trajectories seem to be in agreements with each other. It is seen in Figure 5.8 that increasing the acoustic power results in the increase in the streaming effect in both the experimental and computational results.

For the two computational approaches, while the acoustic streaming force is modelled differently, the acoustic radiation force is the same. Therefore, any difference in the particle trajectories are caused by the difference in the modelling of the acoustic streaming force. By studying the experimental and computational flow fields and microparticle trajectories, It is concluded that the microparticles small in size follow the streamlines of the flow field.

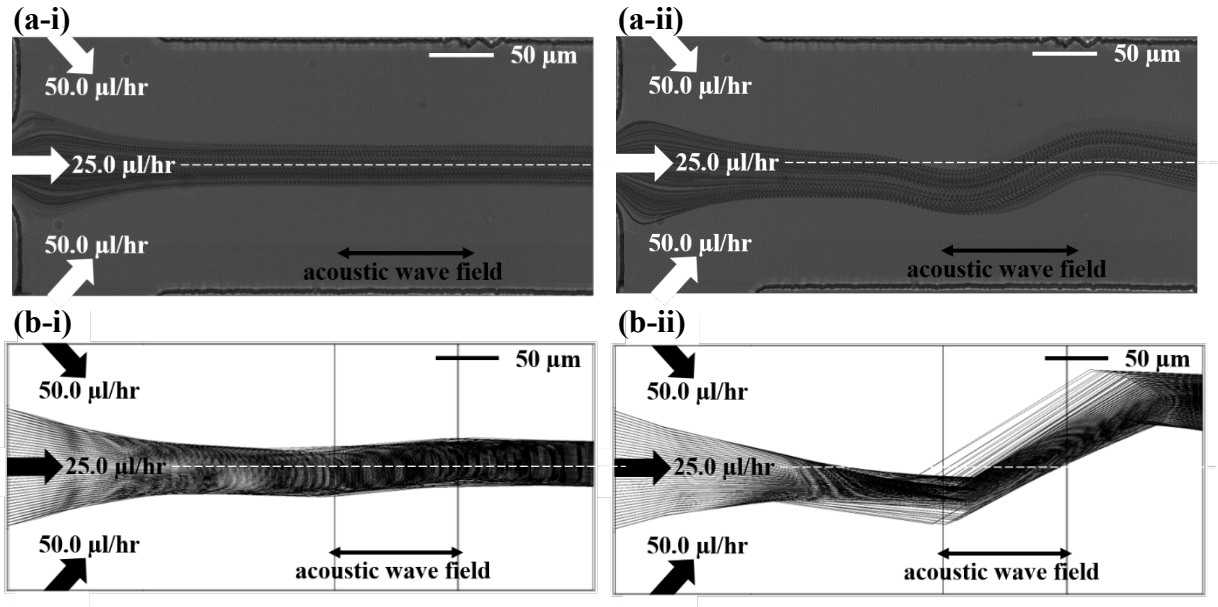

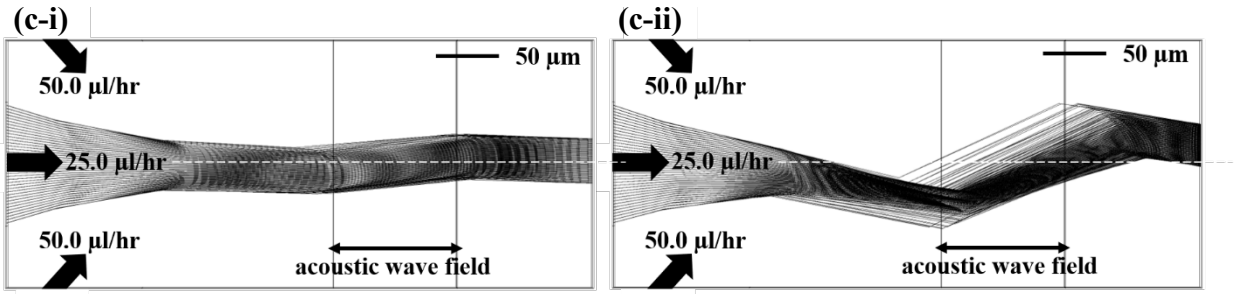

Figure 5.8 Flow field results of (a) experimental, (b) computational with the first approach and (c) computational with the second approach for main inlet volume flow rate and each of the sheath flow volume flow rates of 25.0 µL/hr and 50.0 µL/hr with two different acoustic powers of (i) 16.3 mW and (ii) 65 mW.

5.7 Using Acoustic Steaming in a Microchannel Flow for Droplet Sorting

Acoustic streaming is used to sort droplets into the upper outlet while without acoustic streaming the droplets flow into the lower outlet. The experimental and the first approach computational results for droplet trajectories is shown in Figure 5.9. The results presented are for acoustic power of 200 mW and a pulse width of 0.3 ms, main inlet volume flow rate of 50.0 µL/hr, upper sheath flow volume flow rate of 55.0 µL/hr and lower sheath flow volume flow rate of 45.0 µL/hr.

The droplet trajectories from both experiment and simulation (Figures 5.9(a) and 5.9(b)) are in a good agreement with each other. The volume flow rates of the sheath flows are used that without acoustics the droplets flow into the lower outlet. Switching the SAW device on pushes the droplets along the wave's propagation direction and deflects the droplets into the upper outlet. The graphs for the droplets' velocity magnitude as well as velocity components in x- and z-directions along the length of the microchannel are shown in Figure 5.9(c). In the presence of the acoustic field the droplets' velocity increases and as it exits the TSAW region the droplets' velocity decreases to match the flow velocity.

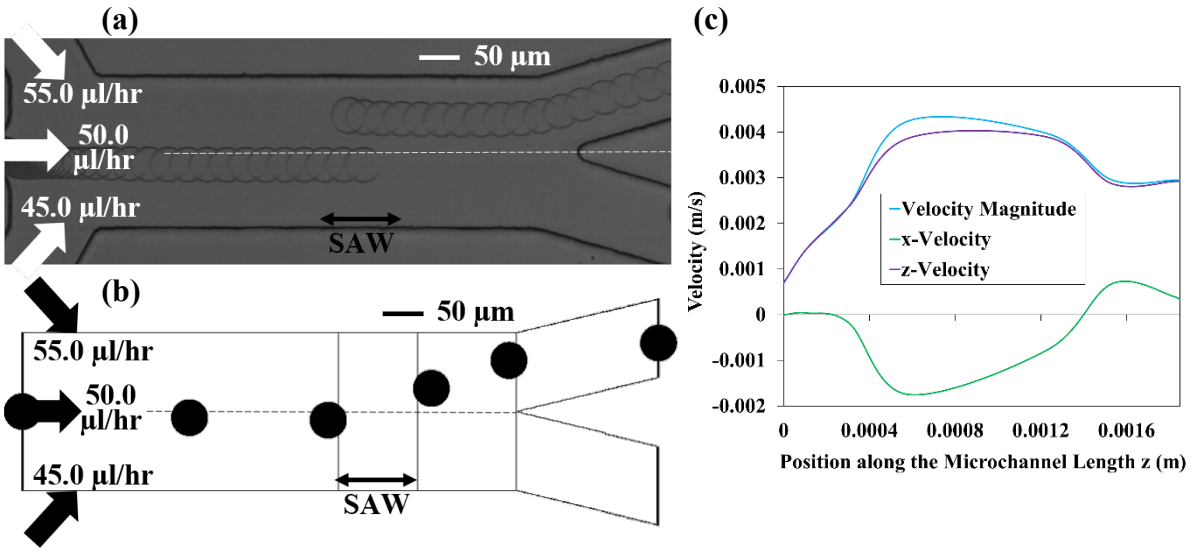

Figure 5.9 Droplet trajectories from (a) experimental and (b) computational results and (c) velocity magnitude and components along the z-direction (length) of the microchannel and for main inlet volume flow rate of 50.0 µL/hr, upper sheath flow volume flow rate of 55.0 µL/hr and lower sheath flow volume flow rate of 45.0 µL/hr with acoustic powers of 200 mW and a pulse width of 0.3 ms.

5.8 Summary

In this chapter, effects of acoustic streaming caused by TSAW on fluid and microparticles in a microchannel flow was investigated using numerical simulations with two different approaches. In the first approach, the whole acoustic field is simulated and coupled to the flow field to get the results and the acoustic streaming force is calculated using the first order density and velocity caused by the acoustic field. Therfore, this approach predicts the acoustofluidic system more accurately. Whereas for the second approach the effect of acoustic streaming on the flow field was simulated using the velocity of a one-dimensional attenuating TSAW in the acoustic streaming force formula. In this approach, the acoustic streaming force is calculated without using the density and velocity caused by the acoustic field. This aproach is more efficient in terms of computational cost and time while still presenting results with a reasonable accuracy.

The first approch calculates the in-plane velocity components (x-velocity and z-velocity) in the TSAW field more accuratly compared to the second approach, as the second approach underestimates the maximum/minimum value of z-velocity by 14 percent and overestimates the maximum value of x-velocity by 9 percent. Thus the velocity magnitude in xz-plane is calculated more accuratly using the first approach compared to the second approach. The out-of-plane velocity component (y-velocity) in the TSAW field calculated by the first approach is 25 times larger than the value given by the second approach. This combined with the

differences between the velocity magnitudes in xz-plane calculated by the first and second approaches, results in the total velocity value to be 6 times larger in the SAW field for the first approach compared to the second approach.

To study the acoustic streaming effects, two main cases were considered. The first case investigates the acoustic streaming effect on the fluid flow inside a microchannel with different inlet and sheath flow rates as well as different acoustic powers with the two different approaches of modelling the acoustic effects. The second case studies the effect of acoustic streaming on the microparticles' movement inside a microchannel with different acoustic powers. For both the cases the computational results are comparable with and verified by experimental data.

Simulation of acoustofluidic setups provides detailed information of the pressure and velocity fields with and without microparticles. It presents the properties of the fluid flow and microparticles under the effect of SAW in a cost and time effective manner which are sometimes hard or even impossible to obtain through experimental work.

Chapter 6. Flexible Thin film SAW Devices Used for Particle Manipulation

6.1 Introduction

For the conventional acoustofluidic platforms, SSAWs can be readily generated between the two electrodes of the SAW devices when an RF signal is applied to the electrodes. The acoustic field generated by the propagation of the SAWs forces the particles to form parallel lines along the width of the microchamber with a constant distance between each two adjacent lines corresponding to the pressure node lines (with minimum acoustic pressure) of the standing acoustic waves (shown in Figure 6.1(a)). This alignment can be clearly observed from the top view, which has been well documented in literature [56, 158, 159]. Particle distribution and alignment along the height of the microchamber have also recently been investigated and it was demonstrated that particles form pattern lines in a three-dimensional matrix [152, 160].

Flexible microfluidic platforms could be used for on-body applications, wearable devices, body conforming technologies, implantable biomedical applications, flexible sensors, or soft robotics, to monitor physiological conditions of a patient, detect infection illness or even cancer at its early stages [16, 52, 53]. They have recently shown promises in constructing medical and bio-inspired devices [12], micro-stretching devices for cell studies [104], cell sorting bandages, wearable [17] and PoC devices [14] for monitoring the body temperature, heart rate or blood pressure, clinical and biomedical technologies for collection, manipulation and investigation of bodily fluids [11, 15] such as detecting antigen and antibody reactions [161], deep brain stimulation [162], artificial retina [162] and wearable devices for flow measurement in a cerebrospinal shunt [163].

Recently, there are studies to design and fabricate flexible (including bendable, deformable, and even stretchable) ultrasonic and SAW devices [87-89]. For example, flexible SAW sensors and acoustofluidics devices were fabricated by depositing a thin layer of a piezoelectric material such as ZnO or AlN onto a flexible substrate (either polymer or metallic foil such as aluminium), followed by patterning of IDTs on top of the piezoelectric thin film [3, 94, 95, 97, 98]. Previous results showed that the SAW devices based on ZnO on Al foil/sheet demonstrate efficient acoustofluidic functions to drive liquid sessile droplets on both flat, inclined, and even randomly bent and curved surfaces [94, 95].

It is crucial to understand the dynamic behaviour and 3D distribution patterns of the particles and biological cells under acoustic waves in a potentially bendable acoustofluidic device.

However, so far, there are no previous studies on flexible and deformable SAW devices used in continuous flow acoustofluidic platforms for patterning of microparticles and biological cells. This chapter aims to understand the acoustofluidic behaviour when the SAW devices are in different bent conditions, and the effects of bending curvatures on microparticle manipulation and patterning of particles and cells inside a microchamber or a microchannel under the SSAWs.

A flexible SAW device can be bent in both concave and convex geometries (see Figures 6.1(b) and 6.1(c)). Accordingly, all the particles or cells could still be aligned in parallel by the SSAWs along the IDT direction. However, from the cross-sectional views along the vertical direction, the patterned lines of particle will not have a constant distance from the bottom of chamber to the top, and particle pattern lines might become converged with a slope towards the centre of the curvature of the geometry from the cross-sectional view. From the top views, the distances between each two adjacent parallel lines ("line distance" in short hereafter) of the particles or cells can be varied. In this chapter, particle patterning using the flexible and bendable devices in both concave (substrate bent-down, (Figure 6.1(b)) and convex (substrate bent-up, Figure 6.1(c)) geometries will be numerically and experimentally studied. Additionally, the effects of twisting configuration (Figure 6.1(d)) using ZnO thin film SAW devices made on aluminium foil/sheets on microparticle patterning will be investigated.

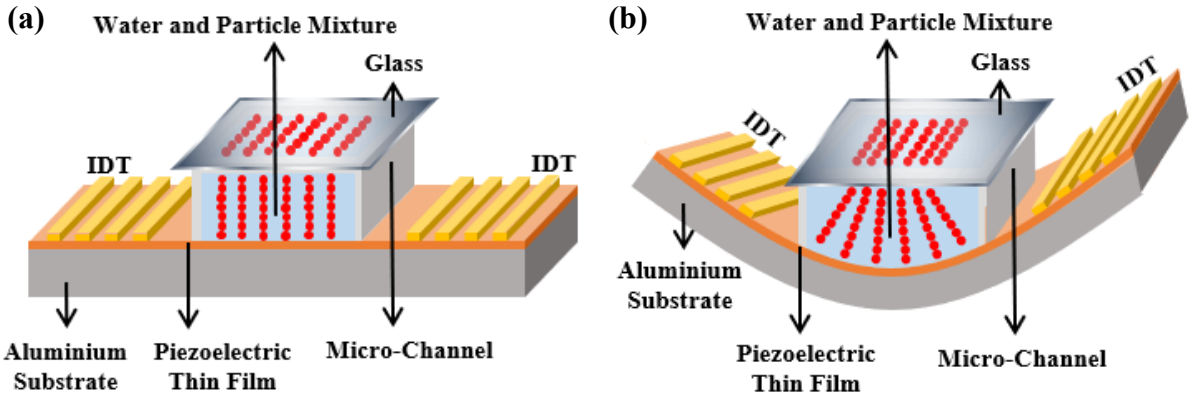

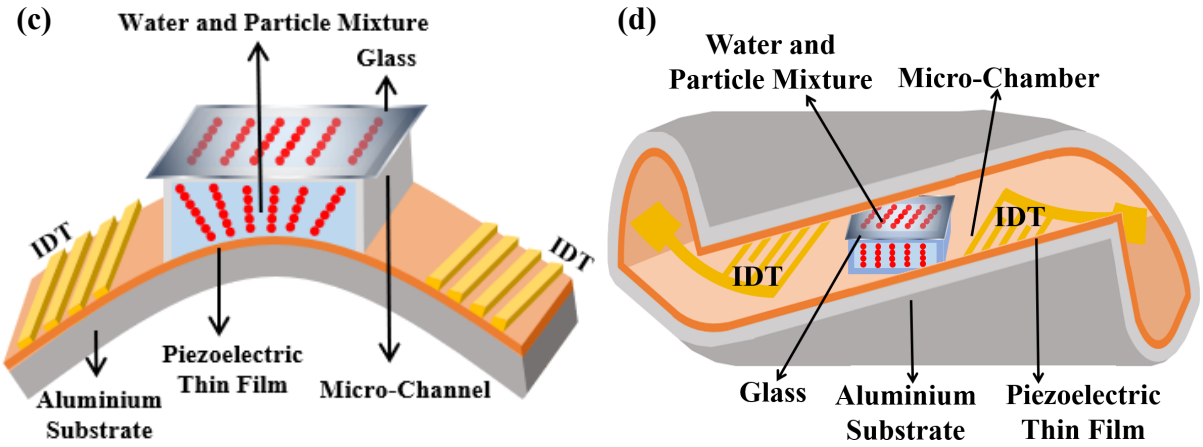

Figure 6.1 Schematic of the effect of bending the flexible SAW device on particle patterning in a microchamber with (a) flat, (b) concave (bent-down), (c) convex (bent-up) and (d) twisting surfaces.

6.2 Numerical Modelling

In order to study the acoustofluidic behaviour and particle distribution patterns using different bent geometries of the flexible SAW devices, the flexible acoustofluidic setup was numerically modelled. Figure 6.2 shows the modelled geometry and mesh for one of the SAW device geometries where the geometry was defined as a two-dimensional cross-sectional view of the microchamber on the bent SAW device. The computational domain was discretized using ~5500 structured quadrilateral elements and mesh dependancy analysis was performed to choose the computational grid which provides the solution with enough accuracy with a reasonable computational time.

The acoustic field in water was modelled using the Helmholtz equations (i.e., Equations (2-22) and (2-23)) with the SSAW propagation on the lower wall as the boundary condition (i.e., Equations (3-16) and (3-17)). FEM and Newton's iterative method were used to dscritise and solve the governing euations, respectively. The solution was converged with 10^{-6} criteria. The movement of the microparticles was modelled using Euler-Lagrange approach (i.e., Equations (2-56) and (2-57)) while also adding the acoustic radiation force caused by the SSAWs (i.e. Equations (2-52) and (2-53)) and the viscous drag force they experince in water to the governing equations. The modelling of microparticles movement was performed for a duration of 10 s and with a time step of 0.001 s.

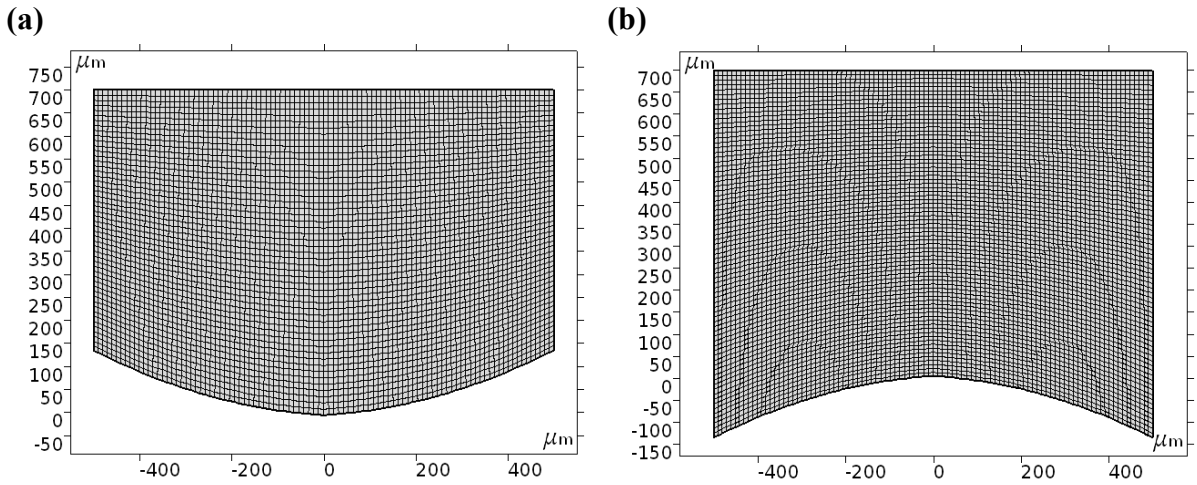

Figure 6.2 Modelled geometry and computational mesh for flexible SAW devices bent in (a) concave and (b) convex geometries.

6.3 Particle Patterning on a Flexible Thin film Lamb Wave SAW Device

Firstly, effects of bending curvatures (Ƙ) of ZnO on Al foil flexible Device 1 (with a substrate thickness of ~ 50 μm and a wavelength of 160 μm and its details are given in Table 6.1) on patterning of silica microparticle in a microchamber were studied. In this case, the Lamb wave modes are the dominant frequency modes.

The curvature formula (K(x)) for any curve with the equation $y = y(x)$ in cartesian coordinates can be calculated as follows:

$$\mathrm{K}(x) = {y''}\Big/{(1 + y'^2)^{3}/_{2}} \qquad (6\text{-}1)$$

where $y'' = {d^2y}/{d^2x}$ is the second order derivative and $y' = {dy}/{dx}$ is the first order derivative of the curve equation $y = y(x)$ in cartesian coordinates. The value of the curvature (Ƙ) for the concave and convex SAW devices was calculated using Equation (6-1) and at the point (0,0) which is in the middle of the SAW device where the chamber is placed at.

Figure 6.3 shows the simulation and experimental results of microparticle patterning when the device was applied with its A0 mode (frequency of 13 MHz) to form SSAWs (the frequency details are given in Table 4.1) from cross-sectional and top views. The curvature (Ƙ) value was changed from 0 (flat) to ±60 m^{-1}, ±200 m^{-1} and then ±600 m^{-1} for simulations and experiments.

Figures 6.3(a-1) and 6.3(a-2) show the cross-sectional view simulation results for acoustic pressure field and particle patterning (after applied with SAW for 10 seconds) on the flat geometry (e.g., the conventional SSAWs case). In this case the microparticles are aligned onto

the pressure nodes of the acoustic pressure field, in parallel lines with a nearly constant line distance.

Figures 6.3(b) to 6.3(d) present the simulation and experimental results of particle patterning on concave geometries of the flexible SAW device. Numbers (1) to (4) in the figures show the acoustic pressure field (Pa) simulation, particle alignment from the cross-sectional view after simulation for 10 seconds, experimental results for particle alignment from cross-sectional view and top view, respectively. For the concave geometries, the patterned lines of particles become converged and have shown a slope towards the centre of the curvature of the device (see Figures 6.3(b) to 6.3(d), with different bending curvatures). For the concave geometries of the SAW device, when the centre of curvature of the device is located inside the chamber (Figure 6.3(b)), the particle lines will be converged towards the centre of curvature of the device but then diverged after passing through the centre of curvature. The line distances start to decrease as the lines converge towards the centre of curvature, and after passing that point the lines start to diverge and the line distances start to increase.

With the increase of curvatures of the concave geometries, there appears a weak acoustic pressure region (acoustic pressure is near zero, e.g., dotted black circle in Figure 6.3(d-1)), however, there are still pressure nodes (zero pressure positions) present in this area and the particles will pattern on the pressure nodes. But since this is a weak pressure region, the particles will not be patterned in complete lines and some still remain in the space between pressure nodes. The accumulation of particle lines can be seen in this area. Additionally, Figure 6.3(d-2) shows that the particles at the two sides of the microchamber do not form any pattern which is attributed to the weak SSAW field at these positions with apparently random distribution of particles. Most of particle aggregation in Figure 6.3(d-2) is at the two sides which have small pressure node regions (see the areas marked with dotted blue circles in Figure 6.3(d-2)). On the concave geometries, clear particle patterning can be seen where the SSAW field is focused on the middle (e.g., the area marked with dotted blue circle in Figure 6.3(c-2)).

The simulation and experimental results of particle patterning on convex geometries of the flexible SAW device are shown in Figures 6.3(e) to 6.3(g). It should be noted that numbers (1) to (4) define the acoustic pressure field (Pa) simulation, particle alignment from the cross-sectional view after simulation for 10 seconds, experimental results for particle alignment from cross-sectional view and top view, respectively. For the convex geometries, the particle lines

have the opposite trends (i.e., compared with those of concave ones). They become diverged and have a slope away from centre of the curvature of the device as shown in Figures 6.3(e) to 6.3(g) at different bending curvatures. The line distances are increased as the lines are diverged away from the centre of curvature. Increasing the bending curvature of the convex devices results in a weaker SSAW field especially near the top of the chamber (e.g., the area marked with dotted blue circles in Figure 6.3(g-2)), and the particles are randomly distributed in these areas. Further increase in the curvature causes the SSAW field to become even weaker and the particles will be randomly distributed inside the chamber. For these convex geometries, the patterning is clearer near the surface of the SSAW device compared to the top of the chamber (e.g., Figure 6.3(g-2)).

The experimental cross-sectional view results (which are located at the bottom of the microchamber) are consistent with the simulation results. The top views presented in Figure 6.3 show that particles are aligned in parallel corresponding to the pressure nodes of the acoustic pressure field of the SSAWs. For both the concave and convex geometries, the line distances are not constant unlike the particle patterning on the flat SSAW devices. For the concave curvature of $K = 600\ m^{-1}$ (Figure 6.3(d-3)), particle patterning seems to be irregular. This can be caused by the large acoustic pressure node area in the middle of the chamber (as has been confirmed from simulation results, e.g., the green area shown in Figure 6.3(d-1)), as the particles tend to move towards the pressure node area, and the patterns become irregular.

Particle patterning was further performed on the concave geometries of Device 1, using the higher resonant frequencies of S0 and A1 modes (details are given in Table 4.1). The obtained results all showed patterning of particles using the SSAWs. With the increase of frequencies, the distributions of lines are similar as those of the A0 mode, but the line distances become smaller.

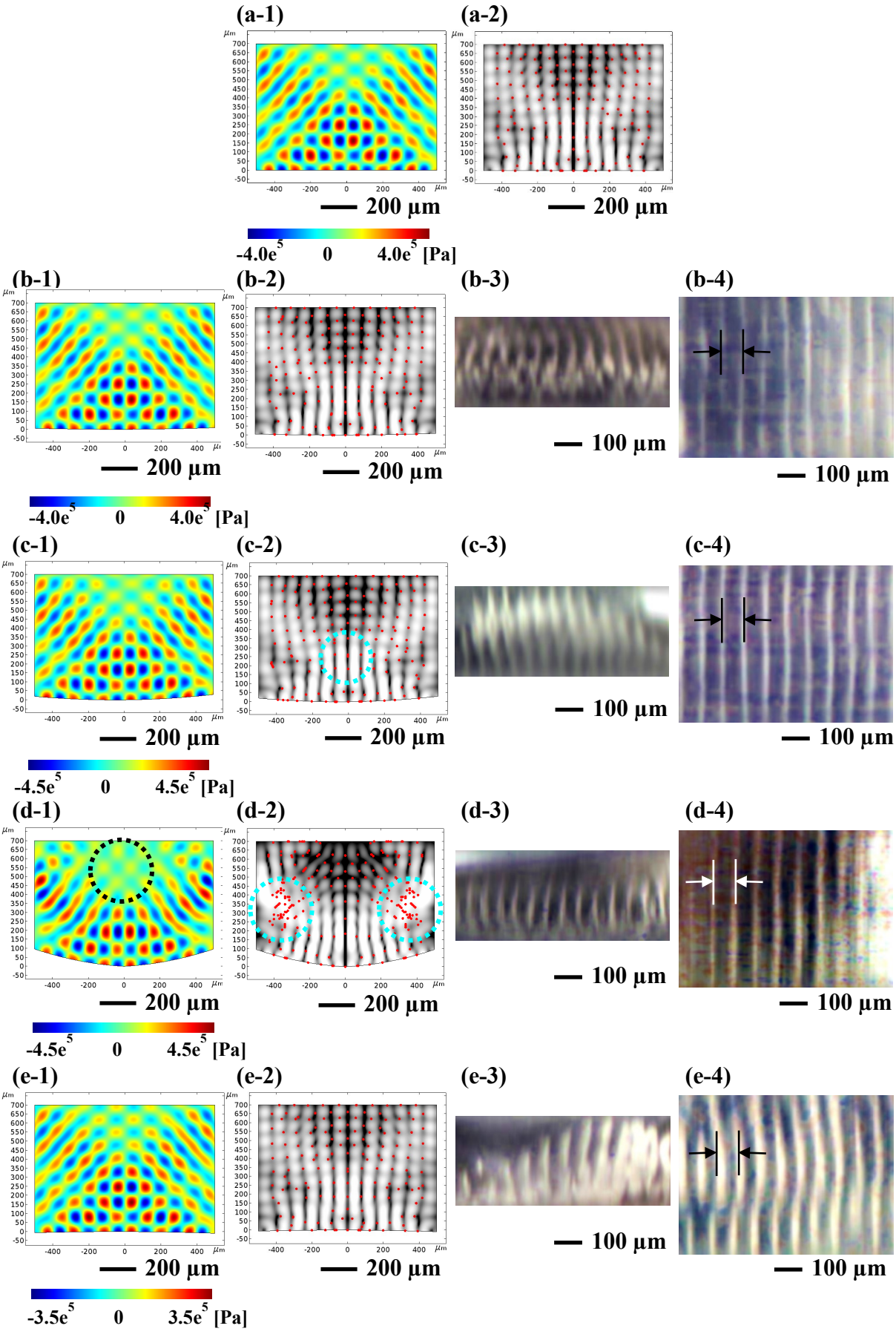
(a-1)
(a-2)
200 µm
200 µm
-4.0e5 0 4.0e5 [Pa]
(b-1)
(b-2)
(b-3)
(b-4)
200 µm
200 µm
100 µm
100 µm
-4.0e5 0 4.0e5 [Pa]
(c-1)
(c-2)
(c-3)
(c-4)
200 µm
200 µm
100 µm
100 µm
-4.5e5 0 4.5e5 [Pa]
(d-1)
(d-2)
(d-3)
(d-4)
200 µm
200 µm
100 µm
100 µm
-4.5e5 0 4.5e5 [Pa]
(e-1)
(e-2)
(e-3)
(e-4)
200 µm
200 µm
100 µm
100 µm
-3.5e5 0 3.5e5 [Pa]

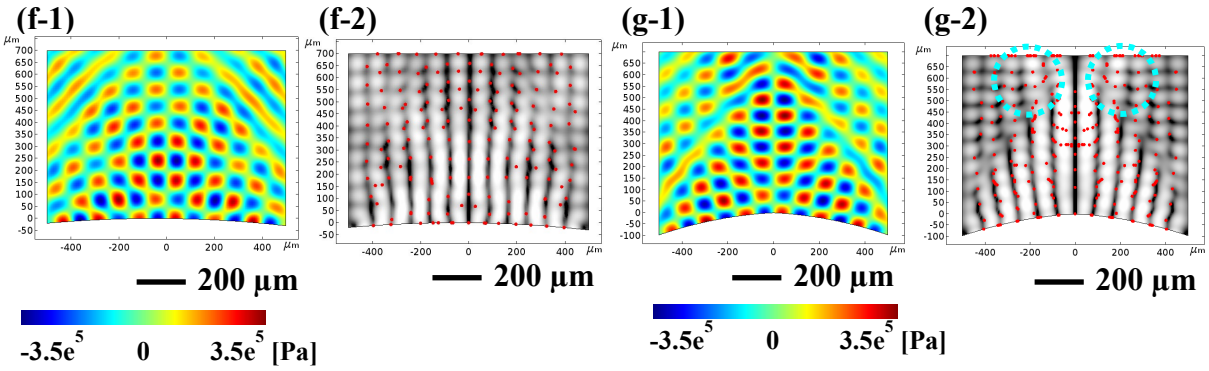

Figure 6.3 Patterning of microparticles on SAW device (Al foil substrate) with frequency f_A0 = 13.00 MHz (a) flat, (b) concave $\mathcal{K}$ = 60 m^{-1}, (c) concave $\mathcal{K}$ = 200 m^{-1}, (d) concave $\mathcal{K}$ = 600 m^{-1}, (e) convex $\mathcal{K}$ = -60 m^{-1}, (f) convex $\mathcal{K}$ = -200 m^{-1}, (g) convex $\mathcal{K}$ = -600 m^{-1}, simulation of (1) acoustic pressure (Pa), (2) particle alignment from cross-sectional view after 10 s and experimental particle alignment from (3) cross-sectional and (4) top views.

Based on the results shown in Figure 6.3, the line distances are different from the top view and cross-section views. Figures 6.4(a) to 6.4(d) summarise the simulation data of line distances through the width of the microchamber at the top (Figures 6.4(a) and 6.4(b)) and also at halfway up from the surface of the SAW device (Figures 6.4(c) and 6.4(d)) for both the concave and convex geometries.

For the concave geometries, at the top of the chamber, the line distances at the two sides of the microchamber are smaller than those in the middle of the chamber (Figure 6.4(a)). However, at halfway up from the surface of the SSAW device, the results are quite different depending on the curvature and geometry of the SSAW device (Figure 6.4(b)). For the two smaller concave curvatures (60 m^{-1} and 200 m^{-1}), there is a similar trend compared with the line distances at the top of the chamber, but there is a decrease in the line distance values in the centre of the chamber. Whereas for the two larger concave curvatures (600 m^{-1} and 2000 m^{-1}), the distribution trends of line distances are the opposite to that at the top of the chamber i.e., the line distances at the sides of the chamber are slightly larger than those in the middle of the chamber.

For the convex geometries, the trends for the line distances at the top of the chamber are dependent on curvature and geometries of the SSAW device (Figure 6.4(c)). For the smallest convex curvature (-60 m^{-1}), the trends for the line distances are nearly the same as the flat device. For the convex curvature of 200 m^{-1}, the line distances at the two sides of the microchamber are smaller than those in the middle of the chamber. But for the 400 m^{-1} convex curvature, there is a slight decrease of the line distance values in the middle of the chamber. Whereas halfway up from the surface of the SAW device, the trends for the line distances at the top of the chamber are reversed compared to the concave geometries (at the top of the

chamber) i.e., the line distances at the sides of the microchamber are slightly larger than those in the middle of the microchamber (Figure 6.4(d)).

Figures 6.4(e) and 6.4(f) are the comparisons of the line distances of the experimental data from the top views through the width of the chamber for concave and convex geometries, respectively. The line distances are nearly constant for the flat device. For the concave geometries, the line distances at the two sides of the microchamber are smaller than those in the middle. Whereas for the convex geometry, the trends are reversed, i.e., the line distances at the sides of the microchamber are larger than those in the middle of the chamber. The experimental results show the same trends as those from the simulation results shown in Figures 6.4(a) to 6.4(d). Since in the experimental cases the SAW devices are not bent into perfectly symmetric curves, there are slight asymmetry of data in the experimental graphs.

In brief, the simulation results shown in Figure 6.4 clearly show the patterns of the particle distributions for both the concave and convex bending situations. For the concave geometries of the SAW device, the acoustic field would be focused, whereas for the convex geometries, the acoustic field would be diverged. These phenomena are similar to the results reported by Lim et al [93], who found that a non-flexible and spherical PZT with outer and inner surfaces representing convex and concave geometries could generate similar phenomena.

The slopes of the particle lines are also compared for both the concave and convex geometries from the cross-sectional views in order to show the convergence and the divergence of the lines. The results are presented in Figures 6.4(g) and 6.4(h). It is shown on all the concave geometries, the particle pattern lines are convergent towards the centre of the curvature of the geometry but on the convex geometry, the particle pattern lines are divergent with a slope away from centre of the curvature of the geometry.

In brief, the results shown in Figure 6.3 and 6.4 clearly reveal the patterns of the particle distributions for both the concave and convex bending situations which are similar to the results reported by Lim et al [93]. They used a non-flexible spherical PZT with outer and inner surfaces representing convex and concave geometries and concluded that a concave transducer will focus the acoustic field while with a convex transducer the acoustic field would diverge.

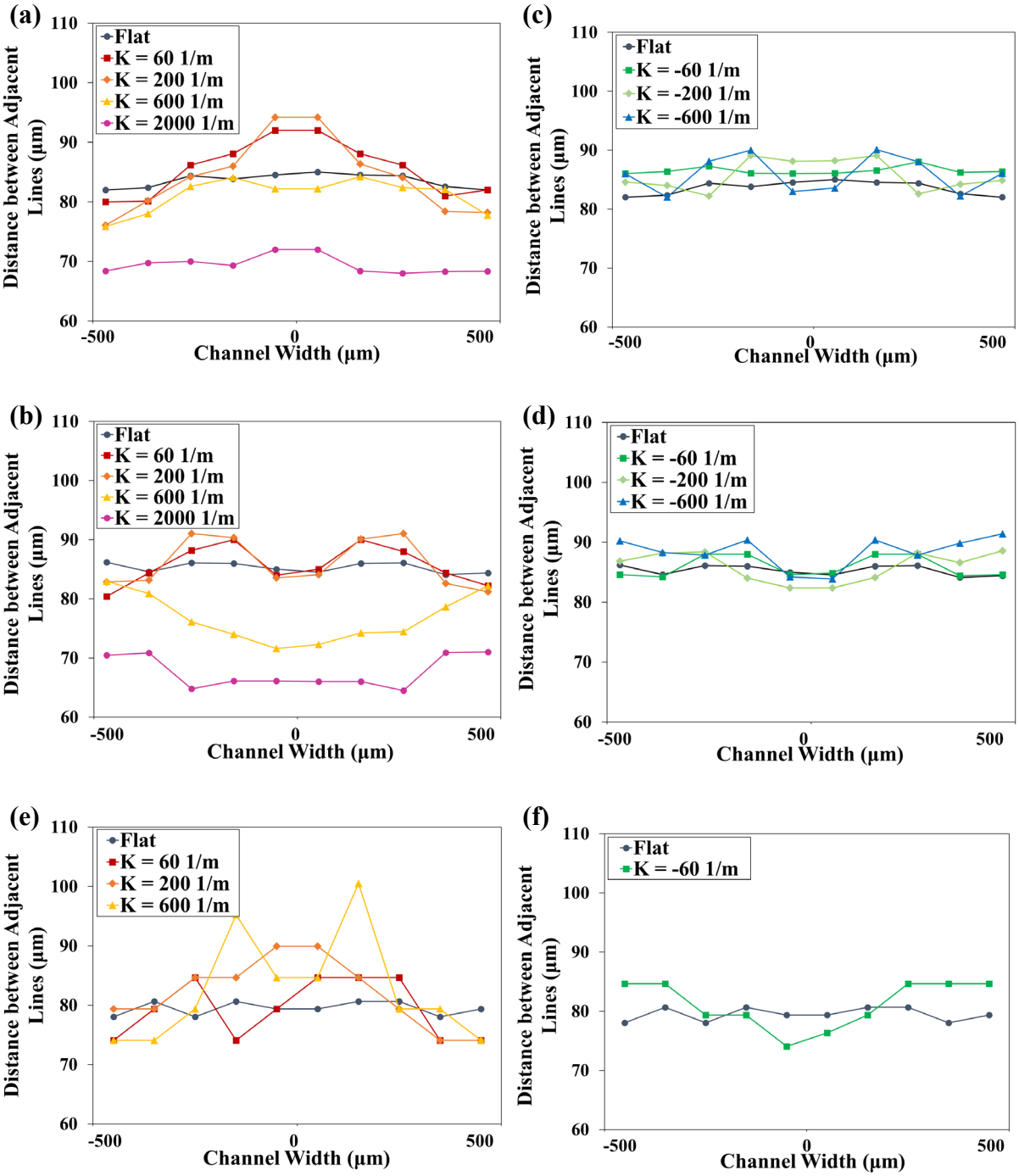
(a)
Flat
K = 60 1/m
K = 200 1/m
K = 600 1/m
K = 2000 1/m
Distance between Adjacent Lines (µm)
Channel Width (µm)
(c)
Flat
K = -60 1/m
K = -200 1/m
K = -600 1/m
Distance between Adjacent Lines (µm)
Channel Width (µm)
(b)
Flat
K = 60 1/m
K = 200 1/m
K = 600 1/m
K = 2000 1/m
Distance between Adjacent Lines (µm)
Channel Width (µm)
(d)
Flat
K = -60 1/m
K = -200 1/m
K = -600 1/m
Distance between Adjacent Lines (µm)
Channel Width (µm)
(e)
Flat
K = 60 1/m
K = 200 1/m
K = 600 1/m
Distance between Adjacent Lines (µm)
Channel Width (µm)
(f)
Flat
K = -60 1/m
Distance between Adjacent Lines (µm)
Channel Width (µm)

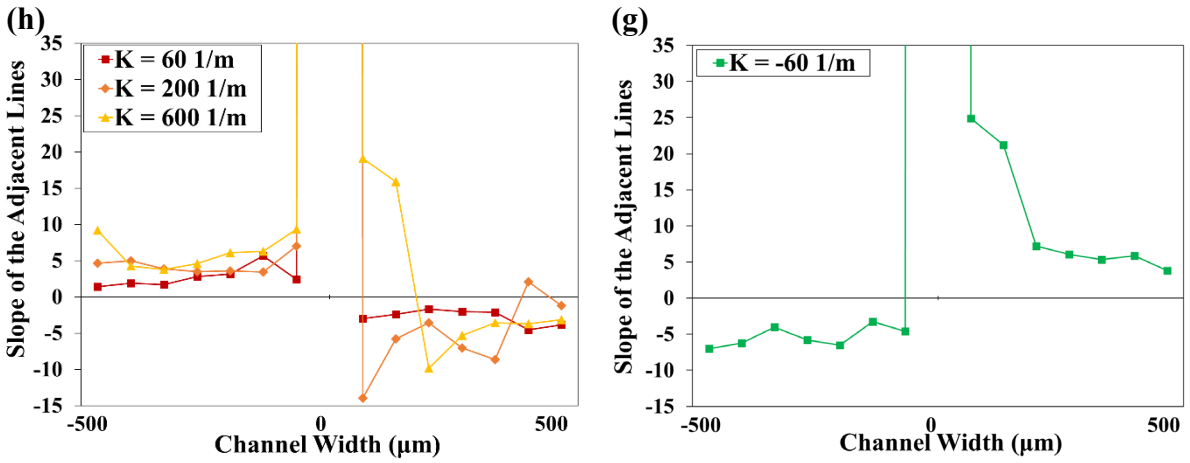

Figure 6.4 Comparison of the line distances with frequency of f_{A0} = 13.00 MHz (a) at the top of the chamber; (b) half way up from the surface of the SAW device for concave geometries; (c) the top of the chamber; (d) half way up from the surface of the SAW device for convex geometries, all simulation results from cross-sectional view; (e) concave; (f) convex geometries, experimental data from top view.
Comparison of the slope of the particle pattern lines for (g) concave geometries of Device 1 from side view and (h) convex geometry of Device 1from side view.

6.4 Particle Patterning on a Flexible Thin film Rayleigh Wave SAW Device

In the second experimental case, effects of bending curvatures of Device 2 with a substrate thickness of 200 µm and a wavelength of 160 µm (details given in Table 4.1) were studied. In this device, Rayleigh mode was dominant (frequency of 17 MHz) and was utilized for generating standing waves (as the wavelength is smaller than the substrate thickness, and more information on Rayleigh wave can be found in the supplementary information). The simulation and experimental results of patterning of silica microparticles from the cross-sectional and top views are shown in Figure 6.5.

Simulations were performed for the particle patterning and modelling acoustic pressure fields on different concave and convex geometries from the cross-sectional views based on the parameters of the Rayleigh mode waves. The simulation results agree well with the experimental data, both of which show the convergence and divergence of the particle lines for concave and convex geometries.

With the increase of the concave bending curvature, a large acoustic pressure node area, formed near the top of the chamber which will cause all the particles in this area to accumulate into two lines in the middle of the chamber. Whereas at the two sides of the chamber, there is a weak SSAW field formed, thus there are accumulations of particles and poor alignment patterns at these locations. With the increase of the convex bending curvature up to 200 m^{-1},

the particle patterning is clear and regular. However further increase of the bending curvature causes the deterioration of alignment patterns for microparticles.

For the concave geometries of the SAW Device 2, the particles are patterned well in line positions in the middle of the chamber. However, for the convex geometries, it is harder to obtain a larger area with regular patterns on all the curvatures (apart from the curvature of -200 m^{-1}), probably because of the weaker acoustic SSAW pressure field. From both experimental and simulation results, it can be concluded that for this Rayleigh wave device, the concave bending geometries result in more regular particle patterns.

The particle patterns obtained from the Rayleigh wave device were further compared to the Lamb wave device results. For the concave geometries with the same curvatures 200 m^{-1}, the Lamb wave device produces regular particle patterns near the lower half of the chamber, but the patterns of the particles are similar at upper heights of the chamber for both devices. Whereas for the convex geometry with the same curvature -200 m^{-1}, particles are patterned more regularly for the Rayleigh wave device through the height of the chamber, if compared with those from the Lamb wave device. Although, for the Lamb wave device the patterning is regular at the lower half of the chamber compared to the upper half. The reason for this can be explained by the fact that the Rayleigh waves (which propagate nearer to the device's surface) could have interacted effectively with the liquid, and thus be dissipated more efficiently into the liquid. This will result in regular patterns of particles in the vertical direction and 3D pattern. Lamb wave (A0 mode) is the flexural wave, which is less efficient to transfer the energy into the liquid.

In summary, the patterning of microparticles is consistent with those obtained from the Lamb wave device. However, for the Rayleigh wave device, the particle patterns are not as well defined when using the Rayleigh wave mode, which might be due to the large values of roughness of the surface of the aluminium plate used in fabricating the SSAW devices. Compared with those of Lamb waves which are propagating mostly along the whole plates, the Rayleigh waves propagate much nearer to the surface of the device, thus the surface roughness will have more significant influence for the distortion of the patterns of particles.

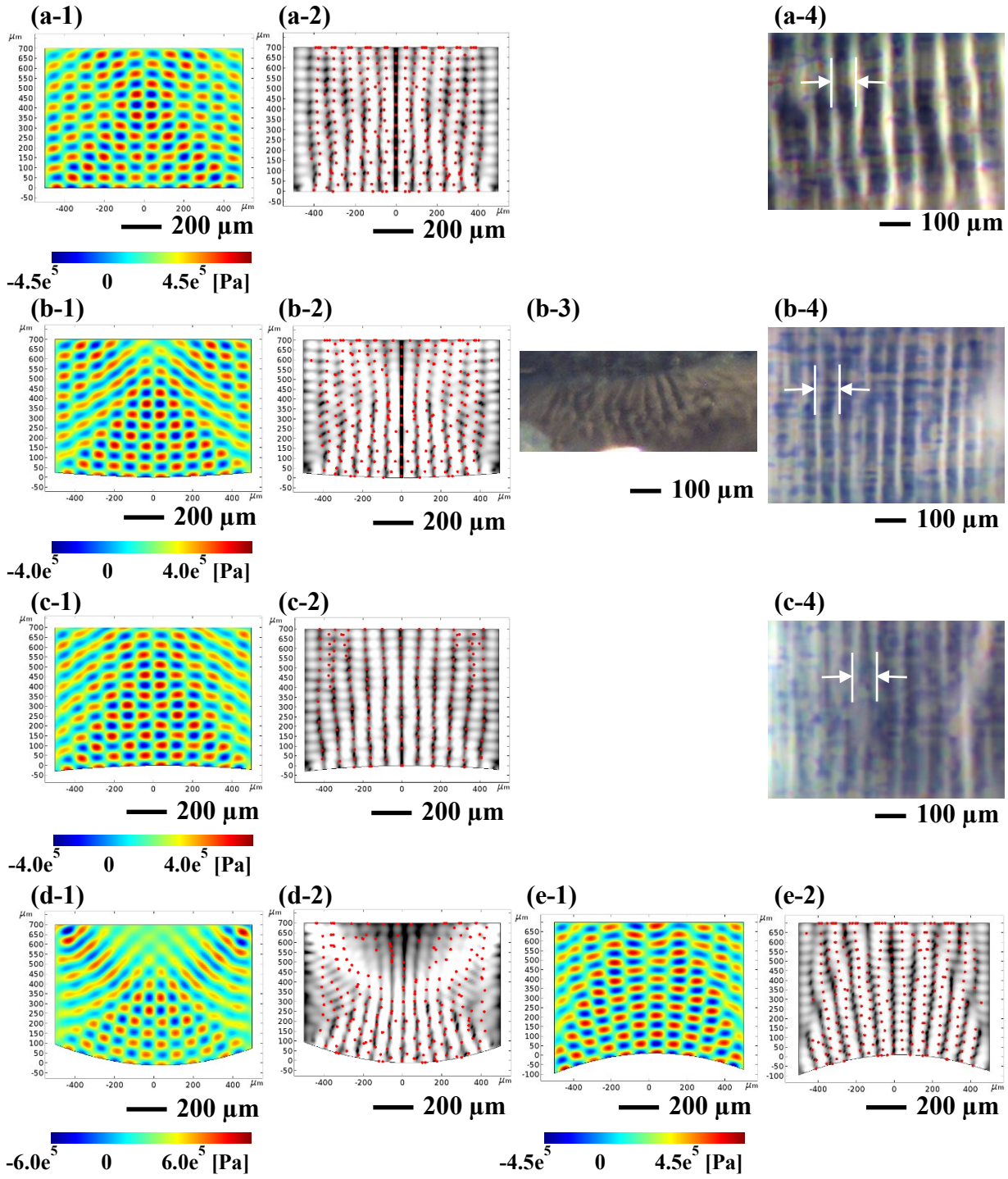

Figure 6.5 Patterning of microparticles on SAW device (Al plate substrate) with frequency f_A0 = 17.00 MHz (a) flat, (b) concave $\mathcal{K}$ = 200 m^{-1}, (c) convex $\mathcal{K}$ = -200 m^{-1}, (d) concave $\mathcal{K}$ = 800 m^{-1} and(e) convex $\mathcal{K}$ = -800 m^{-1} simulation of (1) acoustic pressure (Pa), (2) particle alignment from cross-sectional view after 10 s and experimental particle alignment from (3) cross-sectional and (4) top views.

Figures 6.6(a) to 6.6(g) summarise the comparisons of the simulation data for the line distances and slopes through the width of the microchamber at the top (Figure 6.6(a) and 6.6(c)) and at the halfway up from the surface of the SAW device (Figure 6.6(b) and 6.6(d)), for both the concave and convex geometries, respectively.

For the concave geometries, the line distances at the two sides of the microchamber are relatively smaller than those in the middle width at the of the microchamber (Figure 6.6(a)). Halfway up from the surface of the SAW device (Figure 6.6(b)), the trends of the distances are nearly the same with the trends in the top of the chamber however, there is a large jump in the line distance value at the middle of the chamber for the two smaller concave curvatures.

For the convex geometries, the line distance trends at the top of the chamber depends on curvature and geometries of the SSAW device (Figure 6.6(c)). For the smaller convex curvature, the line distance in the sides of the microchamber is larger than those in the middle of the microchamber while for the larger convex curvature, the trends are opposite to the smaller curvature one. Whereas halfway up from the surface of the SAW device (Figure 6.6(d)) the line distances in the sides of the microchamber are larger than those in the middle of the microchamber i.e., contrary to the results for concave geometry at the top of the chamber.

Figures 6.6(e) and 6.6(f) summarise the comparisons of the line distances of the experimental data from the top view through the width of the chamber for concave and convex geometries, respectively. The line distances are nearly constant for the flat device. For the concave geometries, the line distances at the two sides of the microchamber are smaller than those in the middle however, the difference is very subtle between line distances in the side and in the middle. Whereas for the convex geometry, the trends are reversed, i.e., the line distances at the sides of the microchamber are larger than those in the middle of the chamber. The experimental results show the same trends as those from the simulation results shown in Figure 6.5.

Figure 6.6(g) shows comparison of the slopes of the particle pattern lines on concave geometry of Device 2, using the resonant frequency of R0 (details given in Table 4.1). It is shown on all the concave geometries, the particle pattern lines are convergent towards the centre of the curvature of the geometry but on the convex geometry, the particle pattern lines are divergent with a slope away from centre of the curvature of the geometry.

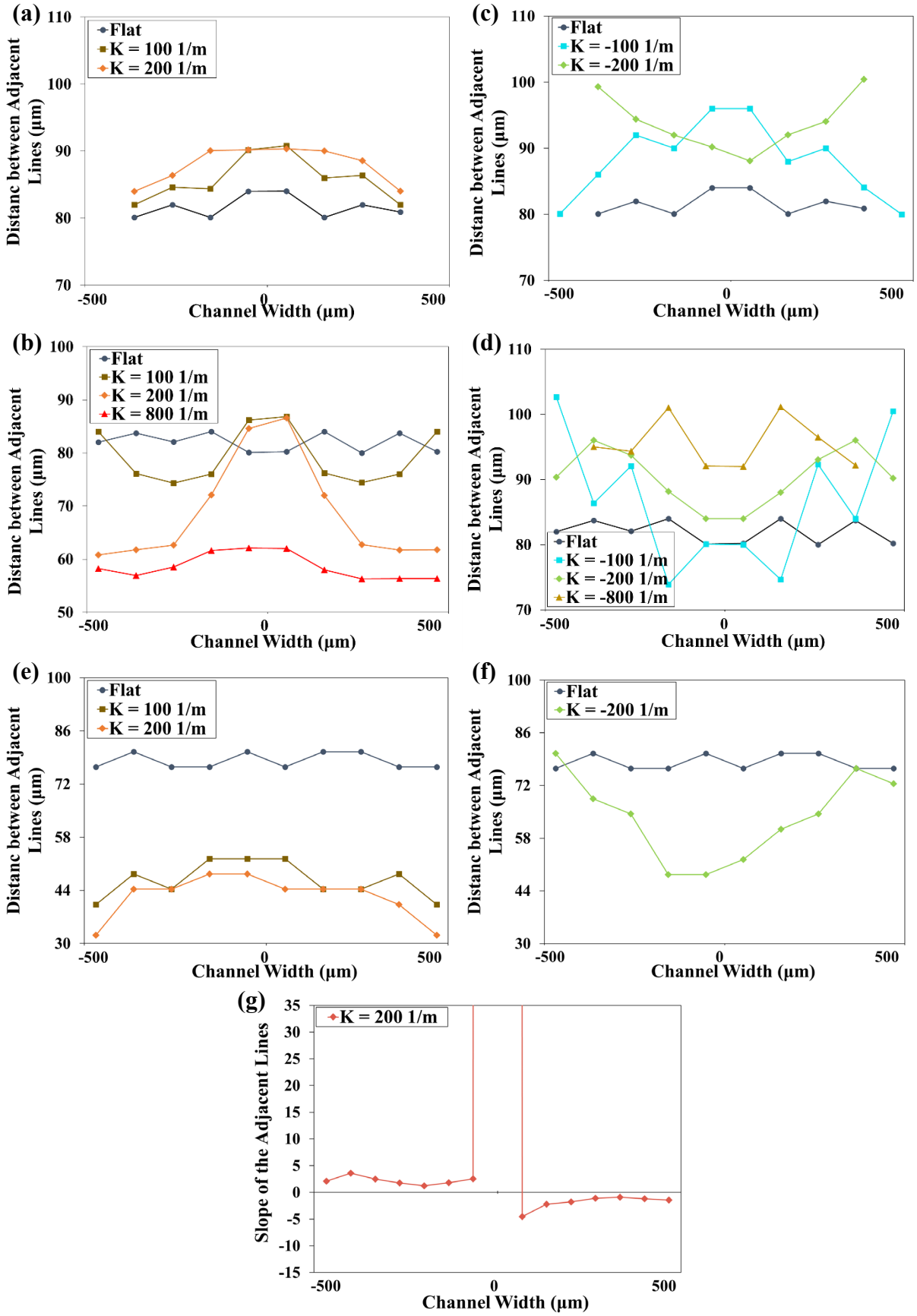

Figure 6.6 Comparison of the line distances (a) at the top of the chamber; (b) half way up from the surface of the SAW device for concave geometries; (c) the top of the chamber; (d) half way up from the surface of the SAW device for convex geometries, all simulation results from cross-sectional view; (e) concave; (f) convex

geometries, experimental data from top view; (g) the slope of pattern lines for concave geometry from cross-sectional view.

6.5 Yeast Particle Manipulation Using Flexible Thin Film SAW Devices

Yeast cells were patterned on different concave geometries using both Devices 1 and 2, and the top and cross-sectional views of examples for the yeast particle patterning are shown in Figure 6.7. Similar to those of the microparticles, these yeast particles can be patterned at the pressure nodes of the acoustic pressure field in lines which are convergent as clearly seen from the cross-sectional views. It was shown that using these flexible SAW devices, it is possible to manipulate and pattern biological cells despite their large size variations and their strong tendency to adhere to each other. In literature, a lot of studies [9, 27, 28, 30, 31] have shown that SAW manipulation is biocompatible, which will conserve cell viability and proliferation with minimal or insignificant change of the cells' functionality. It was reported that after SAW manipulation the cells remained alive and were able to reproduce and function normally even after a day [9, 27]. SAW manipulation was proved to cause no significant damage to the cell's physiology [28]. It was shown that if low voltages are used for SAW manipulation, there are minimal effects on the cell's viability. However increased voltages should be used with caution as it may affect cells' viability adversely [30, 31]. So will be possible to design and build different flexible acoustofluidic systems such as flexible acoustic cell tweezers, flexible acoustic microparticle/cell sorters and even flexible enrichment setups using these flexible/bendable SAW devices.

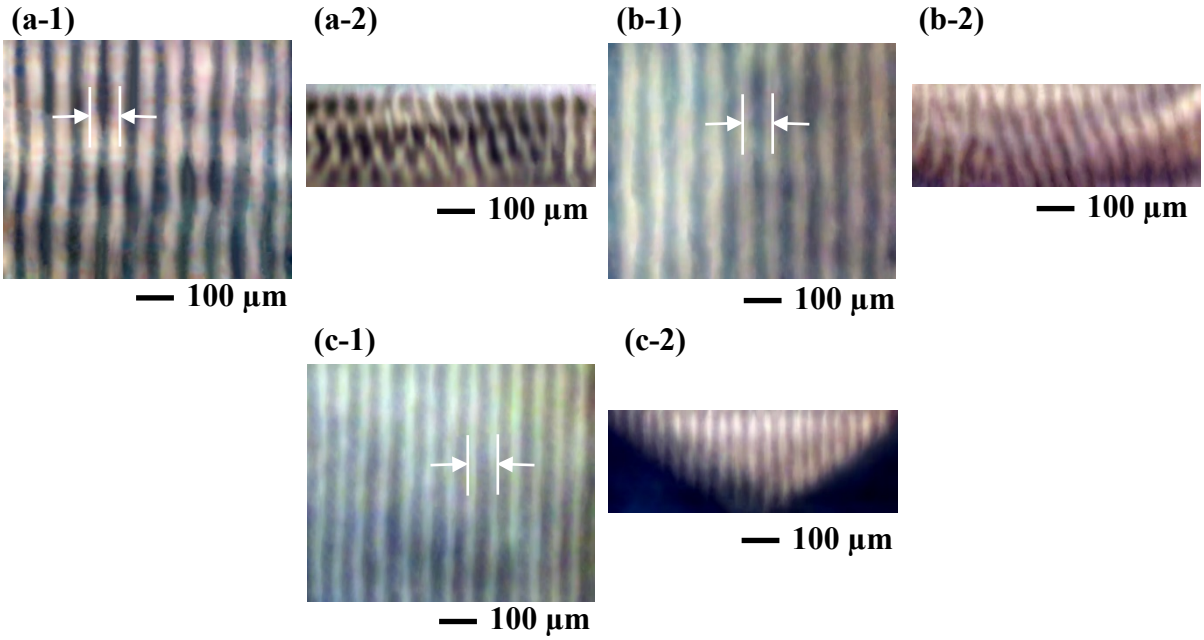

Figure 6.7 Yeast cell patterning on ZnO thin film on Al substrate flexible SAW device (a) concave $\mathcal{K}$ = 200 m^{-1} foil substrate, (b) concave $\mathcal{K}$ = 200 m^{-1} plate substrate and (c) concave $\mathcal{K}$ = 800 m^{-1} plate substrate (1) top view and (2) side view.

6.6 Particle Patterning on a Twisted Flexible Thin Film SAW Device

In addition to being bent into various concave and convex surfaces, these flexible SAW devices can also be twisted in different geometries (e.g., with one illustration in Figure 6.1(d)). Twisting the SAW device actually changes the IDTs' positions from two parallel ones into two IDTs with an inclined direction and a twisting angle (compared with the similarly positioned chamber walls), but also each of IDTs has been bent into a shape with a curvature (see Figure 6.1(d)). Then the effects of different twisting-up geometries of the flexible SAW Device 1 on particle patterning were investigated. Different twisting geometries of the flexible SAW devices are shown in Figure 6.8.

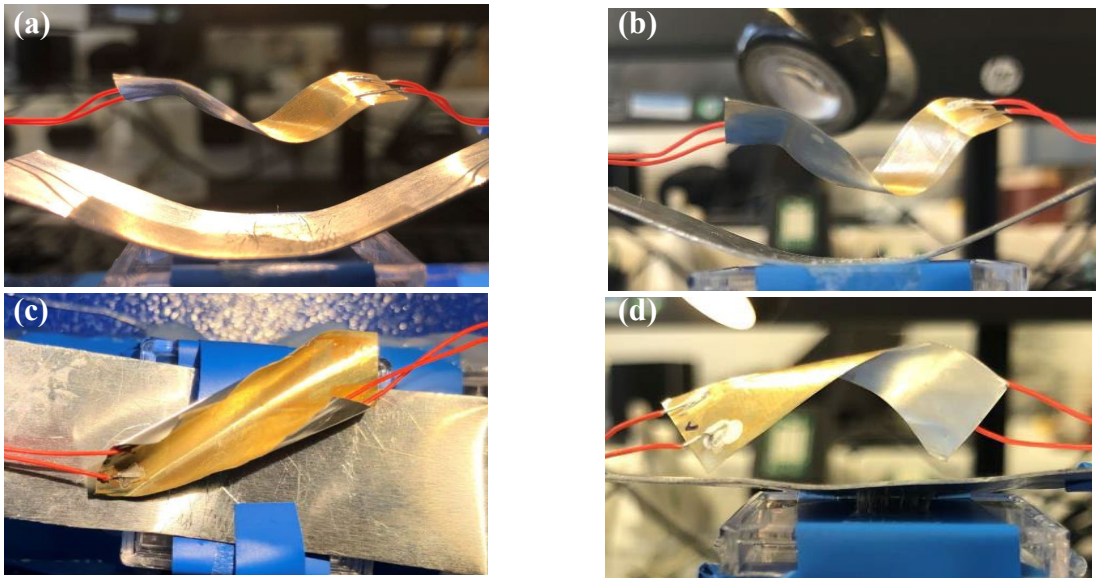

Figure 6.8 Different twisting conditions of Devices 1, (a) twisting angle 115°, (b) twisting angle 95°, (c) twisting angle 85° and (d) twisting angle -115°.

Figures 6.9(a) and 6.9(b) show two selected top view images of microparticle patterning when the flexible Device 1 was twisted up along 45 degrees from the original IDT directions, with twisting angles of (a) 115° and (b) 95°. They were all applied with the A0 mode to form SSAWs (the frequency details are given in Table 4.1). The IDT directions in these two cases are indicated as shown in Figure 6.9(a) and 6.9(b).

The microparticles were found to be patterned into regularly distributed lines which are parallel to the deformed IDTs of the SAW device for all the different twisting geometries. It can also be observed that with the increase of twisting-up curvatures, the lines are inclined but still in parallel to the IDTs, although there are imperfected lines formed, probably due to the

significantly bent and inclined two IDTs (see Figure 6.9(b)). It was also observed that the width of each line is quite broad, due to the deformed and bent IDTs.

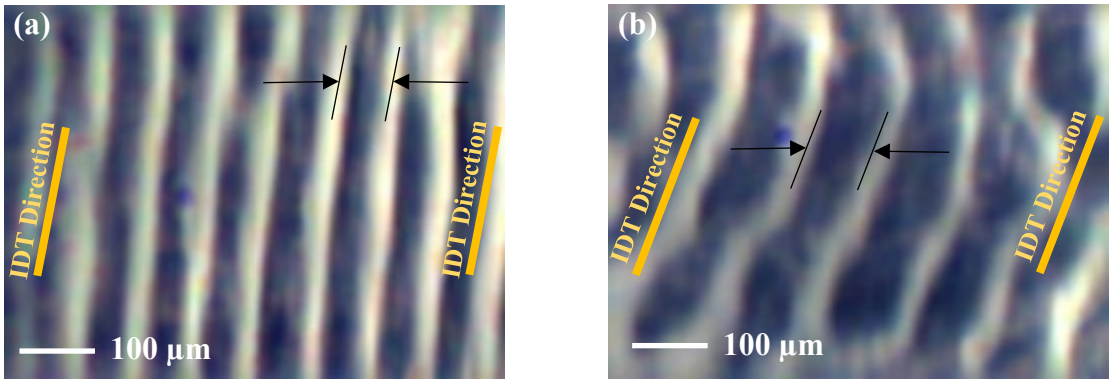

Figure 6.9 Patterning of silica microparticle patterning on twisted ZnO thin film on Al foil substrate flexible SAW device with frequency f_A0 = 13.00 MHz and (a) twisting angle 115°, (b) twisting angle 95° and for a microchamber parallel to the IDTs from the top view.

6.7 Summary

In this chapter, the acoustofluidic behaviour of flexible SAW devices with various vibration modes was investigated and the effects of different bending curvatures and twisting geometries of these flexible SAW devices on patterning of microparticles and cells in a microchamber were studied.

Bending the flexible SAW devices in concave geometries results in the particle pattern lines to become converged with a slope towards the centre of the curvature of the geometry. Significantly increasing the curvature of the concave geometries will result in the alignment of particles approximately parallel in the middle of the chamber. However, weak particle patterning is observed at the two sides of the microchamber due to the weaker SSAW field in these areas.

Bending the flexible SAW devices in convex geometries changes the distribution of particle pattern lines; they become diverged with a slope away from centre of the curvature of the geometry. For the convex geometries, increasing the curvature of the devices will cause a stronger pressure anti-node area near the middle of the microchamber which will drive the particles away from these areas. With further increase in the curvature of the convex geometries, a weaker SSAW field acoustic pressure node area forms in the middle of the chamber near the top, and the particles accumulate there with low patterning efficiency.

For the concave geometry, particle alignment is more efficient near the surface of the Lamb wave device. Whereas, for the same convex geometry, for the Rayleigh wave device the

patterning is more efficient at the top of the chamber, mainly because of the efficiency of wave energy dissipation into the liquid to form SSAWs.

Particle patterning was performed on twisted SAW devices which resulted in changes to the IDTs positions from original flat and parallel ones to those with an inclined direction at a twisting angle. In these cases, the microparticles patterned into lines parallel to the twisted IDTs for each twisting geometry.

Chapter 7. SAW-Based Particle Manipulation inside Glass Microtubes

7.1 Introduction

Conventional acoustofluidic platforms are comprised of microfluidic and acoustic elements such as SAW devices [5, 7]. These platforms have been utilized for biocompatible, and contact-free manipulation, patterning, sorting [9, 44, 69] and separation [4, 10, 25, 29] of microparticles and biological cells, in various chemical and biomedical applications including cell studies [32], cancer diagnosis and tissue engineering [3, 6-8, 33].

Microtubes have also been integrated with acoustic devices and used to manipulate [105, 106], deform [107], trap [108-111] enrich [112, 113], align [114], arrange [115], focus [116], pattern [117] and separate [118] microparticles and biological cells. For applications such as cell studies and continuous flow systems to trap and focus microparticles.

Microtubes can potentially substitute conventional microchannels and become integrated with SAW devices either without fluid flow or in a continuous flow application for manipulating microparticles and cells. However, various patterns generated by using different cross-sections of microtubes and positioning the tubes at different directions compared with the electrode directions have not been systematically studied. Moreover, the published work is focused only on rigid and brittle $LiNbO_3$ SAW devices for enriching [112], aligning [114], and patterning [117] microparticles and cells without addressing flexible thin film SAW devices, which have advantages such as high SAW speed and great piezoelectric and mechanical qualities [51] as well as potential applications in flexible microfluidic platforms, body conforming wearable devices, flexible sensors and electronics as well as soft robotics [16, 52, 53].

In this chapter, the patterning and alignment of microparticles inside glass microtubes using a ZnO thin film-based flexible SAW device and microtubes with circular or rectangular cross-sections was systematically studied at different microtube positioning relative to the direction of the IDTs, as illustrated in Figure 7.1. Experiments were performed to study the particle patterning inside microtubes with different cross-sections using three different sizes of rectangular (Figure 7.1(a-1)) and one circular (Figure 7.1(b-1)) microtubes. The effects of positioning the microtubes on the SAW device at different angles in relation to the IDTs were also investigated. Additionally, both the rectangular and circular microtubes were used in a continuous flow setup (Figures 7.1(a-2) and (b-2)) and studied the effects of different flow rates

on the particle patterning and alignment inside the tube. A computational model of the microtubes were developed to explain the observed particle patterns.

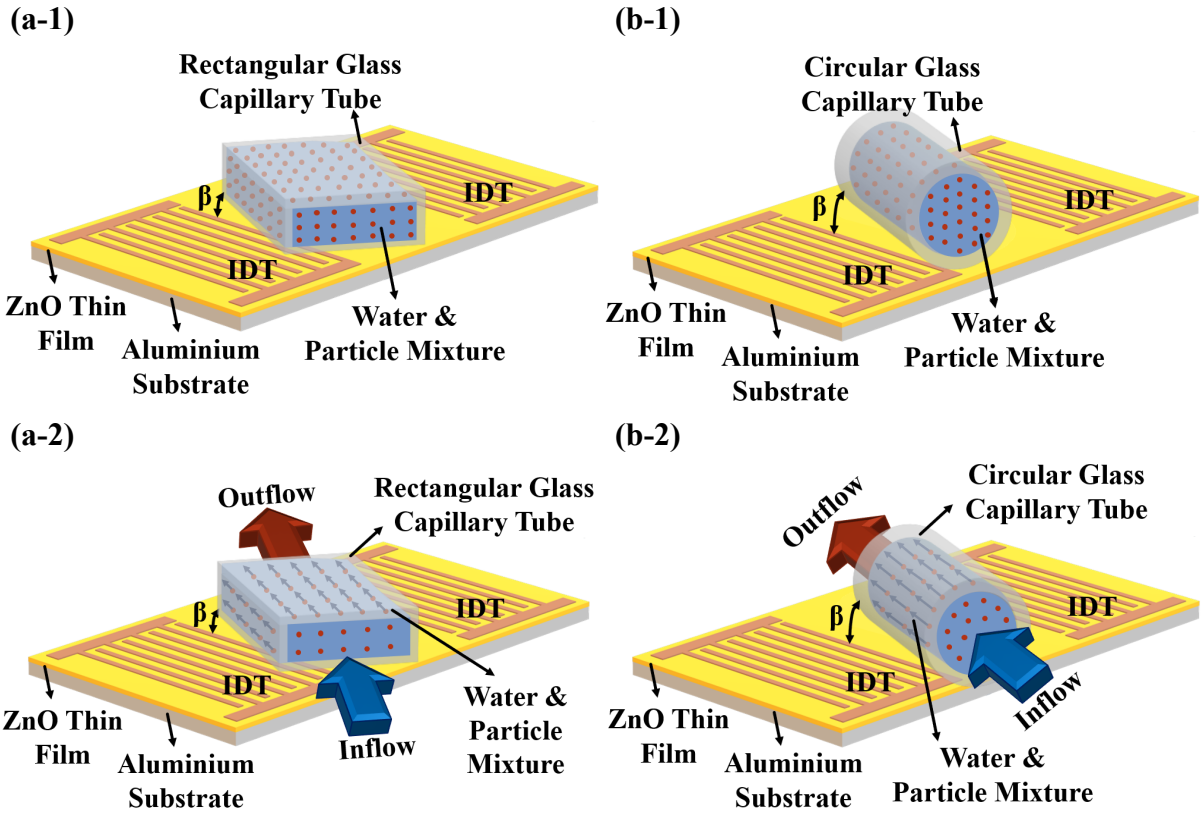

Figure 7.1 Schematic of particle patterning inside glass microtube with (a) rectangular and (b) circular cross-section with an incline angle regarding the direction of IDTs; (1) without flow and (2) with continuous flow in the microtubes. To transfer the wave energy from the SAW device into the glass tube, a water droplet of ~1.0 µL was added under the tube.

7.2 Numerical Modelling

In order to study the acoustic field inside the microtubes with circular or rectangular cross-sections placed on ZnO thin film-based flexible SAW device at different angles in relation to the IDTs, the setup was computationally modelled. The modelled geometry and mesh are shown in Figure 7.2 where a three-dimensional model of the glass microtube filled with water and placed on the SAW device was modelled for the geometry. Discretization of the computational domain was done using ~130,000 and ~250,000 elements for rectangular and circular tubes, respectively. For both microtube geometries, rectangular and circular, mesh dependancy analysis was performed which resulted in selecting a computational grid with minimised effects on the solution whitin a reasonable computational time.

The acoustic fields which was generated inside the microtube and the water filling the tube were modelled using the Helmholtz equations (i.e., Equations (2-22) and (2-23)). The SSAW

propagating on the surface of the SAW device which was placed under the microtubes was modelled with the oscillating wall boundary condition (i.e., Equations (3-16) and (3-17)). The behaviour of the glass microtubes under the effects of the SSAWs was modelled with Hooke's Law with free surface boundary conditions applied to all surfaces. To predict the behaviour of the whole three-dimensional system, it is important to correctly model what happens at the fluid-solid interfaces, where the vibration of the solid surface affects the fluid and the acoustic pressure field inside the fluid causes a pressure effect on the solid surface. In these acoustofluidic systems, the acoustic waves cause movement of the solid parts, which in turn causes the propagation of sound waves into the fluid. Thus, a two-way coupling was employed between the microtube and the water inside to simulate the fluid-solid interfaces. This correctly models how the vibration of the solid components (i.e. the structural acceleration) influences the fluid and how the acoustic pressure field inside the fluid exerts a pressure (i.e. load) effect on the solid parts [145].

FEM was used to discretize the governing equations and Newton's iterative method was used to solve the system of equations. All the solutions were converged with 10^{-6} criteria.

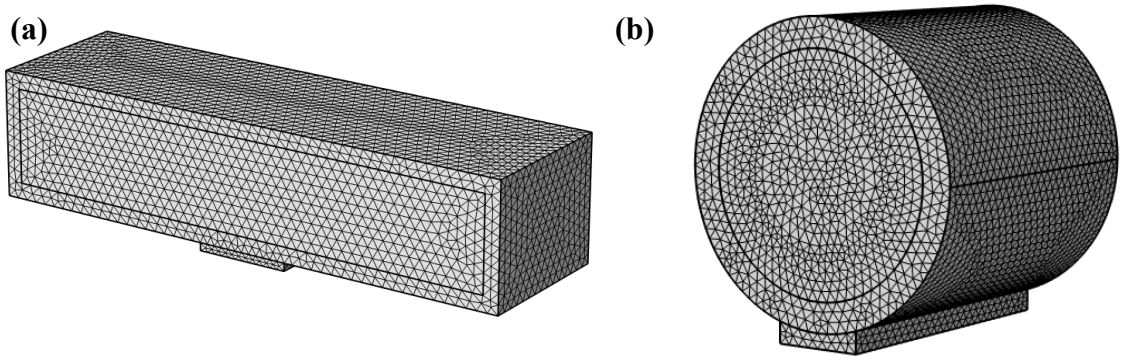

Figure 7.2 Geometry and computational mesh for (a) rectangular, and (b) circular microtubes.

7.3 Particle Patterning inside Glass Microtubes with Rectangular Cross-sections

The experimental results of particle patterns inside a rectangular glass microtube (dimensions: 3.5 mm × 0.8 mm) placed at different angles with respect to the alignment of the IDTs are presented in Figure 7.3. When the rectangular glass tube is parallel to the IDTs (Figure 7.3(a-1)), the particle pattern lines are also parallel to the IDTs. When the rectangular glass tube is at an angle β (shown in Figure 7.3(b-1):15°, (c-1):30°, (d-1):45°, (e-1):60°, (f-1):75° and (g-1):90°) with respect to the alignment of the IDTs, the particle pattern lines are also at an angle which is nearly the same as β to the IDTs (i.e., parallel to the tube walls). The particles were observed which show checker-board patterns, which are normally formed by the particles at the bottom of the tubes (Figures 7.3(a-2) to (g-2)).

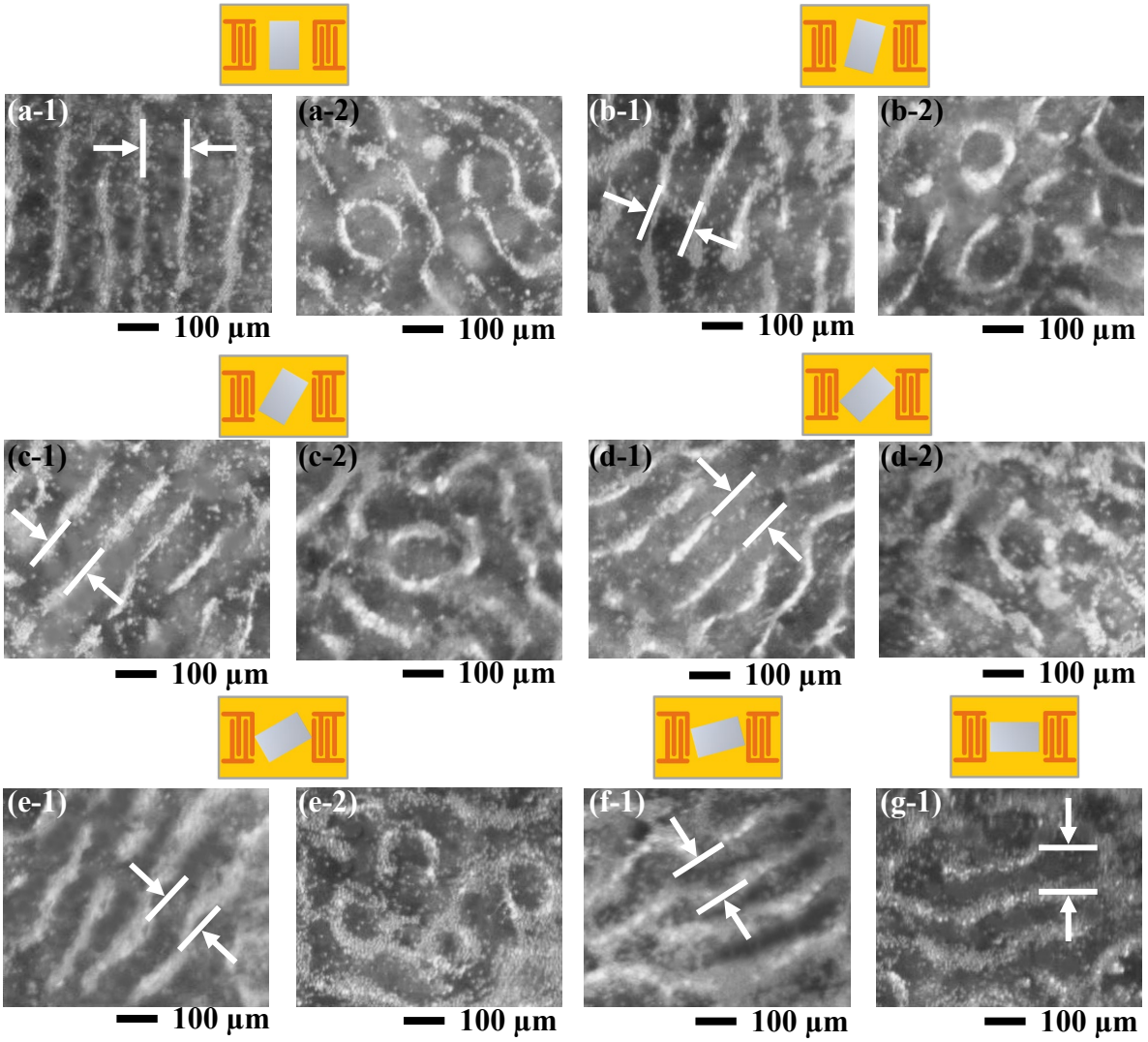

Figure 7.3 Particle patterning inside the rectangular glass microtube with 3.5 mm × 0.8 mm dimensions placed (a) parallel, with (b) 15°, (c) 30°, (d) 45°, (e) 60°, (f) 75° and (g) 90° incline angle relative to the IDTs, experimental data from top view shows particles (1) patterning parallel to the tube walls and (2) forming Lamb wave patterns, with 13.12 MHz frequency.

The particles showed the same patterning behaviours in experiments using another rectangular glass microtube 4.5 mm × 1.0 mm dimensions. The results are similar as shown in Figure 7.4 which showed similar behaviour to Figure 7.3.

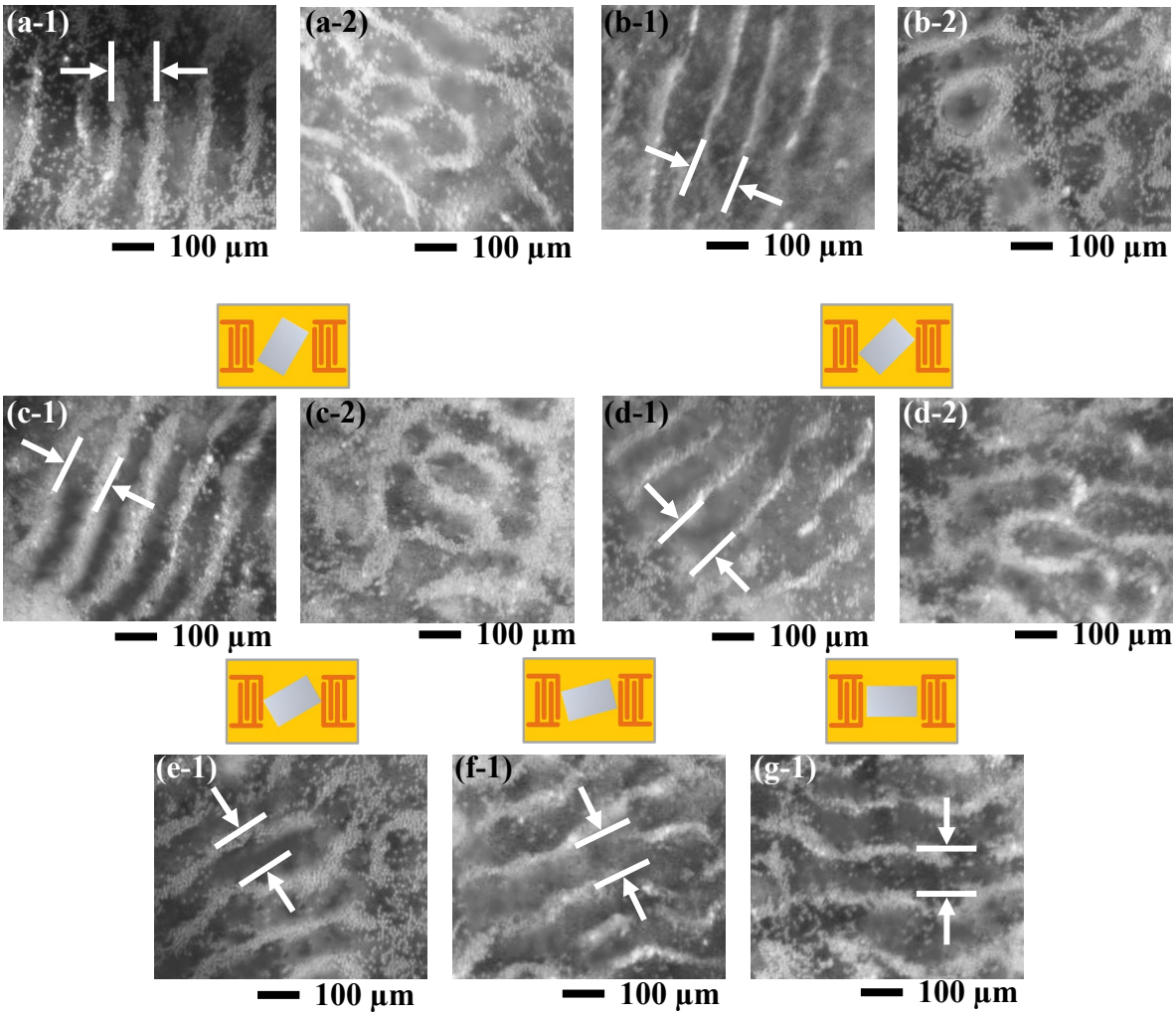

Figure 7.4 Particle patterning inside the rectangular glass microtube with 4.5 mm × 1.0 mm dimensions placed (a) parallel, with (b) 15°, (c) 30°, (d) 45°, (e) 60°, (f) 75° and (g) 90° incline angle relative to the IDTs, experimental data from top view shows particles (1) patterning parallel to the tube walls and (2) forming Lamb wave patterns, with 13.12 MHz frequency.

The above experimental results of particle patterning inside rectangular glass tubes (Figure 7.3 and 7.4) show there are two types of particle patterning. Figures 7.5(a) shows the schematics of the mechanisms of wave and pattern formations. The first type of particle patterning is the line pattern parallel to the rectangular glass tube walls which is caused by the standing wave field inside the rectangular glass tube (see Figure 7.5(a)) formed due to propagation of the acoustic waves into the glass tube and their reflection from the tube walls. Particles were also observed to form checker-board patterns similar to those caused by the Lamb waves [164] (see Figures particle patterning inside rectangular glass tubes (Figure 7.3 and 7.4). These patterns are formed at the bottom of the rectangular glass tube, because the SAWs from the substrate are transferred into the glass tube, forming Lamb waves at the bottom wall of the tube due to the superstrate effect [165].

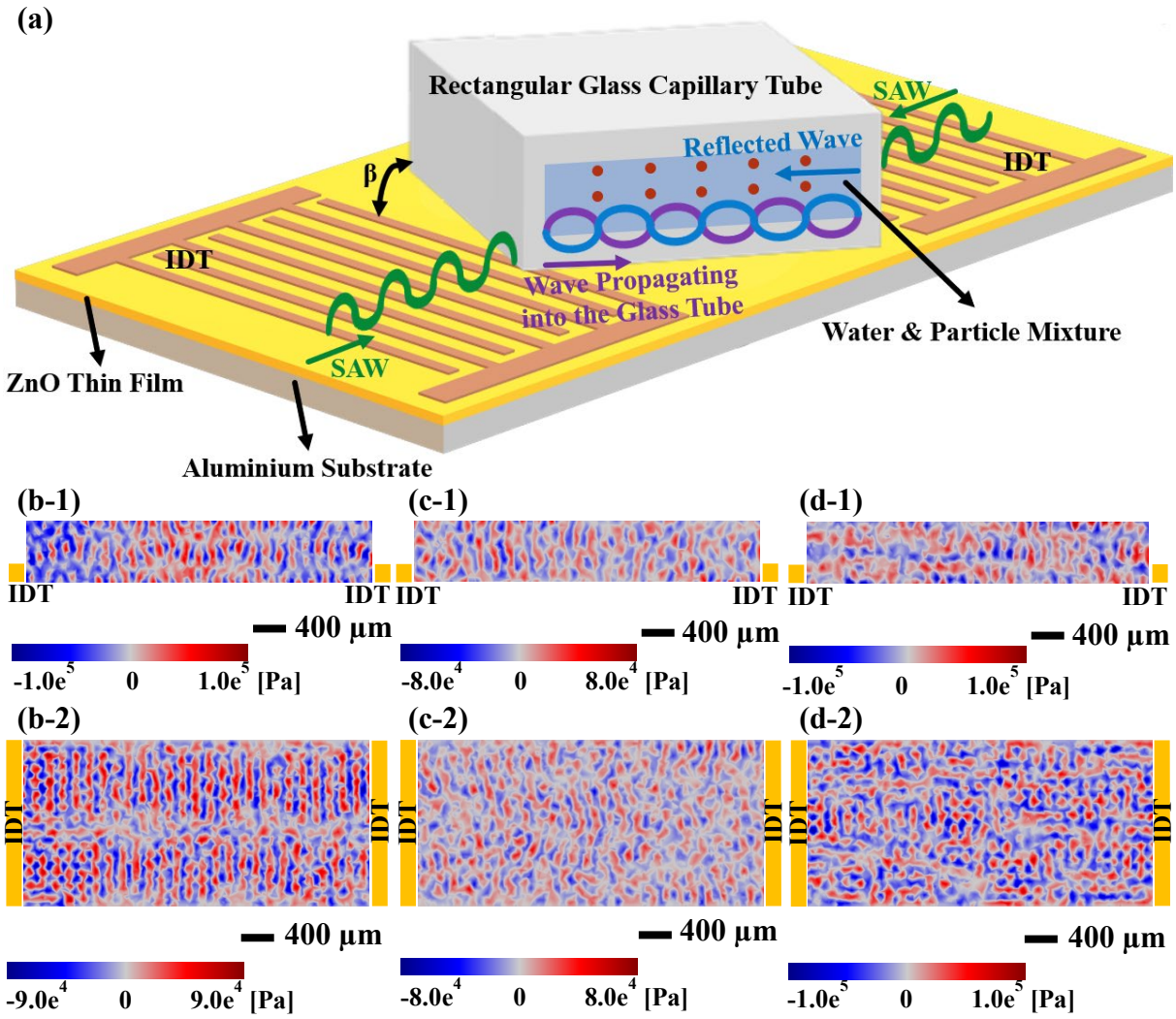

Figure 7.5 (a) Schematic of the particle patterning inside rectangular glass microtube resulted from different wave formations inside the glass. The simulation results of the acoustic pressure field (Pa) inside the water for a microtube placed (b) parallel, with (c) 45°, and (d) 90° incline angle relative to the IDTs, (1) the cross-sectional and (2) top view.

Figures 7.5(b) to 7.5(d) show the simulation results of the acoustic pressure field inside the liquid when the angle β is equal to (a) 0°, (b) 45°, and (c) 90° and from (1) cross-sectional and (2) top views. From Figures 7.5(b-1), 7.5(c-1) and 7.5(d-1) it can be seen that the pressure node lines are mainly vertical and parallel to the side walls of the rectangular microtube for 0°, 45°, and 90°, respectively (see the yellow circle in Figures 7.5(b-1), 7.5(c-1) and 7.5(d-1)).

For β = 0°, Figure 7.4(a-1) can be compared with Figure 7.5(b-2) to show that pattern lines are parallel to the side walls of the rectangular microtube in both experimental and simulation results (see the yellow circle in Figure 7.5(b-2)). Comparing Figure 7.4(d-1) with Figure 7.5(c-2) for β = 45° and Figure 7.4(g-1) with Figure 7.5(d-2) for β = 90°, it can be observed that as the angle between the glass tube and the IDTs increases, the pattern lines remain perpendicular to the side walls of the tube in both simulation and experiment (see the yellow circle in

Figures 7.5(c-2) and 7.5(d-2)). The simulations results show good agreement with experimental data.

7.4 Particle Patterning inside Glass Microtube with Circular Cross-section

Figure 7.6 shows the images of particle patterns that were generated inside circular glass microtubes placed at different angles compared to the direction of the IDTs. When the circular glass tube is at an angle β equal to (a) 0°, (b) 30° and (c) 45° compared to the direction of the IDTs, the particle pattern lines are at an angle β to the IDTs (parallel to the tube walls) near the bottom of the tube (see Figure 7.6(a-1), 7.6(b-1) and 7.6(c-1)). At the middle of the tubes with the above different angles (see Figure 7.6(a-2), 7.6(b-2) and 7.6(c-2)), the particle pattern lines are perpendicular to the tube walls (i.e., at an angle which is equal to 90-β to the IDTs). For a circular glass tube which is placed with an angle β equal to (d) 60° to the IDTs, the pattern lines are also perpendicular to the tube walls (see in Figures 7.6(d)). When the circular glass tube is placed (e) perpendicular to the IDTs, the pattern lines are parallel to the IDTs and perpendicular to the tube walls (Figure 7.6(e)).

It can be seen from Figure 7.6 that the particle pattern lines which are parallel to the tube walls are relatively shorter and have a relatively larger distance between them (e.g., Figure 7.6(b-1)), whereas the particle pattern lines which are perpendicular to the tube walls are relatively longer with smaller distances between them (e.g., Figure 7.6(b-2)).

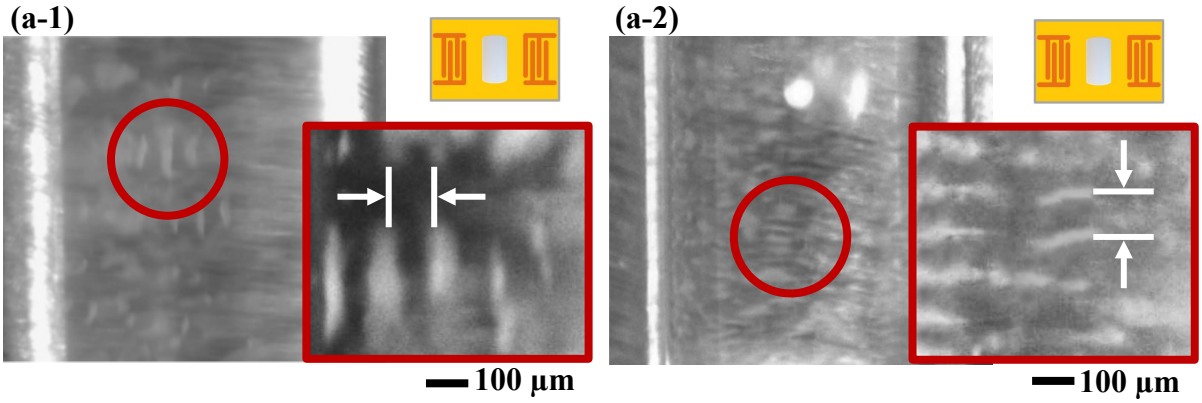

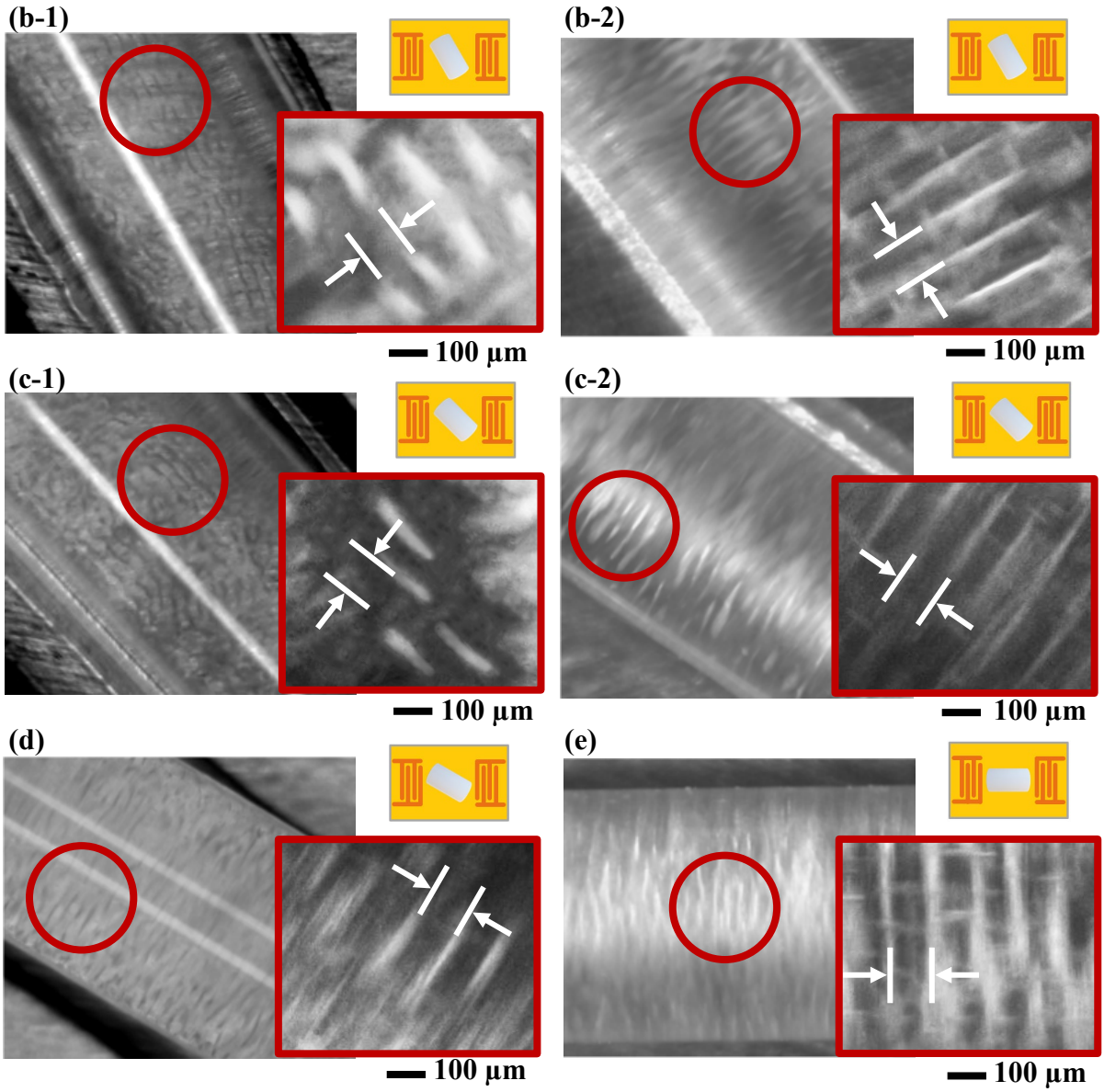

Figure 7.6 Particle patterning inside the circular glass microtube with 1 mm diameter which is placed (a) parallel, with (b) 30°, (c) 45°, (d) 60° and (e) 90° incline angle relative to the IDTs, experimental data from top view shows particle patterning (1) parallel and (2) perpendicular to the tube walls, with 13.12 MHz frequency.

The above experimental results of particle patterning inside circular glass tubes (Figure 7.6) clearly show there are two different types of particle patterning. The first one is that the pattern lines are parallel to the glass tube direction, and the second one is that the pattern lines are perpendicular to the tube direction. Both of these patterns are formed because the SAW energy from the substrate is transferred into the glass tube from each side which results in the generation of a complicated acoustic wave field inside the circular glass tube.

Figure 7.7(a) presents a schematic illustration of the acoustic wave formation inside the glass tube. Figures 7.7(b) to 7.7(d) show simulation images of the acoustic pressure field inside the water for a circular microtube which is placed at (a) 0°, (b) 45°, and (c) 90° and from (1) cross-

sectional view, and top view (2) near the bottom, and (3) at the middle of the glass tube, respectively. The simulations results show good agreement with experimental data.

When the two surface acoustic waves propagate from the SAW device into the glass tube, a standing acoustic wave forms in the glass tube. This acoustic wave then transfers its energy into the water which will cause the patterning of the particles (see Figure 7.7(a)).

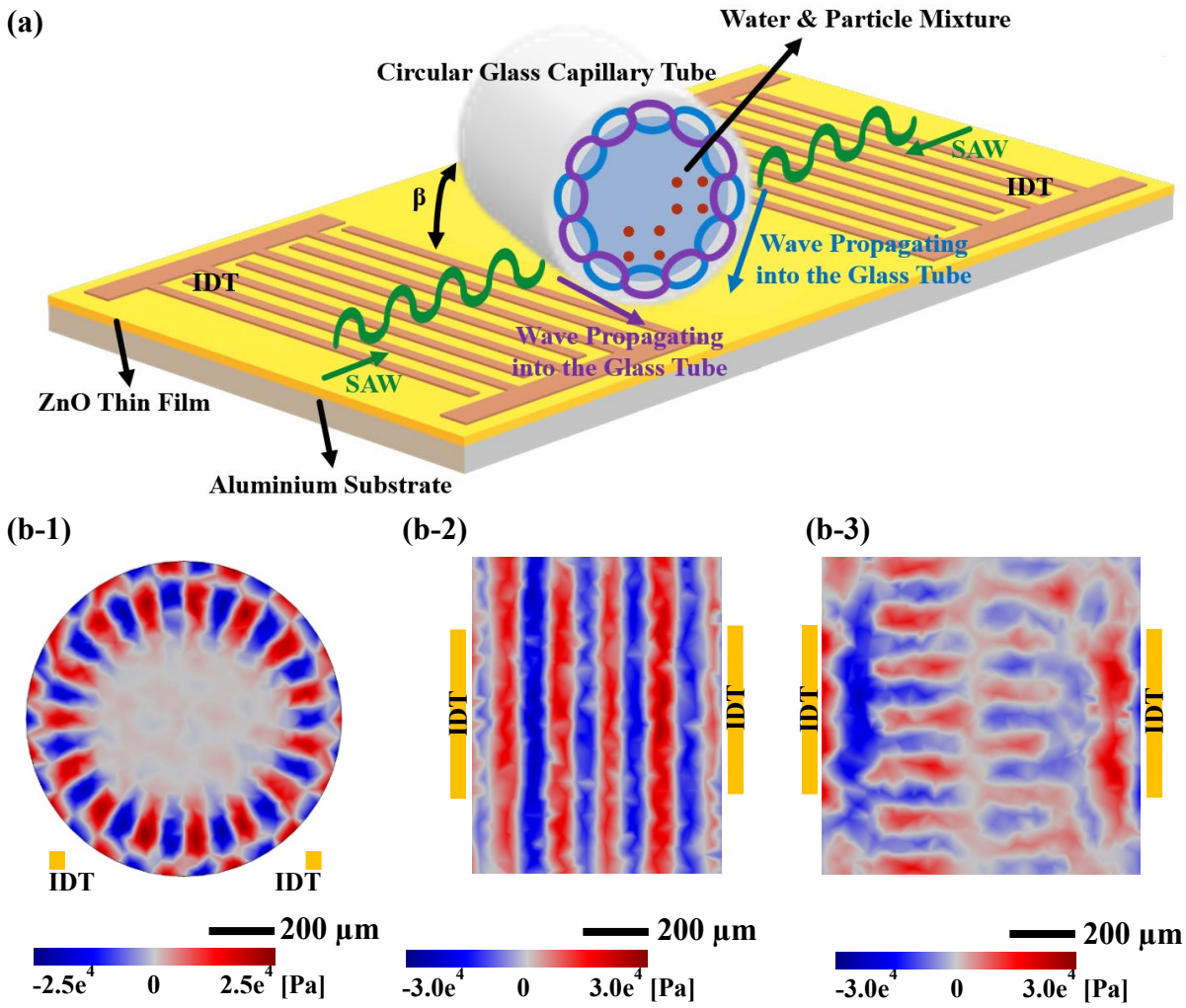

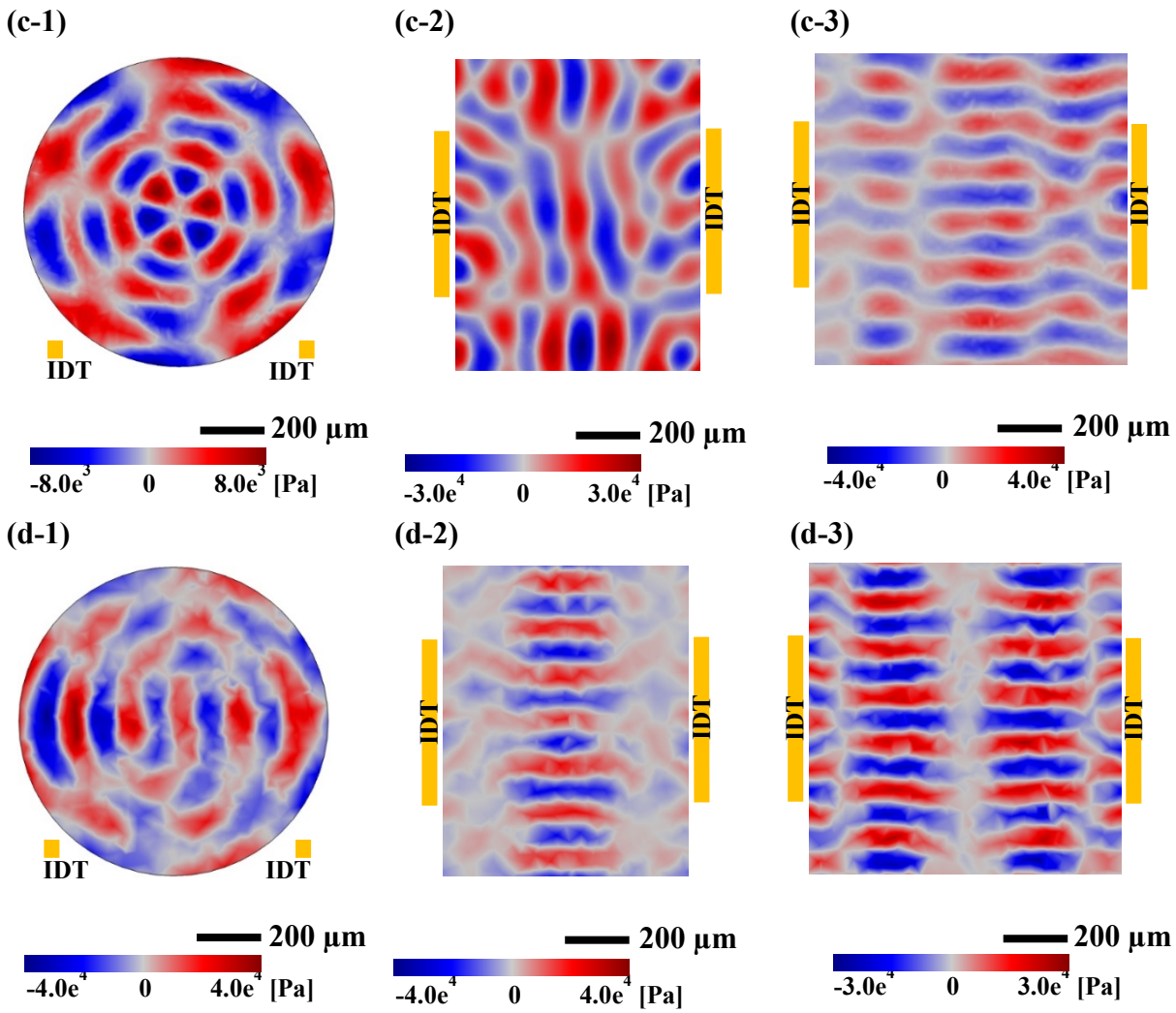

Figure 7.7 (a) Schematic of the particle patterning inside circular glass microtube resulted from different wave formations inside the glass. The simulation results of the acoustic pressure field (Pa) inside the water for a microtube placed (b) parallel, with (c) 45°, and (d) 90° incline angle relative to the IDTs, (1) the cross-sectional view, (2) top view at the bottom of the tube and (3) top view at the middle of the tube.

For $\beta \leq 45°$, near the bottom of the tube (see Figures 7.7(b-2) and 7.7(c-2)), the waves that propagate into the water generate a standing wave along the direction of the tube. This results in the pressure nodes to be parallel to the tube direction, thus causing the particles to be patterned in lines parallel to the glass tube direction. For $\beta = 0°$, Figure 7.7(b-2) can be compared with Figure 7.6(a-1) to see that in both experimental and simulation results, there are pattern lines at the bottom of the tube parallel to the direction of the microtube. Whereas, at the middle of the tube (see Figures 7.7(b-3) and 7.7(c-3)), the standing wave propagates around the circular cross-section of the glass tube and is perpendicular to the direction of the tube and thus the pressure node lines are perpendicular to the tube direction resulting in particle patterning parallel to the tube walls. Figures 7.7(b-3) and 7.6(a-2) both show pattern lines perpendicular to the direction of the tube occurring at the middle height of the tube for $\beta = 0°$ in simulation and experiment, respectively.

For $\beta > 45°$, a standing wave is generated perpendicular to the direction of the tube at whole depth of tubes and the particles are patterned vertically to the tube walls. Comparing Figures 7.7(d-2) and 7.7(d-3) with Figure 7.7(g-2), it can be observed that pattern lines are perpendicular to the direction of the in both simulation and experiment for whole depth of the tube.

Figure 7.8 compares the measured average (a) distances between the particle line patterns inside the (1) rectangular and (2) circular tubes from both experiments and simulations and (b) line pattern angles regarding the direction of the IDTs.

It can be seen from Figures 7.8(a-1) and 7.8(a-2) that for the circular tube, the particle pattern lines which are parallel to the tube walls have a larger distance between them compared to the particle pattern lines which are perpendicular to the tube walls. In addition, the distances between particle pattern lines inside the rectangular tubes is closer to the distances between particle pattern lines that are perpendicular to the circular tube walls which can be observed in the simulation results as well. One reason for this difference can be attributed to the radial formation of the pressure nodes in the cross-section of the circular tube. This results in the increasing distance between the pressure node lines from the middle of the tube to the bottom of the tube. The simulations results show good agreement with experimental data. Figure 7.8(b) shows the measured average angles between the particle line patterns inside the glass tubes and the direction of the IDTs, which shows that for the rectangular tubes the particle pattern lines are parallel to the tube walls and for the circular tube, the particles pattern in lines either parallel to the glass tube direction or perpendicular to it depending on the position of the particles along the height of the tube.

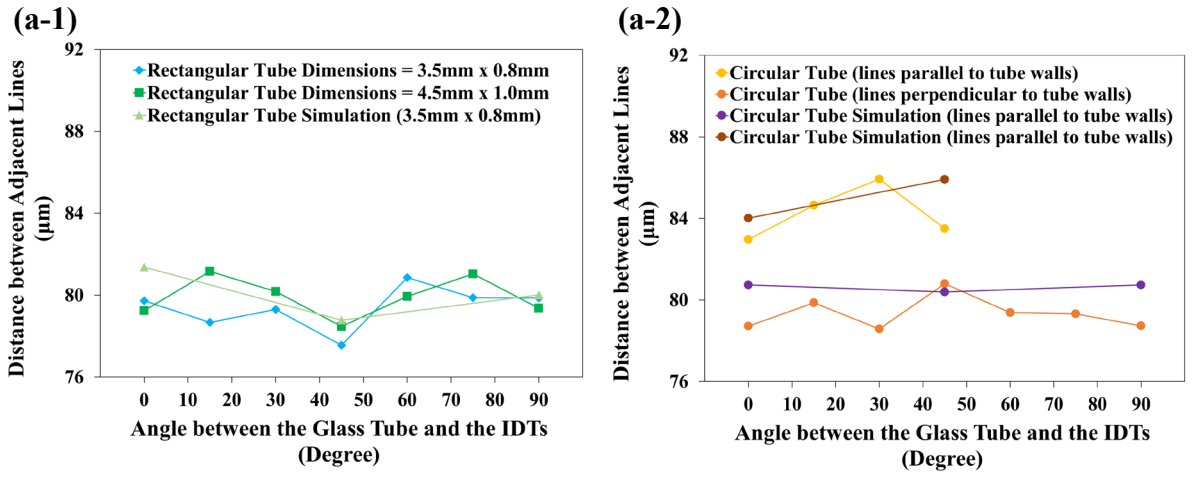

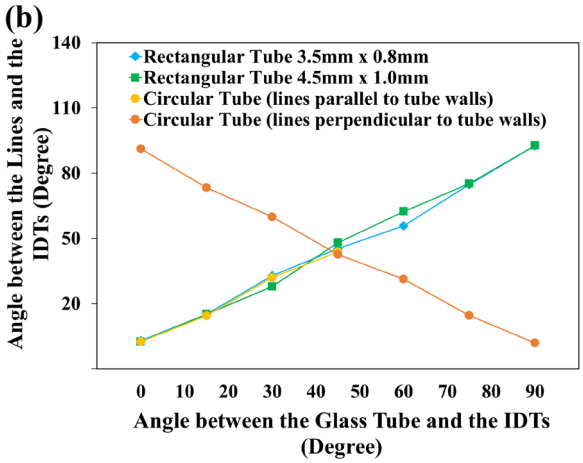

Figure 7.8 Comparison of (a) the distance between two adjacent patterns inside (1) rectangular and (2) circular glass microtubes and (b) the angle between the lines and the IDTs for circular and rectangular glass tubes with 13.12 MHz frequency.

7.5 Particle Patterning inside Glass Microtubes with Continuous Fluid Flow

Particles were patterned inside rectangular (dimensions: 2.3 mm × 0.5 mm) and circular glass microtubes with various fluid flow rates. The obtained experimental results are shown in Figures 7.9 and 7.10, respectively.

Figure 7.9 shows that the particles are patterned and flow in lines parallel to the walls of the rectangular glass microtube for (a) 0°, (b) 30°, (c) 60°, and (d) 90° incline angle relative to the IDTs, with flow rate of (1) 0.2 μL/s, (2) 0.1 μL/s, (3) 0.05 μL/s, and (4) 0.01 μL/s. When the flow velocity is large enough (e.g., Figure 7.9(a-1)), the pattern lines which are parallel to the tube direction (also flow direction) are smooth and enhanced. Whereas previously observed checker-board-type patterns are mostly removed due to the large flow rates. Decreasing the flow rate from to 0.2 μL/s (e.g., Figure 7.9(a-1)) to 0.01 μL/s (e.g., Figure 7.9(a-4)) will cause the particle pattern lines to become rough and then gradually change into the checker-board-type patterns, which is caused by the Lamb waves [53] propagation at the bottom wall of the tube due to the superstrate effect [54].

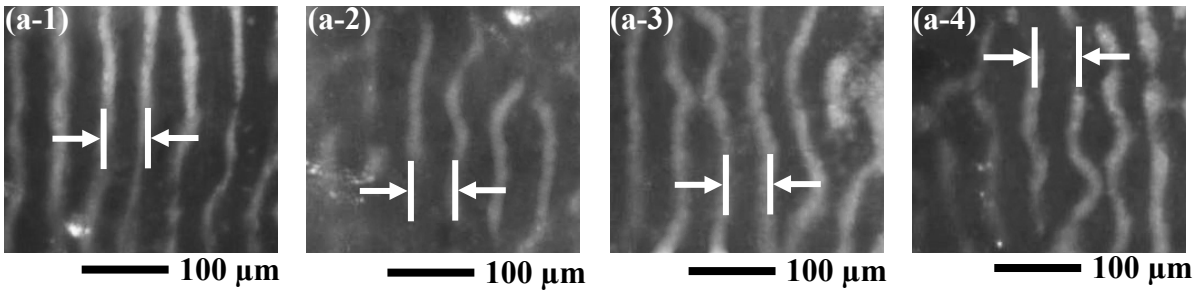

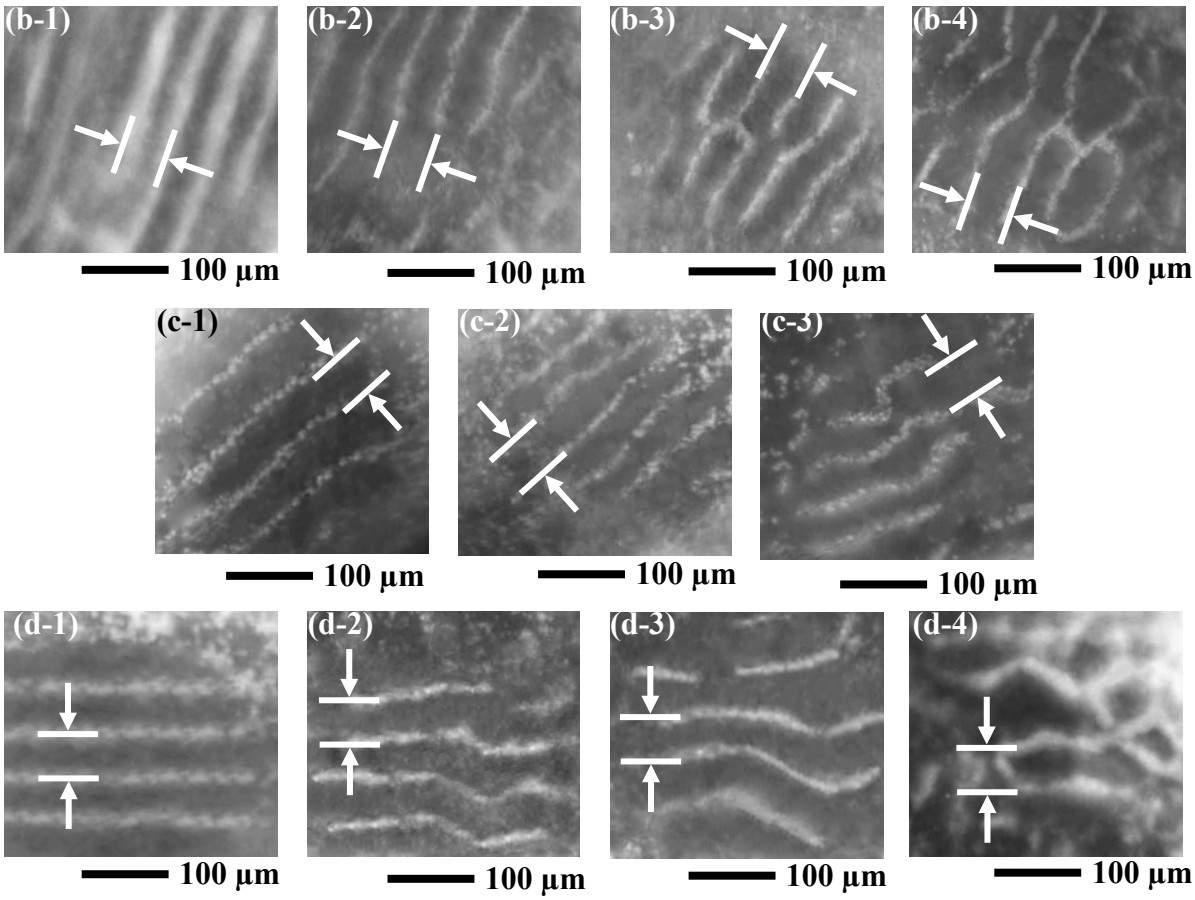

Figure 7.9 Particle patterning in inside the rectangular glass microtube with 2.3 mm x 0.5 mm dimensions which is placed (a) parallel, with (b) 30°, (c) 60°, and (d) 90° incline angle relative to the IDTs, in continuous flow setup with flow rate of (1) 0.2 µL/s, (2) 0.1 µL/s, (3) 0.05 µL/s, and (4) 0.01 µL/s; experimental data from top view and with 13.12 MHz frequency.

Figure 7.10 shows the experimental images of particle patterning inside the circular glass microtube for (a) 0°, (b) 30°, (c) 45°, (d) 60°, and (e) 90° incline angle relative to the IDTs, with flow rate of (1) 0.2 µL/s, (2) 0.1 µL/s, (3) 0.05 µL/s, and (4) 0.01 µL/s. It can be observed from Figure 8 that the flowing particles still form linear patterns parallel to the direction of the flow inside the circular tube. With a large flow rate (e.g., Figure 7.10(a-1)), the pattern lines which are perpendicular to the tube direction are removed by rapid flow and only the pattern lines which are parallel to the tube direction (also flow direction) remain and form smooth lines. When the flow rate is decreased (e.g., Figure 7.10(a-4)), the particle pattern lines become curved and rough.

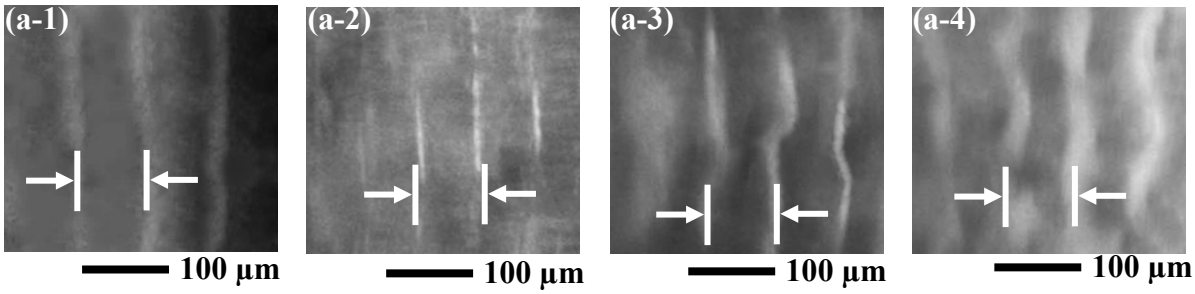

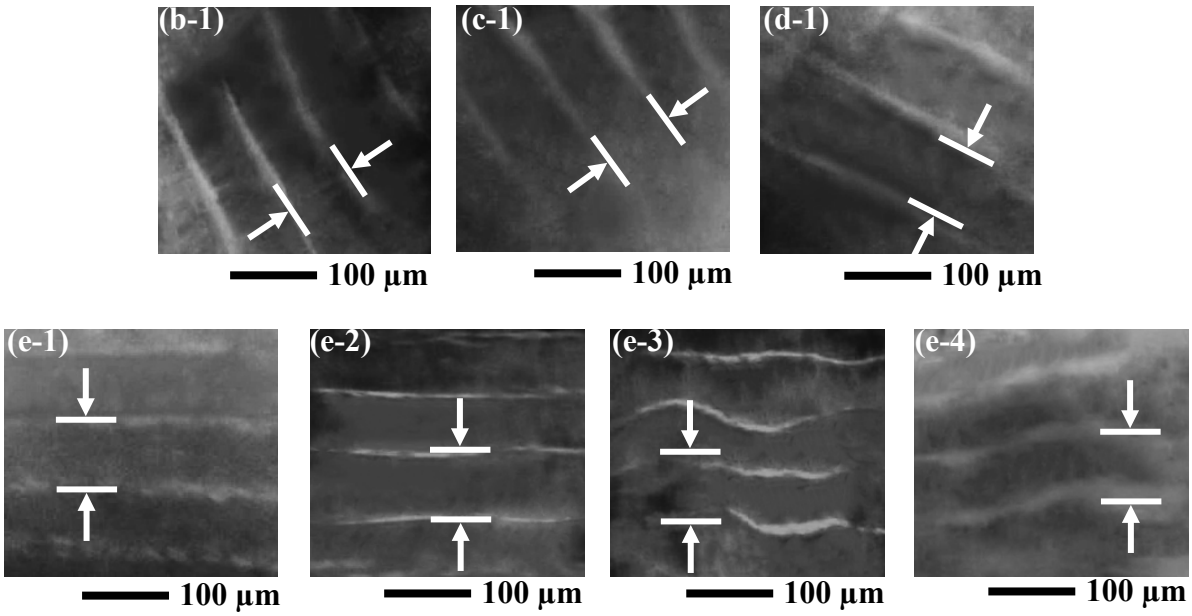

Figure 7.10 Particle patterning in inside the circular glass microtube with 1.00 mm diameter which is placed (a) parallel, with (b) 30°, (c) 45°, (d) 60°, and (e) 90° incline angle relative to the IDTs, in continuous flow setup with flow rate of (1) 0.2 µL/s, (2) 0.1 µL/s, (3) 0.05 µL/s, and (4) 0.01 µL/s; experimental data from top view and with 13.12 MHz frequency.

Figure 7.11 compares the measured average distances between the particle line patterns inside the (a) rectangular and (b) circular tubes with various flow rates. Figure 7.11(a) shows that the average distance between the adjacent particle pattern lines in the rectangular glass tube is nearly equal to the half of the wavelength in the liquid and is not changed by changing the flow rate. Comparing Figures 7.11(a) and 7.11(b), it can be seen that for the circular glass tube, its distance between adjacent particle pattern lines is slightly larger than that in the rectangular case. However, this insignificant difference could be caused by the radial formation of the pressure nodes in the cross-section of the circular tube as previously discussed.

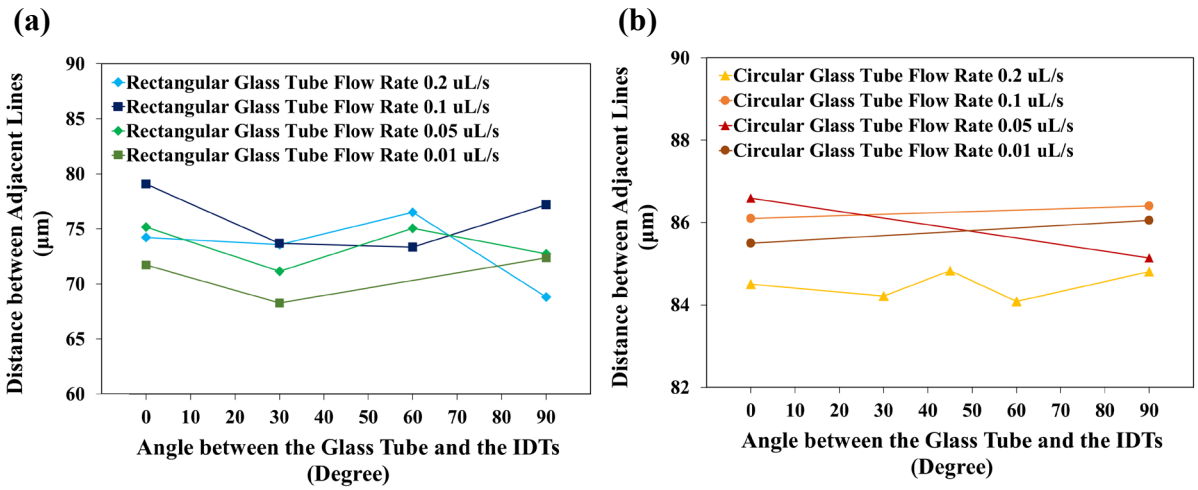

Figure 7.11 Comparison of the distance between two adjacent patterns inside glass microtubes for (a) rectangular and (b) circular glass tubes with 13.12 MHz frequency.

Choosing a proper combination of SAW device properties (frequency, wavelength, etc.), microtube geometry (shape, dimensions, thickness, etc.) and flow parameters will result in the formation of a desirable number of pressure node lines inside the microtube. Figures 7.12(a) and 7.12(b) show the simulation results of acoustic pressure field inside a rectangular glass microtube with dimensions of 0.2 mm × 0.2 mm and a circular glass tube with a diameter of 0.15 mm form (1) cross-sectional and (2) top views, respectively. It can be seen that in these two cases there is a single pressure node forming at the centre of the microtube which the particles/cells will be patterned on. A proper combination of the acoustic frequency with microtube geometry results in the generation of a desirable number of pressure node lines inside the microtube. This can be used in continuous flow systems to focus, pattern and separate microparticles/cells. In brief, these glass microtubes could show great potential to be used in acoustofluidics since they are low-cost, disposable, and simple to integrate in the setups.

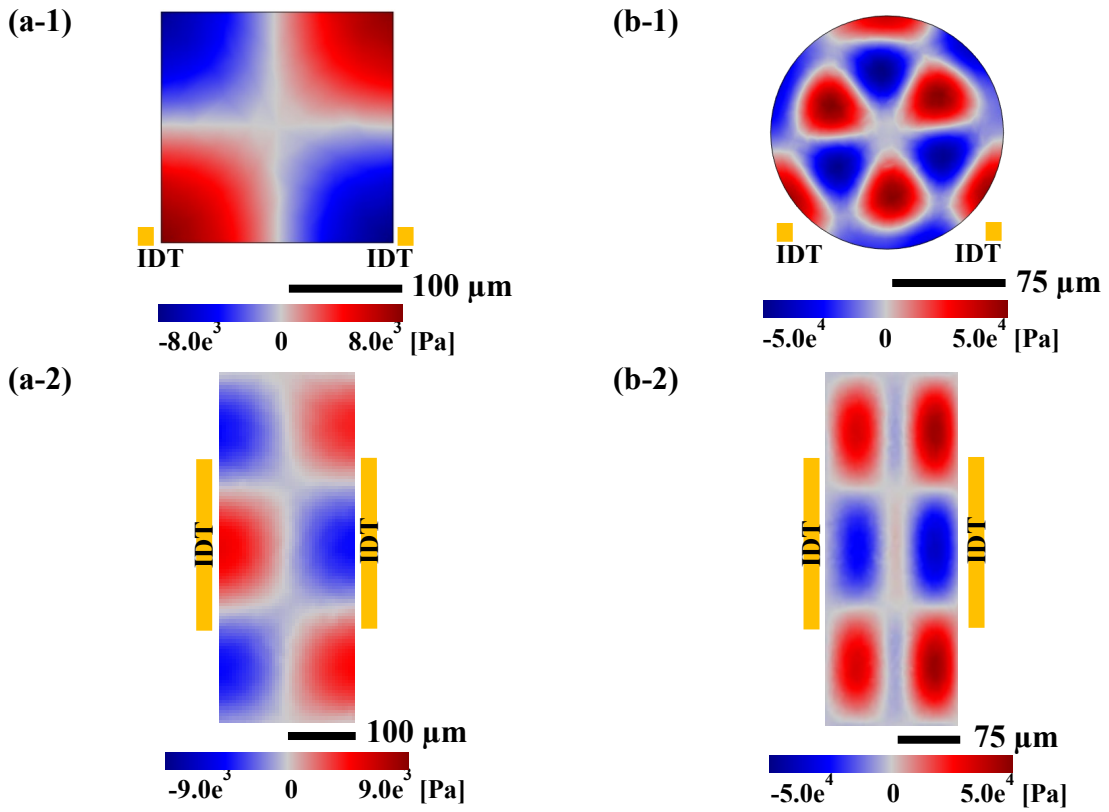

Figure 7.12 Simulation results of the acoustic pressure field (Pa) inside the microtubes with (a) rectangular and (b) circular cross-section from (1) cross-sectional and (2) top views with 13.12 MHz frequency.

7.6 Summary

In this chapter, the patterning and alignment of microparticles inside glass microtubes with and without flow were systematically investigated using ZnO on Al thin film SAW device. The effects of different cross-sections of the microtubes as well as their positions and relative angles

regarding to the directions of the IDTs were studied. For a rectangular glass microtube placed at an angle relative to the IDTs, particle pattern lines are parallel to the tube walls. This is resulted from the standing wave field generation inside the rectangular glass tube. The particles also seem to form some checker-board patterns at the bottom of the tube. For circular glass microtubes, different particles patterns can be observed which depends on their position along the tube's height. In the bottom of the tube, the particle pattern lines are parallel to the tube direction when the tube is placed at an angle in relation to the IDTs. The particle patterns are in lines parallel to the tube direction at the bottom of the circular glass tube, due to the acoustic wave propagation into the water and formation of a standing wave along the direction of the circular tube. Whereas, near the middle of the glass tube with a circular cross-section, the particle pattern lines are perpendicular to the tube direction with the tube positioned at an angle regarding the IDTs. When the circular glass tube is perpendicular to the IDTs, the pattern lines of the particles are parallel to the IDTs. The standing wave then propagates around the circular cross-section of the tube perpendicular to the tube direction and thus at the middle of the tube, the particles forms pattern perpendicular to the tube walls. The continuous fluid flow inside the rectangular and circular glass tubes causes the particles to form smooth line patterns parallel to the direction of the flow for all the angles and eliminates the other type of patterns.

Chapter 8. Integration of Acoustic Wave Devices with Wall-less Capillary Bridge Channels for Particle Manipulation

8.1 Introduction

As already mentioned in Chapter 2, continuous flow acoustofluidics have recently been successfully utilised for manipulating and controlling biological particles such as blood components [25-27], cancer cells [9, 28], bacteria [29], and other types of biological cells [30, 31, 44, 69, 73] while still conserving the cells' viability and proliferation. Most of these acoustofluidic platforms are based on fluid flow through microchannels made of solid or rigid materials such as PDMS [9, 25, 29, 44, 69], PMMA [99, 100], polystyrene [101-103] or glass [10, 63, 74]. Fabricating these microchannels often requires complicated and time-consuming processes such as soft lithography, cleanroom fabrication, milling, or injection moulding [4, 32]. To simplify the process and decrease the fabrication cost, wall-less microfluidic devices have been explored and developed [122-124]. Several types of capillary bridge systems have been developed to produce wall-less microfluidic platforms [124-132].

Capillary bridges are formed by filling fluids into the gap between two solid surfaces due to the fluid's surface tension [133]. The virtual side walls of these capillary bridge channels can be in contact with either air [124-126, 131, 132] or another liquid [122, 123, 128-130, 136]. In order to facilitate the fluid flow, these wall-less microfluidic setups often include a fluid guide which is either a flat surface [122-126, 131, 132] or an array of apertures [127-130] such as micro-rings [128], electrodes [129], or apertures which can inject and withdraw liquid into another fluid medium [130].

These capillary bridge channels have been integrated into various microfluidic systems for different purposes. However, there are not many previous studies that explore the integration of capillary bridge channels with acoustic components, especially using flexible thin film SAW devices. Here a new design strategy is proposed to use a capillary bridge channel combined with an acoustic wave generator in a continuous flow system: using either a PZT disk or a flexible thin film SAW device. In this study, the PZT disk setup is used to verify and demonstrate the principles of acoustic particle manipulation, whereas the flexible thin film SAW device is used for demonstrating the wide range performance of a flexible and wall-less continuous flow acoustofluidic setup for the purpose of particle and cell manipulation. Flexible thin film SAW devices show desirable features such as high power and efficiency, and good piezoelectric and mechanical qualities [51]. Additionally, their deformability offers great

potentials for flexible and wearable applications including surface conforming devices, soft robotics, flexible sensors, and electronics [16, 52, 53].

In this chapter, a wall-less capillary bridge channel formed between a thin polymer sheet (as the fluid guide) and a glass slide (as the wave guide) is explored for acoustic manipulation and alignment of particles and cells during their flow in the channel. The absence of sidewalls in this acoustofluidic setup provides a number of potential advantages. Firstly, the coupling of the solid microchannel with the acoustic field and fluid flow can be eliminated which could help the effectiveness of particle manipulation, simply because less acoustic energy is dampened in the solid materials. Secondly, the wall-less system is simple in design, easy to fabricate, and low cost, without a need for cleanroom manufacturing. Thirdly, it is easier to clean the wall-less channel and the channel is less likely to be blocked by particle/cells flowing inside.

Figures 8.1(a-1) and (a-2) illustrate 3D schematic views of the designed continuous flow channel based on an acoustofluidic capillary bridge integrated with (1) a PZT disk and (2) a SAW device. It comprises of a polymer strip at the bottom as the fluid guide and a glass microscope slide at the top as the wave guide. The liquid with particle/cell suspension enters the wall-less channel through an inlet hole, and flows along the path of the fluid guide, forming a capillary bridge channel between the fluid guide and the glass slide. The channel side walls are the two free surfaces of the fluid which are in contact with air at both sides (air-water interfaces). When the wave guide (glass slide) is driven by a PZT disk (as the acoustic wave source, in Figure 8.1(a-1)) or a flexible SAW device (as the source to generate a standing wave, in Figure 8.1(a-2)), sound waves are generated and propagate from the acoustic wave source to the wave guide (glass slide) and then dissipate their energy into the fluid. The formation of standing waves on the glass at the top of the channel is because the travelling waves propagate into the liquid and the waves reflected from the air-water walls of the capillary bridge channel (which propagates in an opposite direction) come across each other. The radiation force moves the particles/cells towards the pressure node lines of this standing wave-based acoustic field to form patterns inside the continuously flowing wall-less channel. Figures 8.1(b) and (c) schematically show the particle/cell patterning formed inside the capillary bridge channel from cross-sectional and top views, respectively. The particles/cells move towards the pressure nodes of the acoustic field and are patterned into lines inside the channel (Figures 8.1(b) and (c)). The fluid guide could, in principle, be designed with multiple outlets at the end of the channel (for example, three outlets in Figure 8.1(a)), so the particles/cells suspended in the fluid could be separated [9, 74]. In this wall-less acoustofluidic flow setup, acoustic waves

propagate in the wave guide (glass slide) and leak into the water in the capillary bridge, thus generating pressure node lines inside the channel and the particles are attracted to the pressure node lines as shown in Figures 8.1(b) and (c). The proposed wall-less continuous flow acoustofluidic setup could provide a great potential for contact-free manipulation including but not limited to patterning, guiding, sorting, filtering, and separating different particles and biological cells for biomedical applications.

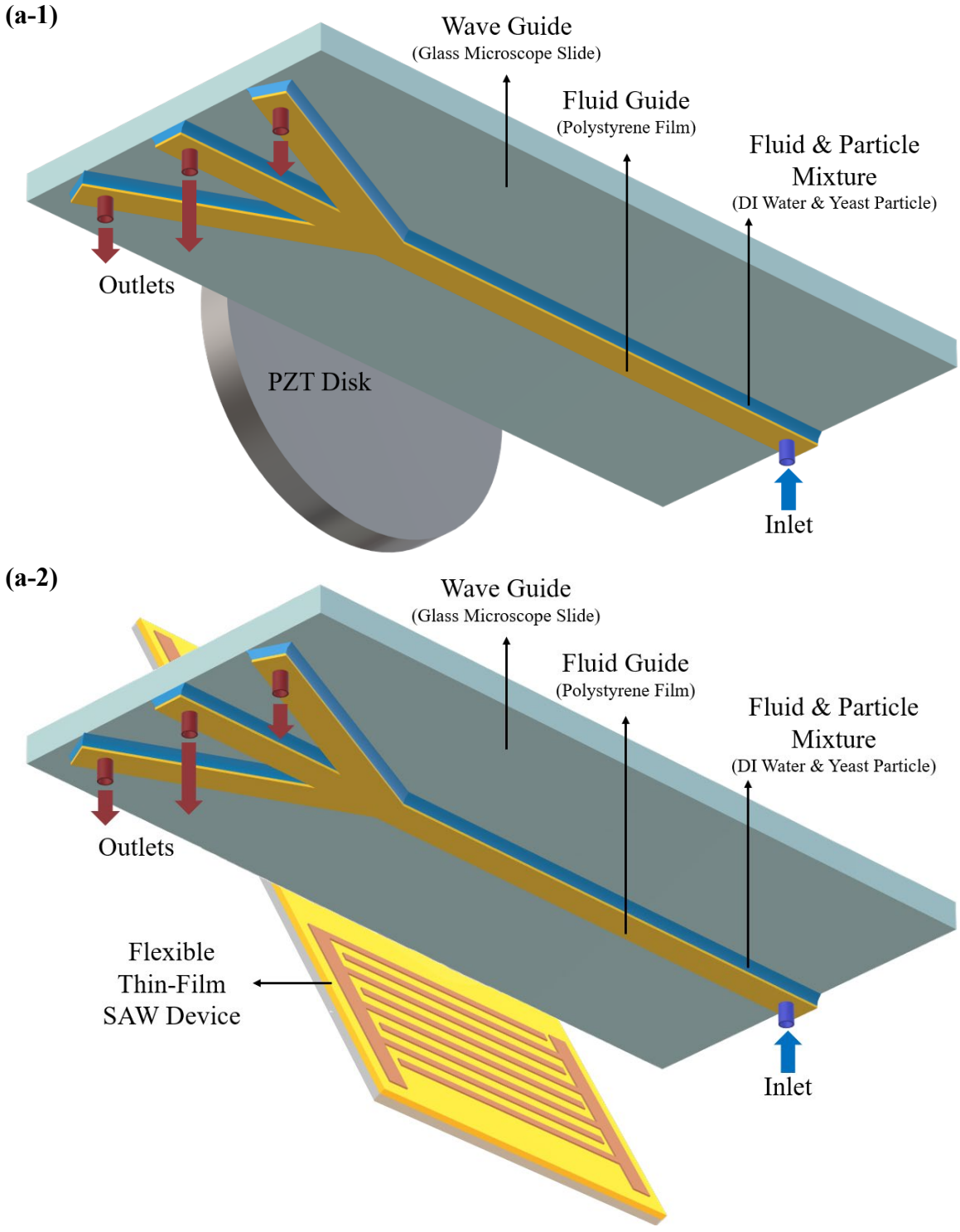

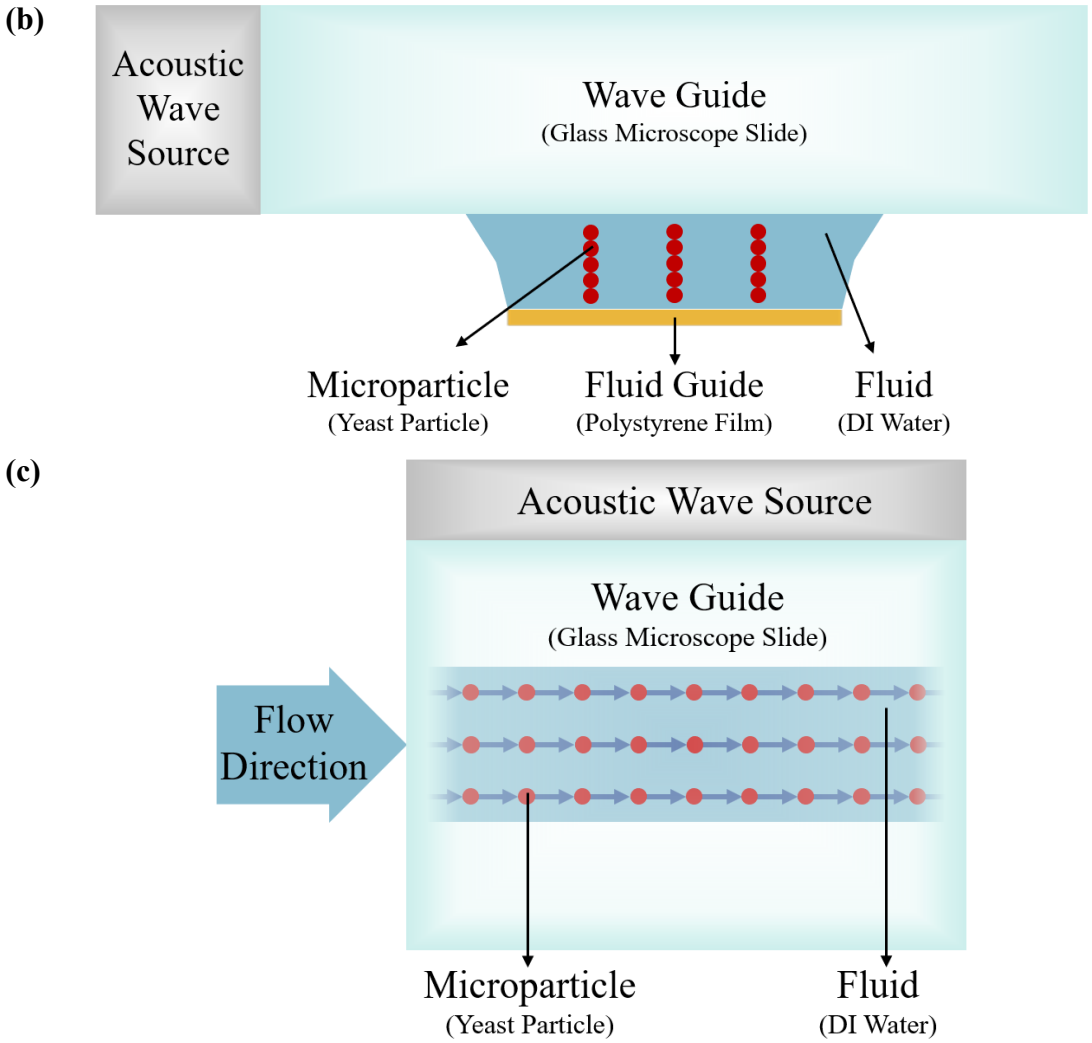

Figure 8.1 Schematic illustrations of the continuous flow capillary bridge acoustofluidic system (a) three-dimensional view of the components for (1) PZT setup, and (2) standing SAW device setup, (b) cross-sectional view, and (c) top view of particle patterning.

Based on the designs shown in Figure 8.1, in this chapter, the particle alignment and flow patterns were modelled and simulated, and the alignment of particles suspended in water at different frequencies and channel dimensions were experimentally and computationally investigated.

8.2 Numerical Modelling

To understand the details of the acoustic and fluid flow fields as well as the behaviours of microparticles under the acoustofluidic effects, the continuous flow capillary bridge system was numerically modelled. The results obtained from the simulations were then compared to the experimental data for the purpose of verification and explanation of the results.

The modelled geometry and mesh are shown in Figure 8.2, where the geometry was defined as a three-dimensional model of the acoustofluidic device including a PZT disk (Figure 8.2(a)) or a SAW device (Figure 8.2(b)), wave guide, fluid guide and the fluid inside the channel with their actual sizes. Discretization of the computational domain was performed using ~550,000 elements, including hexahedron elements for the wave guide, fluid, and fluid guide parts and tetrahedron and pyramid elements for the PZT disk. Mesh dependancy analysis was firstly performed in order to choose the best option for the computational grids with minimal effects on the solution while maintaing a reasonable computational time.

To simulate the multi-physics system including the piezoelectric effects, the solid mechanics, acoustic fields in the fluid, fluid flow and particle movement, different modelling approaches were used. All the solid parts (including the glass slide, the flow guide and the PZT disk) were modelled using the Hooke's Law with their proper boundary conditions of free, fixed and roller constraints on each of the corresponding solid surfaces.

The piezoelectric effects for the PZT disk setup were modelled using the Maxwell's equations with known values of voltages as the boundary conditions. For the flexible SAW setup, the propagation of the SSAW was modelled using the oscillating wall boundary conditions (i.e., Equations (3-16) and (3-17)). For the acoustic effects inside the fluid, the Helmholtz equation (i.e., Equations (2-22) and (2-23)) was solved with impedance and radiation boundary conditions on each of the corresponding boundaries which results in the computation of the properties including the acoustic pressure and the location of the pressure nodes. The steady, laminar, incompressible, and viscous flow was modelled using the Navier-Stokes equations (i.e. Equations (2-6) and (2-7)). The boundary conditions were set to be a fixed value of flow rate at the inlet, a fixed value of pressure at the outlet, and no-slip boundary conditions on the channel walls.

To predict the behaviour of the acoustofluidic system, it is important to correctly model what happens at the fluid-solid interfaces, where the vibration of the solid walls affects the fluid, and the acoustic pressure field inside the fluid causes a pressure effect on the solid walls. In this study, the whole three-dimensional acoustic-fluid-solid system was modelled with a "two-way coupling" among the glass slide, the flow guide, and the water inside to simulate the fluid-solid interfaces. At the fluid-solid interfaces, as the acoustic wave propagates, the acoustic pressure field inside the fluid results in a pressure effect on the solid surface, and the vibration of the solid surface affects the fluid pressure. To correctly model the fluid-solid interactions at the

interfaces, a pressure load is exerted on the solid parts due to the acoustic pressure field inside the fluid while the vibration of the solid components (i.e. the structural acceleration) influences the fluid field [145].

To model the behaviour of the microparticles, the Euler-Lagrange approach was used to derive the governing equations of their motions (i.e., Equations (2-56) and (2-57)) in three dimensions. The acoustic radiation force (i.e. Equations (2-52) and (2-53)) was added to the governing equations of microparticle motions as an external body force applied on the particles. As the particles move along with the fluid flow, they experience a viscous drag force which is modelled by the Stokes drag force. Since the volume fraction of the dispersed microparticle phase is smaller than that of the continuous fluid phase, it is assumed that the fluid particle mixture is sparsely distributed. As the sizes of the microparticles are insignificant compared to the microchannel dimensions and the velocities of the microparticles are low, it is assumed that a "one-way coupling" occurs between the two phases (i.e. fluid and particle), which means that the continuous phase affects the dispersed phase but not vice-versa [145].

To discritise and solve the governing equations of the system, FEM and Newton's iterative method were used. The solution was converged with 10^{-6} criteria for all the simulations. Microparticles movement was simulated for a duration of 50 s and with a time step of 0.001 s. At each time step, the acoustic radiation and drag forces which affect the particles' movement were calculated based on the acoustic and fluid fields and the position of the particles was continuously tracked until the time reached 50 s (at the end time of the simulation).

(a)

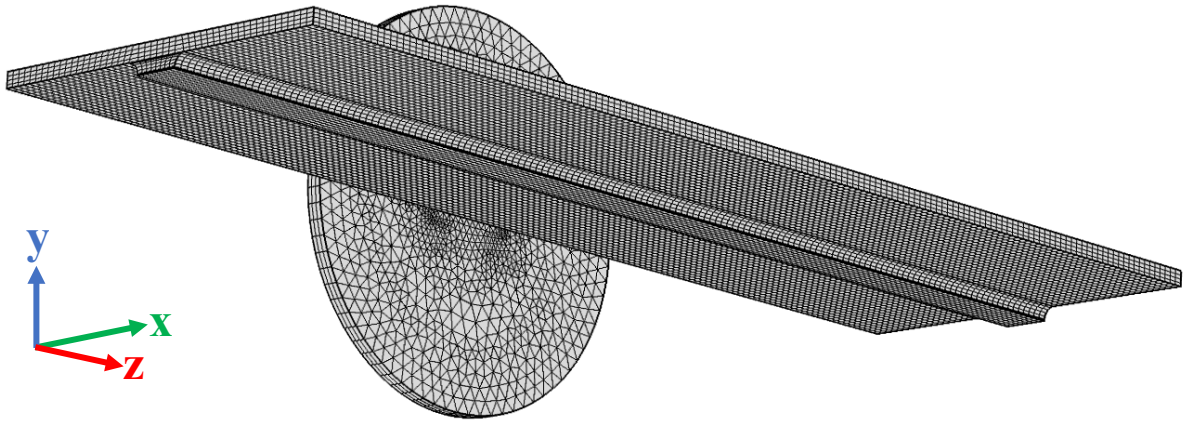

(b)

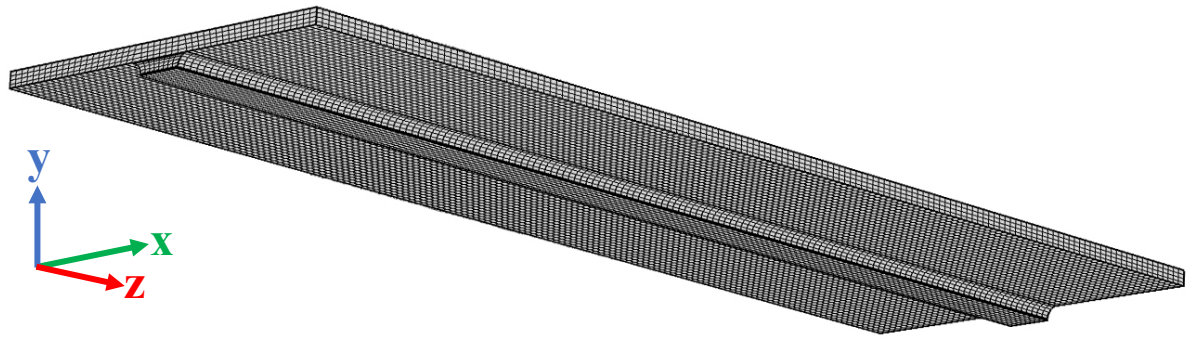

Figure 8.2 Modelled geometry and computational mesh for (a) PZT setup and (b) SAW device setup.

8.3 Experimental Details

The capillary bridge channel was formed between a fluid guide and a wave guide. A standard glass microscope slide was used as the wave guide. The fluid guide was cut from a 0.05 mm polystyrene film (Goodfellow, UK) using a plotter cutter (Brother ScanNCut CM900) [166, 167]. Figure 8.3(a) shows the experimental setup used for thin film SAW device and capillary bridge channel experiments. In this study, wall-less and straight channels of 40 mm long with various widths (0.5 mm, 1 mm, 2.5 mm, 3 mm, and 18 mm wide), as well as tapered channels with a width tapered from 1 mm to 2 mm and from 4 mm to 6 mm (shown in Figure 8.3(b)) were produced from polystyrene film. Additionally, one converging-diverging channel (i.e., width from 2 mm to 1 mm then back to 2 mm) shown in Figure 8.3(c), and one diverging-converging channel (i.e., width from 1 mm to 2 mm then back to 1 mm) shown in Figure 8.3(d) were also produced and used. The fluid guide was held under tension from both sides along its length to create a flat surface for the fluid to flow. A 3D-printed holder was used to hold fluid guide under tension, to fix the position of the wave guide above the fluid guide (this sets the height of the channel be at 0.75 mm or 1 mm, respectively) and facilitate the connection of the wave guide to the acoustic wave generator.

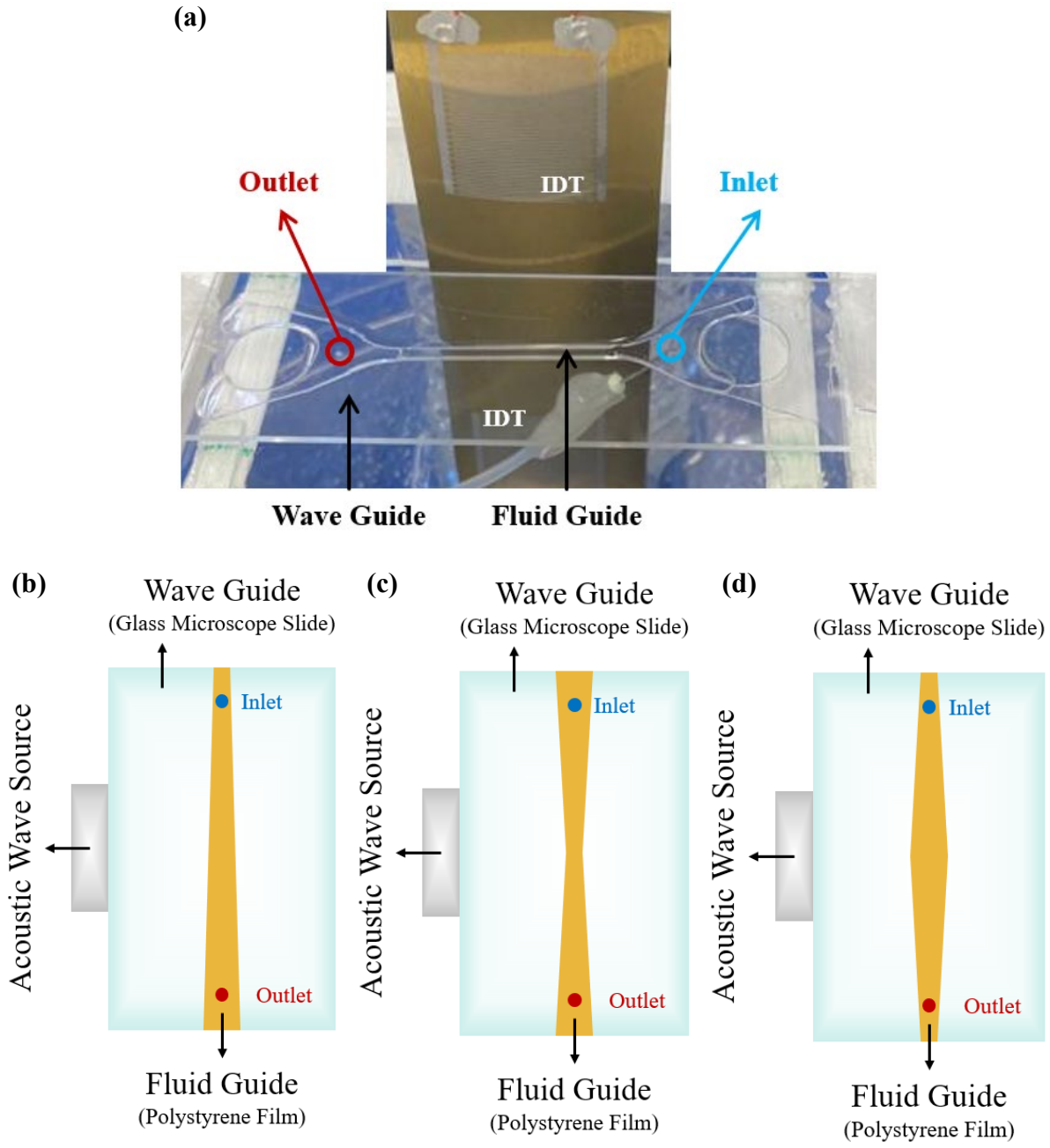

Figure 8.3 (a) Experimental setup used for thin film SAW device and capillary bridge channel experiments; and schematics illustrations of (b) tapered, (c) converging-diverging, and (d) diverging-converging fluid guides.

Two different types of acoustic wave sources were used in this study: (1) a PZT disk with a diameter of 25 mm, a thickness of 2 mm and a nominal operating frequency of 1.035 MHz (with the other harmonic frequency values of 3.34 MHz, 5.57 MHz, and 7.58 MHz); and (2) a ZnO/Al thin film SAW device with the nominal frequency of 1.905 MHz. They were used to produce the acoustic waves which were transferred to the wave guide (glass slide). An RF function generator (Agilent 33220A) was connected to a power amplifier (ENI 240L) in order to generate the amplified RF signals with the applied frequencies to the PZT disk [124]. An RF

signal generator (Marconi Instruments 2024) was connected to another power amplifier (Amplifier Research 75A) to generate the RF signals to the IDTs of the SAW device.

Particle patterning was visualized using polystyrene microparticles with a diameter of 10 μm and a density of 1500 kg/m^3. Yeast particles (*S. Cerevisiae*, Allinson, UK) with a diameter ~5 μm and density ρ_p=1114 kg/m^3 [168] was also chosen for this study in order to demonstrate the potential of biological applications due to yeast cells being easy to manage as model organisms in cellular, biological and biomedical investigations for experimental work [33, 151, 152]. Both polystyrene and yeast particles were suspended in DI water and the solution was then diluted to reach a cell concentration of approximately 3×10^7 ml^{-1}. The particle/water mixture was pumped into and out of the channel in the PZT setup using two peristaltic pumps (Gilson Minipuls 3) with tubes connected to the 1.5 mm diameter and inlet and outlet holes in the fluid guide [169]. For the SAW setup, a syringe pump (ExiGo pump) connected to the inlet hole in the fluid guide as well as a tube connecting the outlet hole to a vial for collecting the exiting fluid were used.

Continuous flows with various flow rates of 0.015 mL/s (for the PZT setup) and 0.2 μL/s, 0.5 μL/s, 1 μL/s, and 2 μL/s (for flexible SAW setup) were maintained in the capillary bridge channels without fluid leaks. The air-water walls (the interfaces between the water inside the channel and the air) was set with negligible deformations by choosing a suitable flow rate and acoustic power. The particle patterning during the continuous flow was studied with different frequencies, flow rates, and channel widths and geometries.

A non-flowing setup was also utilised to investigate the effects of channel geometry on particle patterning. In order to understand the acoustic wave patterns generated inside water when the width of the fluid guide is larger, two glass microscope slides (both with the same sizes) as the wave guide and the fluid guide were also used in a non-flowing setup.

8.4 Patterning in Capillary Bridge Channel with Continuous Flow Using the PZT Disk

Figure 8.4 presents the top views of the experimental and simulation results of particle alignment inside a 2.5 mm wide capillary bridge channel with a continuous flow using three different frequencies of (a) 1.035 MHz, (b) 3.34 MHz, and (c) 5.57 MHz. The results include (1) experimental particle alignment; simulation results of (2) acoustic pressure field, and (3) particle tracks. The patterns generated from the yeast particles in the experimental results (1) follows closely to the pattern of pressure nodes in the simulation results (2). The yeast

particles are seen to flow in the channel with continuous and parallel lines and follow the pressure nodes along the direction of flow. There are some gaps in the pressure nodes, and the yeast lines span these gaps to form unbroken lines (Figures 8.4(a-3) and (b-3)). At lower flow rates, the yeast lines became irregular, and some stationary clumps were formed which did not apparently change in size. At higher frequencies (see Figures 8.4(a-1), (b-1), and (c-1)) the number of lines of yeast particles increases, and they still follow the nodal lines. Whereas at lower flow rates, those particles form clumps. Clearly alignment of yeast particles can be realised using this continuous flow capillary bridge system based on the acoustic waves generated from the PZT disk.

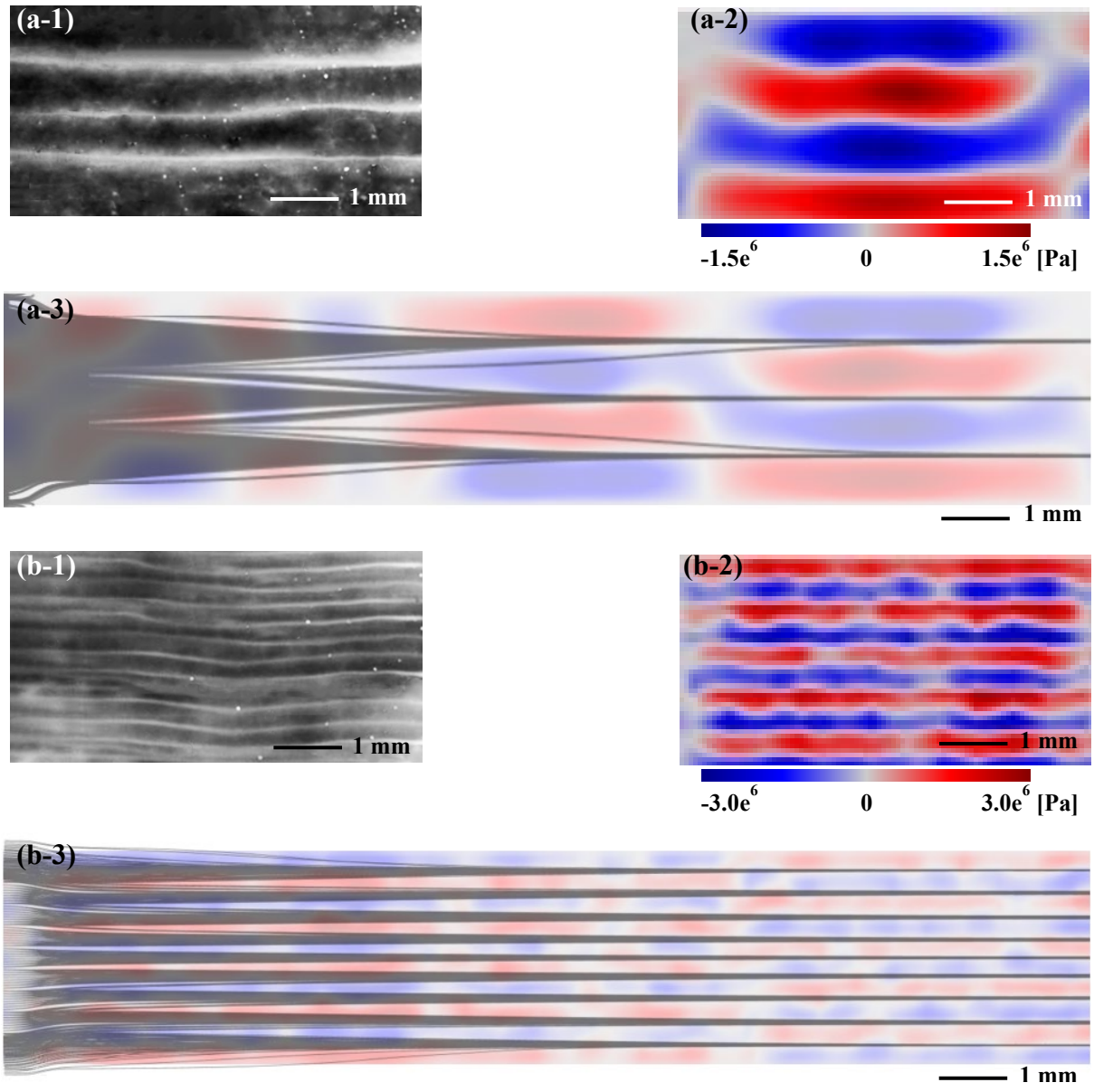

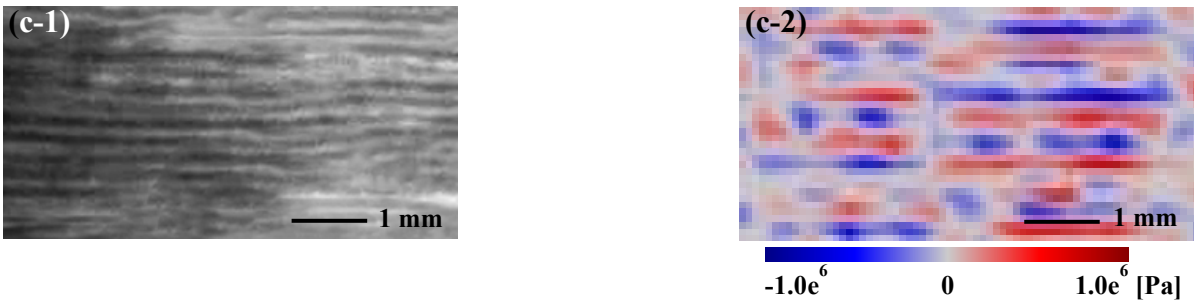

Figure 8.4 Yeast particle patterning in water in a 2.5 mm wide channel with 0.75 mm height and 0.15 mL/min flow rate (1) experimental data, and simulation results of (2) acoustic pressure field and (3) particle tracks form top view using a side-driven PZT disk with (a) 1.035 MHz, (b) 3.34 MHz, and (c) 5.57 MHz frequency.

Figure 8.5 shows the line distances for the 2.5 mm wide channel generated at different frequencies, obtained from the theoretical (based on Equation: $D = \frac{\lambda}{2}$), experimental and simulation results. Clearly good agreements can be seen among these data. As the frequency increases, the average distance between the yeast particle patterns decreases but is still corresponding to half of the wavelength of the acoustic waves as shown in Figure 8.5.

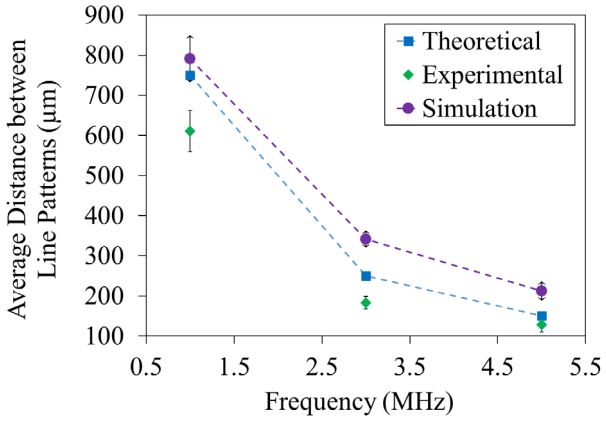

Figure 8.5 Comparison of the theoretical, experimental and simulation results for the distance between the yeast particle patterns in water in wall-less channels with flow for 2.5 mm wide channel using a side-driven PZT disk with different frequencies of 1.035 MHz, 3.34 MHz, and 5.57 MHz.

Figure 8.6 shows experimental results of yeast particle patterning inside the capillary bridge channel with a continuous flow using a larger bridge width of 18 mm. Figures 8.6(a) and (b) present alignment patterns of the particles at two different frequencies. For the frequency of 1.035 MHz, increasing the width of the channel to 18 mm (comparing Figures 8.4(a-1) and 8.6(a)) will cause the pattern lines to become slightly distorted. For the frequency of 3.34 MHz (comparing Figures 8.4(a-2) and 8.6(b)) the distortion of the pattern lines becomes significant. The reason will be discussed later.

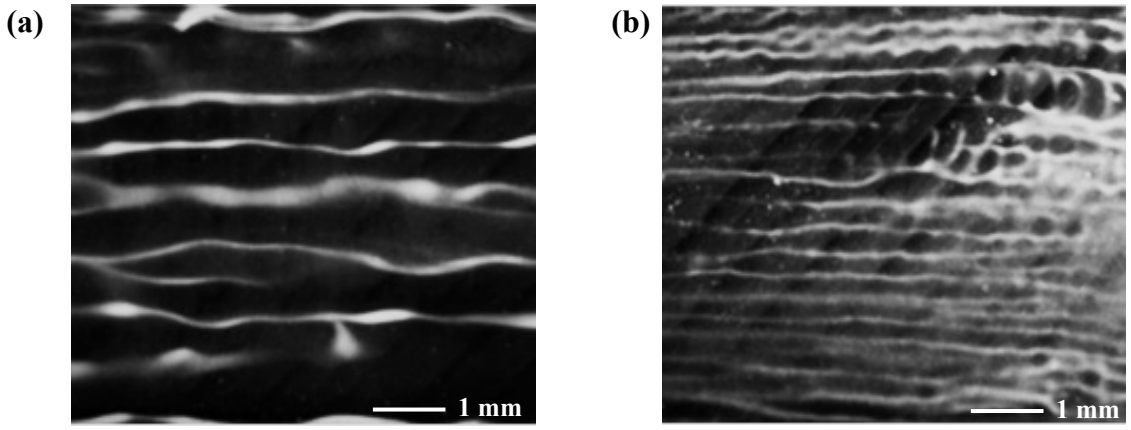

Figure 8.6 Yeast cell patterning in water in an 18 mm wide channel with 0.75 mm height and 0.15 mL/min flow rate using a side driven PZT disk with (a) 1.035 MHz and (b) 3.34 MHz frequency.

8.5 Effects of Channel Geometry on Particle Patterning Using the PZT Disk

In order to study the patterning of microparticles within the acoustic wave field, the particle patterning results were obtained using the same acoustofluidic setup but without apparent liquid flow. Figure 8.7 shows the experimental and simulation results of yeast particle patterning using capillary bridge setup, under three different channel configurations. Figures 8.7(a-1), (a-2) and (a-3) present the experimental results of particle alignments in: (1) a straight wall-less channel; (2) a wall-less channel inclined with 15° angle relative to the PZT disk surface; and (3) a wall-less channel with a tapered width (i.e., with varied width along its length), respectively. Figures 8.7(b-1) to (b-3), and Figures 8.7(c-1) to (c-3) show the simulation results of acoustic pressure fields for the above three microchannel configurations, from their top and cross-sectional views, respectively.

From the results shown in Figures 8.7(a-1), (b-1) and (c-1), the yeast particles are patterned on the acoustic pressure nodes along the length of the channel with similar distances between two adjacent lines, which is about the half wavelength of sound in the water. However, these results could not reveal the fact if the particle pattern lines are following the direction of channel's walls or they are actually following the surface direction of the PZT disk. These two could mean quite different formation mechanisms, but in this case, they are the same. In order to verify this, the particle patterning inside the channel with a 15° incline angle relative to the surface of the PZT disk have been studied. Figures 8.7(a-2), (b-2) and (c-2) prove that the yeast particles are aligned parallel to the channel's water-air walls as opposed to the direction of the surface of the PZT disk. The distance between each two particle lines is still roughly equal to half of the wavelength of acoustic wave in liquid. For both the straight and inclined channel configurations, the patterning of the particles into parallel lines can be attributed to the pressure node lines forming parallel to the channel walls inside the water channel when the waves

propagate from the glass slide into the water [124, 139]. This results in the similar patterns formed due to the SSAWs in the substrate as extensively reported in literature [9, 10, 25, 29, 47, 74].

The particle patterning inside the channel with a tapered geometry (as shown in Figures 8.7(a-3), (b-3) and (c-3)) was further investigated. The particles are patterned in a way that as the width is increased from 4 mm to 6 mm, the number of line patterns can be seen to gradually increase. Due to the gradual change of the channel's width, the number of node lines is also changed, but the line distance remains constant. The acoustic pressure pattern becomes distorted at the middle of the channel due to the change of number of patterned lines (Figure 8.7(a-3) and at several sections of the tapered channel, the acoustic pressure field shows disturbances in the node line patterns (Figure 8.7(b-3)).

The distance between the yeast line patterns in different geometries of wall-less channel with 1.035 MHz frequency are all within 20% of the half wavelength in water. As the frequency increases, the average distance between the yeast line patterns decreases but remain nearly equal to the half wavelength of the acoustic wave in water.

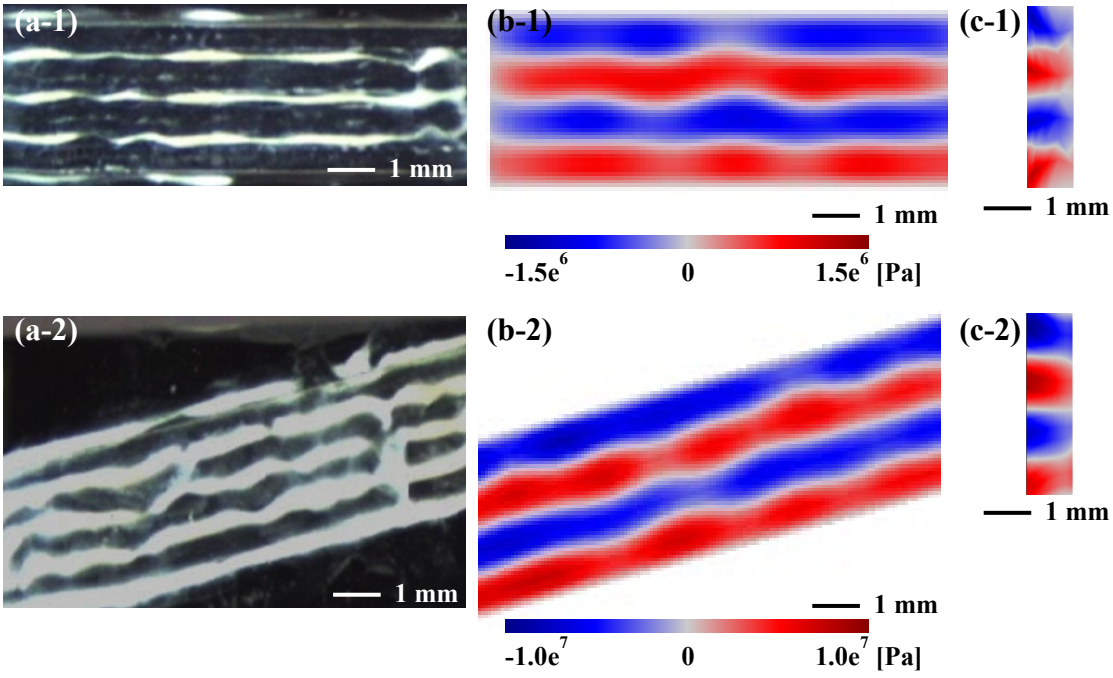

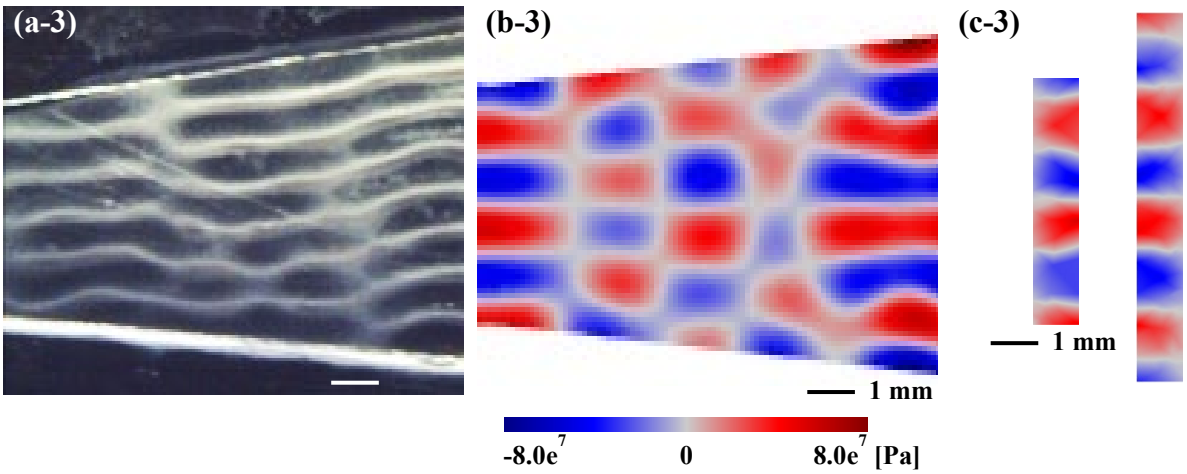

Figure 8.7 Yeast particle patterning in water in a wall-less (1) 3 mm wide straight channel (2) 3 mm wide channel with 10 degree angle relative to the PZT and (3) tapered channel (small base = 4 mm, large base = 6 mm) with 0.75 mm height and without flow (a) experimental data from top view, (b) simulation results of acoustic pressure field form top view, (c) simulation results of acoustic pressure field form cross-sectional view using a side-driven PZT disk with 1.035 MHz frequency.

In brief, it can be seen that without apparent liquid flow, there are already line patterns formed parallel to the channel's air-water walls, which is mainly due to the pressure node line formation inside the water channel [124, 139]. However, without fluid flow, the patterns show lines of particles which are often jagged and non-smooth. With the continuous liquid flow, parallel lines of the microparticles become smoothened due to the fluid flow effects as they continuously flow through the wall-less channel, realising the separation of the yeast particles at the outlet.

To study the effects of the width of the fluid guide on the wave patterns within the water, and investigate the mechanisms of particle patterning, as well as optimise the width of the fluid guide, the acoustic pressure distributions at four different channel widths: 1 mm, 5 mm, 10 mm, and 15 mm have been simulated. The pressure profiles at a frequency of 1.035 MHz viewed from top and cross-section views are shown in Figure 8.8. Comparing these results with the acoustic pressure inside the channel with 3 mm width (Figure 8.4(b-1)), the width of the fluid guide apparently affects the pattern of the acoustic pressure and patterning of yeast particles inside the water channel.

For the channel width of 1 mm (Figure 8.8(a-1)), since the width is less than half of a wavelength, the nodes cannot be formed in the channel. When a slightly larger value (e.g., 2.5 mm, 3 mm or 4 mm as shown in Figures 8.4 and 8.7) is chosen for the width of the fluid guide, the particles are patterned in lines parallel to the channel air-water walls inside the wall-less channel. Increasing the channel width to 5 mm (as shown in Figure 8.8(b-1)) results in some distortion of the pressure node line patterns. However, two lines can still be clearly seen

in the middle of the channel. Further increase in the channel width (i.e., 10 mm and 15 mm, as shown in Figures 8.8(c-1) and (d-1)) results in formation of pressure nodes in various directions. It can be concluded that for the PZT setup, a fluid guide with a width between 2.5 mm and 5 mm can result in good particle patterning in parallel lines inside the channel.

Introducing the fluid flow inside the wall-less channel smoothens the pattern lines and the particles will flow inside the channel along with the liquid (see Figure 8.6). However, it was seen that increasing the width of the channel (see Figure 8.6) causes the pattern lines to become distorted. While the smoothing effect of flow can overcome some of the distortion problem.

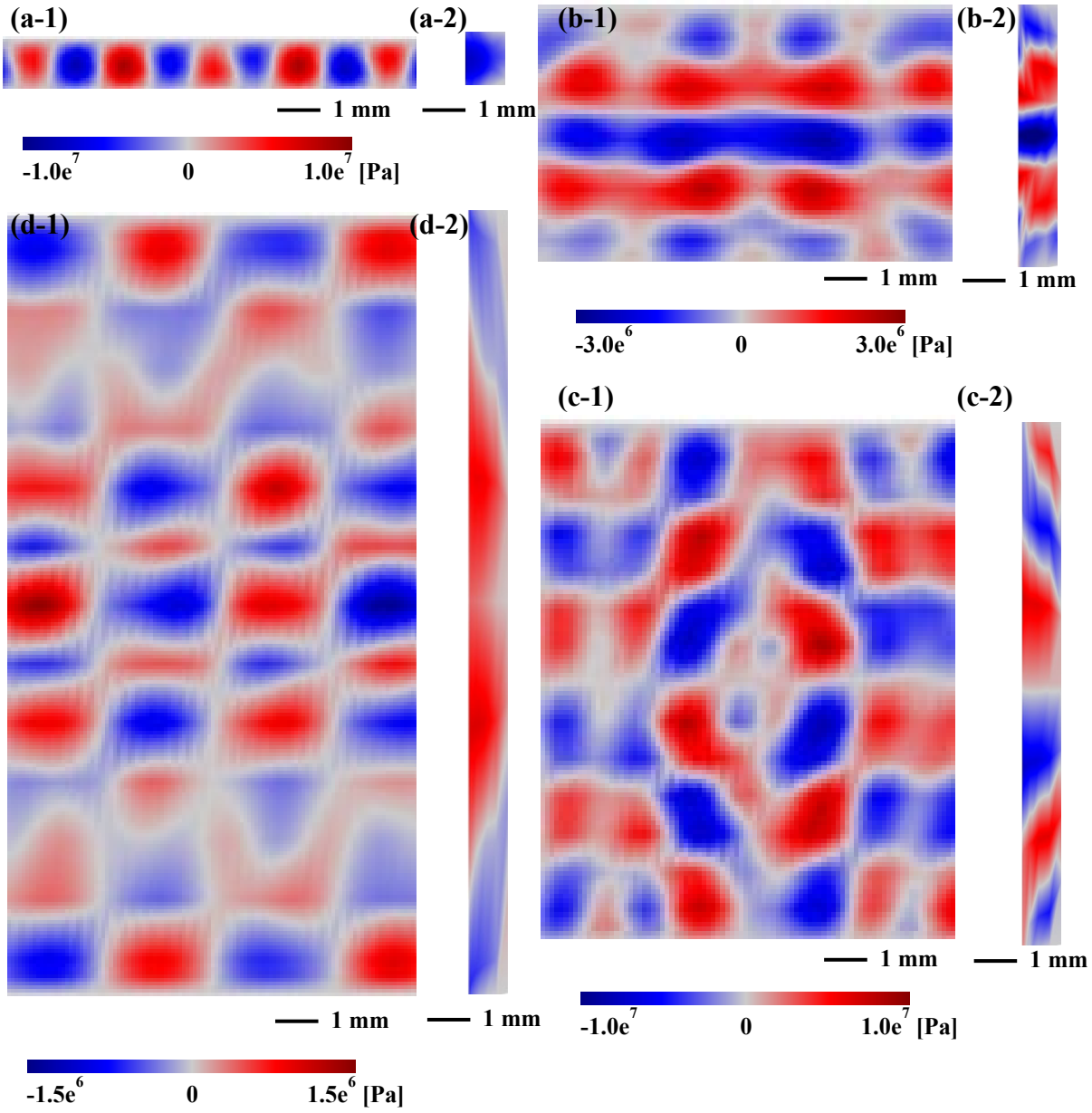

Figure 8.8 Simulation results of acoustic pressure field in a wall-less channel with (a) 1.0 mm, (b) 5.0 mm, (c) 10 mm, (d) 15 mm width, 0.75 mm height and without flow and from (1) top and (2) cross-sectional views with using a side-driven PZT disk with 1.035 MHz frequency.

In order to understand the acoustic wave patterns generated inside water when the width of the fluid guide at its maximum which is equal to the width of the wave guide, two glass microscope slides (both with the same geometry), one as the wave guide and another as the fluid guide, were used for particle patterning. The experimental and simulation results of yeast particle patterns are shown in Figure 8.9. In this case, the bottom glass slide acts as a fluid guide while the top glass slide acts as a wave guide. As shown in Figure 8.9(a), the yeast particles are patterned in grids forming a checker-board-like pattern of the acoustic pressure field. This is generally caused by the Lamb waves [164] in the wave guide when the width of the fluid guid is large (18 mm). There is no clear indication of particle alignment along any direction. Increasing the frequency of the PZT will decrease the dimension of the unit patterns and these Lamb wave patterns become much denser.

Figure 8.9(b) shows the simulation results of the Lamb wave-based pressure field inside water between two glass slides. The checker-board pattern of the acoustic pressure field is in a good agreement with yeast particle patterns of Figure 8.9(a) for each frequency case. As the frequency increases, the checker-board pattern becomes much denser.

The simulated cross-sectional views for acoustic pressure fields inside the water between two glass slides are shown in Figure 8.9(c). Above 1 MHz, node lines parallel to the glass slides are present in the acoustic pressure field. These lines occur mainly due to the wave reflection between the top and bottom glass slides, and their distances are decreased as the frequency increases. The checker-board-like pattern of the acoustic pressure field is also seen from the cross-sectional view at a higher frequency of 3 MHz as shown in Figure 8.9(c-2). With the further increase of frequency, node lines parallel to the glass slides start to appear in the acoustic pressure field. These lines occur mainly due to the wave reflection between the top and bottom glass slides, and their distances decrease as the frequency increases.

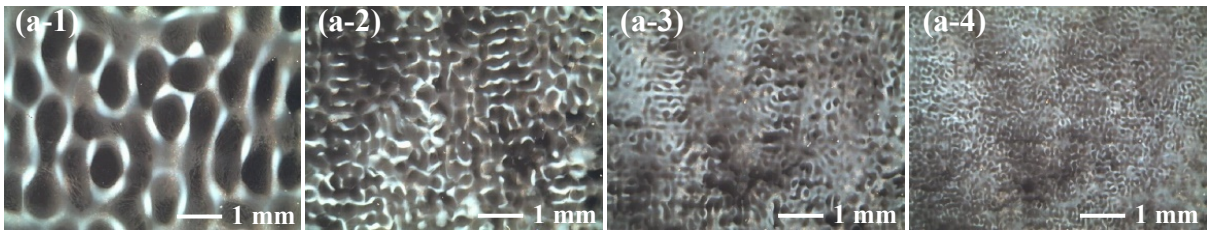

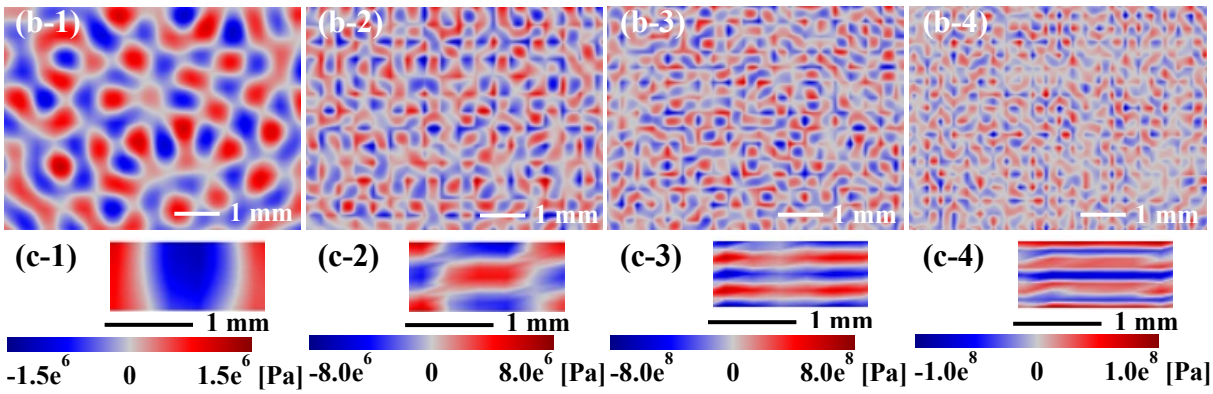

Figure 8.9 Yeast particle patterning in water placed between a glass microscope slide and a glass cover slip (a) experimental data from top view, (b) simulation results of acoustic pressure field form top view at the central height of water, (c) simulation results of acoustic pressure field form cross-sectional view, and using a side-driven PZT disk with (1) 1.035 MHz, (2) 3.34 MHz, (3) 5.57 MHz and (4) 7.58 MHz frequency.

Figure 8.10 presents the comparisons of the average distances of the checker-board patterns of yeast particles at different frequencies driven by the PZT disk. The theoretical results (based on Equation: $D = \frac{\lambda}{2}$), experimental results and simulation results show good agreements among each other as shown in Figure 8.10. As the frequency increases, the average distance between the yeast particle patterns decreases (which corresponds to half of the wavelength of the acoustic wave in the glass).

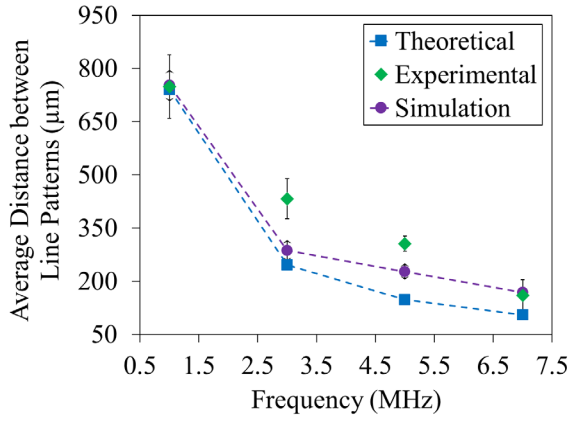

Figure 8.10 Comparison of the theoretical, experimental and simulation results for the distance between the yeast particle patterns in water in placed between two glass slides using a side driven PZT disk with different frequencies of 1.035 MHz, 3.34 MHz, 5.57 MHz, and 7.58 MHz.

From the results presented here, it is verified that using this acoustofluidic setup, Lamb waves have been generated in the top glass slide (the wave guide), and then dissipated into water, generating an acoustic pressure field with a checker-board pattern between the wave guid and the cover slip. The yeast particles are patterned in uniformly distributed nodes (where the acoustic pressure is zero i.e., white areas in Figures 8.9(b-1) to (b-4)) on the acoustic pressure field. Comparing the results of Figure 8.8 with Figure 8.9, clearly, there is a transition from

this checker-board patterns into parallel lines with the significant decrease of the width of the fluid guide.

8.6 Patterning in Capillary Bridge Channel with Continuous Flow Using the Flexible Thin Film SAW Device

Figure 8.11 shows the results of polystyrene particle alignment inside capillary bridge channels, touched by the side using a flexible SAW device with the resonance frequency of 1.905 MHz. The figures are shown from the top view for the results of (1) experimental particle alignment; the simulation results of (2) acoustic pressure field, and (3) particle tracks, respectively, with a continuous flow inside the channel. The results are also presented for various channel geometries (a) 1 mm width parallel to the IDT direction, (b) 1 mm width with 20° incline angle to the IDT direction, and (c) 0.5 mm width. The experimental and simulation results of polystyrene particle alignments show good agreements between each other.

For the channel of 1 mm width parallel to the IDT direction (Figure 8.11(a)), there are either two (Figures 8.11(a-i-1) and (a-i-3)) or three (Figures 8.11(a-ii-1) and (a-ii-3)) particle pattern lines, which are parallel to the air-water walls of the channel. This is based on the positioning of the pressure node lines of the acoustic pressure field which can be seen in the simulation results (Figure 8.11(a-i-2)) and (Figure 8.11(a-ii-2)). With the applied frequency of 1.905 MHz of the flexible SAW device, the distance between particle pattern lines is nearly equal to the half of the wavelength of the acoustic wave in water.

When the fluid guide is positioned with an incline angle of 20° relative to the direction of the IDTs on the SAW device, the simulated pressure node lines of the acoustic field were obtained, and the results are shown in Figure 8.11(b-2). The experimentally obtained particle patterning lines are shown in Figure 8.11(b-1), which indicates that the patterns are parallel to the air-water walls of the capillary bridge channel, i.e., at 20° angle compared to the IDT direction. The distance between the adjacent pattern lines is still roughly equal to the half of the acoustic wavelength in water.

For the above configuration which is parallel to the IDT direction of the SAW device, decreasing the width of the channel from 1 mm to 0.5 mm will reduce both the number of pressure node lines and particle pattern lines into one (Figure 8.11(c-2)). For this case (0.5 mm width), because the width of the channel is smaller than the wavelength of the acoustic wave in water, there is only one line formed at the middle of the capillary bridge channel (Figure

8.11(c-1)) and (Figure 8.11(c-3)). Simulation results shown in Figure 8.11(c-3) verify the experimental ones.

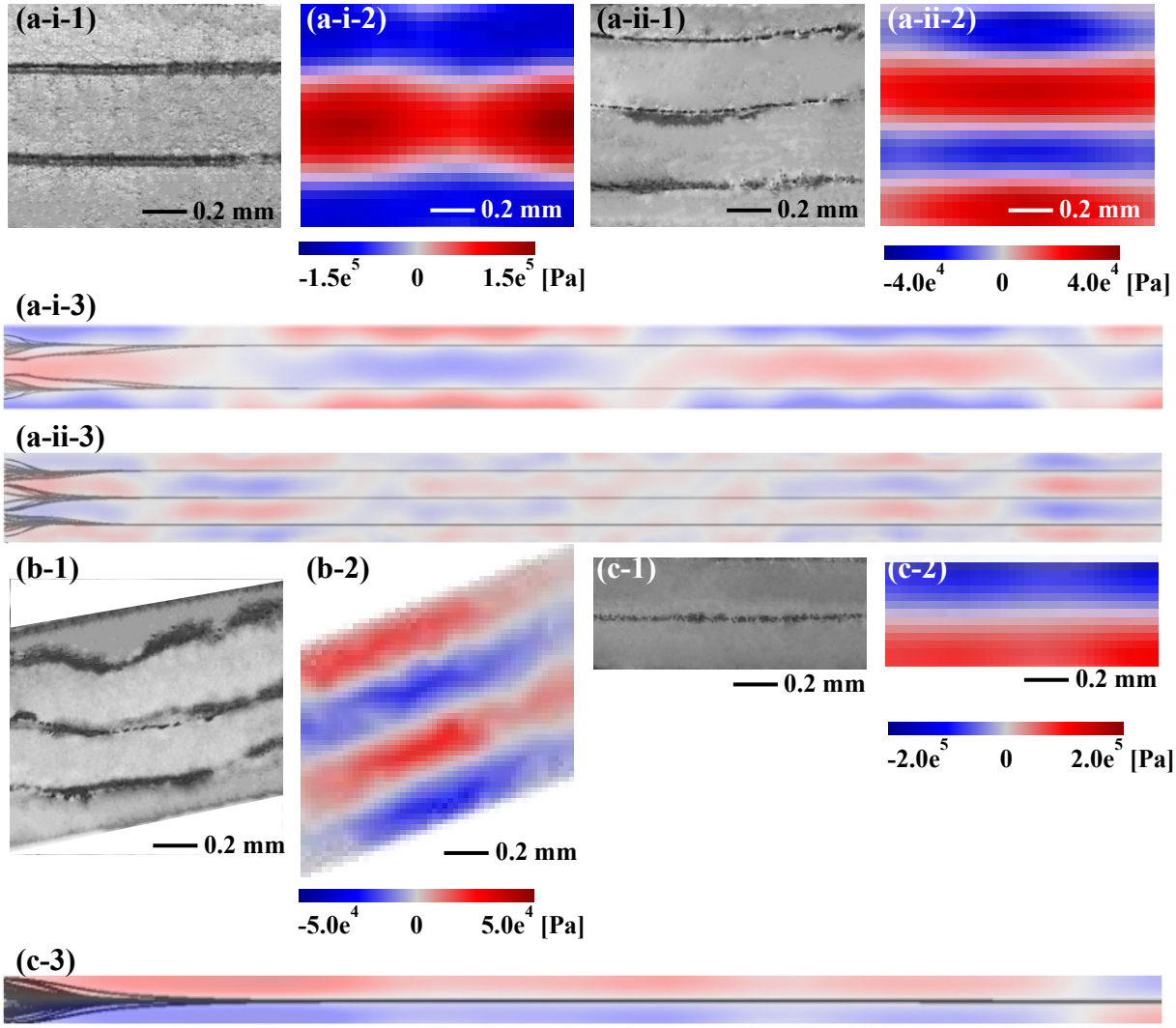

Figure 8.11 Polystyrene particle patterning in water in a capillary bridge channel with (a) 1 mm width with no incline angle, (b) 1 mm width with 20° incline angle, and (c) 0.5 mm width, and 1 mm height and 1 µL/s flow rate (1) experimental data, and simulation results of (2) acoustic pressure field and (3) particle tracks form top view using a flexible SAW device with 1.905 MHz frequency.

The results of yeast alignment inside capillary bridge channels with a continuous liquid flow and with various geometries of (a) 1 mm width, and (b) 0.5 mm width are presented in Figure 8.12. The figure shows the top views of (1) experimentally obtained particle alignment; simulation results of (2) acoustic pressure field, and (3) particle tracks. Both the experimental and simulation results of yeast alignments agree well with each other. The results of yeast particle patterning follow the same trend as the polystyrene particle alignments and the reasons have already been discussed for the polystyrene particles previously.

Manipulation of yeast cell with the present acoustofluidic setup shows the possibility of manipulating and patterning biological cells despite their large size variations and their strong tendency to adhere to each other. In previous literature, SAW devices were shown to be biocompatible, conserving cell viability, proliferation and functionality when using low to moderate voltages [9, 27, 28, 30, 31]. The flexible SAW devices can be bent into any shapes, and easily touch the wave guide. They can also wrap around a circular wave guide such as glass tubes for manipulating the particles or cells inside the tubes.

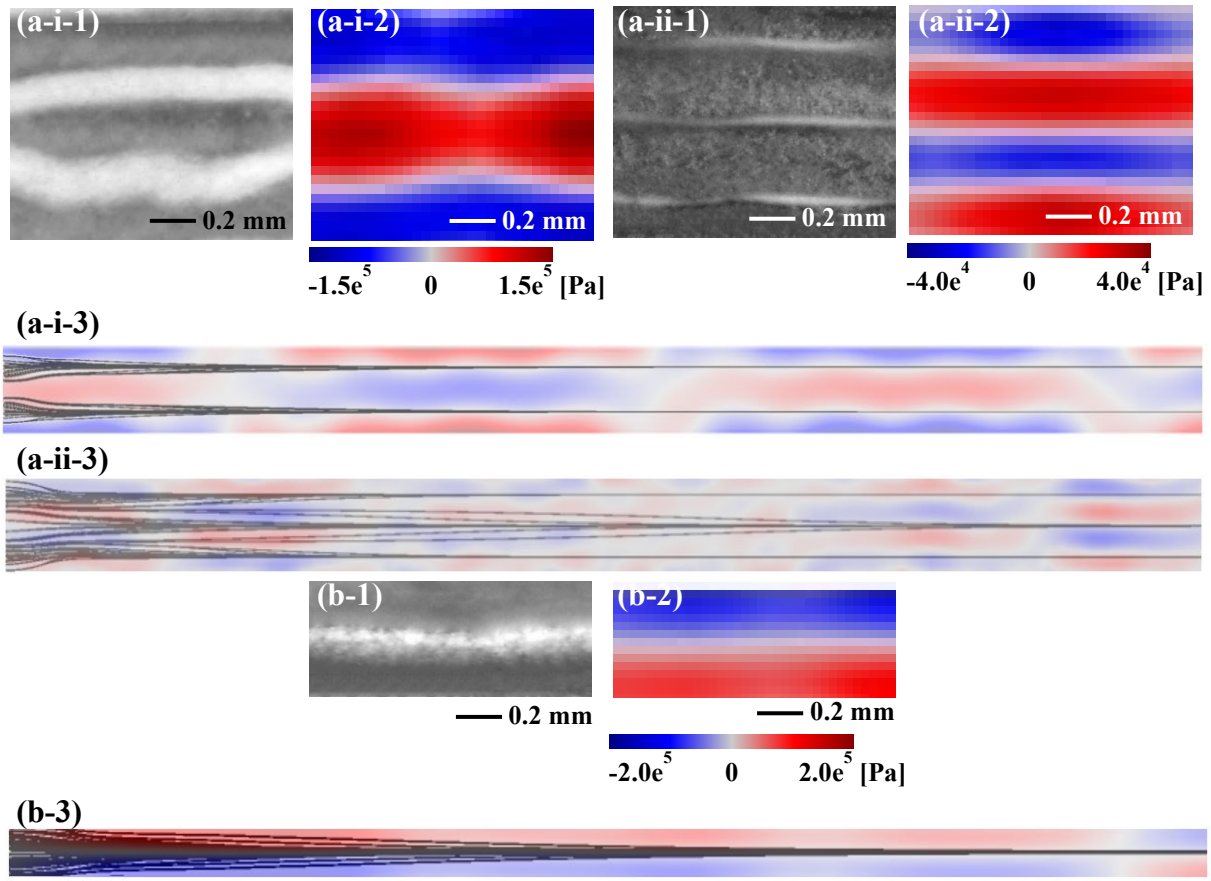

Figure 8.12 Yeast particle patterning in water in a capillary bridge channel with (a) 1 mm width, and (b) 0.5 mm width and 1 mm height and 1 µL/s flow rate (1) experimental data, and simulation results of (2) acoustic pressure field and (3) particle tracks form top view using a flexible SAW device with 1.905 MHz frequency.

Figure 8.13 shows the particle line distances inside the capillary bridge channels with different channel widths using the flexible SAW device with the resonance frequency of 1.905 MHz. The experimental and simulation results are in good agreements with each other. For the 1 mm and 2 mm wide channels, the experimental and simulation results are comparable, and the particle line distances are following the theoretical distances (based on the wavelength of acoustic wave in water and Equation: $D = \frac{\lambda}{2}$). For the channel with 0.5 mm width, the distances between the particle lines and the channel walls were measured from both the experimental

and simulation results, both of which are 33.5% less than the theoretical value of half the wavelength of acoustic wave in water.

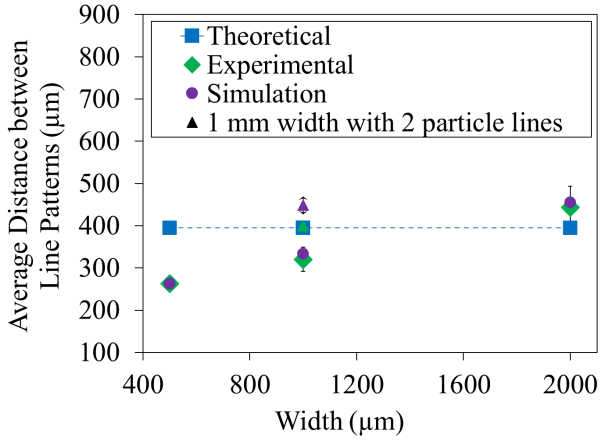

Figure 8.13 Comparison of theoretical, experimental and simulation results for the distance between the polystyrene particle patterns in water in wall-less channels with flow for capillary bridge channels with different widths using a flexible SAW device with 1.905 MHz frequency.

8.7 Effects of Channel Geometry on Particle Patterning Using the Flexible Thin Film SAW Device

In order to study effects of different geometries of the capillary bridge channels, fluid guides with widths of tapered, converging-diverging, and diverging-converging geometries were designed and utilised for particle patterning in a continuous flow setup using a flexible SAW device with a frequency of 1.905 MHz.

For the tapered fluid guide with its width changed form 1 mm to 2 mm, at or and near the position at the region with 1 mm width, the particles are patterned in either two (Figures 8.14(a-i-1) and (a-i-2)) or three (Figures 8.14(a-ii-1) and (a-ii-2)) lines. Whereas at or near the region with 2 mm width, the particles are patterned in four lines (Figures 8.14(a-iii-1) and (a-iii-2)).

Similar results were obtained for both the cases of channels with their widths showing converging-diverging (2 mm to 1 mm to 2 mm) and diverging-converging (1 mm to 2 mm to 1 mm) patterns. Generally, at or near the region with a width of 1 mm in the channels, two lines (Figures 8.14(b-i-1) and (b-i-2) and Figures 8.14(c-i-1) and (c-i-2)) or three lines (Figures 8.14(b-ii-1) and (b-ii-2) and Figures 8.14(c-ii-1) and (c-ii-2)) can be observed. Whereas four lines (Figures 8.14(b-iii-1) and (b-iii-2) and Figures 8.14(c-iii-1) and (c-iii-2)) can be observed at or near the channel region with 2 mm width.

Figure 8.14 show clearly that for the channels with varied widths, the particles are patterned in different numbers of lines according to the width of the channel. However, the distances

between adjacent lines are generally equal to the half of the acoustic wavelength in water (Equation: $D = \frac{\lambda}{2}$). Accordingly, the number of pattern lines increases with the channel's width.

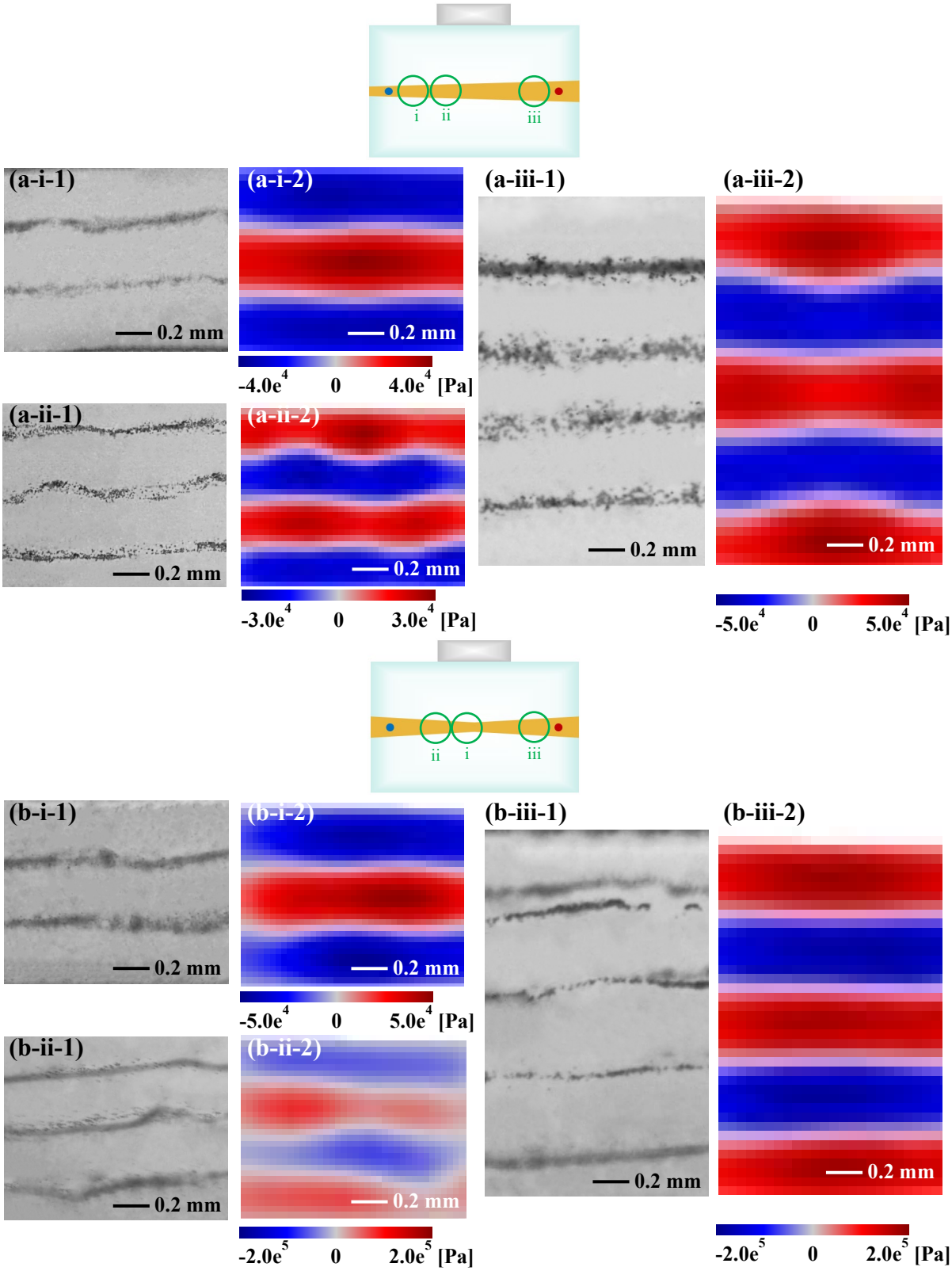

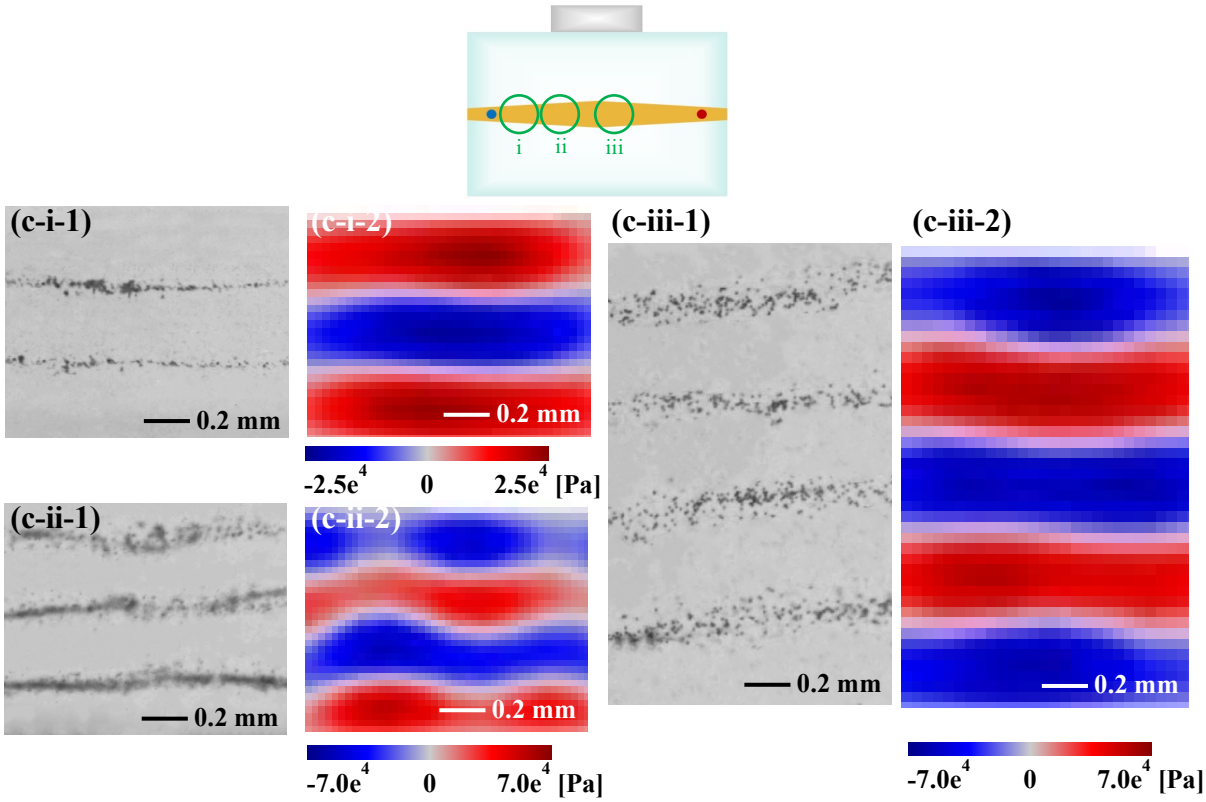

Figure 8.14 Polystyrene particle patterning in water in a capillary bridge channel with (a) tapered with 1 mm to 2 mm width, (b) 2 mm to 1 mm to 2 mm width, and (c) 1 mm to 2 mm to 1 mm width and 1 mm height and 1 µL/s flow rate (1) experimental data, and simulation results of (2) acoustic pressure field form top view using a flexible SAW device with 1.905 MHz frequency.

Patterning of yeast particles were further studied inside a capillary bridge channel with a tapered width (i.e., width is changed from 1 mm to 2 mm). The results in Figure 8.15 clearly show that the similar phenomena with those obtained using the polystyrene particles are observed. It confirms that the distances between adjacent yeast particle lines are roughly the half of the wavelength of the acoustic wave in water.

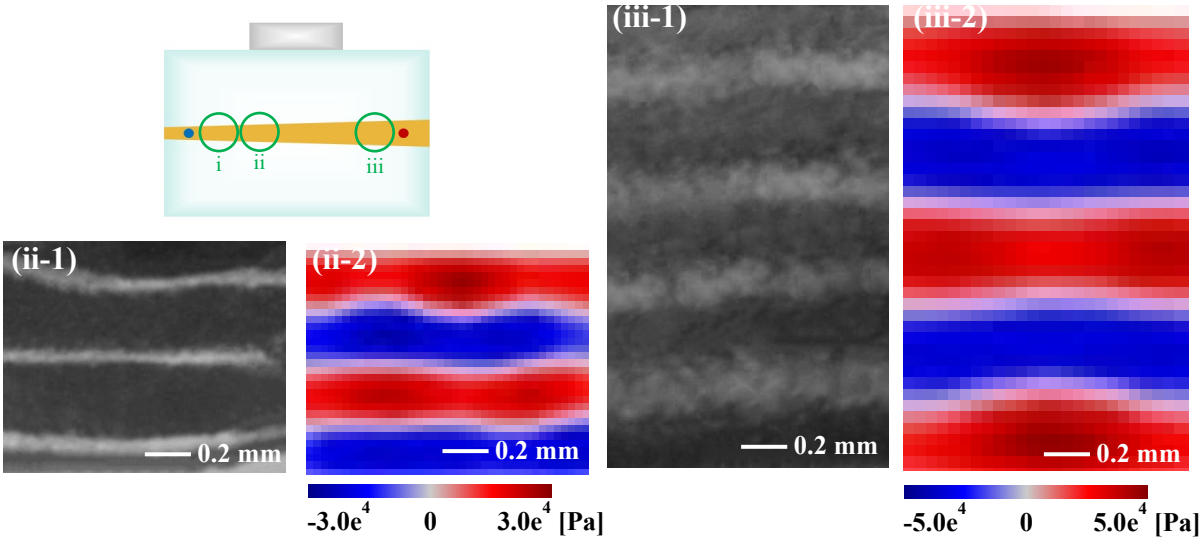

Figure 8.15 Yeast particle patterning in water in a capillary bridge channel with tapered with 1 mm to 2 mm width and 1 mm height and 1 µL/s flow rate (1) experimental data, and simulation results of (2) acoustic pressure field form top view using a flexible SAW device with 1.905 MHz frequency.

Based on all these results, it can be confirmed that the width of the fluid guide (i.e., channel width) determines the acoustic wave field within the capillary bridge channel and thus also the generated patterns of the particles/cells. To find the optimum width for the fluid guide for generating particle line patterns parallel to the channel walls, the acoustic pressure fields generated within the channels with various widths were modelled. Figure 8.16 shows the top-views of the simulated acoustic pressure fields generated using 1.905 MHz frequency of the SAW device with four different channel widths i.e.: 0.2 mm, 2 mm, 5 mm, and 10 mm.

The modelled acoustic pressure fields inside the channels with widths of 1 mm and 0.5 mm have been shown in Figures 8.11(a-2) and (c-2), before. By comparing Figures 8.11 and 8.16, it can be seen that with the width changing from 0.5 mm to 5 mm, as the width of the channel increases, the number of pressure nodes and thus the particles' pattern lines increase. However, when the channel width is only 0.2 mm (Figure 8.16(a)), pressure node lines are not formed in the channel, simply because the width is smaller than half of the acoustic wavelength in water (394.74 µm). For the channels with widths of 0.5 mm (Figure 8.11(c-2)), 1 mm (Figure 8.11(a-2)), and 2 mm (Figure 8.16(b)), the formed pressure node lines are all parallel to the air-water walls of the channel. Increasing the channel width further to 5 mm (Figure 8.16(c)), the distortion of the pressure node lines can be seen. Whereas for the channel width increased up to 10 mm (Figure 8.16(d)), there are only significantly distorted pressure node patterns and therefore no clear parallel lines of particles could be obtained. In brief, we can conclude that in our studied cases, the best width for obtaining the particle alignment is between 0.5 mm and 2.0 mm.

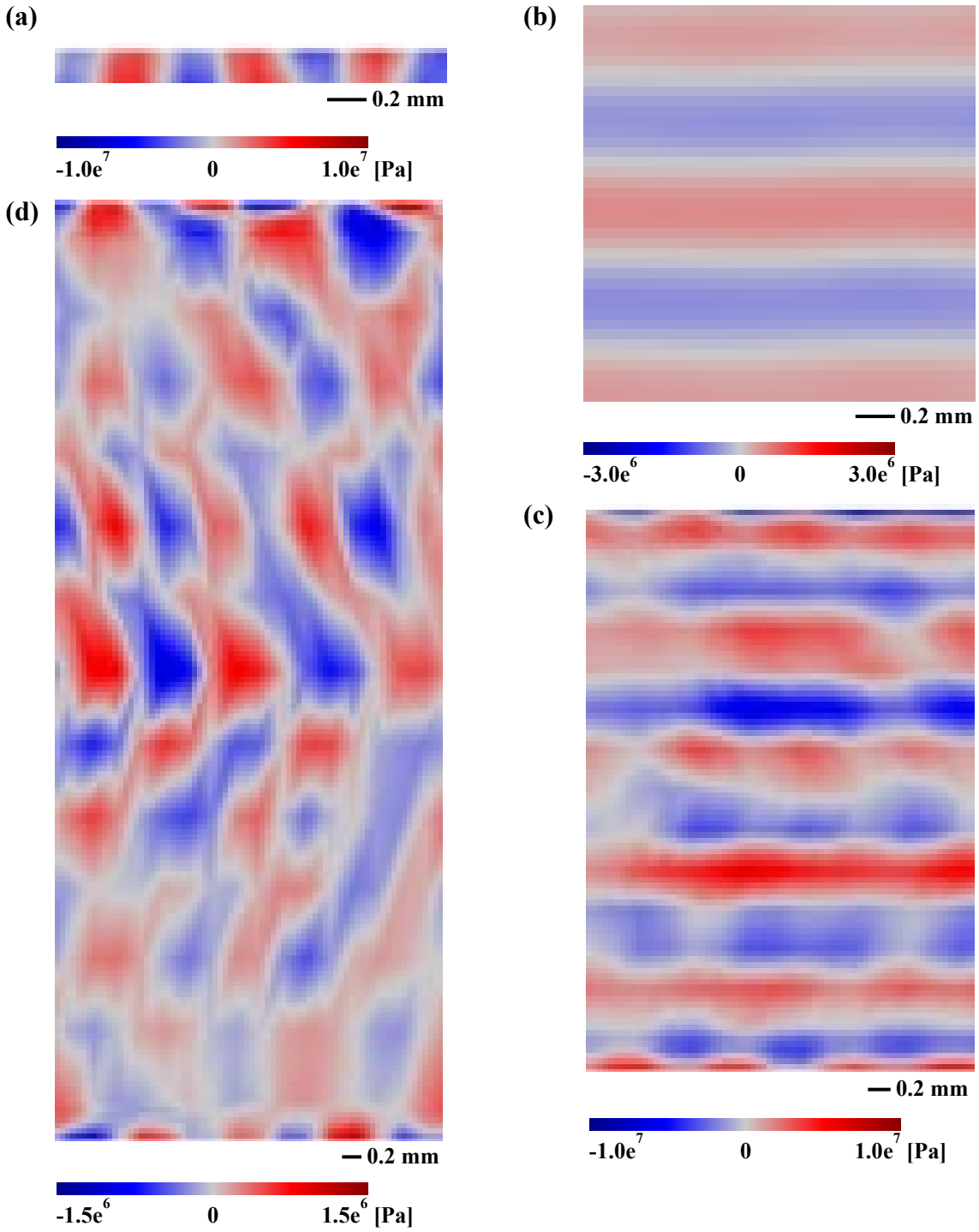

Figure 8.16 Simulation results of acoustic pressure field in a wall-less channel with (a) 0.2 mm, (b) 2.0 mm, (c) 5 mm, (d) 10 mm width, 1 mm height and without flow and from top view using a flexible SAW device with 1.905 MHz frequency.

8.8 Summary

In this chapter, continuous flow acoustofluidic systems were proposed which included a capillary bridge between a wave guide (standard glass microscope slide) and a fluid guide (thin polystyrene film) as a wall-less channel. Both a PZT disk and a flexible thin film SAW device were used as the acoustic wave sources for demonstration of particle manipulation. Polystyrene

microparticles and yeast cells were successfully aligned when they were flowing inside the wall-less channel. The generated patterns of particles at different frequencies, channel widths and geometries have been experimentally and numerically investigated. It was shown that the particles form line patterns parallel to the air-water walls of the channel, but not following the direction of the surface of the PZT disk or the IDTs of the SAW device. The alignment followed pressure nodes in the water channel which are formed from acoustic waves propagating in the glass slide as they leak into the water and generate standing waves. With the continuous flow of liquid, the alignment of particles was smoothened into straight lines parallel to the channel walls. The results demonstrated that the patterns of particles within the flow channel are generated due to the combined effects of (1) the acoustic wave field inside the water channel; and (2) the fluid flow field. Width of the fluid guide (or channel width) had a significant effect on the acoustic pressure field and thus also the particle pattern lines. When the channel width was small compared to the half of acoustic wavelength in water, no pressure node line was formed inside the channel. Whereas increasing the channel width beyond a limit, the particle pattern lines became significantly distorted. Integration of the continuous flow capillary bridge channel with acoustic wave sources, especially the thin film flexible SAW devices, can provide many advantages for acoustofluidics: (1) elimination of the need for solid microchannels; (2) deformability and flexibility of the acoustofluidic setup; (3) ability to run two of more experiments by using more fluid guides in the acoustofluidic setup; and (4) flexibility and convenance to change or control the width of the channel and thus the alignment patterns.

Chapter 9. Conclusions and Future Work

9.1 Conclusions

This research aims to investigate the interactions among fluid, microparticles and SAWs in a microchannel flow through both numerical simulation and experimental studies by:

- developing computational models using the existing commercial software for the solution of multi-physics acoustofluidic problems;
- designing and building an acoustofluidic experimental setup using flexible thin film SAW devices for the purpose of particle and cell manipulations;
- integrating the flexible thin film surface acoustic wave devices with capillary bridge channels to design and build a novel continuous flow acoustofluidic platform.

The distinctiveness and novelty of this research include:

5. investigations of different numerical modelling approaches for acoustofluidic systems in three dimensions;
6. utilisation of flexible thin film SAW devices in particle and cell manipulations;
7. integration of capillary bridge channels with flexible thin film SAW devices to design and build a continuous flow acoustofluidic setup for particle and cell manipulations.

This research demonstrates the complete theory, experimental investigation, and computational modelling of the acoustofluidic systems. Following conclusions were obtained from this study:

- The effects of acoustic streaming phenomena caused by TSAW on fluid and microparticles in a microchannel flow were investigated through both experimental work and numerical modelling with two different approaches; and the simulation results were validated by the experimental data.
- The first modelling approach simulated the whole acoustic field and was coupled to the flow field and the acoustic streaming force was calculated using the first order acoustic density and velocity which predicted the acoustofluidic system more accurately.
- The second approach modelled the effect of acoustic streaming on the flow field using the velocity of a one-dimensional attenuating TSAW using the acoustic streaming force formula and calculated the acoustic streaming force without modelling the acoustic field which is more efficient in terms of computational cost and time while still presenting results with a reasonable accuracy.

- The acoustofluidic behaviour of flexible thin film ZnO/Al SAW devices with various vibration modes and different bending curvatures and twisting geometries was investigated using both experimental data and computational modelling. The bent flexible thin film SAW devices were used, for the first time, for particle manipulation and patterning.
- The concave geometries of the flexible SAW devices resulted in the particle pattern lines to become converged with a slope towards the centre of the curvature of the geometry. Whereas the convex geometries of the flexible SAW devices caused the particle pattern lines diverged with a slope away from centre of the curvature of the geometry.
- Particle patterning was performed on the twisted SAW devices which resulted in changes to the IDTs positions from original flat and parallel ones to those with an inclined direction at a twisting angle. In these cases, the microparticles were patterned into lines parallel to the twisted IDTs for each twisting geometry.
- The flexible thin film ZnO/Al SAW devices were combined with glass microtubes with rectangular and circular cross-sections to study particle manipulation and patterning inside them through both experiments and numerical simulation; and the effects of different flow rates on particle patterning were systematically investigated.
- For a rectangular microtube placed at an angle relative to the IDTs, particle pattern lines were parallel to the tube walls and also formed some checker-board patterns at the bottom of the tube.
- For circular glass microtubes, different particle patterns were observed which were dependent on their positions along the tube's height. In the bottom of the tube, the particle pattern lines were parallel to the tube direction due to the acoustic wave propagation into the water and formation of a standing wave along the direction of the circular tube. Whereas, near the middle of the glass tube height, the particle pattern lines were perpendicular to the tube direction as the standing wave propagated around the circular cross-section of the tube perpendicular to the tube direction.
- The continuous flow inside the rectangular and circular glass tubes caused the particles to form smooth line patterns parallel to the direction of the flow for all the angles and eliminated the other type of particle patterns.
- Finally, the integration of flexible thin film SAW devices with capillary bridge channels in a continuous flow system was proposed, for the first time, for the purpose of particle and cell manipulation and alignment. Effects of different frequencies, channel geometries,

particle properties and flow rates were investigated through both experimental work and three-dimensional numerical modelling.

- The particles were aligned on the pressure node lines of the acoustic pressure field and parallel to the air-water walls of the capillary bridge channels due to the combined effects of the acoustic wave field inside the water channel and the fluid flow.
- Increasing the channel width resulted in the particle pattern lines to be distorted.

Computational modelling can help in predicting and understanding the underlying physics and working principles of the complex acoustofluidic systems by determining the behaviours of the acoustic field, the fluid flow field, and the microparticles. Acoustofluidic systems are multi-physics, and each component operates in a different time and length scale. The most accurate modelling approach to resolve the wide range of length and time scales is DNS which fully couples the acoustic and fluid fields using an extremely fine computational mesh. This approach can most precisely predict the multi-physics of acoustofluidic systems, but it is highly costly and time-consuming and is often impractical using the current available computational resources. A more simplified yet still accurate modelling approach can be used for the typical acoustofluidic systems utilising the perturbation methods to calculate the acoustic effects acting on the fluid and microparticles and adding them to the governing equations as external body forces. This approach can significantly decrease the computational cost and time while still predicting the different physics of acoustofluidic systems with a desirable accuracy but some small details especially regarding the acoustofluidic interactions may be missed.

9.2 Further Work

To advance this research further, the following future studies are suggested:

- In this thesis, spherical microparticles were used to study the acoustic manipulation of the particles. Experimental studies and numerical modelling of the acoustic manipulation of microparticles with different shapes (other than spheres) such as cylinders, spheroids ellipsoids, and arbitrary geometries and microbubbles made from various materials can be performed. This will help the investigation of the effects of particle's geometry, bubble size and compressibility on particle manipulation using flexible thin film SAW devices.
- In this research, yeast particles were used to study the acoustic manipulation of as biological organisms. Experimental studies and numerical modelling of the acoustic manipulation different types of biological cells (other than yeast), bacteria, DNAs, etc. can be done. This

will help to study the effectiveness of acoustic manipulation and the effects of SAW on biological species.

- In this thesis, flexible SAW devices bent in concave and convex shapes as well as various twisted geometries were used for particle patterning and the effects were experimentally and numerically investigated. Experimental studies and numerical modelling of manipulation and patterning of microparticles on different bent and distorted geometries of flexible thin film SAW devices as well as making small indentations with different shapes on the surface of the device and filling them with fluid/particle suspension can be carried out. This will help to investigate microparticles and cell behaviour on different SAW geometries and inside the indentation structures.
- In this thesis, microtubes with different geometries were integrated with flexible SAW devices in their original flat shapes for particle patterning and the effects were experimentally and numerically investigated. Experimental studies and numerical modelling of manipulation and patterning of microparticles inside microtubes with different geometries placed on top of SAW devices bent in concave and convex shapes as well as conforming to the geometries of microtubes can be carried out. This will help to investigate microparticles and cell behaviour on different SAW geometries and inside glass microtube with various shapes.
- In this research, capillary bridge channels were integrated with flexible SAW device with flat surface. Experimental investigation and numerical simulation of the manipulation and patterning of microparticles/cells inside capillary bridge channels using different bent, twisted, and distorted geometries of flexible thin film SAW devices can be performed. This will help the study of the effects of the geometry of the flexible SAW devices on microparticle/cell manipulation and patterning.
- In this thesis, DI water was used as the working fluid in the acoustofluidic systems. Experimental studies and numerical simulation of the effects of using various fluids (other than water) to form continuous flow capillary bridge channels can be carried out. This will help the investigation of the effects of different viscosity and Newtonian vs. non-Newtonian fluids on the performance of capillary bridge channels.
- In this research body forces were used to account for the acoustic effects on fluid and particles. For future works, high fidelity methods can be utilised to model the three-dimensional and compressible Navier-Stokes equations of the fluid flow fully-coupled the acoustic fields in order to simulate the acoustofluidic systems. This will help the

investigation and understanding of the interactions between acoustics and microfluidics with a very high accuracy.

References

[1] X. Ding *et al.*, "Surface Acoustic Wave Microfluidics," *Lab on a chip,* 10.1039/C3LC50361E vol. 13, no. 18, pp. 3626-3649, 2013, doi: 10.1039/C3LC50361E.

[2] J. Nam, H. Lim, and S. Shin, "Manipulation of Microparticles Using Surface Acoustic Wave in Microfluidic Systems: A Brief Review," *Korea-Australia Rheology Journal,* journal article vol. 23, no. 4, pp. 255-267, December 01 2011, doi: 10.1007/s13367-011-0031-5.

[3] Y. Q. Fu *et al.*, "Advances in Piezoelectric Thin Films for Acoustic Biosensors, Acoustofluidics and Lab-on-Chip Applications," *Progress in Materials Science,* vol. 89, pp. 31-91, 2017, doi: 10.1016/j.pmatsci.2017.04.006.

[4] M. Wu, A. Ozcelik, J. Rufo, Z. Wang, R. Fang, and T. Jun Huang, "Acoustofluidic Separation of Cells and Particles," *Microsystems & Nanoengineering,* vol. 5, no. 1, p. 32, 2019/06/03 2019, doi: 10.1038/s41378-019-0064-3.

[5] J. Friend and L. Y. Yeo, "Microscale Acoustofluidics: Microfluidics Driven via Acoustics and Ultrasonics," *Reviews of Modern Physics,* vol. 83, no. 2, pp. 647-704, 06/20/ 2011, doi: 10.1103/RevModPhys.83.647.

[6] P. Li and T. J. Huang, "Applications of Acoustofluidics in Bioanalytical Chemistry," *Analytical chemistry,* vol. 91, no. 1, pp. 757-767, 2018, doi: 10.1021/acs.analchem.8b03786.

[7] T. J. Huang, "Acoustofluidics: Merging Acoustics and Microfluidics for Biomedical Applications," *The Journal of the Acoustical Society of America,* vol. 145, no. 3, pp. 1786-1786, 2019/03/01 2019, doi: 10.1121/1.5101531.

[8] G. M. Whitesides, "The Origins and the Future of Microfluidics," *Nature,* vol. 442, no. 7101, p. 368, 2006, doi: 10.1038/nature05058.

[9] K. Wang *et al.*, "Sorting of Tumour Cells in a Microfluidic Device by Multi-Stage Surface Acoustic Waves," *Sensors and Actuators B: Chemical,* vol. 258, pp. 1174-1183, 2017, doi: 10.1016/j.snb.2017.12.013.

[10] F. Petersson, A. Nilsson, C. Holm, H. Jonsson, and T. Laurell, "Separation of Lipids from Blood Utilizing Ultrasonic Standing Waves in Microfluidic Channels," (in eng), *The Analyst,* vol. 129, no. 10, pp. 938-43, Oct 2004, doi: 10.1039/b409139f.

[11] M. Focke, D. Kosse, C. Müller, H. Reinecke, R. Zengerle, and F. von Stetten, "Lab-on-a-Foil: Microfluidics on Thin and Flexible Films," *Lab on a chip,* vol. 10, no. 11, pp. 1365-1386, 2010.

[12] Z. Yang, Y. Zhang, T. Itoh, and R. Maeda, "A Novel MEMS Compatible Lab-on-a-Tube Technology," *Lab on a chip,* vol. 14, no. 24, pp. 4604-4608, 2014.

[13] Y. Lin, C. Gao, Y. Gao, M. Wu, A. A. Yazdi, and J. Xu, "Acoustofluidic Micromixer on Lab-on-a-Foil Devices," *Sensors and Actuators B: Chemical,* vol. 287, pp. 312-319, 2019.

[14] S. Wang, T. Chinnasamy, M. A. Lifson, F. Inci, and U. Demirci, "Flexible substrate-based devices for point-of-care diagnostics," *Trends in Biotechnology,* vol. 34, no. 11, pp. 909-921, 2016.

[15] Y. Yang, S. Xing, Z. Fang, R. Li, H. Koo, and T. Pan, "Wearable Microfluidics: Fabric-Based Digital Droplet Flowmetry for Perspiration Analysis," *Lab on a chip,* vol. 17, no. 5, pp. 926-935, 2017.

[16] D. P. Holmes, B. Tavakol, G. Froehlicher, and H. A. Stone, "Control and Manipulation of Microfluidic Flow via Elastic Deformations," *Soft Matter,* vol. 9, no. 29, pp. 7049-7053, 2013.

[17] J. Kim, J. B. You, S. M. Nam, S. Seo, S. G. Im, and W. Lee, "Rollable Microfluidic Systems with Microscale Bending Radius and Tuning of Device Function with Reconfigurable 3D Channel Geometry," *ACS Applied Materials & Interfaces,* vol. 9, no. 12, pp. 11156-11166, 2017.

[18] A. Dietzel, *Microsystems for Pharmatechnology*. Springer, 2016.

[19] C.-X. Zhao, "Multiphase Flow Microfluidics for the Production of Single or Multiple Emulsions for Drug Delivery," *Advanced Drug Delivery Reviews,* vol. 65, no. 11, pp. 1420-1446, 2013/11/15/ 2013.

[20] R. Riahi, A. Tamayol, S. A. M. Shaegh, A. M. Ghaemmaghami, M. R. Dokmeci, and A. Khademhosseini, "Microfluidics for Advanced Drug Delivery Systems," *Current Opinion in Chemical Engineering,* vol. 7, pp. 101-112, 2015/02/01/ 2015.

[21] I. U. Khan, C. A. Serra, N. Anton, and T. Vandamme, "Microfluidics: A Focus on Improved Cancer Targeted Drug Delivery Systems," *Journal of Controlled Release,* vol. 172, no. 3, pp. 1065-1074, 2013/12/28/ 2013.

[22] N. T. Nguyen, S. A. Shaegh, N. Kashaninejad, and D. T. Phan, "Design, Fabrication and Characterization of Drug Delivery Systems Based on Lab-on-a-Chip Technology,"

(in eng), *Advanced Drug Delivery Reviews,* vol. 65, no. 11-12, pp. 1403-19, Nov 2013, doi: 10.1016/j.addr.2013.05.008.

[23] H. Mulvana, S. Cochran, and M. Hill, "Ultrasound Assisted Particle and Cell Manipulation on-Chip," *Advanced Drug Delivery Reviews,* vol. 65, no. 11, pp. 1600-1610, 2013/11/15/ 2013.

[24] M. Ghahremani *et al.*, "Surface Acoustic Wave Devices for Ocular Drug Delivery," in *2010 IEEE International Ultrasonics Symposium*, 11-14 Oct. 2010 2010, pp. 872-875, doi: 10.1109/ULTSYM.2010.5935970.

[25] J. Nam, H. Lim, D. Kim, and S. Shin, "Separation of Platelets from Whole Blood Using Standing Surface Acoustic Waves in a Microchannel," (in eng), *Lab on a chip,* vol. 11, no. 19, pp. 3361-4, Oct 7 2011, doi: 10.1039/c1lc20346k.

[26] N. Sivanantha *et al.*, "Characterization of Adhesive Properties of Red Blood Cells Using Surface Acoustic Wave Induced Flows for Rapid Diagnostics," *Applied Physics Letters,* vol. 105, no. 10, p. 103704, 2014.

[27] M. Wu *et al.*, "High-Throughput Cell Focusing and Separation via Acoustofluidic Tweezers," *Lab on a chip,* vol. 18, no. 19, pp. 3003-3010, 2018.

[28] X. Ding *et al.*, "Cell Separation Using Tilted-Angle Standing Surface Acoustic Waves," *Proceedings of the National Academy of Sciences,* vol. 111, no. 36, pp. 12992-12997, 2014.

[29] Y. Ai and B. L. Marrone, "Separation of Biological Cells in a Microfluidic Device Using Surface Acoustic Waves (SAWs)," in *SPIE MOEMS-MEMS*, 2014, vol. 8976: SPIE, p. 7.

[30] K. Mutafopulos *et al.*, "Traveling Surface Acoustic Wave (TSAW) Microfluidic Fluorescence Activated Cell Sorter (μFACS)," *Lab on a chip,* vol. 19, no. 14, pp. 2435-2443, 2019.

[31] J. Nam, H. Lim, C. Kim, J. Yoon Kang, and S. Shin, "Density-Dependent Separation of Encapsulated Cells in a Microfluidic Channel by Using a Standing Surface Acoustic Wave," (in eng), *Biomicrofluidics,* vol. 6, no. 2, pp. 24120-2412010, Jun 2012, doi: 10.1063/1.4718719.

[32] Y. Xie, H. Bachman, and T. J. Huang, "Acoustofluidic Methods in Cell Analysis," *TrAC Trends in Analytical Chemistry,* vol. 117, pp. 280-290, 2019.

[33] W. Connacher *et al.*, "Micro/Nano Acoustofluidics: Materials, Phenomena, Design, Devices and Applications," *Lab on a chip,* vol. 18, no. 14, pp. 1952-1996, 2018.

[34] A. Ozcelik *et al.*, "Acoustic Tweezers for the Life Sciences," *Nature methods,* vol. 15, no. 12, pp. 1021-1028, 2018.

[35] M. Baudoin *et al.*, "Spatially Selective Manipulation of Cells with Single-Beam Acoustical Tweezers," *Nat Commun,* vol. 11, no. 1, pp. 1-10, 2020.

[36] F. Xu *et al.*, "The Assembly of Cell-Encapsulating Microscale Hydrogels Using Acoustic Waves," *Biomaterials,* vol. 32, no. 31, pp. 7847-7855, 2011.

[37] W. L. Nyborg, "Acoustic Streaming due to Attenuated Plane Waves," *The Journal of the Acoustical Society of America,* vol. 25, no. 1, pp. 68-75, 1953, doi: 10.1121/1.1907010.

[38] J. Lighthill, "Acoustic Streaming," *Journal of Sound and Vibration,* vol. 61, no. 3, pp. 391-418, 1978, doi: 10.1007/s001620050068.

[39] L. V. King, "On The Acoustic Radiation Pressure on Spheres," *Proceedings of the Royal Society of London. Series A-Mathematical and Physical Sciences,* vol. 147, no. 861, pp. 212-240, 1934, doi: 10.1098/rspa.1934.0215.

[40] K. Yosioka and Y. Kawasima, "Acoustic Radiation Pressure on a Compressible Sphere," *Acta Acustica united with Acustica,* vol. 5, no. 3, pp. 167-173, 1955.

[41] A. A. Doinikov, "Acoustic Radiation Pressure on a Rigid Sphere in a Viscous Fluid," *Proceedings of the Royal Society of London. Series A-Mathematical and Physical Sciences,* vol. 447, no. 1931, pp. 447-466, 1994, doi: 10.1098/rspa.1994.0150.

[42] A. A. Doinikov, "Acoustic Radiation Pressure on a Compressible Sphere in a Viscous Fluid," *Journal of Fluid Mechanics,* vol. 267, pp. 1-22, 1994, doi: 10.1017/S0022112094001096.

[43] D. J. Collins, Z. Ma, J. Han, and Y. Ai, "Continuous Micro-Vortex-Based Nanoparticle Manipulation via Focused Surface Acoustic Waves," *Lab on a chip,* vol. 17, no. 1, pp. 91-103, 2017, doi: 10.1039/C6LC01142J.

[44] L. Schmid, D. A. Weitz, and T. Franke, "Sorting Drops and Cells with Acoustics: Acoustic Microfluidic Fluorescence-Activated Cell Sorter," *Lab on a chip,* vol. 14, no. 19, pp. 3710-3718, 2014, doi: 10.1039/c4lc00588k.

[45] Z. Ma, D. J. Collins, and Y. Ai, "Detachable Acoustofluidic System for Particle Separation via a Traveling Surface Acoustic Wave," *Analytical chemistry,* vol. 88, no. 10, pp. 5316-5323, 2016.

[46] J. Shi *et al.*, "Three-Dimensional Continuous Particle Focusing in a Microfluidic Channel via Standing Surface Acoustic Waves (SSAW)," (in eng), *Lab on a chip,* vol. 11, no. 14, pp. 2319-24, Jul 21 2011, doi: 10.1039/c1lc20042a.

[47] L. Johansson, J. Enlund, S. Johansson, I. Katardjiev, and V. Yantchev, "Surface Acoustic Wave Induced Particle Manipulation in a PDMS Channel—Principle Concepts for Continuous Flow Applications," *Biomedical Microdevices,* vol. 14, no. 2, pp. 279-289, 2012.

[48] A. Fakhfouri, C. Devendran, A. Ahmed, J. Soria, and A. Neild, "The Size Dependant Behaviour of Particles Driven by a Travelling Surface Acoustic Wave (TSAW)," *Lab on a chip,* 10.1039/C8LC01155A vol. 18, no. 24, pp. 3926-3938, 2018, doi: 10.1039/C8LC01155A.

[49] G. Simon *et al.*, "Particle Separation in Surface Acoustic Wave Microfluidic Devices Using Reprogrammable, Pseudo-Standing Waves," *Applied Physics Letters,* vol. 113, no. 4, p. 044101, 2018.

[50] A. Shamloo and M. Boodaghi, "Design and Simulation of a Microfluidic Device for Acoustic Cell Separation," (in eng), *Ultrasonics,* vol. 84, pp. 234-243, Mar 2018, doi: 10.1016/j.ultras.2017.11.009.

[51] R. Tian, G. Nie, J. Liu, E. Pan, and Y. Wang, "On Rayleigh Waves in a Piezoelectric Semiconductor Thin Film over an Elastic Half-space," *International Journal of Mechanical Sciences,* p. 106565, 2021.

[52] N.-T. Nguyen, "Research Highlight Soft Microsystems - A Paradigm Shift in Engineering Small Systems," *Micro and Nanosystems,* vol. 7, no. 1, pp. 2-3, 07/29 2015, doi: 10.2174/1876402907011507291235 46.

[53] R. Tao *et al.*, "Thin Film Flexible/Bendable Acoustic Wave Devices: Evolution, Hybridization and Decoupling of Multiple Acoustic Wave Modes," *Surface and Coatings Technology,* vol. 357, pp. 587-594, 2019.

[54] E. K. Sackmann, A. L. Fulton, and D. J. Beebe, "The Present and Future Role of Microfluidics in Biomedical Research," (in eng), *Nature,* vol. 507, no. 7491, pp. 181-9, Mar 13 2014, doi: 10.1038/nature13118.

[55] D. J. Beebe, G. A. Mensing, and G. M. Walker, "Physics and Applications of Microfluidics in Biology," *Annual Review of Biomedical Engineering,* vol. 4, no. 1, pp. 261-286, 2002, doi: 10.1146/annurev.bioeng.4.112601.125916.

[56] S. Liu *et al.*, "Investigation into the Effect of Acoustic Radiation Force and Acoustic Streaming on Particle Patterning in Acoustic Standing Wave Fields," *Sensors (Basel, Switzerland),* vol. 17, no. 7, p. 1664, 2017, doi: 10.3390/s17071664.

[57] C. W. I. Shields, C. D. Reyes, and G. P. Lopez, "Microfluidic Cell Sorting: A Review of the Advances in the Separation of Cells from Debulking to Rare Cell Isolation," (in eng), *Lab on a chip,* vol. 15, no. 5, pp. 1230-49, Mar 7 2015, doi: 10.1039/c4lc01246a.

[58] T. Franke, A. R. Abate, D. A. Weitz, and A. Wixforth, "Surface Acoustic Wave (SAW) Directed Droplet Flow in Microfluidics for PDMS Devices," *Lab on a chip,* 10.1039/B906819H vol. 9, no. 18, pp. 2625-2627, 2009, doi: 10.1039/B906819H.

[59] A. Ozcelik and Z. Aslan, "A Practical Microfluidic Pump Enabled by Acoustofluidics and 3D Printing," *Microfluidics and Nanofluidics,* vol. 25, no. 1, pp. 1-10, 2021.

[60] D. R. Gossett *et al.*, "Label-free Cell Separation and Sorting in Microfluidic Systems," *Analytical and Bioanalytical Chemistry,* vol. 397, no. 8, pp. 3249-3267, 2010.

[61] J. Shi, H. Huang, Z. Stratton, Y. Huang, and T. J. Huang, "Continuous Particle Separation in a Microfluidic Channel via Standing Surface Acoustic Waves (SSAW)," *Lab on a chip,* 10.1039/B915113C vol. 9, no. 23, pp. 3354-3359, 2009, doi: 10.1039/B915113C.

[62] J. Nam, Y. Lee, and S. Shin, "Size-Dependent Microparticles Separation through Standing Surface Acoustic Waves," *Microfluidics and Nanofluidics,* vol. 11, no. 3, pp. 317-326, 2011, doi: 10.1007/s10404-011-0798-1.

[63] H. Wang *et al.*, "A Continuous-Flow Acoustofluidic Cytometer for Single-Cell Mechanotyping," *Lab on a chip,* vol. 19, no. 3, pp. 387-393, 2019.

[64] G. Liu *et al.*, "Multi-Level Separation of Particles Using Acoustic Radiation Force and Hydraulic Force in a Microfluidic Chip," *Microfluidics and Nanofluidics,* journal article vol. 23, no. 2, p. 23, January 17 2019, doi: 10.1007/s10404-019-2189-y.

[65] G. Destgeer, K. H. Lee, J. H. Jung, A. Alazzam, and H. J. Sung, "Continuous Separation of Particles in a PDMS Microfluidic Channel via Travelling Surface Acoustic Waves (TSAW)," *Lab on a chip,* vol. 13, no. 21, pp. 4210-4216, 2013.

[66] M. C. Jo and R. Guldiken, "Active Density-Based Separation Using Standing Surface Acoustic Waves," *Sensors and Actuators A: Physical,* vol. 187, pp. 22-28, 2012.

[67] J. Shi, X. Mao, D. Ahmed, A. Colletti, and T. J. Huang, "Focusing Microparticles in a Microfluidic Channel with Standing Surface Acoustic Waves (SSAW)," *Lab on a chip,* 10.1039/B716321E vol. 8, no. 2, pp. 221-223, 2008, doi: 10.1039/B716321E.

[68] Q. Zeng, H. W. L. Chan, X. Z. Zhao, and Y. Chen, "Enhanced Particle Focusing in Microfluidic Channels with Standing Surface Acoustic Waves," *Microelectronic Engineering,* vol. 87, no. 5-8, pp. 1204-1206, 2010, doi: 10.1016/j.mee.2009.12.010.

[69] T. Franke, S. Braunmuller, L. Schmid, A. Wixforth, and D. A. Weitz, "Surface Acoustic Wave Actuated Cell Sorting (SAWACS)," *Lab on a chip,* vol. 10, no. 6, pp. 789-94, Mar 21 2010, doi: 10.1039/b915522h.

[70] V. Skowronek, R. W. Rambach, and T. Franke, "Surface Acoustic Wave Controlled Integrated Band-Pass Filter," *Microfluidics and Nanofluidics,* vol. 19, no. 2, pp. 335-341, 2015.

[71] D. J. Collins *et al.*, "Selective Particle and Cell Capture in a Continuous Flow Using Micro-Vortex Acoustic Streaming," *Lab on a chip,* vol. 17, no. 10, pp. 1769-1777, 2017, doi: 10.1039/c7lc00215g.

[72] R. W. Rambach, K. Linder, M. Heymann, and T. Franke, "Droplet Trapping and Fast Acoustic Release in a Multi-Height Device with Steady-State Flow," *Lab on a chip,* vol. 17, no. 20, pp. 3422-3430, 2017.

[73] J. Shi, D. Ahmed, X. Mao, S.-C. S. Lin, A. Lawit, and T. J. Huang, "Acoustic Tweezers: Patterning Cells and Microparticles Using Standing Surface Acoustic Waves (SSAW)," *Lab on a chip,* vol. 9, no. 20, pp. 2890-2895, 2009, doi: 10.1039/b910595f.

[74] A. Nilsson, F. Petersson, H. Jonsson, and T. Laurell, "Acoustic Control of Suspended Particles in Micro Fluidic Chips," (in eng), *Lab on a chip,* vol. 4, no. 2, pp. 131-5, Apr 2004, doi: 10.1039/b313493h.

[75] G. Destgeer, S. Im, B. Hang Ha, J. Ho Jung, M. Ahmad Ansari, and H. Jin Sung, "Adjustable, Rapidly Switching Microfluidic Gradient Generation Using Focused Travelling Surface Acoustic Waves," *Applied Physics Letters,* vol. 104, no. 2, p. 023506, 2014, doi: 10.1063/1.4862322.

[76] J. Dual and D. Möller, "Acoustofluidics 4: Piezoelectricity and Application in the Excitation of Acoustic Fields for Ultrasonic Particle Manipulation," *Lab on a chip,* vol. 12, no. 3, pp. 506-514, 2012.

[77] B. Watson, J. Friend, and L. Yeo, "Piezoelectric Ultrasonic Micro/Milli-Scale Actuators," *Sensors and Actuators A: Physical,* vol. 152, no. 2, pp. 219-233, 2009.

[78] M. Alghane, Y. Q. Fu, B. X. Chen, Y. Li, M. P. Y. Desmulliez, and A. J. Walton, "Streaming Phenomena in Microdroplets Induced by Rayleigh Surface Acoustic Wave," *Journal of Applied Physics,* vol. 109, no. 11, p. 114901, 2011/06/01 2011, doi: 10.1063/1.3586040.

[79] M. Alghane *et al.*, "Nonlinear Hydrodynamic Effects Induced by Rayleigh Surface Acoustic Wave in Sessile Droplets," *Physical Review E,* vol. 86, no. 5, p. 056304, 2012.

[80] S. S. Sadhal, "Acoustofluidics 13: Analysis of Acoustic Streaming by Perturbation Methods," *Lab on a chip,* 10.1039/C2LC40202E vol. 12, no. 13, pp. 2292-2300, 2012, doi: 10.1039/C2LC40202E.

[81] H. Bruus, *Theoretical Microfluidics*. Oxford university press Oxford, 2008.

[82] H. Bruus, "Acoustofluidics 7: The Acoustic Radiation Force on Small Particles," *Lab on a chip,* vol. 12, no. 6, pp. 1014-1021, 2012.

[83] A. A. Doinikov, "Acoustic Radiation Forces: Classical Theory and Recent Advances," in *Recent Research Developments in Acoustics*, vol. 1, 2003, ch. 3, pp. 39-67.

[84] M. Settnes and H. Bruus, "Forces Acting on a Small Particle in an Acoustical Field in a Viscous Fluid," *Physical Review E,* vol. 85, no. 1, p. 016327, 2012, doi: 10.1103/PhysRevE.85.016327.

[85] R. Barnkob, P. Augustsson, T. Laurell, and H. Bruus, "Acoustic Radiation- and Streaming-Iduced Microparticle Velocities Determined by Microparticle Image Velocimetry in an Ultrasound Symmetry Plane," *Physical Review E,* vol. 86, no. 5, p. 056307, 2012, doi: 10.1103/PhysRevE.86.056307.

[86] L. P. Gorkov, "On the Forces Acting on a Small Particle in an Acoustical Field in an Ideal Fluid," *Soviet Physics - Doklady,* vol. 6, pp. 773-775, 1962.

[87] H. Jin *et al.*, "Flexible Surface Acoustic Wave Resonators Built on Disposable Plastic Film for Electronics and Lab-on-a-Chip Applications," *Scientific Reports,* vol. 3, p. 2140, 2013.

[88] X. He *et al.*, "High Sensitivity Humidity Sensors Using Flexible Surface Acoustic Wave Devices Made on Nanocrystalline ZnO/Polyimide Substrates," *Journal of Materials Chemistry C,* vol. 1, no. 39, pp. 6210-6215, 2013.

[89] J. Chen *et al.*, "Bendable Transparent ZnO Thin Film Surface Acoustic Wave Strain Sensors on Ultra-Thin Flexible Glass Substrates," *Journal of Materials Chemistry C,* vol. 2, no. 43, pp. 9109-9114, 2014.

[90] J. Zhou, S. Dong, H. Jin, B. Feng, and D. Wang, "Flexible Surface Acoustic Wave Device With AlN Film on Polymer Substrate," *Journal of Control Science and Engineering,* vol. 2012, p. 5, 2012.

[91] J. Zhou *et al.*, "Flexible Surface Acoustic Wave Devices and Its Applications In Microfluidics," *MRS Online Proceedings Library Archive,* vol. 1659, pp. 27-33, 2014.

[92] J. Luo *et al.*, "Flexible and Transparent Surface Acoustic Wave Microsensors and Microfluidics," *Procedia Engineering,* vol. 120, pp. 717-720, 2015.

[93] E. Lim, L. Lee, L. Y. Yeo, Y. M. Hung, and M. K. Tan, "Acoustically Driven Micromixing: Effect of Transducer Geometry," *IEEE Transactions on Ultrasonics, Ferroelectrics, and Frequency Control,* vol. 66, no. 8, pp. 1387-1394, 2019.

[94] Y. Liu *et al.*, "Flexible and Bendable Acoustofluidics Based on Zno Film Coated Aluminium Foil," *Sensors and Actuators B: Chemical,* vol. 221, pp. 230-235, 2015.

[95] R. Tao *et al.*, "Hierarchical Nanotexturing Enables Acoustofluidics on Slippery yet Sticky, Flexible Surfaces," *Nano Letters,* vol. 20, no. 5, pp. 3263-3270, 2020/05/13 2020, doi: 10.1021/acs.nanolett.0c00005.

[96] Y. Q. Fu *et al.*, "Recent Developments on ZnO Films for Acoustic Wave Based Bio-Sensing and Microfluidic Applications: A Review," *Sensors and Actuators B: Chemical,* vol. 143, no. 2, pp. 606-619, 2010.

[97] X. Tao *et al.*, "Three-Dimensional Tetrapodal ZnO Microstructured Network Based Flexible Surface Acoustic Wave Device for Ultraviolet and Respiration Monitoring Applications," *ACS Applied Nano Materials,* vol. 3, no. 2, pp. 1468-1478, 2020.

[98] R. Tao *et al.*, "Bimorph Material/Structure Designs for High Sensitivity Flexible Surface Acoustic Wave Temperature Sensors," *Scientific Reports,* vol. 8, no. 1, pp. 1-9, 2018.

[99] T.-F. Hong, W.-J. Ju, M.-C. Wu, C.-H. Tai, C.-H. Tsai, and L.-M. Fu, "Rapid Prototyping of PMMA Microfluidic Chips Utilizing a CO2 Laser," *Microfluidics and Nanofluidics,* vol. 9, no. 6, pp. 1125-1133, 2010.

[100] A. Liga, J. A. Morton, and M. Kersaudy-Kerhoas, "Safe and Cost-Effective Rapid-Prototyping of Multilayer PMMA Microfluidic Devices," *Microfluidics and Nanofluidics,* vol. 20, no. 12, pp. 1-12, 2016.

[101] A. M. Pentecost and R. S. Martin, "Fabrication and Characterization of All-Polystyrene Microfluidic Devices with Integrated Electrodes and Tubing," *Analytical Methods,* vol. 7, no. 7, pp. 2968-2976, 2015.

[102] R. Tran *et al.*, "Simplified Prototyping of Perfusable Polystyrene Microfluidics," *Biomicrofluidics,* vol. 8, no. 4, p. 046501, 2014.

[103] H. Li, Y. Fan, R. Kodzius, and I. G. Foulds, "Fabrication of Polystyrene Microfluidic Devices Using a Pulsed CO2 Laser System," *Microsystem Technologies,* vol. 18, no. 3, pp. 373-379, 2012.

[104] K. Sato, S. Kamada, and K. Minami, "Development of Microstretching Device to Evaluate Cell Membrane Strain Field Around Sensing Point of Mechanical Stimuli," *International Journal of Mechanical Sciences,* vol. 52, no. 2, pp. 251-256, 2010.

[105] J. Lei, P. Glynne-Jones, and M. Hill, "Acoustic Streaming in the Transducer Plane in Ultrasonic Particle Manipulation Devices," *Lab on a chip,* vol. 13, no. 11, pp. 2133-2143, 2013.

[106] Y. Sriphutkiat and Y. Zhou, "Acoustic Manipulation of Microparticle in a Cylindrical Tube for 3D Printing," *Rapid Prototyping Journal,* 2019.

[107] P. Mishra, M. Hill, and P. Glynne-Jones, "Deformation of Red Blood Cells Using Acoustic Radiation Forces," *Biomicrofluidics,* vol. 8, no. 3, p. 034109, 2014.

[108] B. Raiton, J. McLaughlan, S. Harput, P. Smith, D. Cowell, and S. Freear, "The Capture of Flowing Microbubbles with an Ultrasonic Tap Using Acoustic Radiation Force," *Applied Physics Letters,* vol. 101, no. 4, p. 044102, 2012.

[109] I. Gralinski, S. Raymond, T. Alan, and A. Neild, "Continuous Flow Ultrasonic Particle Trapping in a Glass Capillary," *Journal of Applied Physics,* vol. 115, no. 5, p. 054505, 2014.

[110] P. O'Mahoney, C. McDougall, P. Glynne-Jones, and M. MacDonald, "Acoustic Trapping in Bubble-Bounded Micro-Cavities," *Optofluidics, Microfluidics and Nanofluidics,* vol. 3, no. 1, 2016.

[111] B. Hammarström *et al.*, "Non-Contact Acoustic Cell Trapping in Disposable Glass Capillaries," *Lab on a chip,* vol. 10, no. 17, pp. 2251-2257, 2010.

[112] Z. Mao *et al.*, "Enriching Nanoparticles via Acoustofluidics," *ACS Nano,* vol. 11, no. 1, pp. 603-612, 2017.

[113] Y. Xie *et al.*, "Microfluidic Isolation and Enrichment of Nanoparticles," *ACS Nano,* vol. 14, no. 12, pp. 16220--16240, 2020.

[114] J. P. Lata, F. Guo, J. Guo, P. H. Huang, J. Yang, and T. J. Huang, "Surface Acoustic Waves Grant Superior Spatial Control of Cells Embedded in Hydrogel Fibers," *Advanced Materials,* vol. 28, no. 39, pp. 8632-8638, 2016.

[115] G. Lisa, R. Stefan, D.-K. Branka, and B. Ewald, "A New Ultrasound-Based Cell Immobilisation Technique," in *Proceedings of Forum Acusticum*, 2002, pp. 16-20.09.

[116] G. Goddard, J. C. Martin, S. W. Graves, and G. Kaduchak, "Ultrasonic Particle‐Concentration for Sheathless Focusing of Particles for Analysis in a Flow Cytometer," *Cytometry Part A: The Journal of the International Society for Analytical Cytology,* vol. 69, no. 2, pp. 66-74, 2006.

[117] F. Guo *et al.*, "Precise Manipulation and Patterning of Protein Crystals for Macromolecular Crystallography Using Surface Acoustic Waves," *Small,* vol. 11, no. 23, pp. 2733-2737, 2015.

[118] M. A. Sobanski, C. R. Tucker, N. E. Thomas, and W. T. Coakley, "Sub-Micron Particle Manipulation in an Ultrasonic Standing Wave: Applications in Detection of Clinically Important Biomolecules," *Bioseparation,* vol. 9, no. 6, pp. 351-357, 2000.

[119] I. Gralinski, T. Alan, and A. Neild, "Non-Contact Acoustic Trapping in Circular Cross-Section Glass Capillaries: A Numerical Study," *The Journal of the Acoustical Society of America,* vol. 132, no. 5, pp. 2978-2987, 2012.

[120] M. W. Ley and H. Bruus, "Three-Dimensional Numerical Modeling of Acoustic Trapping in Glass Capillaries," *Physical Review Applied,* vol. 8, no. 2, p. 024020, 2017.

[121] J. S. Bach and H. Bruus, "Theory of Acoustic Trapping of Microparticles in Capillary Tubes," *Physical Review E,* vol. 101, no. 2, p. 023107, 2020.

[122] C. Soitu *et al.*, "Microfluidic Chambers Using Fluid Walls for Cell Biology," *PNAS,* vol. 115, pp. E5926–E5933, 2018.

[123] M. H. Panhwar *et al.*, "High-Throughput Cell and Spheroid Mechanics in Virtual Fluidic Channels," *Nat Commun,* Research Support, Non-U.S. Gov't vol. 11, no. 1, p. 2190, May 4 2020, doi: 10.1038/s41467-020-15813-9.

[124] J. J. Hawkes *et al.*, "Capillary Bridge Acoustofluidics," presented at the Acoustofluidics 2020, 26-27 August, 2020.

[125] A. Nag, B. R. Panda, and A. Chattopadhyay, "Performing Chemical Reactions in Virtual Capillary of Surface Tension-Confined Microfluidic Devices," *Pramana,* vol. 65, no. 4, pp. 621-630, 2005.

[126] F. Bunge, S. van den Driesche, and M. J. Vellekoop, "Symmetric Surficial Phaseguides: A Passive Technology to Generate Wall-Less Channels by Two-Dimensional Guiding Elements," *Microfluidics and Nanofluidics,* vol. 20, no. 7, p. 95, 2016.

[127] J. H. Yeon, H. R. Ryu, M. Chung, Q. P. Hu, and N. L. Jeon, "In Vitro Formation and Characterization of a Perfusable Three-Dimensional Tubular Capillary Network in Microfluidic Devices," *Lab on a chip,* vol. 12, no. 16, pp. 2815-2822, 2012.

[128] W. Lee, Y. Heo, and S. Takeuchi, "Wall-Less Liquid Pathways Formed with Three-Dimensional Microring Arrays," *Applied Physics Letters,* vol. 101, no. 11, p. 114108, 2012.

[129] R. Renaudot *et al.*, "A Programmable and Reconfigurable Microfluidic Chip," *Lab on a chip,* vol. 13, no. 23, pp. 4517-4524, 2013.

[130] D. P. Taylor and G. V. Kaigala, "Reconfigurable Microfluidics: Real-Time Shaping of Virtual Channels Through Hydrodynamic Forces," *Lab on a chip,* vol. 20, pp. 1720–1728, 2020, doi: 10.1039/d0lc00197j.

[131] H. Gao *et al.*, "Capillary‐Bridge Mediated Assembly of Conjugated Polymer Arrays toward Organic Photodetectors," *Advanced Functional Materials,* vol. 27, no. 34, p. 1701347, 2017.

[132] J. Feng *et al.*, "“Capillary‐Bridge Lithography” for Patterning Organic Crystals toward Mode‐Tunable Microlaser Arrays," *Advanced Materials,* vol. 29, no. 1, p. 1603652, 2017.

[133] P. A. Kralchevsky and K. Nagayama, "Capillary Bridges and Capillary-Bridge Forces," in *Studies in Interface Science*, vol. 10: Elsevier, 2001, pp. 469-502.

[134] S. P. Zhang *et al.*, "Digital Acoustofluidics Enables Contactless and Programmable Liquid Handling," *Nat Commun,* vol. 9, no. 1, pp. 1-11, 2018.

[135] X. Weng, Y. Kang, Q. Guo, B. Peng, and H. Jiang, "Recent Advances in Thread-Based Microfluidics for Diagnostic Applications," (in eng), *Biosens Bioelectron,* Review vol. 132, pp. 171-185, May 1 2019, doi: 10.1016/j.bios.2019.03.009.

[136] P. Dunne *et al.*, "Liquid Flow and Control without Solid Walls," *Nature,* vol. 581, no. 7806, pp. 58-62, 2020.

[137] J. J. Hawkes, N. J. Goddard, P. R. Fielden, S. Mohr, B. Bastani, and M. Mcdonnell, "Thin Plastic Walls and Flexural Waves for Attracting Cells," in *International Congress of Ultrasonics*, Gadansk, 2011.

[138] J. J. Hawkes, N. J. Goddard, S. Mohr, and M. B. McDonnell, "Flexural Waves and Some Simple Resonators," presented at the USWNet 2010 Conference, Groningen , The Netherlands, 2010.

[139] M. Wiklund, S. Radel, and J. J. Hawkes, "Acoustofluidics 21: Ultrasound-Enhanced Immunoassays and Particle Sensors," *Lab on a chip,* vol. 13, no. 1, pp. 25-39, 2013.

[140] G. K. Batchelor, *An Introduction to Fluid Dynamics* (Cambridge Mathematical Library). Cambridge: Cambridge University Press, 2000.

[141] S. Shiokawa, Y. Matsui, and T. Ueda, "Study on SAW Streaming and Its Application to Fluid Devices," *Japanese Journal of Applied Physics,* vol. 29, no. S1, p. 137, 1990.

[142] C. T. Crowe, J. D. Schwarzkopf, M. Sommerfeld, and Y. Tsuji, *Multiphase Flows with Droplets and Particles*. CRC press, 2011.

[143] C. T. Crowe, *Multiphase Flow Handbook*. CRC press, 2005.

[144] C. Devendran, T. Albrecht, J. Brenker, T. Alan, and A. Neild, "The Importance of Travelling Wave Components in Standing Surface Acoustic Wave (SSAW) Systems," *Lab on a chip,* vol. 16, no. 19, pp. 3756-3766, 2016, doi: 10.1039/C6LC00798H.

[145] COMSOL, "COMSOL User's Guide," 5.6 ed, 2018.

[146] D. Kuzmin and J. Hamalainen, *Finite Element Methods for Computational Fluid Dynamics: A Practical Guide*. Society for Industrial and Applied Mathematics, 2014.

[147] D. J. Mavriplis, "Accelerating Newton Method Continuation for CFD Problems," in *AIAA Scitech 2019 Forum*, 2019, p. 0100.

[148] W. Thielicke and E. Stamhuis, "PIVlab–towards User-Friendly, Affordable and Accurate Digital Particle Image Velocimetry in MATLAB," *Journal of Open Research Software,* vol. 2, no. 1, 2014.

[149] W. Thielicke, "The Flapping Flight of Birds: Analysis and Application," University of Groningen, 2014.

[150] W. Thielicke and E. J. Stamhuis, "The Effects of Wing Twist in Slow-Speed Flapping Flight of Birds: Trading Brute Force Against Efficiency," *Bioinspiration & Biomimetics,* vol. 13, no. 5, p. 056015, 2018.

[151] D. Botstein and G. R. Fink, "Yeast: An Experimental Organism for 21st Century Biology," *Genetics,* vol. 189, no. 3, pp. 695-704, 2011.

[152] X. Tao *et al.*, "3D Patterning/Manipulating Microparticles and Yeast Cells Using ZnO/Si Thin Film Surface Acoustic Waves," *Sensors and Actuators B: Chemical,* vol. 299, p. 126991, 2019.

[153] W. S. Rasband, "ImageJ," ed: Bethesda, MD, 1997.

[154] M. D. Abràmoff, P. J. Magalhães, and S. J. Ram, "Image Processing with ImageJ," *Biophotonics International,* vol. 11, no. 7, pp. 36-42, 2004.

[155] C. A. Schneider, W. S. Rasband, and K. W. Eliceiri, "NIH Image to ImageJ: 25 Years of Image Analysis," *Nature Methods,* vol. 9, no. 7, pp. 671-675, 2012.

[156] P. L. Walls and B. Abedian, "Bivelocity Gas Dynamics of Micro-Channel Couette Flow," *International Journal of Engineering Science,* vol. 79, pp. 21-29, 2014.

[157] X. Chen, K. Toh, J. Chai, and C. Yang, "Developing Pressure-Driven Liquid Flow in Microchannels Under the Electrokinetic Effect," *International Journal of Engineering Science,* vol. 42, no. 5-6, pp. 609-622, 2004.

[158] G. Destgeer and H. J. Sung, "Recent Advances in Microfluidic Actuation and Micro-Object Manipulation via Surface Acoustic Waves," *Lab on a chip,* vol. 15, no. 13, pp. 2722-2738, 2015.

[159] Z. Tian *et al.*, "Wave Number–Spiral Acoustic Tweezers for Dynamic and Reconfigurable Manipulation of Particles and Cells," *Science Advances,* vol. 5, no. 5, p. eaau6062, 2019.

[160] T. D. Nguyen, V. T. Tran, Y. Q. Fu, and H. Du, "Patterning and Manipulating Microparticles into a Three-Dimensional Matrix Using Standing Surface Acoustic Waves," *Applied Physics Letters,* vol. 112, no. 21, p. 213507, 2018.

[161] S. Y. Lee *et al.*, "Water-Resistant Flexible GaN LED on a Liquid Crystal Polymer Substrate for Implantable Biomedical Applications," *Nano Energy,* vol. 1, no. 1, pp. 145-151, 2012.

[162] G. T. Hwang, M. Byun, C. K. Jeong, and K. J. Lee, "Flexible Piezoelectric Thin‐Film Energy Harvesters and Nanosensors for Biomedical Applications," *Advanced Healthcare Materials,* vol. 4, no. 5, pp. 646-658, 2015.

[163] S. R. Krishnan *et al.*, "Epidermal Electronics for Noninvasive, Wireless, Quantitative Assessment of Ventricular Shunt Function in Patients with Hydrocephalus," *Science Translational Medicine,* vol. 10, no. 465, 2018.

[164] A. R. Rezk, J. K. Tan, and L. Y. Yeo, "HYbriD Resonant Acoustics (HYDRA)," *Advanced Materials,* vol. 28, no. 10, pp. 1970-1975, 2016.

[165] R. P. Hodgson, M. Tan, L. Yeo, and J. Friend, "Transmitting High Power RF Acoustic Radiation via Fluid Couplants into Superstrates for Microfluidics," *Applied Physics Letters,* vol. 94, no. 2, p. 024102, 2009.

[166] N. C. Speller *et al.*, "Cutting Edge Microfluidics: Xurography and Microwave," *Sensors and Actuators B: Chemical,* vol. 291, pp. 250-256, 2019.

[167] I. González, I. C. Navarrete, A. Vargas, and M. M. Camacho, "Aluminium-Foil Chip for Ultrasonic Particle Manipulation," in *Acoustofluidics*, Lille, France, 2018.

[168] J. J. Hawkes and W. T. Coakley, "A Continuous Flow Ultrasonic Cell-Filtering Method," *Enzyme and Microbial Technology,* vol. 19, no. 1, pp. 57-62, 1996.

[169] J. J. Hawkes and W. T. Coakley, "Force Field Particle Filter, Combining Ultrasound Standing Waves and Laminar Flow," *Sensors and Actuators B: Chemical,* vol. 75, no. 3, pp. 213-222, 2001.